3-10-2010

Improved Modeling of Midlatitude D-region Ionospheric Absorption of High Frequency Radio Signals during Solar X-ray Flares

Evelyn A. Schumer

IMPROVED MODELING OF MIDLATITUDE D-REGION IONOSPHERIC ABSORPTION OF HIGH FREQUENCY RADIO SIGNALS DURING SOLAR X-RAY FLARES

DISSERTATION

Evelyn A. Schumer, Major, USAF
AFIT/DS/ENP/09-J01

DEPARTMENT OF THE AIR FORCE
AIR UNIVERSITY

AIR FORCE INSTITUTE OF TECHNOLOGY

Wright-Patterson Air Force Base, Ohio

The views expressed in this dissertation are those of the author and do not reflect the official policy or position of the United States Air Force, Department of Defense, or the United States Government.

AFIT/DS/ENP/09-J01

IMPROVED MODELING OF MIDLATITUDE D-REGION IONOSPHERIC ABSORPTION OF HIGH FREQUENCY RADIO SIGNALS DURING SOLAR X-RAY FLARES

DISSERTATION

Presented to the Faculty

Department of Engineering Physics

Graduate School of Engineering and Management

Air Force Institute of Technology

Air University

Air Education and Training Command

In Partial Fulfillment of the Requirements for the

Degree of Doctor of Philosophy

Evelyn A. Schumer, BS, MS

Major, USAF

March 2010

AFIT/DS/ENP/09-JO1

IMPROVED MODELING OF MIDLATITUDE D-REGION IONOSPHERIC ABSORPTION OF HIGH FREQUENCY RADIO SIGNALS DURING SOLAR X-RAY FLARES

Evelyn A. Schumer, BS, MS
Major, USAF

Approved:

//SIGNED//	
Lt Col Christopher G. Smithtro (Chairman)	Date
//SIGNED//	
William F. Bailey, PhD (member)	Date
//SIGNED//	
Steven C. Gustafson, PhD (member)	Date

Accepted:

//SIGNED//	
M. U. Thomas, PhD Dean, Graduate School of Engineering and Management	Date

Abstract

High frequency (HF) radio communication is widely used for real-time, medium to long range communications due to its low cost of operation and maintenance. However, HF communication is strongly dependent on the state of the ionosphere, which is sensitive to solar X-ray flares. The lowest region of the ionosphere, the D-region, is the region in which the majority of the absorption of HF radio wave energy occurs. D-region HF absorption depends on the local electron density, which is enhanced during a solar X-ray flare. HF propagation data obtained during the HF Investigation of D-region Ionospheric Variation Experiment (HIDIVE) and obtained at the Canadian Space Agency NORSTAR riometer in Pinawa, Manitoba, Canada and X-ray flux data, as reported by GOES satellites, are analyzed here for the purpose of validating and improving the performance of two HF absorption models, the operational Space Weather Prediction Center (SWPC) D-region Absorption model and the physical AbbyNormal model. The SWPC D-region absorption model is an empirical model providing real-time global predictions of D-region absorption, and the physical Absorption by the D and E Region of HF Signals with Normal Incidence (AbbyNormal) model is based on simple D-region chemistry and provides near real-time predictions of midlatitude D-region HF absorption. Analysis of the HIDIVE data revealed an absorption dependence on signal frequency of $f^{-1.24}$, where f is signal frequency, and a $Cos^{0.9}(\chi)$ dependence on solar zenith angle, χ. These relations differ from what is used in the SWPC model, and from these relations, a new empirical model, the Empirical HIDIVE Absorption (EHA) model, is developed. The EHA model can be used to improve the SWPC model performance. NO density data obtained with the Student Nitric Oxide Explorer (SNOE) and during the Halogen Occultation Experiment (HALOE) are used to improve the method by which the AbbyNormal model defines the nitric oxide (NO) profile within the atmosphere. Improved NO profiles allows for better AbbyNormal characterization of the ionosphere and HF propagation and for better prediction of solar flare-induced HF absorption. This research is sponsored by the Air Force Office of Scientific Research and the Air Force Weather Agency.

To my husband and my parents.

Thank you for your support and encouragement throughout the years.

Acknowledgments

I would like to express my deepest appreciation to my faculty advisor, Lt Col Christopher Smithtro, and my mentor, Dr William Bailey, for their guidance and support throughout this effort. I will forever be grateful for their wisdom and patience.

I am also indebted to Jeffrey and Eileen Sitler whose encouragement and assistance throughout my time at AFIT was vital to my success.

Evelyn A. Schumer

Table of Contents

Page

1. INTRODUCTION 1

2. BACKGROUND 5

2.1 THE IONOSPHERE 5
2.1.1 Ionospheric Layers 6
2.1.2 The Chapman Function 8
2.2 D-REGION CHEMISTRY 13
2.2.1 D-region Chemistry 13
2.2.2 D-region Plasma Density Profile. 18
2.2.3 First Order Relationship between Solar Zenith Angle and N_e. 19
2.2.4 NO in the Atmosphere. 21
2.3 D-REGION MIDLATITUDE IONOSPHERIC VARIABILITY 22
2.3.1 Diurnal and Seasonal Variability. 22
2.3.2 Variations in Solar Radiation Flux. 23
2.4 REFRACTION OF RADIO WAVES IN THE IONOSPHERE 26
2.4.1 Wave Equations. 26
2.4.2 Wave Propagation in the Ionosphere. 28
2.4.3 No Collisions, No External Magnetic Field. 31
2.4.4. Significant Collisions, No External Magnetic Field. 31
2.4.5 Propagation Modes. 33
2.5. HF ABSORPTION IN THE D-REGION 35
2.6 SOLAR FLARES 38
2.6.1 Flare Spectrum 38
2.6.2 Flare Classification 41

3. IONOSPHERIC ABSORPTION AND PROPAGATION PREDICTION METHODS 45

3.1 OYINLOYE 45
3.2 STONEHOCKER 46
3.3 SWPC D-REGION ABSORPTION MODEL 49
3.4 THE ABBYNORMAL PHYSICAL MODEL 52

4. HF PROPAGATION DATA 54

4.1 HIDIVE DATA 54
4.2 RIOMETER DATA 58

5. SOLAR QUIET REFERENCE CURVES 60

5.1 SQ CURVE 60
5.2 MONTH-SPECIFIC SQ CURVES 61
5.3 DAY-SPECIFIC SQ CURVES 64
5.4 DETERMINATION OF COSINE DEPENDENCE 69

6. FLARE INDUCED HF ABSORPTION MEASUREMENTS 72

6.1 INITIAL CRITERIA FOR FLARE SELECTION 72
6.2 "PREMIER" FLARES 73
6.2.1 Problematic Issues Affecting Absorption Data. 73
6.2.2 Local Interference. 73
6.2.3 Propagation Mode Changes. 74
6.2.4 Lag in Flare-Induced Absorption 76
6.2.5 Sporadic Signal Strength Enhancements. 80
6.2.6 The "Premier" Flares. 81
6.3 NORMALIZATION OF FLARE-INDUCED ABSORPTION DATA 82

6.3.1 Normalization Scheme. 82
6.3.2 Normalization Scheme Validation....84
6.4 ABSORPTION DEPENDENCE ON SIGNAL FREQUENCY 87
6.4.1 HIDIVE Absorption Dependence of Frequency.....87

7. EMPIRICAL HIDIVE D-REGION ABSORPTION (EHA) MODEL 98

7.1 EHA MODEL....98
7.2 OPERATIONAL EHA MODEL 100

8. VALIDATION OF ABBYNORMAL, SWPC, AND EHA MODEL PERFORMANCES 102

8.1 VALIDATION OF MODEL PERFORMANCES 102
8.2 ANALYSIS OF MODEL DAYTIME SIGNAL STRENGTH PERFORMANCE 111
8.3 ANALYSIS OF MODEL FLARE-INDUCED ABSORPTION PERFORMANCE 112

9. ABBYNORMAL ANALYSIS....116

9.1 ABBYNORMAL VALIDATION ANALYSIS....116
9.2 ABBYNORMAL SEASONAL VARIATION OF N_E PROFILES 117
9.3 ORIGINAL ABBYNORMAL NO PROFILE COMPARED TO DATA 125
9.4 NEW METHODS FOR DEFINING ABBYNORMAL NO PROFILES....128
9.4.1 Rescaling MSIS Densities. *128*
9.4.2 Empirical NO Model Profile.....*136*
9.4.3 HALOE Data Profile....*138*
9.5 MSR MODEL-BASED AND SNOE-BASED ABBYNORMAL RESULTS 139
9.5.1 Predictions for 5 MHz blo-wwv transmission. *139*
9.5.2 Predictions for 10 MHz blo-wwv transmission. *145*
9.5.3 Predictions for 5 MHz kf-wwv transmission. *149*
9.5.4 Predictions for 10 MHz kf-wwv transmission. *154*
9.5.5 AbbyNormal Performances for 15 MHz kf-wwv Transmission. *161*
9.6 ABBYNORMAL RESULTS SUMMARY 165
9.6.1 Summary of 5 MHz blo-wwv Analysis....*166*
9.6.2 Summary of 10 MHz blo-wwv Analysis....*166*
9.6.3 Summary of 5 MHz kf-wwv Analysis....*167*
9.6.4 Summary of 10 MHz kf-wwv Analysis....*167*
9.6.5 Summary of 15 MHz kf-wwv Analysis....*167*
9.7. ABBYNORMAL ANALYSIS SUMMARY 168

10. DISCUSSION....171

10.1 DATA 171
10.2 SOLAR QUIET CURVES....172
10.2.1 Flare-Induced Absorption....*172*
10.2.2 Local NO Density....*172*
10.3 FREQUENCY DEPENDENCE OF MIDLATITUDE HF ABSORPTION 175
10.4 FUTURE WORK FOR ABBYNORMAL IMPROVEMENT....176
10.5 CONCLUSION....178

APPENDIX A. SIGNAL STRENGTHS AND ABSORPTION PREDICTIONS OF THE ABBY NORMAL, EHA, AND SWPC MODELS....180

A.1 SIGNAL STRENGTH PREDICTIONS FOR THE 5 MHZ BLO-WWV HIDIVE TRANSMISSION....180
A.2 X-RAY FLARE INDUCED ABSORPTION PREDICTIONS FOR THE 5 MHZ BLO-WWV SIGNAL 182
A.3 SIGNAL STRENGTH PREDICTIONS FOR THE 10 MHZ KF-WWV HIDIVE TRANSMISSION....184
A.4 X-RAY FLARE INDUCED ABSORPTION PREDICTIONS FOR THE 10 MHZ KF-WWV SIGNAL....186
A.5 SIGNAL STRENGTH PREDICTIONS FOR THE 15 MHZ KF-WWV HIDIVE TRANSMISSION....188
A.6 X-RAY FLARE INDUCED ABSORPTION PREDICTIONS FOR THE 15 MHZ KF-WWV SIGNAL....190

APPENDIX B. ABBYNORMAL MODEL VERSIONS PREDICTIONS OF 5 MHZ BLO-WWV TRANSMISSION....192

APPENDIX C. ABBYNORMAL MODEL VERSIONS PREDICTIONS OF 10 MHZ BLO-WWV TRANSMISSION 199

APPENDIX D. ABBYNORMAL MODEL VERSIONS PREDICTIONS OF 5 MHZ KF-WWV TRANSMISSION 206

APPENDIX E. ABBYNORMAL MODEL VERSIONS PREDICTIONS OF 10 MHZ KF-WWV TRANSMISSION 213

APPENDIX F. ABBYNORMAL MODEL VERSIONS PREDICTIONS OF 15 MHZ KF-WWV TRANSMISSION 220

APPENDIX G. FLARE AVAILABILITY 227

BIBLIOGRAPHY 230

List of Figures

Figure		Page
2.1.1	Ionospheric Electron Density	6
2.1.2	Relationship between the radiation path length, solar zenith angle, and change in altitude	10
2.1.3	Normalized Chapman Functions	12
2.2.1	Production Rate Profiles	14
2.3.1	The Monthly Averages of the F10.7 Index	24
2.3.2	Variation in N_e profile from solar cycle minimum to solar cycle maximum	26
2.4.1	Snell's Law	33
2.4.2	Various propagation modes available to a 10 MHz radio signal on 15 January 2004 at 19:00 UT	35
2.5.1	Ionospheric profiles of ν, N_e, and their product and the expected loss of a 5 MHz signal	37
2.6.1	The relative radiation flux for various emissions	39
2.6.2	Temporal evolution of soft and hard X-rays during two flares on 5 November 1980	40
2.6.3	GOES X-Ray Flux Data on 14 July 2000	44
3.2.1	Stonehocker's Data	47
3.2.2	Stonehocker's relationship between SWF duration and the importance classification of a solar flare	48
3.3.1	The D-region Absorption Prediction product produced by SWPC	51
3.4.1	The DDDR model	53
4.1.1	Typical HIDIVE data for the WWV transmissions received at the KF station during solar quiet conditions on 9 Feb 2003	56
4.1.2	HIDIVE data on 26 Feb 2004	57
4.2.1	The riometer data during the X18 flare on 2 April 2001	59
5.1.1	An example of fitting an SQ curve to HIDIVE data	61

Figure		Page
5.1.2	HIDIVE data for the 5 MHz blo-wwv signal for several dates in December 2003	62
5.2.1	Shown are the HIDIVE data for the 5 MHz blo-wwv signal for several dates in December 2003	64
5.3.1	HIDIVE data and the SQ curves resulting from fitting equations 5.3.1 and 5.3.2 to HIDIVE data occurring during solar quiet conditions on 26 February 2004	66
5.3.2	The SQ curves resulting from fitting equations 5.3.1 and 5.3.2 to HIDIVE data occurring during solar quiet conditions on 26 February 2004	67
5.3.3	HIDIVE data and the SQ curves resulting from fitting equations 5.3.1 and 5.3.2 to HIDIVE data occurring during solar quiet conditions on 15 July 2004	68
5.3.4	The SQ curves resulting from fitting equations 5.3.1 and 5.3.2 to HIDIVE data occurring during solar quiet conditions on 15 July 2004	69
5.4.1	Results of fitting equation 5.3.1 to the quiet-time HIDIVE data on 21 December 2004	71
6.2.1	HF signal strength data collected at the BLO HIDIVE receiver on 26 February 2004 show local interference	74
6.2.2	Change in propagation modes is seen in daytime HIDIVE data	75
6.2.3	Flare-induced absorption of the 5 MHz blo-wwv HIDIVE transmission lags the peak of the M2.4 flare	77
6.2.4	HIDIVE data for the 5 MHz blo-wwv transmission on 23 July 2004	79
6.2.5	HIDIVE data for the 10 MHz kf-wwv transmission on 23 July 2004	79
6.2.6	HIDIVE data for the 15 MHz kf-wwv transmission on 23 July 2004	80
6.2.7	HIDIVE data for the 5 MHz blo-wwv transmission on 9 September 2005 are shown along with the soft and hard GOES X-ray flux	81
6.3.1	Local signal elevation angle during i^{th} pass through the D-region	83

Figure		Page
6.3.2	Normalized flare-induced absorption data for the 10 MHz blo-wwv and 10 MHz kf-wwv HIDIVE transmissions during the M2.4 and C5.6 flares on 24 October 2004	85
6.3.3	Normalized flare-induced absorption data for the 10 MHz blo-wwv and 10 MHz kf-wwv HIDIVE transmissions during the C2.5 flare on 17 July 2004	86
6.4.1	The normalized absorption data for the HIDIVE and riometer signals	88
6.4.2	An LS line fit to the normalized absorption versus square root of solar X-ray flux data for the 5 MHz kf-wwv HIDIVE signal	91
6.4.3	An LS line fit to the normalized absorption versus square root of solar X-ray flux data for the 10 MHz kf-wwv HIDIVE signal	91
6.4.4	An LS line fit to the normalized absorption versus square root of solar X-ray flux data for the 15 MHz kf-wwv HIDIVE signal	92
6.4.5	An LS line fit to the normalized absorption versus square root of solar X-ray flux data for the 30 MHz riometer signal	92
6.4.6	Equation 6.4.1 fitted to the LS line slope versus signal frequency data	94
6.4.7	Equation 6.4.1 fitted to the LS line slope versus signal frequency data when C_2 is set to -2	95
6.4.8	HASEL ray path predictions	97
7.2.1	HIDIVE data and EHA model predictions for the 10 MHz kf-wwv signal on 15 January 2005	101
8.1.1	The baseline signal strength curve for the AbbyNormal prediction for the 5 MHz blo-wwv transmission on 24 March 2004	105
8.1.2	The AbbyNormal, EHA, and SWPC predictions for signal strength for the 5 MHz blo-wwv HIDIVE transmission on 24 March 2004	106
8.1.3	The AbbyNormal, EHA, and SWPC predictions for signal strength for the 10 MHz kf-wwv HIDIVE transmission on 24 March 2004	107

Figure		Page
8.1.4	The AbbyNormal, EHA, and SWPC predictions for signal strength for the 15 MHz kf-wwv HIDIVE transmission on 24 March 2004	108
8.1.5	The AbbyNormal, EHA, and SWPC predictions for absorption due to solar X-ray flux for the 5 MHz blo-wwv HIDIVE transmission during two flares on 24 March 2004	109
8.1.6	The AbbyNormal, EHA, and SWPC predictions for absorption due to solar X-ray flux for the 10 MHz blo-wwv HIDIVE transmission during two flares on 24 March 2004	110
8.1.7	The AbbyNormal, EHA, and SWPC predictions for absorption due to solar X-ray flux for the 15 MHz kf-wwv HIDIVE transmission during two flares on 24 March 2004	111
8.3.1	SWPC model predictions for X-ray induced absorption on 24 March 2004	114
8.3.2	SWPC model predictions for X-ray induced absorption on 15 July 2004	114
8.3.3	SWPC model predictions for X-ray induced absorption for 17 August 2004	115
8.3.4	SWPC model predictions for X-ray induced absorption for 2 August 2004	115
9.2.1	HIDIVE data and AbbyNormal predictions for 16 January 2004 and 28 January 2004	118
9.2.2	Electron densities predicted by AbbyNormal for several dates throughout 2004	119
9.2.3	AbbyNormal predicted E-mode ray paths for the 5 MHz blo-wwv signal for the dates throughout 2004	121
9.2.4	AbbyNormal predicted available propagation paths for the 15 MHz kf-wwv transmission	123
9.2.5	AbbyNormal predicted E-mode ray paths for the 15 MHz kf-wwv signal for six dates throughout 2004	124
9.3.1	AbbyNormal and MRS model NO density predictions for and SNOE and HALOE observations on three consecutive days	127

Figure		Page
9.4.1	NO density predictions and observations for three consecutive days, 9 July, 10 July, and 11 July 1998	131
9.4.2	HIDIVE data for the 5 MHz and 10 MHz blo-wwv signals on 10 July 2004	132
9.4.3	HIDIVE data for the 5 MHz and 10 MHz blo-wwv signals on 27 December 2003	133
9.4.4	AbbyNormal predicted propagation paths for the 5 MHz and 10 MHz blo-wwv signals on 10 July 2004	134
9.4.5	AbbyNormal predicted propagation paths for the 5 MHz and 10 MHz blo-wwv signals on 27 December 2003	135
9.4.6	NO profiles based on the MSR empirical NO model for the dates, 10 July 2004 and 9 September 2000	137
9.5.1	HIDIVE signal strength data for 15 January 2004 for the 5 MHz blo-wwv transmission	140
9.5.2	HIDIVE signal strength data for 27 January 2004 for the 5 MHz blo-wwv transmission	140
9.5.3	Dominant propagation paths predicted by HASEL for the 5 MHz blo-wwv transmission on 15 January 2004 at 19:30 UT	142
9.5.4	N_e profiles and $N_e\nu$ profiles produced by the three AbbyNormal versions on 15 January 2004 at 19:30 UT	143
9.5.5	NO profiles produced by the original version of AbbyNormal, the MSR-based version, and the HALOE-based version for 15 January 2004	144
9.5.6	HIDIVE signal strength data for 15 January 2004 for the 10 MHz blo-wwv transmission	146
9.5.7	N_e profiles predicted by the three AbbyNormal versions and the resulting $N_e\nu$ profiles at 19:00 UT on 15 January 2004	147
9.5.8	HIDIVE signal strength data for 13 January 2004 for the 5 MHz kf-wwv	150
9.5.9	NO profiles produced by the three AbbyNormal versions for 13 January 2004	151
9.5.10	N_e and $N_e\nu$ profiles produced by the three AbbyNormal versions for 13 January 2004	152

Figure Page

9.5.11 Dominant propagation paths predicted by HASEL for the 5 MHz kf-wwv transmission on 13 January 2004 at 19:00 UT..... 153

9.5.12 HIDIVE signal strength data for 13 January 2004 for the 10 MHz kf-wwv transmission along with signal strength predictions..... 156

9.5.13 NO profiles produced by the three AbbyNormal versions for 13 January 2004..... 157

9.5.14 N_e and $N_e\nu$ profiles for the AbbyNormal versions at 17:45 UT on 13 January 2004..... 158

9.5.15 E-mode propagation paths predicted by HASEL for the 10 MHz kf-wwv transmission on 13 January 2004 at 17:45 UT..... 159

9.5.16 F-mode propagation paths predicted by HASEL for the 10 MHz kf-wwv transmission on 13 January 2004 at 17:45 UT..... 160

9.5.17 N_e and $N_e\nu$ profiles for the AbbyNormal versions at 17:45 UT on 13 January 2004 within the D- and E-regions..... 161

9.5.18 HIDIVE signal strength data and predictions for 15 January 2004 for the 15 MHz kf-wwv transmission..... 163

9.5.19 F-mode propagation paths predicted by HASEL for the 15 MHz kf-wwv transmission on 15 January 2004 at 19:00 UT..... 164

9.5.20 N_e and $N_e\nu$ profiles for the three AbbyNormal versions at 19:00 UT on 15 January 2004..... 165

10.2.1 Signal strength data for the 5 MHz blo-wwv HIDIVE transmission and daily average F10.7 values are shown during solar quiet conditions during December 2003..... 174

10.2.2 Signal strength data for the 10 MHz kf-wwv HIDIVE transmission and daily average F10.7 values are shown during solar quiet conditions during December 2003..... 175

List of Tables

Table		Page
2.2.1	Summary of D-region Reactions.....	17
2.3.1	Summary of how the F10.7 index relates to solar activity.....	24
2.3.2	Summary of solar X-ray background flux levels.....	26
2.6.1	Solar Flare Importance Classifications.....	42
2.6.2	Optical Flare Brightness Classifications.....	42
2.6.3	X-ray Flare Classifications.....	43
3.3.1	Empirical relations used in SWPC D-region Absorption model to predict the HAF.....	50
4.1.1	Calibrated signal amplitudes of the HF transmissions.....	54
4.1.2	Summary of HIDVIE monitoring sites and dates on which data collection began.....	55
5.3.1	The RMS errors for the SQ curves resulting from fitting equations 5.3.1 and 5.3.2 to the quiet-time HIDIVE data on 26 February 2004 for the 10 MHz kf-wwv transmission.....	66
5.3.2	The RMS errors for the SQ curves resulting from fitting equations 5.3.1 and 5.3.2 to the quiet-time HIDIVE data on 15 July 2004 for the 10 MHz kf-wwv transmission.....	68
5.4.1	SQ curves of the functional form given in equation 5.3.1 are fitted to HIDIVE data for dates during the months listed.....	70
6.3.1	The propagation path characteristics for the predicted 10 MHz kf-wwv and 10 MHz blo-wwv HIDIVE signals.....	85
6.4.1	The equations for the LS lines that best fit the normalized absorption versus square root solar X-ray flux data.....	90
6.4.2	The mean residual, standard deviation of the residuals, and the RMS error for each absorption versus flux dataset.....	90
6.4.3	The RMS errors for the curves fitting the LS line slope versus signal frequency data.....	95
7.1.1	HIDIVE baseline signal strengths.....	100
8.1.1	Dates and flare peak times for the flare-induced absorption cases used to validate the AbbyNormal, SWPC, and EHA models.....	104

Table		Page
8.1.2	DSS RMS values for the 5 MHz blo-wwv, 10 MHz kf-wwv, and 15 MHz kf-wwv HIDIVE transmission.....	108
8.1.3	FTA RMS values for AbbyNormal predictions of flare-induced absorption.....	109
8.1.4	FTA RMS values for EHA model predictions of flare-induced absorption.....	110
8.1.5	FTA RMS values for SWPC model predictions of flare-induced absorption.....	111
9.2.1	RMS errors for daytime AbbyNormal signal strength predictions.....	120
9.3.1.	NO densities (cm^{-3}) observed by the SNOE and HALOE satellites and predicted by the MSR empirical and AbbyNormal models on 9, 10 , and 11 July 1998 at the altitudes of 100 km and 140 km.....	128
9.4.1	Signal strength RMS errors for the Original AbbyNormal and Modified AbbyNormal models.....	130
9.5.1	Available propagation paths predicted for the 10 MHz blo-wwv transmission on 15 January 2004 for the three versions of AbbyNormal.....	148
9.5.2	The available propagation paths predicted by the AbbyNormal versions at 17:45 UT on 13 January 2004.....	155

IMPROVED MODELING OF MIDLATITUDE D-REGION IONOSPHERIC ABSORPTION OF HIGH FREQUENCY RADIO SIGNALS DURING SOLAR X-RAY FLARES

1. Introduction

High frequency (HF) signals are widely used in both the military and civilian sectors as a low-cost, real-time, and robust method for medium to long range terrestrial communication. Since medium and long range HF radio waves travel through the ionosphere and rely on refraction within regions of the ionosphere, ionospheric disturbances due to solar X-ray flares can greatly affect HF wave propagation. Solar X-ray flares lead to an increase in the amount of ionizing solar radiation incident on the earth, resulting in an increase in electron density, N_e, throughout the ionosphere. Sudden enhancements in N_e can cause increased HF signal absorption within the lower region of the ionosphere, known as the D-region, and can alter HF wave propagation paths by changing the altitude at which the wave is refracted. During some large X-ray flares, HF signals can be attenuated to below the noise as they pass through the D-region. HF blackouts can last for minutes to hours after a significant X-ray flare. In the event of sudden loss of HF communication, it is important for users of HF systems to be aware of any current solar activity and if recent solar flares are the likely cause of the loss of HF communication. If it appears the cause is solar flares, loss of HF communication will likely be temporary; however, if there was no significant solar activity, hardware failure or another cause may be to blame and HF communication loss could be prolonged. In 1984 during President Regan's trip to China, a large solar flare occurred disrupting HF communication and completely severing all communication with Air Force One for several hours [*Bonadonna*, 2000; *The Universe*, 2007]. An accurate operational model of flare-induced HF absorption in this case would have gone far to alleviate fears of malicious intent, hardware failure, or sabotage.

Military use of HF communication continues to increase since it provides long range voice and data communication at a fraction of the cost of communication via satellite. Satellite communication channels are heavily burdened and in high demand due to competition with commercial service providers. Not only is the cost of using and establishing HF communication drastically lower than satellite communication, maintaining HF systems is also much less costly when compared to the cost of launching and repairing satellites. As technology evolves, military requirements for data and voice communication increase, leading to more reliance on HF communication [*Cook*, 1997; *Keller*, 2002; *Renfree*, 2001]. The military dependence on HF communication requires improved forecasts and modeling of HF absorption and requires timely products which notify the warfighter of possible effects of solar activity on HF communication [*Bonadonna*, 2000]. The ability to forecast possible HF blackouts for users with time critical or time sensitive missions, such as search and rescue and military operations, is priceless. For example, a commander, whose troops rely on HF communication and who has learned a large solar flare just occurred, would have the option of postponing an operation until the threat of a HF blackout passed.

The goal of this research is to improve real-time HF propagation and flare-induced HF absorption prediction and modeling capabilities, firstly, by validating two current HF absorption models, and secondly, by identifying relationships between HF absorption and solar flare characteristics. To accomplish these goals, HF propagation data obtained during the HF Investigation of D-region Ionospheric Variation Experiment (HIDIVE) and obtained at the Canadian Space Agency NORSTAR riometer in Pinawa, Manitoba, Canada are used to validate current HF absorption models. The first model is an operational and empirical model widely used by both the civilian and governmental sectors and is produced by the National Oceanic and Atmospheric Administration (NOAA) Space Weather Prediction Center (SWPC) division [*http://www.swpc.noaa.gov/dregion/dregionDoc.html*]. The second model is the Absorption by the D and E Region of HF Signals with Normal Incidence (AbbyNormal) model, a physical model based on simple ionospheric chemistry [*Eccles et al*., 2005]. Several HF absorption models, including the two mentioned above, are discussed in §3

and the HF propagation data is described in §4. The background ionospheric physics and radio propagation concepts which are the foundation of this research are discussed in §2.

In order to achieve the goal of identifying relationships between HF absorption and solar flares, the amount of HF absorption due to an X-ray flare must first be calculated from the HIDIVE HF propagation data. HIDIVE data reports the signal strengths in dBs of several HF signals; thus, in order to determine the amount of the signal that was absorbed, a baseline signal strength must be established. Section 5 describes the method used to determine baseline signal strengths for a given HF signal on individual days. It is a goal of this research to create a reproducible and automated method for determining baseline signal strengths. As a consequence of this goal, criteria are required for selecting solar flares for which HIDIVE data will be analyzed. The selection criteria for solar flares and a list of the flares used in this research are given in §6.1 and §6.2. The procedure for obtaining and normalizing the absorption data for the HIDIVE data during the selected flares is described in §6.3. Normalization of the absorption data to a common solar zenith angle and a common elevation angle is required to compare data from different flares and to quantify the dependences of absorption on signal frequency and solar zenith angle. These empirical relations are presented in §6.4.

From these empirical relations, the Empirical HIDIVE D-region Absorption (EHA) model is developed in §7. The EHA model predicts the amount of absorption an HF signal will suffer given characteristics of the signal propagation path and specifics about solar radiation output and activity. The EHA model absorption and signal strength prediction performances are compared to those of the SWPC and AbbyNormal models in §8.1. The validation of the SWPC model suggests model performance has a signal frequency dependence, and in §8.2 improvements to the SWPC model which are based on the empirical relations used to build the EHA model are suggested.

Further analysis of AbbyNormal model performance in §9 uncovers an inconsistency in model performance for the various transmissions used to obtain the HIDIVE HF propagation data. Trends in AbbyNormal signal strength predictions for several transmissions for which the model performs poorly suggest the seasonal variation of the AbbyNormal electron density (N_e) profile is incorrect due to the nitric oxide (NO)

density profile defined by AbbyNormal being erroneous. NO provides one of the three primary sources for free electrons in the D-region; thus, work is done here to improve AbbyNormal's ability to model ionospheric NO. In §9.3, NO density observations obtained by the Student Nitric Oxide Explorer (SNOE) satellite and by the Halogen Occultation Experiment (HALOE) are compared to the AbbyNormal model of the atmospheric NO profile, and results of the comparison are used to investigate three alternate methods of defining the NO profile within AbbyNormal. The signal strength and absorption predictions resulting from employing these three different methods of defining the AbbyNormal NO profile are then analyzed and compared to HIDIVE data in §9.5. The results of addressing the AbbyNormal NO profile, comparing the profile to NO density observations, and producing HF propagation predictions while using the various methods of defining the NO profile suggest there exist other opportunities for improvement within the AbbyNormal model. Other promising areas of future work, discussed in §10, include using HIDIVE data to infer information about local atmospheric NO densities and include determining the signal frequency dependence of absorption due to Lyman-α ionization of neutral particles in the D-region.

2. Background

This chapter focuses on the background needed to understand and predict HF absorption within the ionosphere, particularly within the lower region of the ionosphere called the D-region. Section 2.1 introduces a simple model of the ionosphere and the various regions of the ionosphere. This chapter also shows the majority of HF absorption occurs within the D-region and is dependent on local electron density, N_e, and from §2.1 and the simple model of the ionosphere, we see N_e is strongly dependent on solar radiation flux, U_o, and solar zenith angle, χ. These dependencies are then analyzed in detail in §2.2 to determine first order relationships governing D-region N_e. Periodic variabilities in U_o and χ are discussed in §2.3 to explain why there are seasonal and diurnal patterns to HF absorption. The varying N_e ionospheric profile greatly affects the propagation of radio waves, and §2.4 discusses radio wave propagation within the different layers of the ionosphere and how different modes of propagation can affect HF absorption. With the foundation laid, a detailed analysis of absorption within the D-region is done in §2.5, and D-region absorption dependencies on U_o and χ are quantified. These dependencies are used in chapter 7 to develop an empirical model of HF absorption which uses information about a radio wave's propagation mode, solar radiation flux, and solar zenith angle to predict the amount of absorption the wave will suffer.

2.1 The Ionosphere

The ionosphere exists between the altitudes of approximately 50 km and 600 km [*McNamara,* 1991] and consists of distinct regions distinguished by their electron density, N_e, as shown in Figure 2.1.1. Figure 2.1.1 depicts ionospheric electron density as a function of altitude for night and daytime conditions. In general, electron density increases with altitude up to the F2 layer peak, whereafter N_e decreases with altitude. Medium and long range HF transmissions propagate through the ionosphere and depend on an electron density gradient for refraction back towards the earth surface. The ionospheric plasma at the high altitudes of the E- and F-regions that makes HF

communication possible is also responsible at the lower altitudes of the D-region for HF signal attenuation and, at times, total loss of the signal. The ionosphere is a region of earth's atmosphere characterized by significant thermal electron and ion densities. These free thermal electrons and ions are created via ionization of neutral particles through energetic collisions and photoionization. These charged particles constitute a plasma which affects the propagation and characteristics of electromagnetic waves passing thought the plasma. Such effects include refraction of the wave (§2.4) and attenuation of wave energy (§2.5).

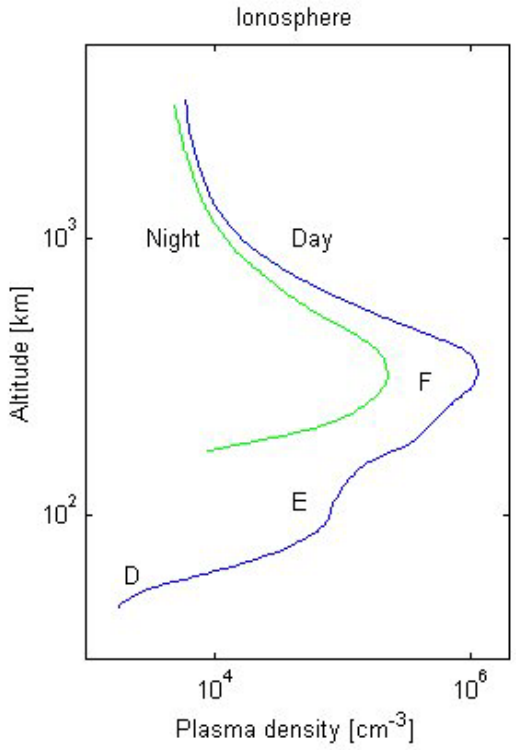

Figure 2.1.1. Ionospheric electron density as a function of altitude for night and daytime conditions. In general, electron density increases with altitude up to the F2 layer peak, whereafter N_e decreases with altitude. [*http://www.oulu.fi/~spaceweb/textbook/ionosphere.html*]

2.1.1 Ionospheric Layers

The D-region exists between the altitudes of 50 km to 90 km and is the region in which the majority of HF signal strength loss occurs, which is discussed in §2.5. The D-

region has as major constituents both positive and negative molecular ions and molecular neutrals and is further characterized by its relatively low electron density ($N_e \approx 10^3 cm^{-3}$) and relatively high electron-neutral collision frequency ($\nu_{en} \approx 10^6$ s^{-1}) [*Davies*, 1990]. The D-region is produced mainly by photoionization of nitric oxide (NO) by Lyman-α radiation (121.6 nm) and photoionization of molecular nitrogen N_2 and oxygen O_2 by solar X-rays [*Tascione*, 1994]. D-region chemistry is discussed in further detail in §2.2. The peak N_e within the D-region occurs at an altitude of 90 km during the day, and at night, without an ionization source, the D-region disappears [*Gombosi*, 1998].

The E-region is found above the D-region between the altitudes of 90 km and 120 km and is one of the regions in which N_e is at times large enough to refract radio waves back towards earth. Refraction of HF waves is discussed in §2.4. The E-region is populated by positive molecular ions, and ionization within the E-region is primarily due to soft X-rays (0.8 nm – 14 nm) and the photoionization of O_2 by ultraviolet (UV) radiation (100 nm - 102.7 nm) [*Davies*, 1990; *Rishbeth and Garriott*, 1969]. The E-region N_e peak occurs at approximately 110 km with $N_e \approx 10^5 cm^{-3}$. During the day, E-region ion production is balanced by losses due to dissociative recombination. At night, the E-region does not disappear since there is ion production due to starlight and light scatter in the atmosphere [*Strobel et al*., 1980].

The F-region is unique in that it can be further divided into three regions based on which of the two mechanism governing electron density, photochemistry or diffusion, is dominant. It is also within the F-region HF waves can be refracted back towards earth. Ion production in the F1-region is primary due to photoionization of atomic oxygen by extreme ultraviolet (EUV) radiation of wavelengths between 14 nm and 91.1 nm with peak absorption near 175 km. The F2-region marks the location where the dominant mechanism governing N_e transitions from photochemistry to diffusion. In the F2-region, geomagnetic field effects and transport processes of electrons become important. The F2-peak occurs near 250 km where time constants for diffusion and chemical processes are equal. The uppermost region is the topside F-region in which diffusion dominates the determination of the N_e profile. At night the F1-region disappears, while the topside F-region and the F2-region remain due to upward plasma drifts induced by equatorward

neutral winds. The upward drifts raise the F-layer to higher altitudes where the loss rates of electrons and O^+ are lower [*Schunk and Nagy*, 2000]. It is refraction in the E- and F-regions that makes HF communication possible, see §2.4.

2.1.2 The Chapman Function

The distinct layers of the ionosphere described briefly in the last section arise due to changes in atmospheric composition and constituent densities with altitude. This altitude dependence leads to absorption of different parts of the solar spectrum at various heights and to region-defining chemistry and electron densities. Since it will be shown absorption of HF signals depends on N_e in §2.4 and §2.5, a simple model of ionospheric N_e production is examined in this section in order to establish ionospheric plasma dependencies to be referenced in future sections. The Chapman production function is the simple model for the production of ionospheric photoelectrons examined here. The Chapman production function suggests ionospheric N_e production is due to differential absorption of ultraviolet solar radiation incident on the upper atmosphere, U_o, and the function constructs a simple N_e production profile by employing the following assumptions.

1) Incident solar radiation is monochromatic
2) The atmosphere is plane and horizontally stratified
3) There exists a single absorbing atmospheric gas to which the ideal gas law applies
4) The atmosphere is in steady state and static equilibrium
5) Molecular velocities in the atmosphere have Maxwellian distributions

[*Rishbeth and Garriott*, 1969]. From these assumptions, the momentum equation, which governs the diffusion and transport of a gas, for the absorbing atmospheric gas is

$$\nabla p = \frac{dp}{dz} = mN_n\vec{g} \tag{2.1.1}$$

where p is the absorbing gas pressure, z is the altitude, m is the particle mass, N_n is the number density of the absorbing gas, and g is the force of gravity. From the ideal gas law $p=N_nkT$ and equation 2.1.1 [*Gombosi*, 1998; *Schunk and Nagy*, 2000]

$$\frac{dp}{p} = -\frac{mg}{kT}dz = \frac{-1}{H}dz \tag{2.1.2}$$

where H is the scale height and describes the vertical distance over which the number density decreases by 37% of the initial value. Integrating equation 2.1.2 gives

$$p(z) = p_o Exp\left(\frac{-(z - z_o)}{H}\right) \tag{2.1.3}$$

where p_o is the pressure at a reference altitude, z_o. From the ideal gas law and the assumption of an isothermal atmosphere, equation 2.1.3 can be rewritten

$$N_n(z) = N_n(z_o) Exp\left(\frac{-(z - z_o)}{H}\right) \tag{2.1.4}$$

Let the σ be the absorption cross section for a given wavelength of solar radiation in the atmosphere, and define the change in radiation flux, dU, due to absorption as it passes through an infinitesimal distance, ds, in the atmosphere as

$$dU = -N_n(z)\,\sigma\,U_o ds = -N_n(z)\,\sigma\,U_o\,Sec(\chi)\,dz \tag{2.1.5}$$

Figure 2.1.2 shows the relationship, $ds = Sec(\chi)dz$, between the radiation path length (ds), solar zenith angle (χ), and change in altitude (dz).

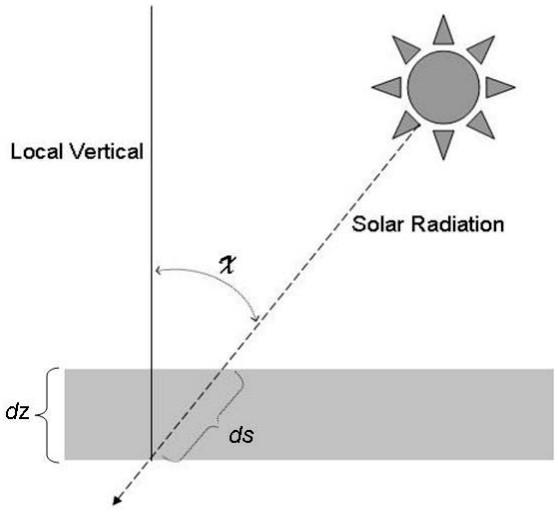

Figure 2.1.2. Relationship between the radiation path length, solar zenith angle, and change in altitude

Integrating equation 2.1.5 gives

$$U(z) = U_o Exp\left(- Sec(\chi)\, \sigma \int_z^\infty N_n(z') \cdot dz' \right) = U_o Exp(-\tau) \qquad (2.1.6)$$

$$\tau = Sec(\chi)\, \sigma \int_z^\infty N_n(z')\, dz \qquad (2.1.7)$$

where τ is the optical depth of the atmosphere for the gas. Substituting for N_n given in equation 2.1.4, we obtain

$$\tau = Sec(\chi)\, \sigma \int_z^\infty N_n(z_o)\, Exp\left(\frac{-(z - z_o)}{H} \right) dz \qquad (2.1.8)$$

Given the number of particles in a column of atmospheric gas of unit cross section above the altitude z is equal to the product, $N_n(z) \cdot H$, and assuming σ_a is independent of altitude, the relationship between τ and H is

$$\tau = Sec(\chi)\,\sigma\, N_n(z)\, H \tag{2.1.9}$$

[*Rishbeth and Garriott*, 1969; *Gombosi*, 1998].

Since the majority of the solar radiation incident on the atmosphere is absorbed through ionization processes, let σ be equal to the ionization cross section and *q* be the total electron production rate. The electron production rate is found by assuming each solar radiation photon absorbed creates a new electron-ion pair. Thus, the number of electron-ion pairs created along a path, *ds*, due to the solar radiation flux at a given altitude, $U(z)$, is

$$q\, ds = N_n(z)\,\sigma\, U(z)\, ds \tag{2.1.10}$$

Substituting in the expressions for $N_n(z)$ and $U(z)$ from equations 2.1.4 and 2.1.5, respectively, yields

$$q = \sigma\, N_n(z_o)\, U_o\; Exp\left(\frac{-(z - z_o)}{H} - \tau\right)$$

and using the expression for τ from 2.1.9

$$q = \sigma\, N_n(z_o)\, U_o\; Exp\left(\frac{-(z - z_o)}{H} - Sec(\chi)\,\sigma\, N_n(z)\, H\right)$$

Substituting in equation 2.1.4 gives,

$$q = \sigma\, N_n(z_o)\, U_o\; Exp\left(\frac{-(z - z_o)}{H} - Sec(\chi)\,\sigma\; HN_n(z_o) Exp\left(\frac{-(z - z_o)}{H}\right)\right) \tag{2.1.11}$$

[*Gombosi*, 1998]. Equation 2.1.11 is the Chapman production function which predicts the production rate due to the absorption of a single wavelength of ionizing solar radiation by a given neutral species given the assumptions listed above [*Gombosi*, 1998].

Normalized Chapman functions for various solar zenith angles are shown in Figure 2.1.3. The curves plotted in Figure 2.1.3 represent the production rate profiles summed over all absorbing species and all ionizing wavelengths.

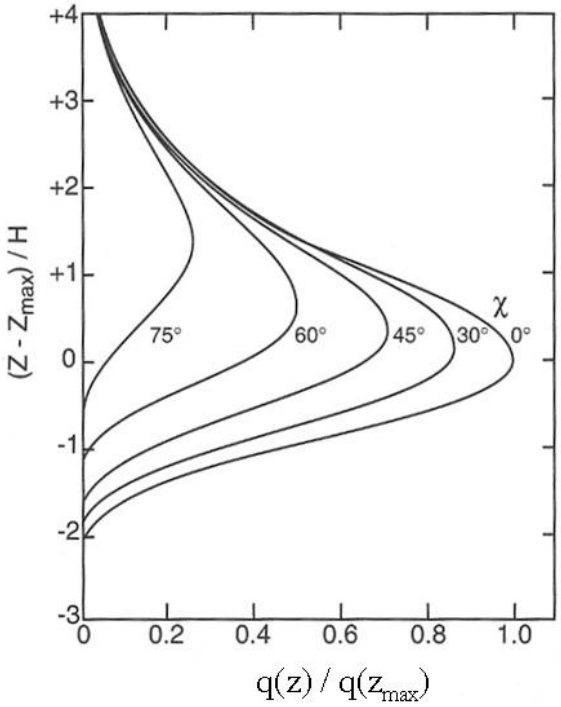

Figure 2.1.3. Normalized Chapman functions for various solar zenith angles [*Schunk and Nagy*, 2000].

The Chapman production function provides a good first step in understanding the formation and structure of the ionospheric electron density profile and shows the production of free electrons in the ionosphere is dependent on solar zenith angle, solar ionizing radiation, and neutral density. The N_e profile in Figure 2.1.1 is the result of a balance between the Chapman production formula and the chemical reactions and transport processes summarized earlier in §2.1.1. The following section goes into further detail about this balance within the D-region and provides an overview of D-region chemistry governing local N_e during normal, solar quiet conditions.

2.2 D-Region Chemistry

2.2.1 D-region Chemistry.

Loss of HF signal energy occurs primarily in the D-region, and to understand how solar X-ray flares can enhance HF absorption within the D-region, the chemistry and processes occurring in the D-region during solar quiet conditions must be understood. The chemistry of the D-region is the most complicated of all the ionospheric layers involving both negative and positive ions, hydrated cluster ions, numerous atomic and molecular neutral species, and high neutral densities.

As mentioned briefly in §2.1, the primary sources of free electrons and positive ions in the D-region are ionization of the major neutral constituents, molecular nitrogen (N_2) and molecular oxygen (O_2), by solar X-rays (0.1-0.8 nm) and Lyman-α (121.6 nm) ionization of the minor constituent, nitric oxide (NO). The production rates of the photoionization of a neutral species, M, by solar X-rays and Lyman-α radiation, $h\nu$,

$$\mathrm{M} + h\nu \rightarrow \mathrm{M}^{+} + e \tag{2.2.1}$$

can be seen in Figure 2.2.1 [*Davies*, 1990]. The production profile of free electrons due to the sum of ionization by solar X-rays and Lyman-α during solar quiet conditions is given by curve "*A*" in Figure 2.2.1, and the dashed line labeled "Ly α" in Figure 2.2.1 is the production rate profile of free electrons solely due to Lyman-α ionization. Curve "*B*" is the production rate during a moderate X-ray flare. Notice during an X-ray flare the production rate of free electrons is dominated by ionization due to X-rays. According to Figure 2.2.1, at the altitudes where ionization due to Lyman-α occurs, approximately 65 km to 95 km, the production rate due to X-rays during a flare can be as much as three orders of magnitude greater than the production rate of free electrons due to Lyman-α ionization. During a large flare, X-ray emissions can increase by several orders of magnitude, while the increase in Lyman-α emissions may only be a few percent [*Rishbeth and Garriott*, 1969]. Thus, ionization during a solar flare is primarily due to solar X-rays; whereas, during solar quiet conditions, the contribution of Lyman-α ionization is more prevalent [*Poppoff et al.*, 1964]. Also shown in the figure are the

production rate profiles due to ionization via cosmic rays at solar cycle min (CR-SS min) and solar cycle max (CR-SS max). See §2.3.2 for more discussion on solar cycles.

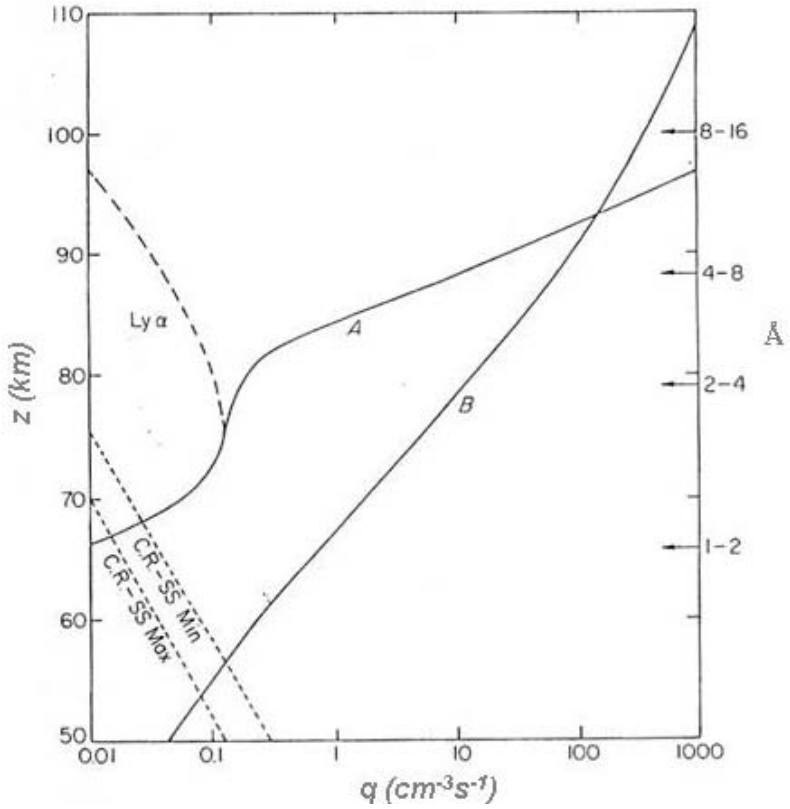

Figure 2.2.1. Production rate profiles in response to a moderate X-ray flare (curve B) and due to the sum of ionization rates due to Lyman-α and solar X-rays during solar quiet conditions (curve A). The two dashed lines in the lower left corner are the ionization profiles due to cosmic rays at solar cycle min (CR-SS min) and solar cycle max (CR-SS max) [*Rishbeth and Garriott,* 1969].

Solar X-rays are capable of ionizing most neutral particles in the D-region; however, the major neutral species, N_2 and O_2, account for 78% and 21% of the atmospheric neutral gas, respectively. Thus, focusing on only the ionization reactions involving N_2, O_2, and NO provides an adequate description of the D-region source for ions and free electrons [*Rees,* 1989]. A more detailed discussion of the minor neutral constituent, NO, and how ionization of NO impacts the atmospheric N_e profile and HF absorption is given in §2.2.2. In this section, we will look at the chemistry involving the major neutral constituents, N_2 and O_2.

The primary positive ions formed via ionization of the major neutral constituents, N_2 and O_2, in the D-region are N_2^+ and O_2^+; however, N_2^+ is short lived and rapidly converted to the major ions, O_2^+ and NO^+, in the reactions,

$$N_2^+ + O_2 \xrightarrow{k} O_2^+ + N_2 \qquad k = 5\times10^{-11}\ cm^3/s \qquad (2.2.2)$$

$$N_2^+ + O \xrightarrow{k} NO^+ + N \qquad k = 10^{-10}\ cm^3/s \qquad (2.2.3)$$

where *k* is the reaction rate constant [*Cravens*, 1997]. NO^+ can also be created in the charge-transfer processes,

$$O_2^+ + N_2 \xrightarrow{k} NO^+ + NO \qquad (2.2.4)$$

$$O_2^+ + NO \xrightarrow{k} NO^+ + O_2 \qquad k = 5\times10^{-10} cm^3/s \qquad (2.2.5)$$

and is created via ionization of the minor constituent, NO, via Lyman-α radiation in the reaction

$$NO + h\nu \xrightarrow{k} NO^+ + e \qquad k = 7.3\times10^{-7}(cm^3 s^{-1}) \qquad (2.2.6)$$

[*Rusch*, 1973; *Torr et al.*, 1995].

The hydration of the primary positive ions, NO^+ and O_2^+, begins the chain of reactions leading to cluster ions in the D-region, which dominate D-region chemistry below 85 km [*Schunk and Nagy*, 2000]. The D-region chemistry involving the hydrated cluster ions is complex and is dominated by the primary water cluster ions, $H^+(H_2O)_n$, $NO^+(H_2O)_n$, and $O_2^+(H_2O)_n$, where *n* can range from one to eight. For altitudes above 70 km, $NO^+(H_2O)_n$ is the most important cluster ion, and for altitudes below 70 km, hydration of O_2^+ is the most important source of cluster ions [*Schunk and Nagy*, 2000]. Loss of the major positive ions is primarily due to electron-ion dissociative recombination [*Cravens*, 1997; *Davies*, 1990; *Rees*, 1989; *Schunk and Nagy*, 2000]

$$O_2^+ + e \xrightarrow{k} O + O \qquad k = 10^{-7}\ cm^3/s \qquad (2.2.7)$$

$$NO^+ + e \xrightarrow{k} N + O \qquad k = 5\times10^{-7}\ cm^3/s \qquad (2.2.8)$$

It can be assumed D-region plasma exhibits charge neutrality; thus, $N_+ = N_- + N_e$ where N_+ and N_- are the positive and negative ion densities, respectively. Negative ions are primary found in the D-region and are formed by three-body attachment

$$O_2 + e + M \rightarrow O_2^- + M \qquad (2.2.9)$$

and to a lesser extent by collisions between and electron and a single neutral particle resulting in radiative attachment

$$O_3 + e \rightarrow O^- + O_2$$
$$O_2 + e \rightarrow O_2^- + h\nu \qquad (2.2.10)$$

[*Schunk and Nagy*, 2000; *Tascione*, 1994]. The neutral species providing the largest reaction rate for the three-body attachment given in equation 2.2.9 is O_2 with a reaction rate of $5\times10^{-31}\ cm^3/s$, and the reaction rate of the radiative attachment in equation 2.2.10 is $10^{-19}\ cm^3/s$ [*Tascione*, 1994]. According to reaction rate coefficients, the three-body attachment reaction,

$$O_2 + e + O_2 \rightarrow O_2^- + O_2 \qquad (2.2.11)$$

is the primary source of O_2^- in the D-region due to the large O_2 density of approximately $10^{14}\ cm^{-3}$ at these altitudes [*Tascione*, 1994]. The chemical reactions following the formation of the primary negative ions are numerous and complex, leading to many more negative ion species.

The loss processes for free electrons and ions are summarized in Table 2.2.1. The primary loss process for the negative ion, O_2^-, occurring both day and night, is collisional detachment

$$O_2^- + O_2 \rightarrow O_2 + e + O_2 \qquad (2.2.12)$$

and photodetachment due to visible light is the loss process for O_2^-.

$$O_2^- + h\nu \rightarrow O_2 + e \qquad (2.2.13)$$

The principle loss of positive ions is through recombination [*Tascione*, 1994; *Schunk and Nagy*, 2000]. Since, the reaction rate of the three-body recombination loss process depends on the neutral density, it varies with altitude, is important in the D-region, and becomes less important at higher altitudes [*Rishbeth and Garriott*, 1969].

Table 2.2.1: Summary of D-region reactions for the loss of free electrons and ions [*Cravens*, 1997; *Rishbeth and Garriott*, 1969].

Loss Process	Reaction	Rate (cm^3/s)	Notes
Ion-Ion Recombination	$X^+ + Y^- \rightarrow X + Y$	10^{-7}	
Three-Body Recombination	$X^+ + M + e \rightarrow X + M$		Rate is altitude dependent since it depends on neutral densities
Electron-Ion Dissociative Recombination	$XY^+ + e \rightarrow X^* + Y^*$	10^{-7}	* denotes atoms in an excited state
Collisional Detachment	$X^- + M \leftrightarrow e + X + M$	10^{-20}	Important at night
Photo-Detachment	$X^- + h\nu \leftrightarrow X + e$	1	$h\nu$ in the visible, Leads to night and day variation in N_-/N_+

2.2.2 D-region Plasma Density Profile.

The previous section discusses the primary reactions within the D-region, and this section focuses on the defining characteristics of the D-region electron density profile, $N_e(z)$. $N_e(z)$ within the D-region is determined by the continuity equation,

$$\frac{\partial N_e}{\partial t} + \nabla \cdot (N_e \mathbf{u}_e) = \text{Production} - \text{Loss} \tag{2.2.14}$$

[*Cravens*, 1997]. However, due to the very high neutral densities within the D-region, the time rate of change of the electron density, dN_e/dt, and transport processes, $\nabla \cdot (N_e \mathbf{u}_e)$, are typically assumed to be negligible. Thus, the continuity equation for the D-region reduces to $\text{Production} = \text{Loss}$. The primary sources of free electrons in the D-region are photoionization of molecular neutrals by soft X-rays and photoionization of nitric oxide (NO) by Lyman-α radiation [*Rees*, 1989; *Hargreaves and Friedrich*, 2003]. The reaction dominating the loss of free electrons in the D-region is dissociative recombination given by $L = \alpha N_e^2$, where α is the loss reaction rate coefficient [*Cravens*, 1997]. The function governing the production rate of free electrons in the D-region due to the ionization of a specific neutral constituent by a single wavelength of solar radiation is given by the Chapman production function, equation 2.1.11. Recall the following assumptions were made during the derivation of equation 2.1.11,

1. The atmosphere contains only one absorbing neutral species,
2. The density of the absorbing species decreases exponentially with altitude with respect to a constant scale height *H*,
3. The atmosphere is planar and horizontally stratified.

Substituting the Chapman production function and the function for losses due to recombination into the continuity equation for electron density within the D-region given in equation 2.2.14 yields

$$\alpha N_e^2 = \sigma\, N_n(z_o)\, U_o\, Exp\left(\frac{-(z-z_o)}{H} - Sec(\chi)\sigma\, H(z) N_n(z_o) Exp\left(\frac{-(z-z_o)}{H}\right)\right) \quad (2.2.15a)$$

$$N_e = \sqrt{\frac{\sigma\, N_n(z_o)\, U_o}{\alpha}}\, Exp\left(\frac{-(z-z_o)}{2H} - \frac{Sec(\chi)\sigma\, H(z) N_n(z_o)}{2} Exp\left(\frac{-(z-z_o)}{H}\right)\right) \quad (2.2.15b)$$

From equation 2.2.15b, we see the electron density due to ionization of a given neutral species by a single wavelength of solar radiation is proportional to the square root of the ionizing radiation flux as measured at the top of the earths atmosphere, $N_e \propto \sqrt{U_o}$. The relationship between N_e and $U_o^{1/2}$ will addressed in §6 with regard to characterizing HF absorption due to ionization via solar X-ray flux and will be used in the development of the Empirical HIDIVE D-region Absorption (EHA) model in §7.

2.2.3 First Order Relationship between Solar Zenith Angle and N_e.

The N_e dependence on $U_o^{1/2}$ is shown in equation 2.2.15b in the last section, and in this section a first order relationship between N_e and the solar zenith angle, χ, is established. The first order dependence determined here is then used in §5 to quantify the relationship between N_e and χ and allows for the determination of HF absorption during solar quiet times (i.e. during times in which there is no solar flare activity). The relationship is determined by first obtaining an expression for the maximum electron density within the D-region, N_{max}.

Determining the expression for N_{max} begins by first determining the altitude, z_{max}, at which the rate of photoionization within the D-region is maximized. z_{max} corresponds to the altitude for which the solar optical depth of the atmosphere for a gas equals one for a given wavelength of solar radiation. Since we are concerned with photoionization within the D-region in this section, z_{max} here represents the altitude at which $\tau = 1$ for solar X-rays and Lyman-α radiation, which are the primary wavelengths of solar radiation responsible for ionization in the D-region. Setting the expression for τ, given in equation 2.1.9, equal to one and substituting equation 2.1.4 in for $N_n(z_{max})$, we obtain

$$1 = Sec(\chi)\,\sigma\,H\,N_n(z_o)\,Exp\left(\frac{z_o - z_{\max}}{H}\right) \tag{2.2.16}$$

and

$$z_{\max} = z_o - H\ln\left(\frac{Cos(\chi)}{\sigma\,H\,N_n(z_o)}\right) \tag{2.2.17}$$

The expression for the peak rate of photoionization due to solar X-rays and Lyman-α radiation in the D-region is found by substituting equation 2.2.17 into equation 2.1.11 and is

$$q_{\max} = \frac{U_o}{H\,Exp(1)}Cos(\chi) \tag{2.2.18}$$

Solving the electron continuity equation within the D-region (Production = Loss) at z = z_{max}, we see N_{max} is proportional to $Cos^{1/2}(\chi)$.

$$\alpha N_{\max}^2 = \frac{U_o}{H\,Exp(1)}\,Cos(\chi)$$

$$N_{\max} = \sqrt{\frac{U_o}{\alpha\,H\,Exp(1)}}\,Cos^{1/2}(\chi) \tag{2.2.19}$$

Equation 2.2.19 gives an expression for the peak electron density as a function of $Cos^{1/2}(\chi)$. This result suggests N_e at D-region altitudes other than z_{max} might be dependent on some power of $Cos(\chi)$, and in fact N_e is shown in many studies to be dependent on $Cos^r(\chi)$, where the exponent, *r*, has taken on values ranging from 0.2 to 1.0 [*Davies*, 1990]. From these studies the value of *r* seems to vary with respect to latitude and time of year. We will see in §2.4 and §2.5 HF wave propagation and absorption are directly proportional to N_e and, thus, must also have a $Cos^r(\chi)$ dependence. In §5, HIDIVE HF propagation data is used to quantify the dependence of

HF absorption on $Cos(\chi)$ and to determine the value of *r* in order to predict solar quiet time, midlatitude, diurnal HF absorption and to measure flare-induced HF absorption.

2.2.4 NO in the Atmosphere.

As the previous sections show, N_e depends on the square root of ionizing solar radiation flux and on $Cos^r(\chi)$. N_e is also shown in equation 2.1.11 in § 2.1 to be dependent on the density of the neutral species to be ionized. Ionization of the major neutral constituents, N_2 and O_2, by solar X-rays is discussed in§2.2.1, and this section covers the ionization of the minor neutral specie, nitric oxide (NO), by Lyman-α solar radiation and addresses NO's role in the atmosphere and its contribution to midlatitude D-region N_e and HF absorption.

Of the three neutral species, N_2, O_2, and NO, primarily responsible for production of free electrons in the D-region, NO is the only one whose density can vary by orders of magnitude from day to day. The densities of the major neutral atmospheric constituents, N_2 and O_2, are fairly constant. Thus, to properly determine ionospheric N_e profiles, NO densities must be known. Presently, work continues on improving our understanding of what factors drive NO densities and on improving modeling of atmospheric NO profiles [*Bailey et al.*, 2002; *Marsh et al.*, 2004]. In §9 the impact of a fluctuating NO profile on HF absorption predictions is discussed and predicted NO profiles are compared to satellite observations.

NO is produced in the polar regions by precipitating electrons and in the lower latitudes by solar ultraviolet radiation [*Barth et al.*, 2004; *Marsh et al.*, 2004; *Torr et al.*, 1995]. Production of NO at low to mid latitudes is primarily due to the reaction between molecular oxygen (O_2) and an excited nitrogen atom (N*),

$$N^* + O_2 \xrightarrow{k} NO + O \qquad k = 6\times10^{-12}(cm^3 s^{-1}) \qquad (2.2.20)$$

[*Lin and Kauffman*, 1971]. The main sources of N* include collisional and radiative recombination given by the reactions,

$$N_2 + e^* \xrightarrow{k} N^* + N + e \qquad k = 5.13\times10^{-7}(cm^3 s^{-1}) \qquad (2.2.21)$$

$$NO^+ + e \xrightarrow{k} N^* + O \qquad k = T_e \times10^{-9}(cm^3 s^{-1}) \qquad (2.2.22)$$

where the reaction in equation 2.2.22 is dependent on electron temperature (T_e) [*Kley et al.,* 1977; *Lin and Kauffman,* 1971; *Queffelec et al.*, 1985; *Rishbeth and Garriott,* 1969]. The loss process for NO which leads to the production of free electrons is

$$NO + h\nu \xrightarrow{k} NO^+ + e \qquad k = 7.3\times10^{-7}(cm^3 s^{-1}) \qquad (2.2.23)$$

[*Rusch,* 1973; *Torr et al.*, 1995]. Given the sources and sinks of NO and the reaction dependences on the densities of the products, NO concentration in the ionosphere peaks near 110 km [*Barth et al.*, 2004; *Marsh et al.*, 2004; *Titheridege*, 1997; *Torr et al.*, 1995]; however, atmospheric winds can transport NO to lower altitudes leading to significant enhancements in NO densities below 110 km. NO densities also vary significantly with latitude. During periods of enhanced geomagnetic activity and precipitating electron flux, NO densities in the auroral regions can be orders of magnitude greater than densities at midlatitudes. It is believed local enhancements of NO density at subauroral latitudes are then brought about by thermospheric winds transporting NO equatorward from polar regions. Such transport could explain the considerable day-to-day variation in local ionization and observed HF absorption, which will be further discussed in §2.3.1 and §9.

2.3 D-Region Midlatitude Ionospheric Variability

2.3.1 Diurnal and Seasonal Variability.

As is discussed in §2.5, D-region absorption is dependent on the local electron density which is greatly influenced by solar flares and exhibits diurnal, seasonal, and solar cycle variations. During solar quiet times, N_e and ionospheric absorption are, in general, greatest at local noon when photoionization in the ionosphere is at its peak due to lower solar zenith angles and greatest in the summer due to longer periods of daylight and ionization. For times not close to sunrise or sunset, mid-latitude ionospheric absorption generally follows the form

$$L = A \cdot Cos^{r}(\chi) \qquad (2.3.1)$$

as was suggested in §2.2.3, where the exponent, *r*, has been found to be between 0.2 and 1.0. r has been found to take on values of 0.85±0.15 at low latitudes, 0.5-0.9 in mid-latitudes, and can be as high as 0.2 in the auroral zones. A depends on current ionospheric, space weather, and seasonal conditions [*Davies*, 1990].

Contradictory to the solar zenith angle dependence equation 2.3.1 describes, there are periods during winter months marked by abnormally high ionospheric absorption. During a winter HF absorption anomaly, absorption can be significantly higher than daytime summer values. Although the causes of the anomaly are not completely understood, current popular belief is winter HF absorption anomalies are due to localized increases in ionization brought about by local enhancements of NO due to thermospheric winds transporting NO equatorward from polar regions [*Hunsucker and Hargreaves*, 2003; *Titheridge*, 1997].

2.3.2 Variations in Solar Radiation Flux.

Variations in the amount of solar EUV radiation incident on the atmosphere due to solar cycle changes, emerging solar active regions, and solar X-ray flares lead to variations in D-region N_e and ionospheric absorption. One cause of solar flux variation is the periodic varying of solar activity, measured in terms of the number of observed sunspots, over a period of 11 years. The peak of the 11-year solar cycle is marked by a peak in the number of observed sunspots and in solar radiation flux. The period of the 11-year solar cycle can be seen in the historical observations of the F10.7 index, which is a measure of solar flux at a wavelength of 10.7 cm over the entire sole disk. The F10.7 index is also used as a proxy for Lyman-α radiation flux which ionizes NO in the D-region (§2.2). Monthly averages of the F10.7 index, shown in Figure 2.3.1, follow the 11-year solar cycle, and Table 2.3.1 summarizes approximate F10.7 index values and how they relate to solar activity. Figure 2.3.2 shows how the ionospheric N_e profile varies from solar cycle minimum to solar cycle maximum.

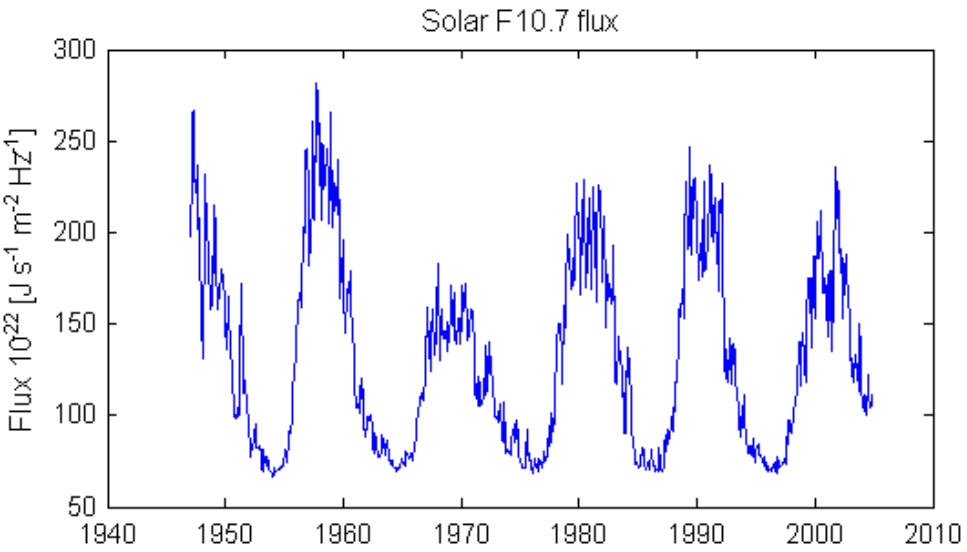

Figure 2.3.1. The monthly averages of the F10.7 index follow the 11 year solar cycle. F10.7 is a measure of solar flux at a wavelength of 10.7 cm (2800 MHz) over the entire solar disk. [*http://www.oulu.fi/~spaceweb/textbook/f107.html*]

Table 2.3.1. Summary of how the F10.7 index relates to solar activity. [*http://www.ips.gov.au/Category/Educational/Space%20Weather/Solar%20Terrestrial/Facts_on_Space_Weather_Indices.pdf*]

F10.6 Index	Level of Solar Activity
>279	Extreme
193-279	Very High
128-193	High
106-128	Moderate
85-106	Low
63-85	Very Low

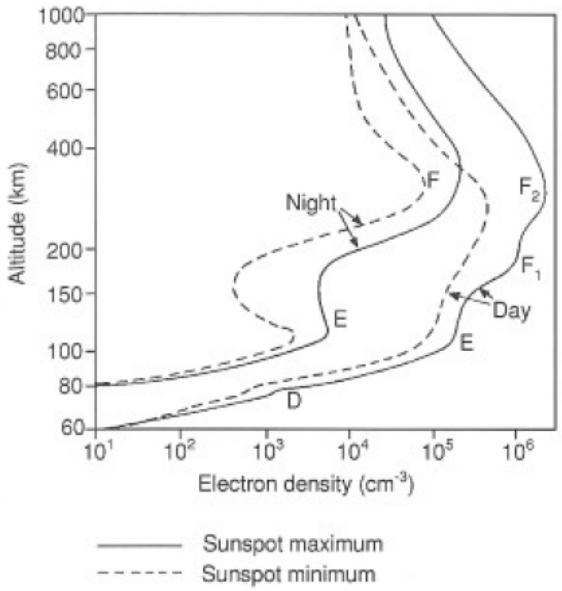

Figure 2.3.2. Variation in N_e profile from solar cycle minimum to solar cycle maximum [*Hargreaves,* 1992].

Background solar flux levels also vary with respect to the solar cycle and can reach as high as $10^{-5}\,{}^{W}\!/_{m^2}$ in the absence of a solar flare during solar cycle max. Table 2.3.2 summarizes the different X-ray flux levels as measured by Geostationary Operational Environmental Satellites (GOES). Consequently, HF signal strength is expected to be relatively lower and D-region absorption and N_e to be greater for time periods near local noon when χ is minimized during the day and during the summer months when χ is lower and there are more hours of daylight. D-region absorption and N_e are also greater during times of high background solar flux and near the peak of the solar cycle when ionizing radiation is enhanced.

Table 2.3.2. Summary of solar X-ray background flux levels.

Background Level	X-ray Flux $\left(W/m^2\right)$	Description
A	$< 10^{-7}$	Low Background
B	10^{-7} to 9×10^{-7}	Moderate Background
C	10^{-6} to 9×10^{-6}	High Background, Small Flare
M	10^{-5} to 9×10^{-5}	Moderate Flare
X	$\geq 10^{-4}$	Large Flare

2.4 Refraction of Radio Waves in the Ionosphere

2.4.1 Wave Equations.

In the previous sections, important factors governing the ionospheric N_e profile are identified and functional forms of N_e dependencies are suggested. This section outlines how the N_e profile governs propagation of radio waves in the ionosphere by first deriving the refractive index, and then from the refractive index, deriving the absorption coefficient, which governs the amount of absorption a wave will suffer as it propagates though a plasma. Understanding how ionospheric plasma refracts radio waves allows for the determination of the signal ray path, bounce location and altitude, signal attenuation, and the cutoff frequency for a given N_e.

To determine the expression for the refractive index, an electromagnetic wave is represented by a periodically oscillating plane wave traveling in the x-direction and whose instantaneous electric field is in the y-z plane and amplitude is given by

$$E = E_o \cdot \exp(ikx - i\omega t) \tag{2.4.1}$$

where k is the wave number and ω is the wave frequency and equal to $2\pi f$, where f is the frequency of our radio signal. By decomposing the periodic motion of the wave through Fourier analysis, Maxwell's equations now take on the form

$$\nabla \times \vec{H} = \vec{J} + \frac{\partial \vec{D}}{\partial t} \quad \rightarrow \quad ikH_z = i\omega D_y \tag{2.4.2a}$$

$$ikH_y = i\omega D_z \tag{2.4.2b}$$

$$\nabla \times \vec{E} = -\mu_o \frac{\partial \vec{H}}{\partial t} \quad \rightarrow \quad ikE_z = i\omega \mu_o H_y \tag{2.4.2c}$$

$$ikE_y = i\omega \mu_o H_z \tag{2.4.2d}$$

[*Chen*, 1984]. Information in the wave travels at the group velocity, u_g, given by $u_g = d\omega / dk$. The phase velocity given by the dielectric permittivity, ε, of the plasma is

$$u_{ph} = \frac{\omega}{k} = \sqrt{\frac{1}{\varepsilon \mu_o}} \tag{2.4.3}$$

where ε is determined by the relationship between the electric field of the wave and the volume polarization of the plasma, $\vec{D}$,

$$\vec{D} = \varepsilon \vec{E} = \varepsilon_o \vec{E} + \vec{P} \tag{2.4.4}$$

When collisions are important and absorption is present, the index of refraction, $\tilde{n}$, is complex and given by

$$\tilde{n} = \mu + i\beta \tag{2.4.5}$$

where μ is the real part of the refractive index and

$$\mu = \frac{c}{u_{ph}} = \sqrt{\frac{\varepsilon}{\varepsilon_o}} = \sqrt{1 + \frac{P_j}{\varepsilon_o E_j}} \tag{2.4.6}$$

The refractive index determines the direction and extent to which the wave will propagate through plasma. The influence refractive index has on the direction of wave propagation

is further discussed in §2.4.5. Here, j is one of the coordinate components *x*, *y*, or *z*, $\beta = \left(\frac{\kappa c}{\omega} \right)$ is the extinction coefficient, and κ is the absorption coefficient [*Jackson*, 1999].

2.4.2 Wave Propagation in the Ionosphere.

Here the ionospheric plasma is assumed to be a cold, weakly ionized plasma immersed in the geomagnetic field, which can be approximated locally by a constant and uniform external magnetic field, $\vec{B}_o$. Consider the situation in which the geomagnetic field lies in the x-y plane of an orthogonal axes system and the wave propagates in the x-direction. As the wave interacts with free electrons in ionospheric plasma, the equation of motion for the free electrons is

$$m\vec{a} = e\vec{E} + e(\vec{u} \times \vec{B}_o) - m\nu\vec{u} \tag{2.4.7}$$

where the first term on the right ($e\vec{E}$) is the electrostatic force, the second term $e(\vec{u} \times \vec{B})$ is the Lorentz force due to electron motion in the presence of the external magnetic field, $\vec{B}_o$, and ($m_e \nu \vec{u}$) is the frictional force due to collisions with neutral particles [*Davies*, 1990]. Furthermore, $\vec{a}$ is the acceleration vector, $\vec{u}$ is the velocity vector, *m* is electron mass, and ν is the electron-neutral collision frequency. The spatial components of equation 2.4.7 are

$$ma_x = eE_x - eu_z B_\perp - m\nu u_x \tag{2.4.8a}$$

$$ma_y = eE_y + eu_z B_{//} - m\nu u_y \tag{2.4.8b}$$

$$ma_z = eE_z + eu_x B_\perp - eu_y B_{//} - m\nu u_z \tag{2.4.8c}$$

where $B_{//}$ and $B_\perp$ are the parallel and transverse external magnetic field components with respect to the wave propagation vector, $\vec{k}$. The initial, non-perturbed plasma is assumed to be stationary and exhibit charge neutrality and the oscillating electron gas parameters are also assumed to be sinusoidal due to the passing wave. Through Fourier

transforms, the substitutions $\left(u_j \rightarrow iwj\right)$ and $\left(a_j \rightarrow -\omega^2 j\right)$ are made in equation 2.4.8. Multiplying each side by the charge density (eN_e) and letting $P_j = ejN_e$ be the volume polarization in the direction j due to the wave propagating through the plasma, the following equations are obtained.

$$\varepsilon_o E_x\left(\frac{\omega_p^2}{\omega^2}\right) = -P_x\left(1-\frac{i\nu}{\omega}\right) + iP_z\frac{\omega_\perp}{\omega} \tag{2.4.9a}$$

$$\varepsilon_o E_y\left(\frac{\omega_p^2}{\omega^2}\right) = -P_y\left(1-\frac{i\nu}{\omega}\right) - iP_z\frac{\omega_{//}}{\omega} \tag{2.4.9b}$$

$$\varepsilon_o E_z\left(\frac{\omega_p^2}{\omega^2}\right) = -P_z\left(1-\frac{i\nu}{\omega}\right) - iP_z\frac{\omega_\perp}{\omega} + iP_y\frac{\omega_{//}}{\omega} \tag{2.4.9c}$$

where $\omega_p^2 = \dfrac{N_e e^2}{\varepsilon_o m}$ is the plasma frequency and $\omega_{//} = \dfrac{eB_{//}}{m}$ and $\omega_\perp = \dfrac{eB_\perp}{m}$ are the gyrofrequencies of the electrons about the parallel and perpendicular components of the external magnetic field, respectively [*Budden*, 1961].

By applying a definition of wave polarization $S = P_z / P_y$ and solving for the resulting polynomial equation, solutions for the index of refraction for an electromagnetic wave propagating in the x-direction through a cold, weakly ionized plasma are determined. From equation 2.4.9b and equation 2.4.9c and after some algebraic manipulations

$$S^2 = \left(\frac{P_z}{P_y}\right)^2 = \frac{i\,S\left(\dfrac{\omega_\perp^2}{\omega^2}\right)\left(\dfrac{\omega}{\omega_{//}}\right)}{1-\left(\dfrac{\omega_p^2}{\omega^2}\right)-\left(\dfrac{i\nu}{\omega}\right)} - 1 \tag{2.4.10}$$

Letting $\varsigma = \frac{\omega_p^2}{\omega^2}$, $\psi_{//} = \frac{\omega_{//}}{\omega}$, $\psi_{\perp} = \frac{\omega_{\perp}}{\omega}$, and $\xi = \nu/\omega$ and solving for the roots of the quadratic equation 2.4.10, we see there are two solutions for *S*.

$$S = P_z/P_y = \frac{i}{2\psi_{//}}\left[\frac{\psi_{\perp}^2}{(1-\varsigma-i\xi)} \mp \sqrt{\frac{\psi_{\perp}^4}{(1-\varsigma-i\xi)^2} + 4\psi_{//}^2}\right] \qquad (2.4.11)$$

By rearranging equation 2.4.6 , equation 2.4.9b, and equation 2.4.9c and substituting the expression from equation 2.4.11 in for the ratio P_z/P_y , we obtain the Appleton-Hartree formula for $\tilde{n}$ in equation 2.4.5, for a wave of frequency ω in a plasma in which collisions are important and an external magnetic field is present [*Davies*, 1990].

$$\tilde{n}^2 = (\mu - i\beta)^2 = 1 - \frac{\varsigma}{1 - i\xi - \left(\frac{\psi_{\perp}^2}{2-2\varsigma-2i\xi}\right) \pm \left(\frac{\psi_{\perp}^4}{4(1-\varsigma-i\xi)^2} + \psi_{//}^2\right)^{1/2}} \qquad (2.4.12)$$

Thus far, we have neglected the effect of heavy ions since the mass of an electron is much greater than the mass of an ion, $m << m_{ion}$. According to the Appleton-Hartree formula, heavy ions only come into play when

$$\left(\frac{\omega_{ion\_plasma}}{\omega_{signal}}\right)^2 = \left(\frac{\omega_{electron\_plasma}}{\omega_{signal}}\right)^2 \qquad (2.4.19)$$

This situation exists for radio waves at very low altitudes where the ion density is approximately 60,000 times greater than the electron density [*Budden*, 1966]. Thus, for radio waves in the D-region and above, the effect of heavy ions is neglected.

2.4.3 No Collisions, No External Magnetic Field.

If effects from collisions and the external magnetic field, $\bar{B}_o$, are neglected, $\nu = 0,\ \omega_\perp = 0,$ and $\omega_{//} = 0$. Thus, $\psi_\perp = \psi_{//} = \xi = 0$, and from equation 2.4.3 and equation 2.4.6,

$$\tilde{n}^2 = (1-\varsigma) = \left(1 - \frac{\omega_p^2}{\omega^2}\right) = \frac{c^2}{u_{ph}^2} \tag{2.4.13}$$

From the definition of u_{ph} in equation 2.4.3 and solving equation 2.4.13 for ω, the dispersion relation for a wave in a cold, collisionless plasma with no external magnetic field is

$$\omega^2 = \omega_p^2 + c^2 k^2 \tag{2.4.14}$$

From the relationship in equation 2.4.14, there exists a limiting frequency for a wave in a plasma below which the wave can not propagate. As a wave of frequency ω propagates through a medium of plasma frequency ω_p, its wavelength $(\lambda = 2\pi / k)$ is governed by the dispersion relation, and as the wave encounters plasma of increasing N_e, k decreases, and λ increases. Thus, there will be a critical plasma density at which k is zero and the wave ceases to propagate. For this situation, $\omega = \omega_p = \omega_c$ where ω_c is the cutoff (or critical) frequency.

2.4.4. Significant Collisions, No External Magnetic Field.

In the lower ionosphere, particularly in the D-region, ν and ω are of the same order of magnitude and are both much larger than the plasma gyrofrequencies. Thus, $\psi_\perp = \psi_{//} = 0$, and equation 2.4.12 reduces to

$$\tilde{n}^2 = (\mu - i\beta)^2 = 1 - \frac{\varsigma}{1 - i\xi} = 1 - \frac{\omega_p^2}{\omega^2 - i\omega\nu} \tag{2.4.15}$$

In the situation where $\nu \sim \omega$, $\tilde{n}$ is imaginary and there is significant attenuation of the radio wave as it propagates through the medium in which the collision frequency between free electrons and neutrals cannot be neglected. The imaginary part of the index of refraction, β, gives the value of the absorption coefficient, κ, which describes the rate of wave energy attenuation during propagation [*Budden,* 1966].

$$\kappa = \frac{\beta\,\omega}{c} \tag{2.4.16}$$

We can solve for β by expanding equation 2.4.15 and multiplying by the complex conjugate.

$$\mu^2 - 2i\mu\beta - \beta^2 = 1 - \frac{\varsigma}{1-i\xi}\cdot\frac{1+i\xi}{1+i\xi} = 1 - \frac{\varsigma + i\varsigma\xi}{1+\xi^2} \tag{2.4.17}$$

Setting the imaginary parts of equation 2.4.17 equal to each other gives the result,

$$2i\mu\beta = \frac{i\varsigma\xi}{1+\xi^2}$$

$$\beta = \frac{\varsigma\xi}{2\mu(1+\xi^2)}$$

$$\kappa = \frac{\omega_p^2\,\nu}{2\mu c(\omega^2+\nu^2)} = \left(\frac{N_e e^2}{2\mu c\varepsilon_o m}\right)\frac{\nu}{\omega^2+\nu^2} \tag{2.4.18}$$

As seen in equation 2.4.18, κ linearly depends on N_e and ν. Thus, absorption of radio waves in the D-region is proportional to N_e and ν, which change with altitude. In §2.5 the profile of the product of N_e and ν is determined in order to determine the region of maximum HF absorption.

2.4.5 Propagation Modes.

The relationship between $\tilde{n}$ and the attenuation of a radio wave as it passes through ionospheric plasma is discussed in the last section. The relationship between $\tilde{n}$ and the direction of wave propagation is discussed here and is given by Snell's law,

$$\mu_1 \, Sin\theta_1 = \mu_2 Sin\theta_2 \tag{2.4.20}$$

where μ is the real part of $\tilde{n}$ given in equation 2.4.5 and θ is the angle between the direction of wave propagation and the normal of the plane of the refracting layer [*Jackson*, 1999]. Figure 2.4.1 shows how the direction of wave propagation is determined as the wave travels through plasma of varying index of refraction. The figure shows a wave entering a region of higher μ will be refracted towards the normal, shown as the vertical dashed line. A wave will be refracted away from the normal upon incidence onto a region of lower μ.

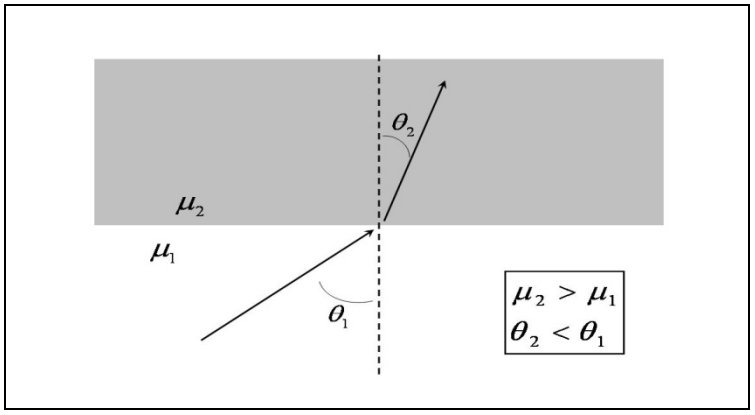

Figure 2.4.1. Snell's Law, given in equation 2.4.20, describes the influence of a medium's refractive index on the propagation path of a wave.

From the equation for the index of refraction for a collisionless plasma, given in equation 2.4.13, and for D-region plasma, given in equation 2.4.15, we see μ is directly related to N_e and inversely related to the frequency of the radio wave. Thus, as a radio wave travels to high altitudes and encounters increasing N_e values, it also encounters

plasma of decreasing μ. According to Snell's law, it will then be refracted away from the local vertical. The altitude at which the wave is refracted back towards the earth depends on wave frequency and elevation angle, the angle between the local horizontal and the direction of wave propagation. As seen in equations 2.4.13 and 2.4.15, as wave frequency increases, the value of N_e needed to refract a wave also increases. Thus, waves of higher frequency will be refracted at higher altitudes.

The terminologies used here to describe the altitudes at which radio waves are refracted include E-mode, F2- mode, and F1-mode propagation. A wave propagation mode describes the ionospheric region in which the wave is refracted back towards the earth. The number of hops a signal takes to reach a receiver is also used to differentiate between different modes of propagation. Figure 2.4.2 shows examples of the possible propagation modes available to a 10 MHz signal transmitted from Fort Collins, Colorado and received 1409 km away at Klamath Falls, Oregon. Propagation paths that attain a maximum altitude and are refracted back towards the earth within the E-region (90 km to 120 km) are called E-mode propagation paths, and those that attain a maximum altitude within the F1-region (120 km – 200 km) and F2-region (200 km- 400 km) of the ionosphere are called F1-mode and F2-mode propagation paths, respectively [*Hunsucker and Hargreaves*, 2003]. In Figure 2.4.2, one F2-mode path and three E-mode paths are available for the radio signal transmitted from Fort Collins to Klamath Falls.

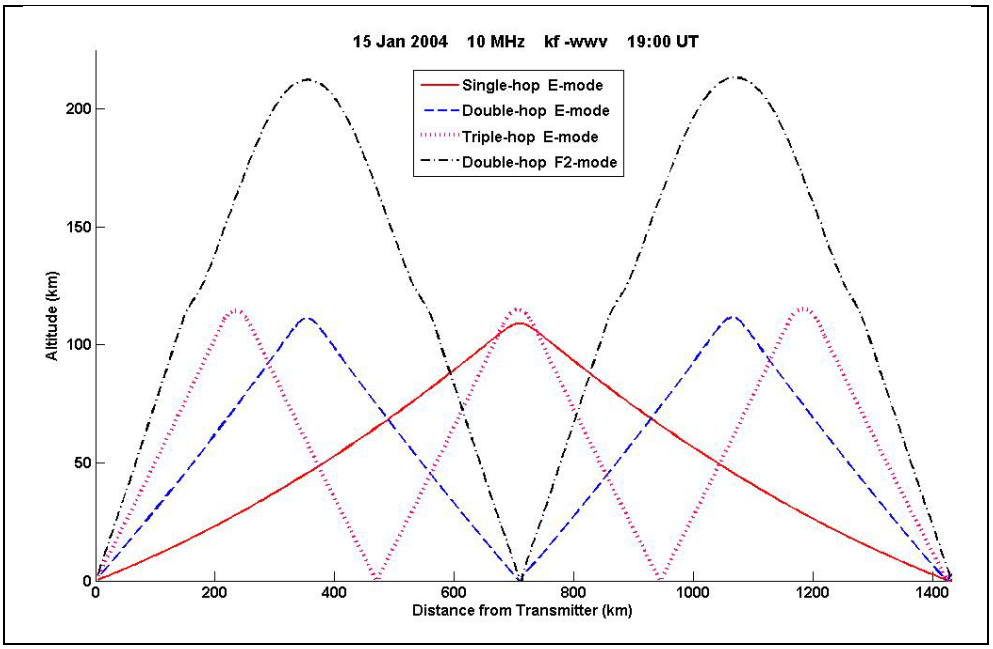

Figure 2.4.2. Various propagation modes available to a 10 MHz radio signal on 15 January 2004 at 19:00 UT transmitted from Fort Collins, Colorado to Klamath Falls, Oregon (ground distance of 1409 km), which include a single-hop E-mode, double-hop E-mode, triple-hop E-mode, and double-hop F2-mode.

2.5. HF Absorption in the D-region

In §2.4.4 an expression for the absorption coefficient is developed for the case of a plasma in which the frequency of collisions between electrons and neutral particles is significant and there is no external magnetic field. This case describes the D-region of the ionosphere, and as a radio wave travels through the D-region and encounters significant concentrations of free electrons, some of the wave energy is converted to kinetic energy of the free electrons. The electric field of the passing wave sets the free electrons into oscillations at a frequency equal to that of the wave. If the free electrons suffer no collisions, the kinetic energy gained by the electrons will eventually radiate as electromagnetic energy, restoring most of the wave energy. However, in the D-region the plasma density, N_e, and neutral density, N_n , are significant, and the collision rate between free electrons and neutral particles, ν , is high. Figure 2.5.1 shows ν ranges in value from 10^5-10^8 s^{-1} in the D-region and is of similar order of magnitude to the angular frequencies ($\omega = 2\pi f$) of HF radio waves considered here. As a result of these

collisions, much of the kinetic energy gained by the oscillating electrons is transferred to the neutral particles and is lost to the wave. Note $\nu \propto N_n$ and $N_n \approx 10^{16}\text{cm}^{-3}$ in the D-region, which is greater than the value of N_n in the E- and F-region by factors of 10^3 and 10^7 respectfully. From equation 2.4.18, $\kappa \propto N_e\nu$, and Figure 2.5.1 shows the product, $N_e\nu$ peaks between the altitudes 50 km to 100 km, which corresponds to the D-reigon. Thus, the majority of loss suffered by a radio wave in the ionosphere occurs within the D-region [*Davies*, 1990; *Gombosi*, 1998; *U.S. Standard Atmosphere*, 1976]. Figure 2.5.1 also compares the values of ν, N_e, and $N_e\nu$ during solar quiet conditions and solar active conditions and shows the predicted loss for a 5 MHz signal as calculated from κ given by equation 2.5.1.

Within the D-region, $\mu \approx 1$ for radio waves and the expression given in equation 2.4.18 for κ within the D-region reduces to

$$\kappa = \left(\frac{N_e e^2}{2\varepsilon_o mc} \right) \frac{\nu}{\omega^2 + \nu^2} \tag{2.5.1}$$

The equation governing the intensity of the HF wave, *I*, as it travels through the D-region is

$$I(s) = I_o \exp[-\kappa s] \tag{2.5.2}$$

where *s* is the distance traveled and I_o is the initial wave intensity [*Chandrasekhar*, 1960]. From equation 2.5.2, the total loss suffered by the HF wave is

$$L \propto \int_{s_1}^{s_2} \kappa \, ds \tag{2.5.3}$$

and the absorption in decibels is given by

$$L = -10Log\left(\frac{P_r}{P_t}\right) \tag{2.5.4}$$

where P_t is the power transmitted, and P_r is the power of the radio wave received [*Davies*, 1990].

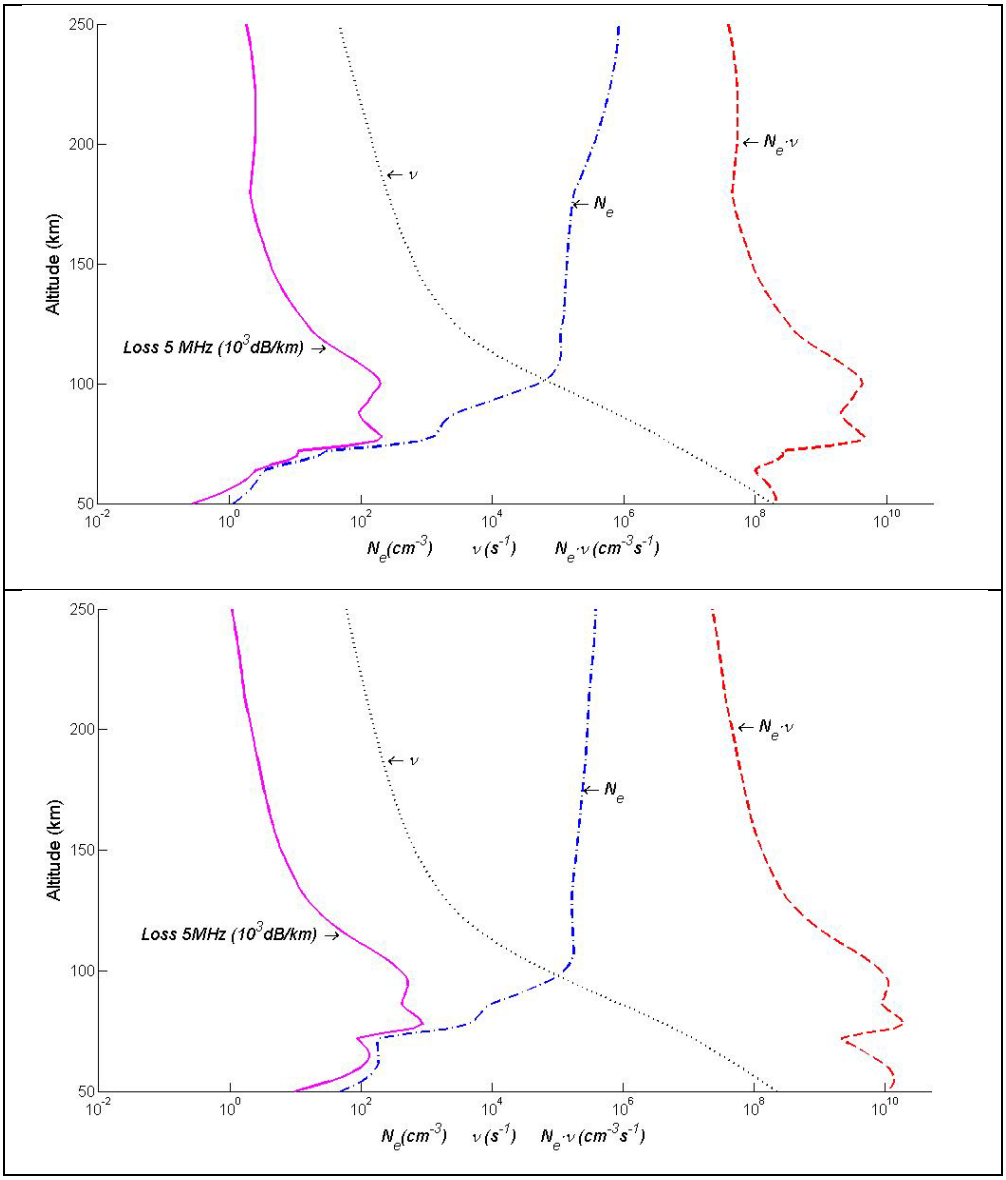

Figure 2.5.1. Ionospheric profiles of ν, N_e, and their product and the expected loss of a 5 MHz signal are shown during solar quiet conditions (top) and during solar activity (bottom) [*Goodman and Uffelman*, 1984; *Davies*, 1990].

From equations 2.5.1 and 2.5.3, D-region absorption is proportional to signal frequency and N_e, and N_e is shown to be proportional to $\sqrt{U_o}$ in §2.2.2, which means D-region absorption is also proportional to $\sqrt{U_o}$. D-region absorption is also shown to be proportional to $Cos^r(\chi)$ by first substituting the expression for N_e from equation 2.2.15b into equation 2.5.1 and, then, executing the integral in equation 2.5.3.

$$\kappa = \frac{\nu}{\omega^2 + \nu^2}\sqrt{\frac{\sigma\, N_n(z_o)\, U_o\, e^4}{\alpha\left(2\varepsilon_o mc\right)^2}}\, Exp\left(\frac{-(z - z_o)}{2H} - \frac{Sec(\chi)\sigma\, H(z) N_n(z_o)}{2} Exp\left(\frac{-(z - z_o)}{H}\right)\right) \tag{2.5.5}$$

Since the exponential term in the expression for κ in equation 2.5.5 contains a $Sec(\chi)$ term, the D-region absorption expression obtained from the integration in equation 2.5.3 is in terms of a $Cos^r(\chi)$. D-region absorption dependencies on $Cos^r(\chi)$, $\sqrt{U_o}$, and signal frequency (f) are further analyzed with respect to HF propagation data in §5.1 and §6.4.

2.6 Solar Flares

2.6.1 Flare Spectrum.

The connection between sudden HF radio transmission loss, also known as shortwave fadeout (SWF), and solar flares was first recognized by J.H. Dellinger in 1937 [*Dellinger*, 1936]. Given the simultaneity of the observation of a SWF and a solar flare and the similarity in their temporal duration and magnitude with respect to time, Dellinger suggested the electromagnetic energy produced by a solar flare includes "highly penetrating solar radiation of ultraviolet frequencies" capable of increasing D-region ionization rates and N_e, resulting in an enhancement of HF absorption. The radiation produced by a solar flare spans the electromagnetic spectrum with the majority of the UV radiation produced by a flare shortward of 14 nm [*Woods et al.*, 2006]. Flare radiation flux can double the amount of Lyman-α radiation incident on the upper atmosphere and can increase the solar X-ray flux by orders of magnitude [*Chamberlin*; 2005; *Lean*, 1997]. Recall from §2.2.1 solar Lyman-α and X-ray radiation are the

primary wavelengths for photoionization in the D-region. Observations have shown the enhanced solar radiation flux due to a flare is capable of increasing D-region N_e by two orders of magnitude [*Grubor et al.*, 2005]. A solar flare can be divided into three phases based upon the temporal evolution of the X-ray emissions of two separate bands, hard X-rays (0.05 - 0.4 nm) and soft X-rays (0.1 – 0.8 nm). The characteristic time profiles of the flux in hard and soft X-rays for two flares on 5 November 1980 are shown in Figure 2.6.1, and the typical relative radiation fluxes of a flare for different wavelengths and the phases of an X-ray flare with respect to time are shown in Figure 2.6.2.

As seen in Figures 2.6.1 and 2.6.2, the precursor phase of an X-ray flare (identified in the bottom panel of Figure 2.6.2) is marked by a gradual increase in soft X-rays and EUV radiation flux; however, it is not until the impulsive phase that the D-region N_e profile dramatically responds to the X-ray flare [*Liu et al.*, 2004]. The impulsive phase lasts for seconds to minutes during which large magnitude spikes in hard X-ray and EUV flux are observed, resulting in an immediate increase in D-region N_e. The hard X-ray signature during the impulsive phase is generally absent from the soft X-ray time profile and generally marks the onset of the soft X-ray enhancement characterizing the main phase [*Phillips*, 1995]. The main phase of an X-ray flare is distinguished by low hard X-ray flux and the rise and gradual decrease of soft X-ray flux.

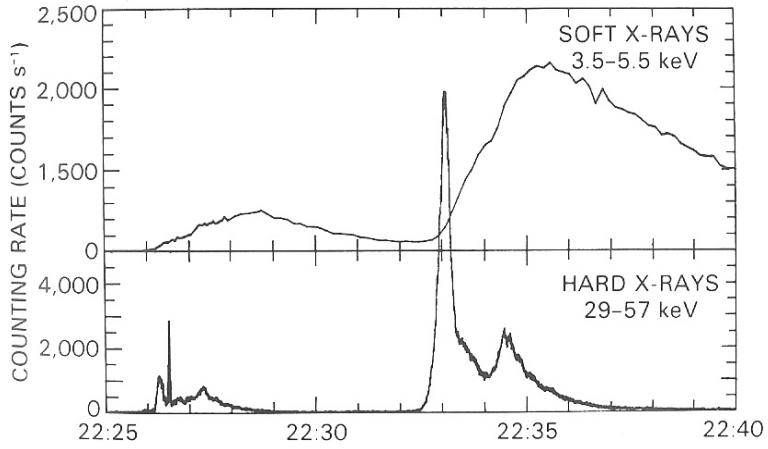

Figure 2.6.1 Temporal evolution of soft and hard X-rays during two flares on 5 November 1980 [*Phillips*, 1995].

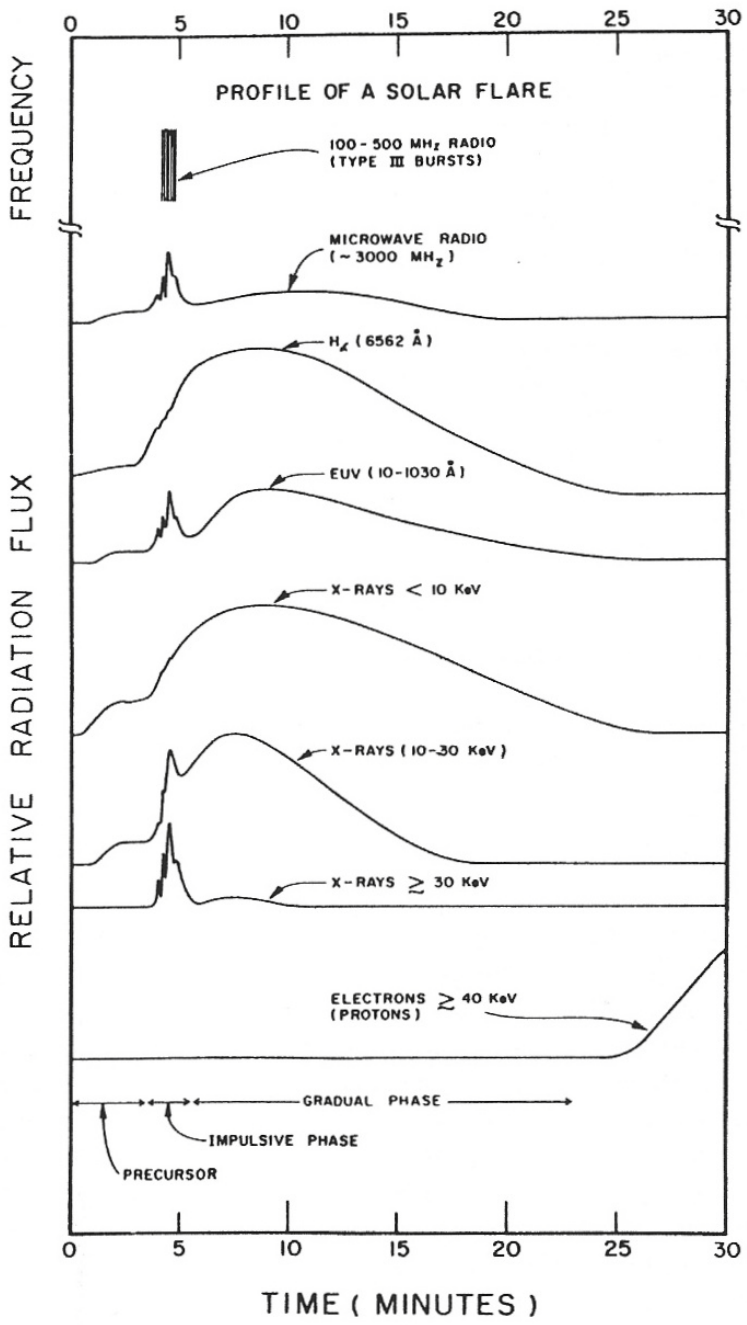

Figure 2.6.2. The relative radiation flux for various emissions with respect to time are shown along with the three phases of an X-ray flare, which shown at the bottom of the figure [Chaimberlin, 2005].

Both bands of X-ray radiation, hard and soft, are absorbed in the D-region and are responsible for the dramatic enhancement in D-region N_e and HF absorption; however, it

is not presently known how the ratio of the soft X-ray flux to the hard X-ray flux during a solar flare influences the duration, magnitude, and recovery of HF absorption in the D-region. Although the characteristics of the three phases described above generally apply to most solar X-ray flares, the ratio of soft to hard X-ray flux throughout the flare event differs for each flare. The different types of X-rays are also absorbed at different altitudes within the D-region which can alter the N_e altitude profile. *Deshpande et al.* [1972] define the ratio of the hard X-ray flux to the soft X-ray flux of a flare as the spectral hardening factor or effective flare temperature and show the magnitude of the hardening factor generally increases as the X-ray flux of the flare increases. The hardening factor is investigated in §6.2 as a possible explanation for cases in which there are delays in flare-induced absorption of up to fifteen minutes after the onset of an X-ray flare.

2.6.2 Flare Classification.

Solar flares are classified according to their intensity in the visible wavelengths, by their area or size, and by total X-ray emission. These characteristics are good indicators of the amount of energy released in the form of electromagnetic radiation and particle emissions [*Phillips*, 1995]. Importance is the measure of an optical flare area or size at the time of maximum intensity as viewed in hydrogen-α (Hα). As is discussed in §3, many automated HF absorption prediction models use flare classification as an input and as a proxy for solar radiation flux. One of the first automated absorption prediction models was developed by Stonehocker in the 1960's prior to the ability to monitor solar X-ray emissions and uses flare importance as the primary input for predictions of the duration of a flare-induced absorption event [*Stonehocker*, 1970]. Stonehocker's model was a precursor to the SWPC D-region Absorption Model widely used today, see §3.3 and §3.4.

A unit often used to describe flare area is one millionth of the visible solar hemisphere, which is approximately equal to 3 million square kilometers. Another unit used is hemispheric square degree which is roughly equivalent to 48.5 hemispheric millionths. Table 2.6.1 summarizes importance classification for flares [*Phillips*, 1995].

Table 2.6.1. Solar Flare Importance Classifications

Importance Designator	Flare Area	
	Hemispheric Square Degrees	Millionths of Hemisphere
0	0 – 2.0	10 – 99
1	2.1 – 5.1	100 – 249
2	5.2 – 12.4	250 – 599
3	12.5 – 24.7	600 – 1199
4	≥ 24.8	≥ 1200

Another classification generally appended to the Importance numeral designator and summarized in Table 2.6.2 is Brightness. An optical flare's Brightness is a quantitative term describing the intensity of the flare at ± 0.04 nm, ± 0.06 nm, and ± 0.1 nm off the Hα line center as compared to background intensity. If the area does not brighten to at least 150% of the solar disk background, it is only considered to be a plage fluctuation [*Phillips*, 1995].

Table 2.6.2. Optical Flare Brightness Classifications

Brightness Designator	Brightness (% of Background)
F (Faint)	150% - 259%
N (Normal)	260% - 359%
B (Brilliant)	≥ 360%

Observations obtained by the Geostationary Operational Environmental Satellites (GOES) of solar X-rays in the bands 0.05 - 0.4 nm and 0.1 - 0.8 nm allow for X-ray

classification of flares. Table 2.6.3 summarizes X-ray flare classifications according to peak soft X-ray flux within the 0.1 – 0.8 nm band. The letter associated with the X-ray classification of a flare designates the exponent (X) in the expression 10^X as summarized in Table 2.6.3. Thus, a flare of X-ray classification C4 produced a peak soft X-ray flux of $4\times10^{-6}\,{}^{W}\!/_{m^2}$. GOES data for M- and X-class flares on 14 July 2000 in shown in Figure 2.6.3. The red line on top in Figure 2.6.3 represents the flux of soft X-rays (0.1-0.8 nm), and the blue line below represents the flux of hard X-rays (0.05-0.4 nm). Most automated methods of predicting flare-induced HF absorption rely on flare X-ray classification. However, as mentioned in the last section, prior to the ability to measure solar X-ray flux due to a flare, several automated methods used flare importance and brightness classification to make predictions of HF absorption, namely Stonehocker's HF absorption model which is discussed §3.3.

Table 2.6.3. X-ray Flare Classifications

Class	Corresponding Exponent 10^X
C	-6
M	-5
X	-4

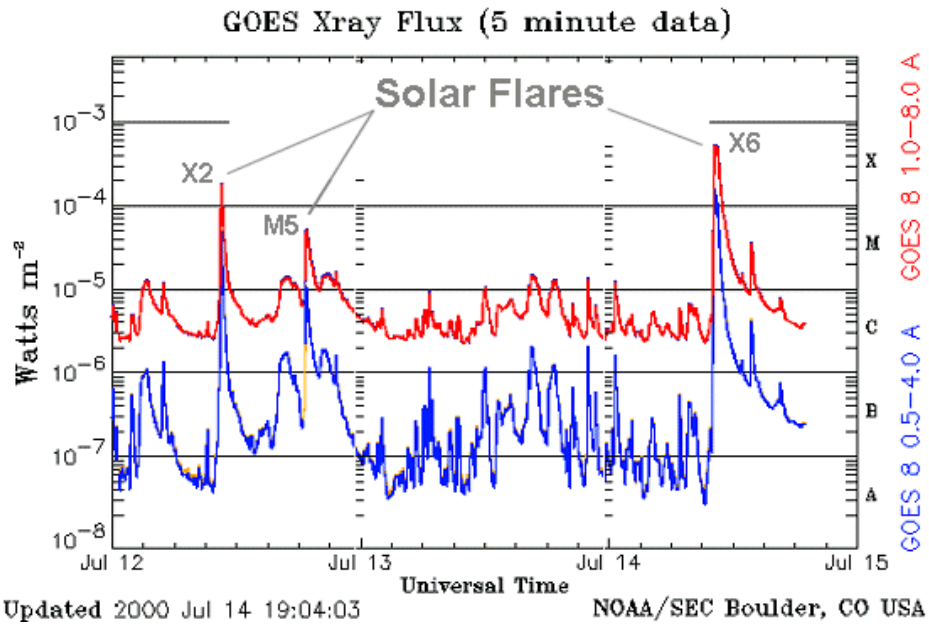

Figure 2.6.3. GOES X-Ray Flux Data on 14 July 2000. http://www.swpc.noaa.gov/today.html#xray

3. Ionospheric Absorption and Propagation Prediction Methods

For several decades, there has been a desire to develop an automated method of analyzing space weather conditions in real-time for prediction of ionospheric HF absorption and propagation. As sensor and computer technology evolved, so did the type of input data used by ionospheric models and our understanding of space weather effects on the ionosphere and HF propagation. In 1970 an automated system for forecasting HF propagation by monitoring the importance classification of solar flares and the occurrence of solar radio bursts was proposed by *Stonehocker* (1970). With improved measurements of solar X-ray flux, *Oyinloye* (1979) presented an empirical formula for HF absorption in the ionosphere as a function of solar ionizing flux. Current ionospheric absorption and HF propagation models [*Butcher*, 2005; *Eccles*, 2004; *SEC*, 2007] allow for the inclusion of solar X-ray flux in real-time and are able to update or modify predictions accordingly. In this section, the automated methods of predicting ionospheric conditions and HF propagation introduced above are discussed in more detail.

3.1 Oyinloye

Using absorption data from various HF monitoring stations throughout the world from 1957 to 1970 and solar X-ray flux observations from the satellite Solarad9-Explorer37, *Oyinloye* (1980) derived an empirical formula for forecasting HF absorption which included an ionizing flux term. Oyinloye's work focused on obtaining an equation of the form in equation 3.1.1 for the absorption, *L*, of a 2.2 MHz signal at vertical incidence as a function of ionizing flux, *U*, magnetic dip angle, α, and solar zenith angle, χ.

$$L = r(\alpha) \cdot \psi(U, \chi) \tag{3.1.1}$$

Oyinloye (1978) found ionospheric absorption to vary in harmony with the intensity of the 0.1-0.8 nm solar X-ray flux and represented the ionizing flux, *U*, by the 0.1-0.8 nm solar X-ray flux. He then evaluated the relationship between *L* and *U* by performing a least squares (LS) fit to the plot of $\log_{10}(L)$ versus $\log_{10}(U)$ for constant χ. He also

determined the relationship between L and $Cos(\chi)$ from the least squares fit of the plot of $\log_{10}(L)$ versus $\log_{10}(Cos(\chi))$ for constant U. The result of these relations is

$$L = r(\alpha) L_o U^{0.143} Cos^m(\chi) \tag{3.1.2}$$

where m is 0.96 and 0.78 for morning and afternoon hours respectively. The receiver latitude is taken into account with the term $r(\alpha)$, which is the ratio of the 2.2 MHz signal absorption at the receiver to the absorption measured at a reference site at Colombo, Sri Lanka [*Oyinloye*, 1978], and the value of L_o is given by the absorption observed at noon at the reference site at Colombo when $U = 1^{erg}/_{cm \cdot s}$.

Winter use of equation 3.1.2 for prediction of HF absorption at mid-latitudes shows large errors of about 20%, while errors of about 10% are seen for predictions during summer and equinox. Although the Oyinloye model for HF absorption is specifically for a 2.2 MHz signal and not specifically for flare-induced absorption, this model is one of the first attempts at producing automated HF predictions using real-time solar ionizing radiation flux and a term dependent on the solar zenith angle.

3.2 Stonehocker

Unlike previous radio propagation forecasting methods which relied mostly on the experiences and subjective interpretations of forecasters, *Stonehocker* (1970) outlines an automated method of predicting HF signal attenuation given real-time solar radio burst energy, E_{radio}, and an automated method of predicting SWF duration given the importance classification of a solar flare. His method produces a probability of SWF given current flare probability forecasts and the historical probabilities of SWF occurrence for each level of flare importance. The historical probabilities of SWF occurrence and the correlation between signal attenuation and solar radio flux were determined by *Harvey* [1964] through her observations of solar radio bursts, solar flares, and SWF from July 1957 to December 1960.

Stonehocker recorded the averaged signal attenuation of the 5 MHz US Standard Time transmission from the WWV station in Fort Collins, Colorado to White Sands, New Mexico during summer months and the hours of 1000-1400 LT and assumed a one-hop

propagation path. 46 solar flares occurred during the observations, and the attenuation data were grouped according to flare importance and to whether or not a solar radio burst accompanied the flare. The LS fit to the plot of the observed signal attenuation in decibels, L, versus the logarithm of solar radio burst energy, E_{radio}, at 10,000 MHz is

$$L(dB) = (11.33 \cdot 10^{-22})\, Log_{10}(E_{radio}) \left(Watts / m^3 \right) \qquad (3.2.1)$$

and is shown in Figure 3.2.1 with standard error of the residuals at 6.2 dB. The dotted line in the figure is the least squares fit of the observed signal attenuation in decibels for the 5 MHz signal transmitted from Fort Collins, Colorado to White Sands, NM versus the logarithm of solar radio burst energy at 10,000 MHz. The solid line has been rotated to coincide with Stonehocker's desired limits [*Stonehocker*, 1970].

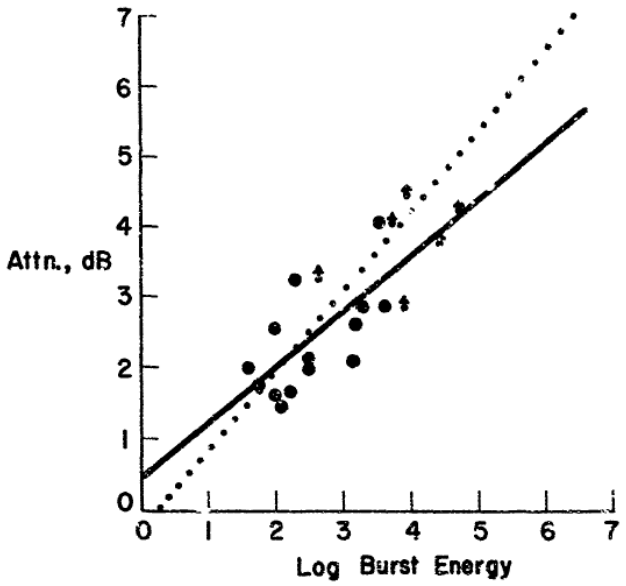

Figure 3.2.1. Stonehocker's Data: The dotted line is the least squares fit of the observed signal attenuation in decibels for a 5 MHz signal transmitted from Fort Collins, Colorado to White Sands, NM versus the logarithm of solar radio burst energy at 10,000 MHz. The solid line has been rotated to coincide with Stonehocker's desired limits [*Stonehocker,* 1970].

Stonehocker's least squares fit of the plot of SWF duration versus solar flare importance is shown in Figure 3.2.2 and is approximately

$$T = 16 + 2.8\,B \qquad (3.2.2)$$

where T is the duration of the SWF in minutes and B is the flare importance classification in deg^2 .

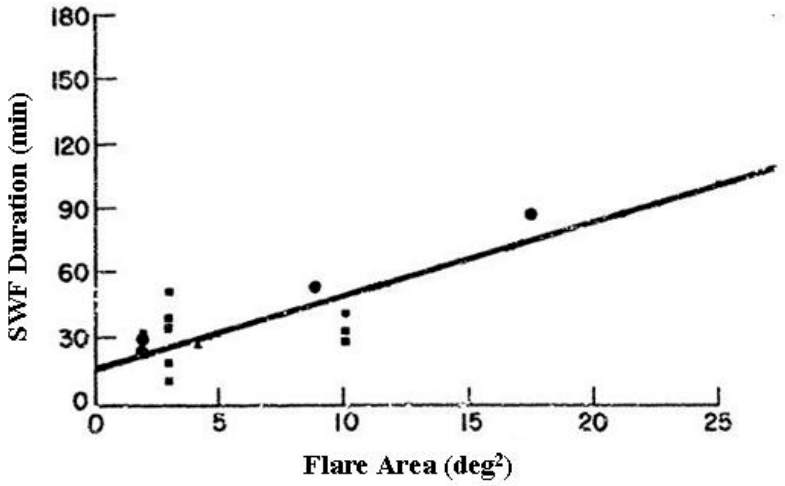

Figure 3.2.2. Stonehocker's relationship between SWF duration and the importance classification of a solar flare [*Stonehocker,* 1970].

The predictions governed by the Stonehocker equations 3.2.1 and 3.2.2 are only valid for the 5 MHz signal around noon for the signal transmitted from Fort Collins to White Sands. Stonehocker scales the 5 MHz attenuation prediction by the factor, f^{-2}, to obtain attenuation predictions at other frequencies. Stonehocker verified the relationship for frequencies between 5 and 12 MHz and found less than 9% error in the predictions and suggested equation 3.2.1 can be applied to other propagation paths by scaling by $Cos(\chi)$, where χ in the solar zenith angle.

Stonehocker found "very good" correlation between SWF duration and solar radio burst duration; however, when flare importance was used to predict SWF occurrence,

only one out of eleven SWF events was correctly predicted resulting in a 0.09 correct prediction rate. Since the development of Stonehocker's model, solar X-ray flux observations have become available, and currently X-ray flare classification is used instead of optical flare classification or solar radio flux as input in most operational autonomous methods of predicting flare-induced HF absorption since solar radiation in the X-ray realm is responsible for ionization of the major constituents, N_2 and O_2, in the D-region (§2.2). The Space Weather Prediction Center (SWPC) D-region Absorption Model is one model which is built upon the findings of Stonehocker, but which uses X-ray flux instead of solar radio flux and is discussed in the next section.

3.3 SWPC D-region Absorption Model

With the availability of direct observation of the solar X-ray radiation responsible for D-region ionization, Stonehocker's model is modified and used as a starting point for the National Oceanic and Atmospheric Administration (NOAA) Space Weather Prediction Center (SWPC) division D-region Absorption model. The SWPC model is a widely used operational ionospheric HF propagation and absorption model. The SWPC D-region Absorption model, found at *http://www.swpc.noaa.gov/dregion/index.html,* provides predictions of signal attenuation as a function of frequency and geographical location. The model is driven by GOES X-ray flux observations at a one-minute cadence and is updated continuously.

The SWPC model is built upon the work done by *Stonehocker* (1970) (§3.2); however, unlike the Stonehocker model that relates flare importance to absorption in decibels, the SWPC model relates flare X-ray classification to absorption. From observations of flare-induced HF absorption and the X-ray classification and importance of the responsible flares, relationships between flare importance and X-ray classification which result in the same magnitude of HF absorption were determined. From these relationships, equation 3.2.1 of the Stonehocker model is modified and becomes

$$HAF(MHz) = 10 \cdot \log_{10}[\, flux(W/m^2)] + 65 \qquad (3.3.1)$$

which is the SWPC model equation for determining the Highest Affected Frequency (HAF) at the sub-solar point.

The HAF is the frequency of a signal that is predicted to suffer a loss of 1 dB during vertical propagation under current ionospheric and space weather conditions. The SWPC model begins by calculating the HAF as a function of geographical location. The empirical SWPC D-region absorption model relations between X-ray flare class and HF absorption which are used to determine the HAF at the sub-solar point are given in Table 3.3.1.

Table 3.3.1: Empirical relations used in SWPC D-region Absorption model to predict the HAF given current GOES X-ray flux data.

Observed GOES X-ray Flux (0.1-0.8 nm) (W m^{-2})	X-ray Flux Classification	Predicted HAF (MHz)
10^{-5}	M1.0	15
5×10^{-5}	M5.0	20
10^{-4}	X1.0	25
5×10^{-4}	X5.0	30

The SWPC model determines HAF values for $\chi \neq 0°$ by scaling the sub-solar value by $Cos^{0.75}(\chi)$. The global map in Figure 3.3.1 shows the SWPC prediction of HAF as a function of geographical location in response to the X3.0 solar flare on 16 July 2004.

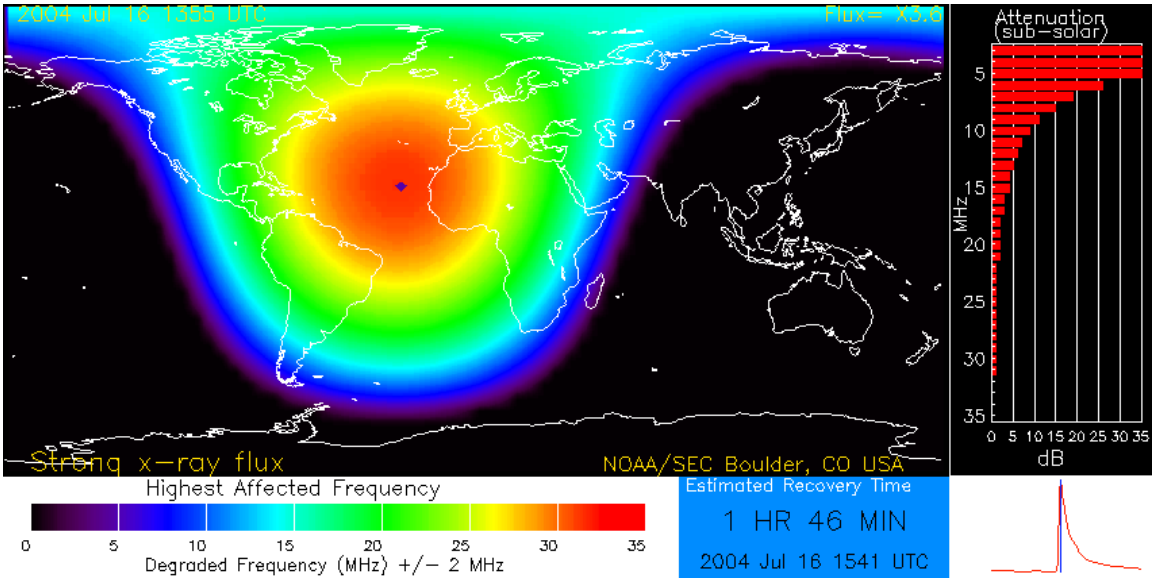

Figure 3.3.1. The D-region Absorption Prediction product produced by SWPC for the date 16 July 2004 on which an X3.0 solar X-ray flare occurred. The background X-ray flux classification for this date was C8.1, and the sub-solar point is marked by the yellow diamond (*http://swpc.gov/rt_plots/dregion.html*).

The SWPC model also makes predictions of signal attenuation as a function of frequency for vertical propagation at the sub-solar point and displays these predictions in a bar graph as shown on the right of Figure 3.3.1. The SWPC model approximates the absorbing region of the ionosphere as a horizontal slab so that attenuation for signals of oblique propagation are determined by scaling the predictions of vertically propagating signals by $1/Sin(\phi)$, where ϕ is the elevation angle of the signal. Given the loss of the HAF is defined to be 1 dB, the SWPC model predicts attenuation L at other frequencies (f) using the relation

$$L(dB) = \left(\frac{HAF}{f} \right)^2 \qquad (3.3.2)$$

Like the Stonehocker model, the SWPC model assumes an f^{-2} dependence on signal frequency.

3.4 The AbbyNormal Physical Model

The *Absorption by the D and E Region of HF Signals with Normal Incidence* (AbbyNormal) model is a physics-based model which calculates mid-latitude ionospheric electron and ion density profiles for prediction of HF propagation and absorption. For determining HF absorption, the AbbyNormal model generates an electron density profile by combining two ionospheric models, the Data-driven D-region (DDDR) model and the International Reference Ionosphere (IRI) model [*Bilitza*, 2001]. After generating its 3-dimensional representation of the ionosphere, AbbyNormal uses the HASEL ray tracing code developed by *Coleman* (1993) to determine ray propagation and calculates HF signal loss along the path in decibels. Antenna gain and focusing effects are also included, resulting in a final prediction of received signal strength.

AbbyNormal uses the IRI model to describe the ionosphere above 130 km and uses the DDDR model profiles between 50 km and 110 km. The model outputs are blended together to define the ionosphere between 110 km and 130 km. Profiles of neutral species are determined by the empirical models, MODerate spectral resolution atmospheric TRANSsmittance model (MODTRAN) and Mass-Spectrometer Incoherent Scatter model (MSIS), with MSIS [*Hedin*, 1991] providing the profiles of major species and MODTRAN [*Anderson, et. al.*, 1986] determining minor species profiles. Ionization of the minor species, nitric oxide (NO), plays an important role in determining D-region N_e and HF absorption. Unfortunately, MODTRAN does not adequately solve for NO densities throughout the ionosphere, and recall from §2.4, ionization of NO via Lyman-α radiation is one of the two major sources of free electrons in the D-region. Thus, to properly determine ionospheric N_e profiles and diurnal HF absorption, NO densities must be known. Representations of ionospheric NO densities that are lower than actual values lead to lower predictions of HF absorption in the absence of flare activity, and NO densities that are higher than actual values lead to over-predicting diurnal HF absorption. See §9.3 for comparisons between observed NO densities and AbbyNormal predicted NO densities and for a discussion on improving the method by which AbbyNormal defines the NO profile within the ionosphere.

The DDDR model uses simple D-region chemistry to represent the dominant loss and source processes responsible for HF absorption [*Eccels, et. al.*, 2005]. Inputs driving the chemistry of DDDR are GOES observations of solar X-ray flux and F10.7 flux. F10.7 observations along with the Extreme Ultraviolet Flux for Aeronomic Calculations (EUVAC) Model are used to determine solar ultraviolet (UV) flux [*Richards, et. al.*, 1994]. Observations of F10.7 are also used to determine cosmic ray background and Lyman-α flux. Figure 3.4.1 summarizes the chemical processes used by DDDR to determine the electron density profile below 110 km. These processes include 3-body attachment, photo-detachment, collisional detachment, and recombination.

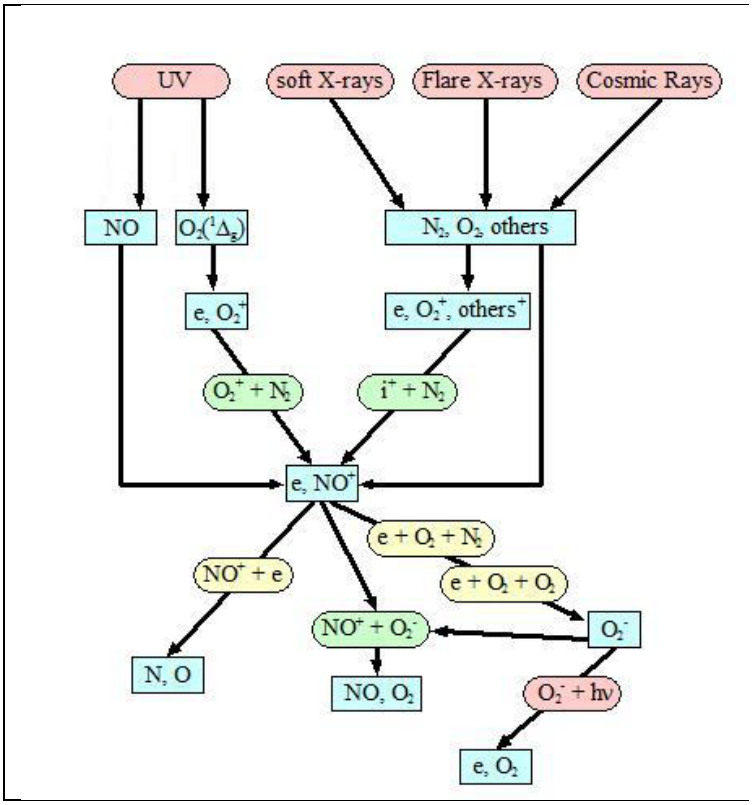

Figure 3.4.1. The DDDR model uses simple positive and negative ion chemistry to generate an electron density profile between 50 km and 110 km [*Eccles*, 2005].

4. HF Propagation Data

4.1 HIDIVE Data

HF propagation data analyzed here are provided by the Space Environment Corporation and were obtained during the HF Investigation of D-Region Ionospheric Variation Experiment (HIDIVE) over a period of five years [*Eccles et al.,* 2005]. The experiment involves three HF receivers which continuously record the calibrated signal amplitudes from the U.S. standard time station, WWV, in Fort Collins, Colorado. The transmissions from WWV are summarized in Table 4.1.1.

Table 4.1.1. Calibrated signal amplitudes of the HF transmissions from the U.S. standard time station, WWV, in Fort Collins, Colorado are monitored continuously by a network of three HIDIVE receivers.

WWV Fort Collins, Colorado	
Frequency (MHz)	Power (kW)
2.5	2.5
5.0	10
10.0	10
15.0	10
20.0	2.5

The HIDIVE receivers record signal amplitude data and are located at the monitoring stations BLO in Garden City Utah, PRV in Providence, Utah, and KF in Klamath Falls, Oregon. The locations of each monitoring site and their distances from the WWV transmitter are given in Table 4.1.2, and signal amplitude data for the WWV transmissions measured at the KF station (i.e. the signal amplitude data for the kf-wwv transmission) on 9 February 2003 are shown in Figure 4.1.1. The top panel in Figure 4.1.1 shows the signal amplitude data for the 2.5 MHz kf-wwv transmission from 00:01

UT to 24:00 UT on 9 February 2004. The second panel from the top shows the 5 MHz kf-wwv signal strength data for the same time period and date, the third panel from the top shows the 10 MHz kf-wwv signal strength data, the fourth panel from the top shows the 15 MHz kf-wwv signal strength data, the fifth panel from the top shows the 20 MHz kf-wwv signal strength data, and the bottom panel in Figure 4.1.1 shows the GOES X-ray 0.1-0.8 nm flux data from 00:01 UT to 24:00 UT on 9 February 2004. The units for the reported signal strength data are dBuV, where 0 dBuV corresponds to a signal with 1 uV peak-to-peak amplitude and

$$1\ dBuV = 20\ Log\left(\frac{V_{peak-to-peak}}{1uV}\right) \tag{4.1.1}$$

Local sunset at 03:12 UT and sunrise at 14:30 UT are clearly discernable in Figure 4.1.1.

Table 4.1.2. Summary of HIDVIE monitoring sites and dates on which data collection began.

Receiver	Location	Latitude (°N)	Longitude (°W)	WWV Distance
BLO	Garden City, UT	41.934	111.421	550 km
PRV	Providence, UT	41.712	111.830	579 km
KF	Klamath Falls, OR	42.173	121.850	1409

Of the nine transmissions monitored by HIDIVE, three consistently provide daytime propagation data relatively low in noise and interference and, thus, are used here to investigate flare-induced HF absorption. These three transmissions are the 5 MHz blo-wwv, 10 MHz kf-wwv, and 15 MHz kf-wwv signals. Figure 4.1.2 shows daytime HIDIVE data during a solar active period on 26 Feb 2004. During the day, the 2.5 MHz signals are completely absorbed and are unavailable. Recall from §2.4.4 and equation 2.5.1 absorption along a path is proportional to N_e and inversely proportional to signal frequency. Thus, as N_e increases after sunrise due to ionization via solar X-rays and

Lyman-α, 2.5 MHz is below the frequency range available for the kf-wwv and blo-wwv propagation paths and the 2.5 MHz signals are not available.

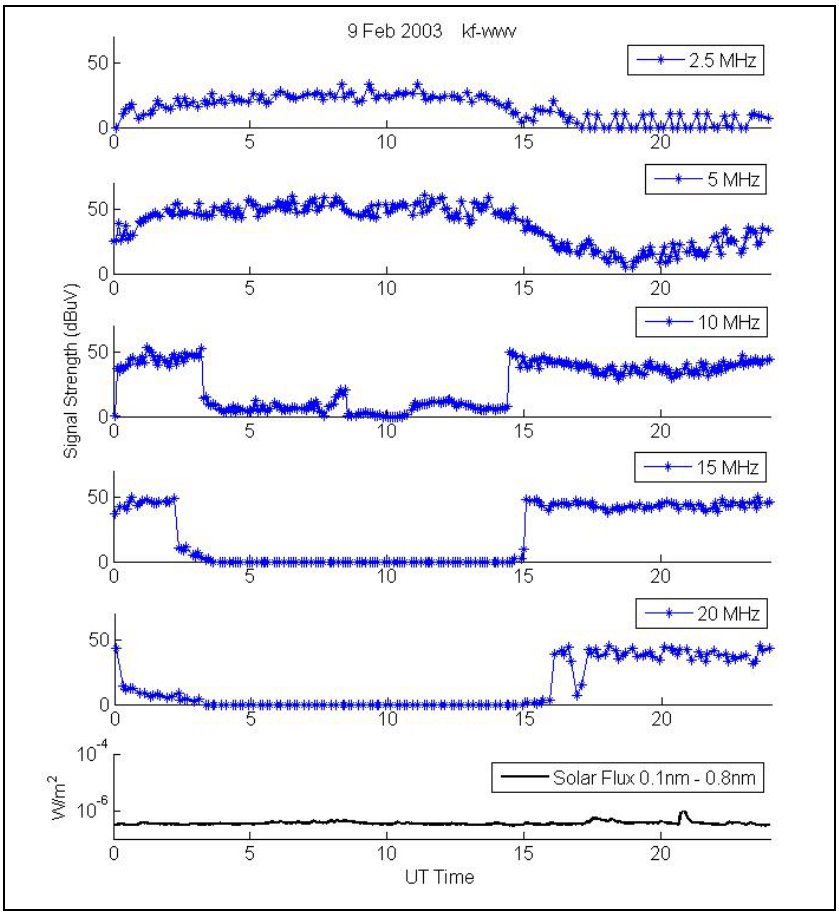

Figure 4.1.1. Typical HIDIVE data for the WWV transmissions received at the KF station during solar quiet conditions on 9 Feb 2003. GOES 0.1-0.8nm X-ray flux is shown in the bottom panel.

Furthermore, the 20 MHz signals are often unavailable during the day due to daytime ionospheric N_e values not being large enough to refract the radio wave back towards the earth. Thus, the 20 MHz signals often penetrate the ionosphere. Recall from §2.4.4 and §2.4.5, the index of refraction governs the direction of a radio wave as it propagates through the ionosphere and is dependent on signal angular frequency and N_e. Thus, as ω increases, the value of N_e needed to refract the wave back towards the earth

increases. unfortunately, N_e often does not reach the level needed to refract the 20 MHz kf-wwv and 20 MHz blo-wwv back towards the earth. Also, the 10 MHz blo-wwv signal often becomes unavailable for time periods of minutes to hours during the day due to its propagation path changing. The altitude and value of N_e at which the 10 MHz signal refracts back towards the earth is at a boundary such that small changes in N_e change the propagation path enough that the signal does not make it to the kf and blo receiver sites. Thus, the 2.5 MHz kf-wwv, 2.5 MHz blo-wwv, 20 MHz kf-wwv, 20 MHz blo-wwv, and 10 MHz blo-wwv signals are not used in this analysis since determining if an observed decrease in signal strength is flare-induced or due to a change in propagation path would be difficult.

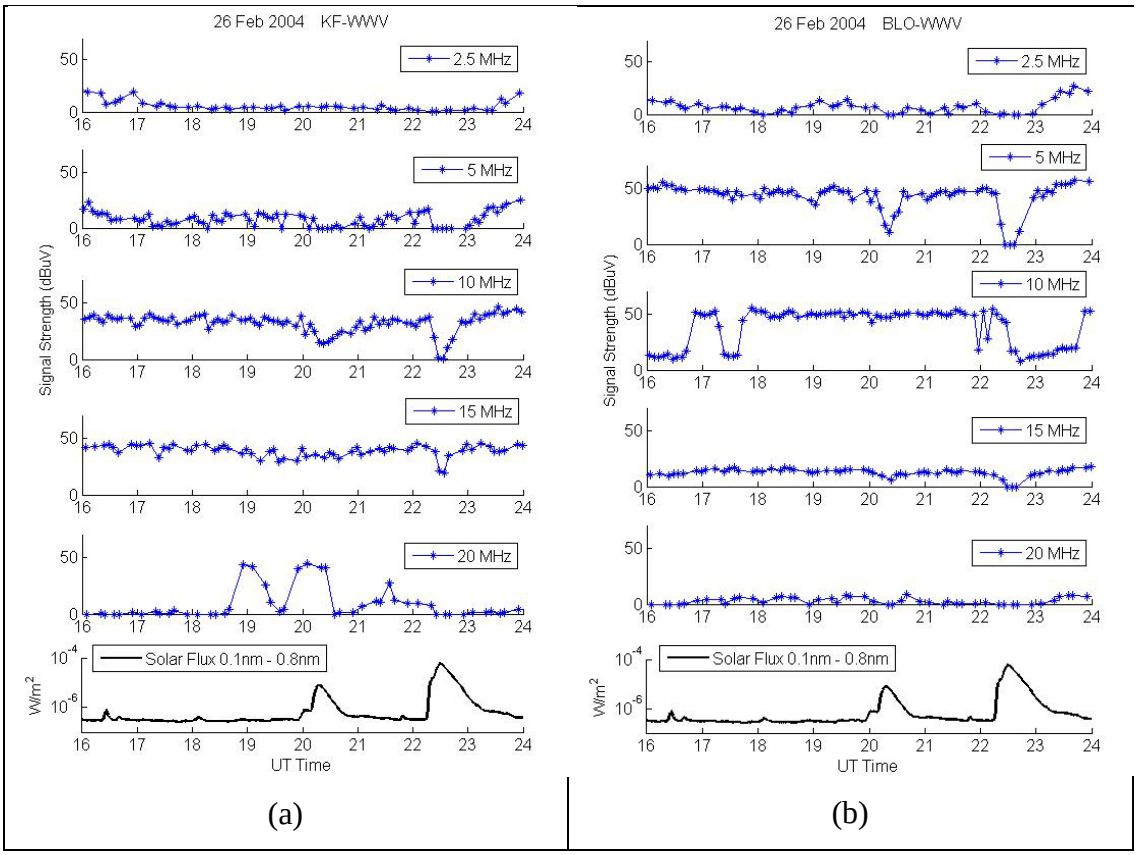

Figure 4.1.2. HIDIVE data on 26 Feb 2004 captures the flare-induced absorption of the (a) kf-wwv transmissions and (b) blo-wwv transmissions due to a C7.5 and an M5.7 solar X-ray flare at 20:00 UT and 22:18 UT, respectively.

4.2 Riometer Data

Given signals of frequencies 20 MHz and greater can penetrate the ionosphere during the day, riometer data were needed in order to expand the frequency range of the HF data used for this work. Data obtained at the Canadian Space Agency sponsored NORSTAR riometer located at 50.2° N latitude and 263.96° longitude in Pinawa, Manitoba, Canada are used [*Spanswick et al*, 2005]. The Pinawa riometer measures the signal strength of the cosmic background noise at 30 MHz from the portion of the sky directly overhead at a 5-second cadence.

The source of the cosmic background noise is radio emissions from stars and galaxies, and although, the magnitude of the noise can be treated as constant with respect to time, it does vary with respect to location in the sky [*Hargreaves*, 1969]. Riometers are passive devices that measure the cosmic radio noise after it has passed through the ionosphere. When D-region ionization is enhanced during flares, cosmic radio signals suffer additional absorption, and the riometer data can be used to study flare-induced HF absorption. Riometer data during a flare is shown in Figure 4.2.1. The top panel of Figure 4.2.1 shows the raw signal strength of the cosmic background radio emissions in Volts from 15:00 UT to 24:00 UT on 2 April 2001 during an X18 flare at 21:30 UT, and the middle panel in the figure shows the absorption of the cosmic background signal during the same time period as calculated by the University of Calgary staff managing the Pinawa riometer.

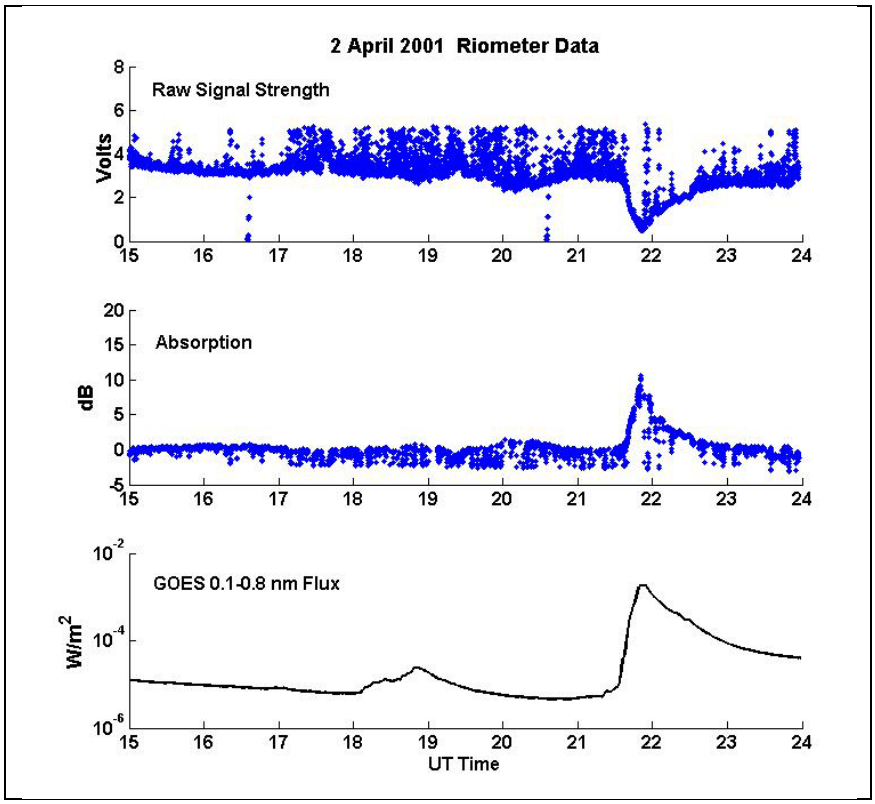

Figure 4.2.1. The riometer data during the X18 flare on 2 April 2001 shows significant absorption of the cosmic background radio noise during the flare.

5. Solar Quiet Reference Curves

5.1 SQ Curve

As discussed in §4.1, HIDIVE data only provides signal strength versus time information for a given transmission; thus, a solar quiet (SQ) reference curve is needed in order to distinguish between the diurnal absorption due to background solar X-ray flux and Lyman-α flux and absorption due to the enhanced solar X-ray flux produced by a flare. Diurnal absorption during solar quiet conditions, as discussed in §2.2 and §2.3, is due to Lyman-α ionization of NO and due to the background solar X-ray flux ionization of O_2 and N_2. An SQ curve represents the expected diurnal, quiet-time signal strengths of a given transmission and is used as a reference curve from which flare-induced absorption is calculated. SQ reference curves are used here to capture the diurnal variation of HF absorption and to make possible the calculation of flare-induced absorption. The goal is to determine a reproducible and automated method of defining daytime SQ reference curves for any HIDIVE transmission.

Figure 5.1.1 is an example of how an SQ curve is used with signal strength data to determine flare-induced absorption. The red dashed line in the top panel represents an SQ curve fitted to HIDIVE data used to determine the flare-induced absorption due to an C7.5 and M5.8 flares occurring at 20:00 UT and 22:15 UT. The HIDIVE data in the top panel are the 10 MHz kf-wwv signal strengths on 26 Feb 2004. The GOES X-ray 0.1-0.8 nm flux is shown in the lower panel. Using the example SQ curve, shown in the figure as the red dashed line, as reference signal strength values, the maximum flare-induced absorptions during the C7.5 and M5.8 flares are 19.3 dB and 37.2 dB, respectively.

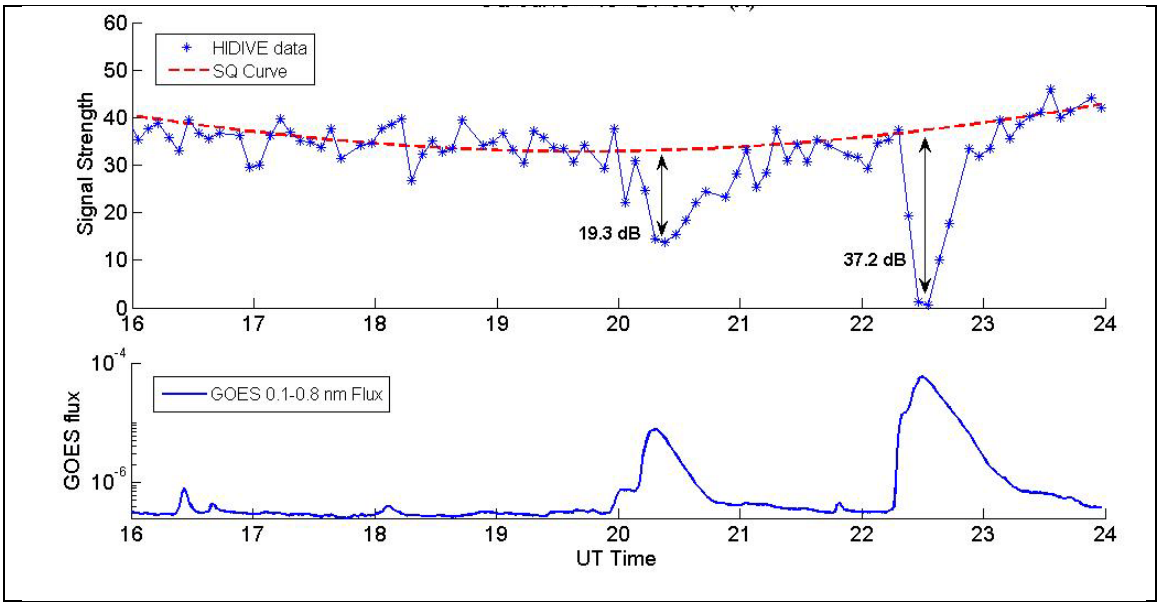

Figure 5.1.1. An example of fitting an SQ curve to HIDIVE data in order to determine flare-induced absorption is the red dashed line in the top panel. Here the flare-time absorption is due to the C7.5 and M5.8 flares occurring at 20:00 UT and 22:15 UT, respectively. The HIDIVE data in the top panel are the 10 MHz kf-wwv signal strengths on 26 Feb 2004. The GOES X-ray 0.1-0.8 nm flux is shown in the lower panel. Using the SQ curve as reference signal strength values, the maximum absorptions during the C7.5 and M5.8 flares are 19.3 dB and 37.2 dB, respectively.

For a given transmission, the SQ curve represents the time dependent signal strength expected during solar quiet conditions, and flare-induced absorption is defined here as the difference between the SQ curve for a given transmission and the observed HIDIVE signal strength for the transmission. SQ curves are used to define numerous space weather parameters, and several methods for defining SQ curves exist. Two methods for defining SQ curves are described in this section and include a month-specific SQ curve and a day-specific SQ curve. Also, different functional forms are evaluated as possible representations of SQ curves.

5.2 Month-Specific SQ Curves

The procedure for producing a month-specific SQ curve for a given HIDIVE transmission emulates the way in which solar quiet geomagnetic indices are produced and is investigated here since this method is often used to produce expected quiet time values for space weather parameters, such as the geomagnetic K-index and Dst Index [*Chapman and Bartels*, 1940; *Hargreaves*, 1992; *Jursa*, 1985]. However, the month-

specific method fails here since it is unable to capture the day to day fluctuation in diurnal absorption. Recall from §2.2.4, local NO densities can vary by orders of magnitude from day to day, which can lead to significant variations in diurnal HF absorption during solar quiet conditions. Figure 5.1.2 shows HIDIVE data for the 5 MHz blo-wwv signal for several dates in December 2003 during solar quiet conditions. The figure shows the variation of diurnal absorption from day to day in the absence of flare activity can be as large as 40 dB.

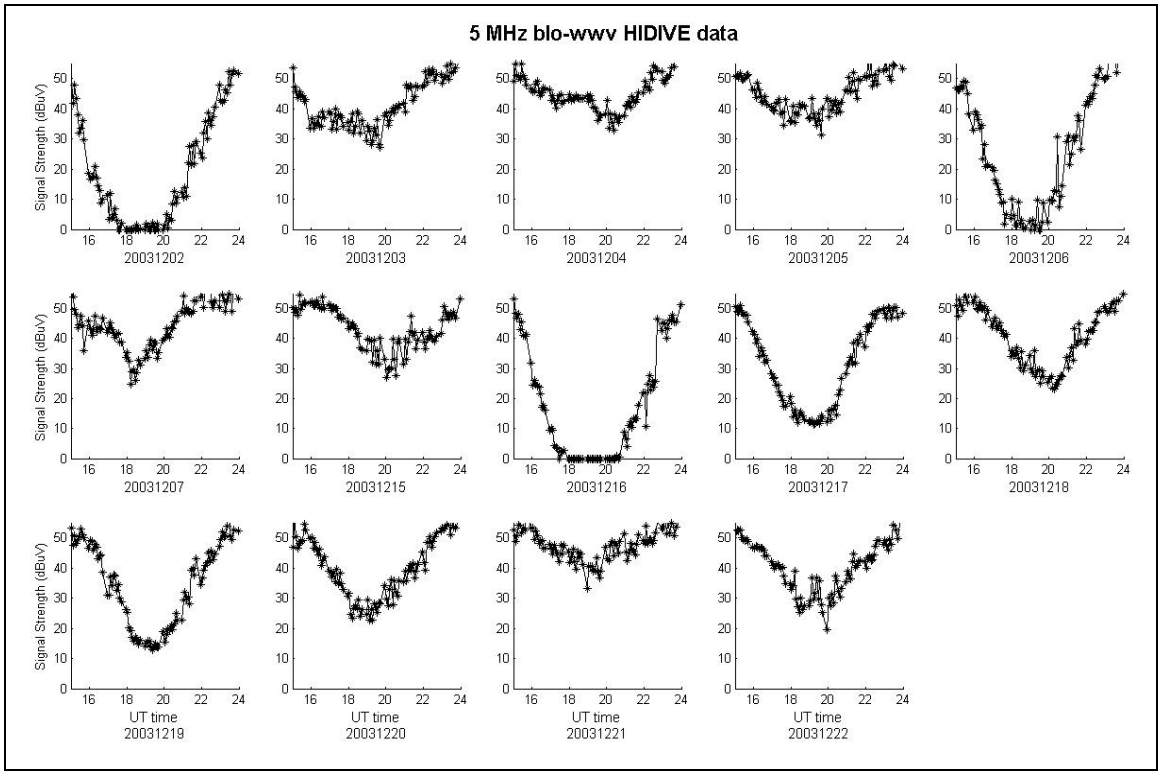

Figure 5.1.2. HIDIVE data for the 5 MHz blo-wwv signal for several dates in December 2003 during solar quiet conditions show the variation of diurnal absorption from day to day in the absence of flare activity can be as large as 40 dB.

Here the method of producing month-specific SQ curves entails selecting the five days of a given month for which solar activity was minimal and for which the HIDIVE data are smoothest and least noisy. These five days are then deemed the best

representations of solar quiet signal strength values for the transmission during that month. The SQ curve to be applied to each day of the given month is then defined as the time dependent averages of the HIDIVE data from the five selected SQ days. The problem with the month-specific method as applied to HF signal strengths can be seen in the data in Figure 5.1.1. Since the solar quiet daytime 5 MHz blo-wwv signal strengths vary significantly from day to day in December 2003, an SQ curve produced by averaging data from that month fails to represent the time-dependent signal strengths on most dates during the month, see Figure 5.2.1.

In Figure 5.2.1, HIDIVE data for the dates in December 2003, shown in Figure 5.1.2, are compared to the month-specific SQ curve produced by computing the time-dependent, daytime HIDIVE data for the dates 3, 4, 5, 15, and 21 December 2003, which are deemed the best representation of quiet-time data in December 2003. The month-specific SQ curve for December 2003 poorly represents the quiet time signal strength values for the 5 MHz blo-wwv signal on 2, 6, 16, and 19 December 2003, and had a flare occurred on those dates, the month-specific method would result in erroneous flare-induced absorption measurements. Since the month-specific method, in which the same SQ curve is applied to all days in a given month, is not capable of capturing the day-to-day variation in signal strength, a method for producing day-specific SQ curves is considered.

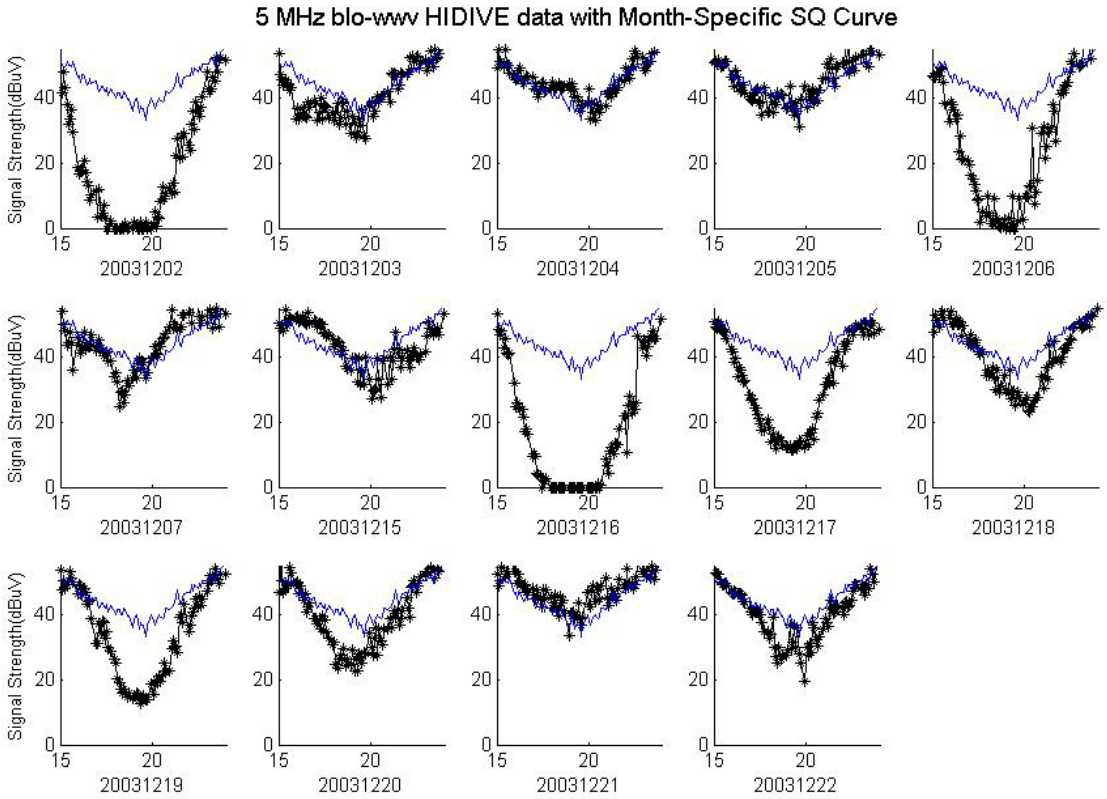

Figure 5.2.1. Shown are the HIDIVE data for the 5 MHz blo-wwv signal for several dates in December 2003 during solar quiet conditions. Also shown in each panel is the month-specific SQ curve for December 2003 produced by averaging the time-dependent, daytime HIDIVE data for the dates 3, 4, 5, 15, and 21 December 2003.

5.3 Day-Specific SQ Curves

Unlike the month-specific SQ curve method, the day-specific SQ curve method is able to account for day-to-day changes in the time-dependent daytime signal strengths seen in the HIDIVE data during solar quiet conditions. For the day-specific method, a functional form is fitted to the daytime signal strength data on a given day not occurring during a solar flare, an absorption event, or local interference. The goal is to fit the SQ curve function to the daytime data that best represents the solar quiet signal strengths on the given date. Two functional forms for the SQ reference curve are evaluated and include

$$I(t) = A \cdot Cos^{r}(\chi_t) + B \tag{5.3.1}$$

and

$$I(t) = C_o + C_1 t + C_2 t^2 + C_3 t^3 \ldots \quad (5.3.2)$$

where $I(t)$ is the SQ curve signal strength value; A, B, and r are fit parameters, and χ_t is the solar zenith angle at time t. The functional from of equation 5.3.1 is considered here since the diurnal variation of HF signal strength is suggested in literature and in §2.2.3 to vary as $Cos^r(\chi_t)$ [*Davies*, 1990; *McNamara*, 1991; *Rishbeth and Garriott*, 1969, *Oyinloye*, 1978]. Equation 5.3.2 does not include a $Cos^r(\chi_t)$ term, but it is considered as a candidate daily SQ curve function since polynomials with linear coefficients, C_i, are commonly used in modeling and pattern recognition due to their simplicity and ease of implementation [*Bishop*, 1995].

Equations 5.3.1 and 5.3.2 are fitted to HIDIVE data during solar quiet conditions, and root mean squared (RMS) error is the measure used here to quantify the goodness of the fits. Figure 5.3.1 and Figure 5.3.3 show the SQ curves resulting from fitting equations 5.3.1 and 5.3.2 to HIDIVE data occurring during solar quiet conditions on 26 February 2004 and 15 July 2004, respectively, for the 10 MHz kf-wwv transmission. The HIDIVE data are shown by the solid blue line, the black circles represent data occurring during a solar flare and which are omitted from the data to which the SQ curves are fitted, and the red dashed line is the SQ curve of the functional form given in equation 5.3.1. Also shown in the figure are the SQ curves resulting from fitting equation 5.3.2. The SQ curves resulting from equations 5.3.1 and 5.3.2 are shown without the HIDIVE data in Figure 5.3.2 and Figure 5.3.4, and the RMS errors for the SQ curves on 26 February 2004 and 15 July 2004 are given in Table 5.3.1 and Table 5.3.2, respectively. The purple solid lines in Figure 5.3.2 and Figure 5.3.4 are two-degree polynomials fitted to the quiet-time HIDIVE data, the blue dotted lines are four-degree polynomials, and the green dashed lines are 10-degree polynomials.

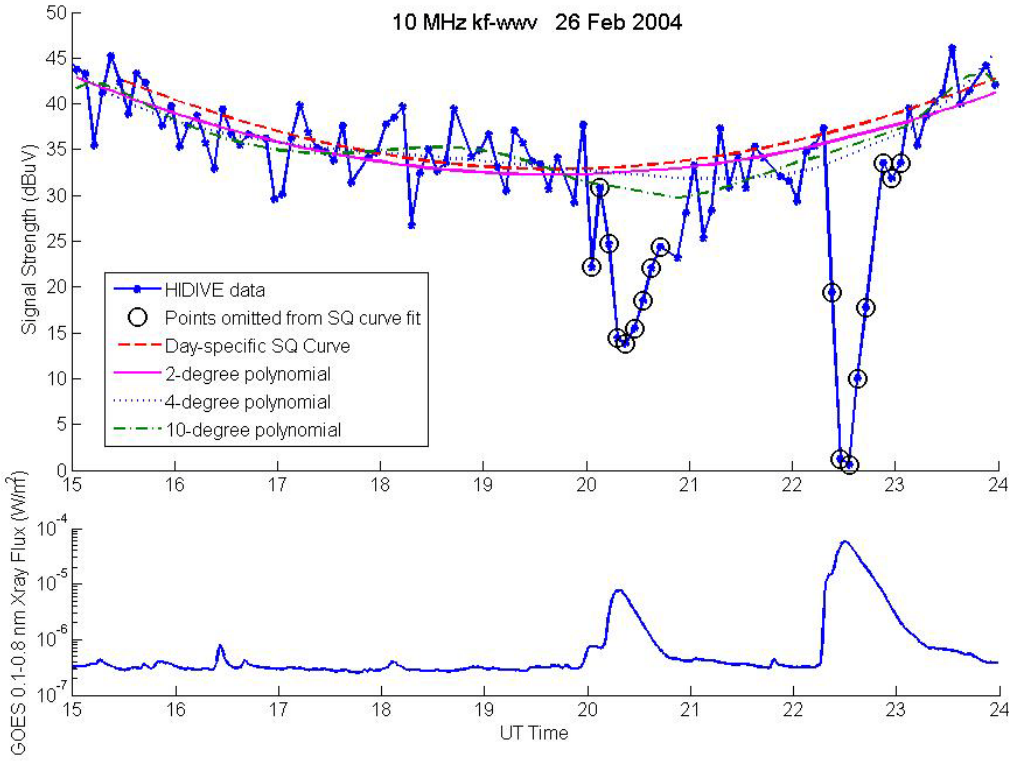

Figure 5.3.1. HIDIVE data and the SQ curves resulting from fitting equations 5.3.1 and 5.3.2 to HIDIVE data occurring during solar quiet conditions on 26 February 2004 for the 10 MHz kf-wwv transmission are shown. The HIDIVE data are shown by the solid blue line, the black circles represent data occurring during a solar flare, which are omitted from the data to which the SQ curves are fitted, and the red dashed line is the SQ curve of the functional form given in equation 5.3.1. Also shown are the SQ curves resulting from fitting equation 5.3.2 and setting the degree of the polynomial to two, four, and ten.

Table 5.3.1. The RMS errors for the SQ curves resulting from fitting equations 5.3.1 and 5.3.2 to the quiet-time HIDIVE data on 26 February 2004 for the 10 MHz kf-wwv transmission.

SQ Curve	RMS Error (dBuV)
Equation 5.3.1	3.4
Equation 5.3.2: 2-degree polynomial	3.3
Equation 5.3.2: 4-degree polynomial	3.1
Equation 5.3.2: 10-degree polynomial	2.9

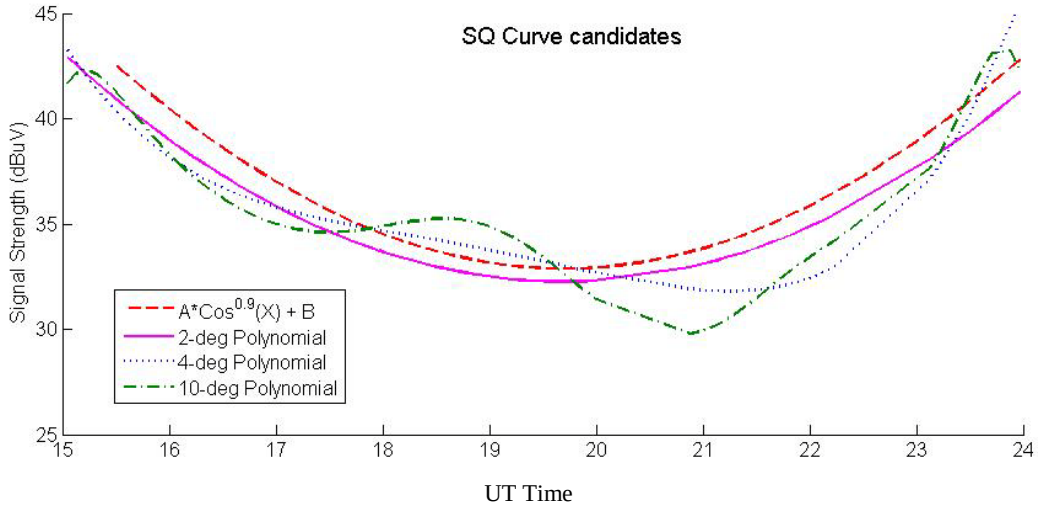

Figure 5.3.2. The SQ curves resulting from fitting equations 5.3.1 and 5.3.2 to HIDIVE data occurring during solar quiet conditions on 26 February 2004 for the 10 MHz kf-wwv transmission are shown. The red dashed line is the SQ curve resulting from fitting equation 5.3.1 to the quiet-time data. The purple solid line is a two-degree polynomial fitted to the quiet-time HIDIVE data, the blue dotted line is a four-degree polynomial, and the green dashed line is a 10-degree polynomial.

A well posed SQ curve should be symmetric around local noon with its minimum occurring at noon and its maxima at local sunrise and sunset. Although the RMS error of equation 5.3.2 decreases as the order of the polynomial increases, the shape of the curve begins to deviate from what is expected for an SQ curve once the degree of the polynomial is greater than two. For a polynomial of order 3 or more, the fit is asymmetric about local noon and, at times, has more than one local minimum. When compared to fits of equation 5.3.1, the RMS errors of the second-degree polynomials are either comparable or significantly larger. SQ curves produced from fitting equation 5.3.1 are consistently of the desired shape and are dependent on $Cos^{r}(\chi)$ as observations suggest, and no significant improvement in RMS error is obtained when using a second degree polynomial to define the SQ curve. Thus, the functional form given in equation 5.3.l is used here to produce SQ reference curves.

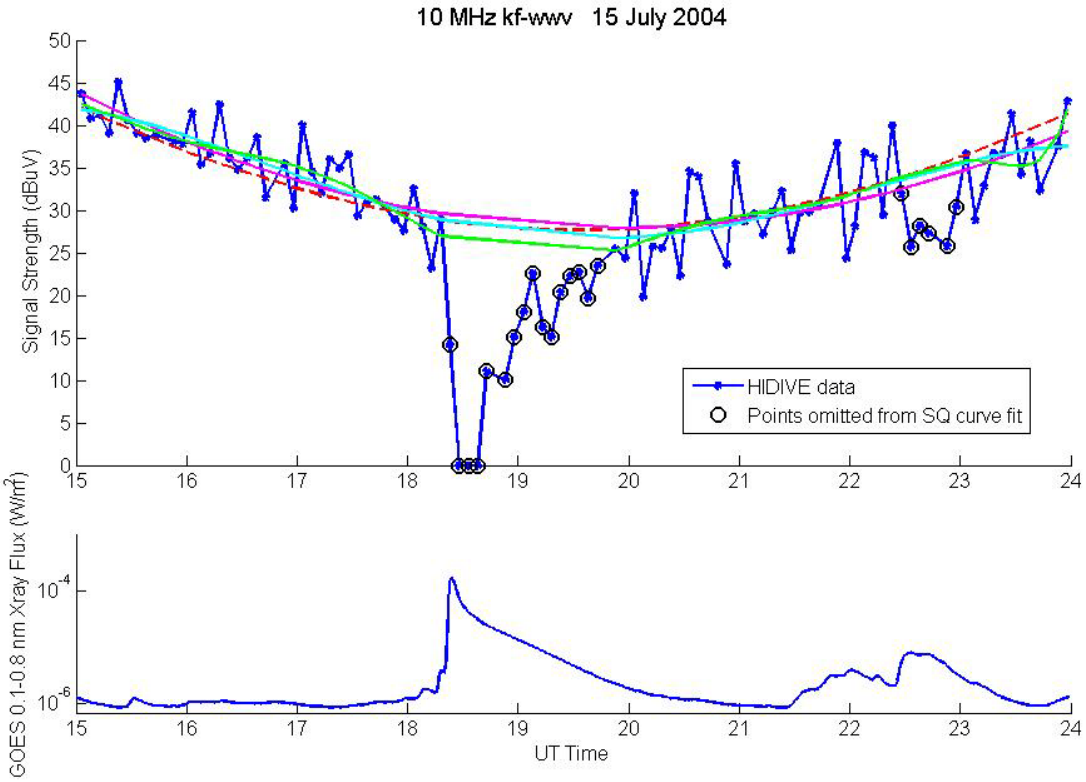

Figure 5.3.3. HIDIVE data and the SQ curves resulting from fitting equations 5.3.1 and 5.3.2 to HIDIVE data occurring during solar quiet conditions on 15 July 2004 for the 10 MHz kf-wwv transmission are shown. The HIDIVE data are shown by the solid blue line in the top panel, the black circles represent data occurring during a solar flare, which are omitted from the data to which the SQ curves are fitted, and the red dashed line is the SQ curve of the functional form given in equation 5.3.1. Also shown are the SQ curves resulting from fitting equation 5.3.2. GOES 0.1-0.8 nm data is shown in the bottom panel.

Table 5.3.2. The RMS errors for the SQ curves resulting from fitting equations 5.3.1 and 5.3.2 to the quiet-time HIDIVE data on 15 July 2004 for the 10 MHz kf-wwv transmission.

SQ Curve	RMS Error (dBuV)
Equation 5.3.1	3.6
Equation 5.3.2: 2-degree polynomial	3.5
Equation 5.3.2: 4-degree polynomial	3.4
Equation 5.3.2: 10-degree polynomial	3.3

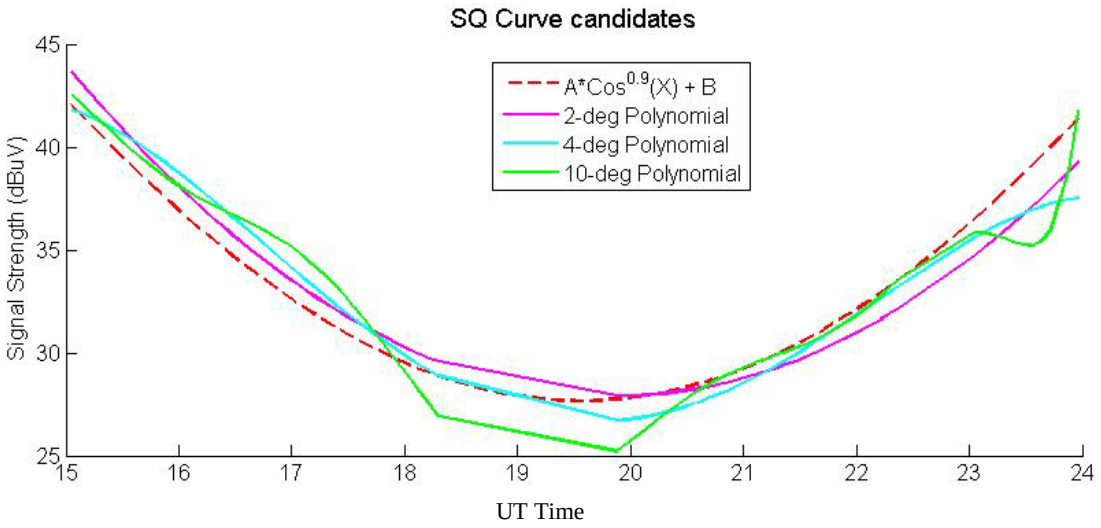

Figure 5.3.4. Shown are the SQ curves resulting from fitting equations 5.3.1 and 5.3.2 to HIDIVE data occurring during solar quiet conditions on 15 July 2004 for the 10 MHz kf-wwv transmission. The red dashed line is the SQ curve resulting from fitting equation 5.3.1 to the daytime quiet-time data. The purple solid line is a two-degree polynomial fitted to the quiet-time HIDIVE data, the blue dotted line is a four-degree polynomial, and the green dashed line is a 10-degree polynomial.

5.4 Determination of Cosine Dependence

As discussed in §2.3.1 and shown in equation 2.3.1, HF absorption can be expressed as $L(t) = A \cdot Cos^{r}(\chi_t)$, and comparing equation 2.3.1 to equation 5.3.1, we see the predicted signal strengths equation 5.3.1 yields are determined by subtracting the predicted absorption from a baseline signal strength. Recall from §2.2.1, there are two sources of ionization within the D-region which are responsible for HF absorption, solar X-rays and solar Lyman-α radiation. Contained within the parameter, *A*, in the expression for absorption and in equation 5.3.1 is information on the densities of the neutrals being ionized, O_2, N_2, and NO, and the fluxes of the ionizing radiation, X-ray and Lyman-α. Currently, solar X-ray flux observations are provided by GOES spacecraft, and the F10.7 index serves as a proxy for Lyman-α flux. Since the atmospheric densities of O_2 and N_2 are assumed constant, NO density is the unknown parameter contained in *A*. By assigning a value to the exponent, *r*, and knowing the baseline signal strength, it should be possible to make relative comparisons of local NO densities by noting the value of *A* when equation 5.3.1 is fitted to quiet-time HIDIVE

data during the production of an SQ curve for a given date. The baseline signal strength is the strength of the signal measured at the receiver site in the absence of D-region absorption.

As discussed in §2.2.3, diurnal variation of HF absorption goes as $Cos^{r}(\chi)$, where *r* has been fitted in various studies and has taken on values ranging from 0.2 to 1.0 [*Davies*, 1990]. The determination of *r* begins by fitting the parameters in equation 5.3.1, *A, B,* and *r,* simultaneously with the goal of minimizing RMS error. Equation 5.3.1 is fitted to the quiet-time data for all dates during the months given in Table 5.3.3 for which solar activity was minimal.

Table 5.4.1. SQ curves of the functional form given in equation 5.3.1 are fitted to HIDIVE data for dates during the months listed below and during which solar activity was minimal.

Year	Months
2004	June, July, August, November, December
2005	July, November, December
2006	January, July

The result of the fits is a value of the exponent, *r* , ranging from 0.7 to 1.3. Figure 5.4.1 shows the results of fitting equation 5.3.1 to the quiet-time HIDIVE data on 21 December 2004 when *r* is set to the values 0.75 (blue dotted line), 1.0 (red dashed line), and 1.3 (green solid line). The average value of *r* in equation 5.3.1 that minimizes the RMS error with respect to the HIDIVE quiet-time data is r=0.9. As Figure 5.4.1 shows, the value of *r* affects the shape of the SQ curve, with higher values of *r* producing more shallow SQ curves and lower values yielding steeper SQ curves. The average value of *r* and the value of *r* occurring with the greatest frequency for the fits of equation 5.3.1 to the quiet-time data during the months given in Table 5.4.1 is 0.9. In summary, r=0.9 is the optimal value for the exponent in equation 5.3.1 when characterizing the solar zenith angle dependence of HIDIVE data, and

$$I(t) = A \cdot Cos^{0.9}(\chi_t) + B \tag{5.4.1}$$

is the equation used here to define day-specific SQ curves, where *A* and *B* are fit parameters.

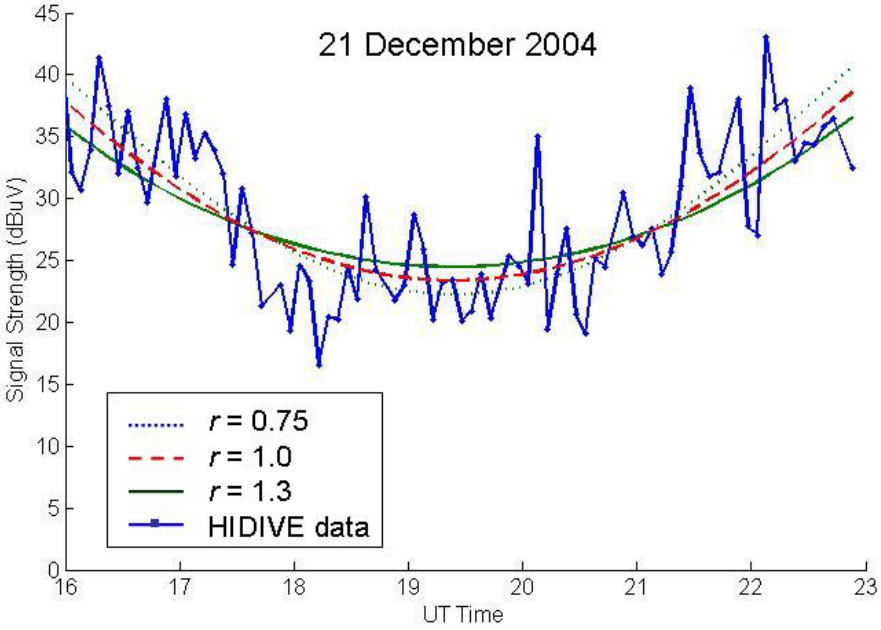

Figure 5.4.1. Results of fitting equation 5.3.1 to the quiet-time HIDIVE data on 21 December 2004 when *r* is set to the values 0.75 (blue dotted line), 1.0 (red dashed line), and 1.3 (green solid line) are shown. The HIDIVE data are shown as the solid blue line.

6. Flare Induced HF Absorption Measurements

6.1 Initial Criteria for Flare Selection

The criteria initially used for selection of flare events, from which flare-induced absorption data would be calculated, were established to maximize the likelihood absorption would be seen in multiple HIDIVE signals and in order to minimize interference and problems associated with calculations involving large solar zenith angles. The first criterion for flare selection is the flare had to occur during the time period covered by the HIDIVE dataset, from 1 November 2003 until 31 December 2006. The second criterion is flare duration longer than 20 minutes in order to ensure four or more absorption data points are available since the HIDIVE dataset used here has a five-minute cadence. Thirdly, flare onset must be after 1800 UT in order to avoid large zenith angle complications during the normalization process discussed in §6.3. In the normalization process, the term, $Cos^{0.9}(\chi)$, appears in the denominator, and $Cos^{0.9}(\chi)$ equals zero for a zenith angle of 90°. By limiting analysis of absorption events to only those flares occurring between 1800 UT and 2400 UT, zenith angles are always less than 80°, and division by values approaching zero is avoided.

Also, only flares larger than C7.0 were initially considered in order to increase the likelihood of one flare inducing absorption in all HIDIVE signals considered here. Recall from equations 2.4.18 and 2.5.5, D-region HF absorption is inversely proportional to $(\omega^2 + \nu^2)^{-1}$, where ν ranges from 10^5 s^{-1} to 10^7 s^{-1} within the D-region. For signal frequencies of 15 MHz or greater, $\omega^2 >> \nu^2$ in the D-region, and in general, X-ray flares of classification smaller than C7.0 have little to no effect on HIDIVE transmissions of frequency 15 MHz or greater. The objective of limiting the selection of flares to classifications of C7.0 or larger was to analyze the effects of a single flare on signals of various frequencies in order to determine the frequency dependence of flare-induced HF absorption.

Forty eight X-ray flares fit the criteria above, and from the six HIDIVE signals considered here, 138 flare-induced absorption events were initially available. Table G.1

in Appendix G lists the availability of the HIDIVE signals for the flares selected via the initial criteria.

6.2 "Premier" Flares

6.2.1 Problematic Issues Affecting Absorption Data.

In examining flare-induced absorption of the HIDIVE signals and the dependence of D-region absorption on signal frequency (§6.4), several issues arose that put further restrictions on the selection criteria for X-ray flares discussed in §6.1. These issues include signal interference, daytime propagation mode changes, and delay in apparent flare effects. In some cases in which there is significant noise in the HIDIVE data during a flare, it can be impossible to distinguish whether the effects seen in the signal strength data are due to local interference, propagation mode changes, ionospheric delay in response to flare effects, or noise. The effects of these issues on HIDIVE data and the reasoning for excluding these data are discussed below.

6.2.2 Local Interference.

In the presence of one of any of these issues, it is difficult, if not impossible to determine during an X-ray flare the amount of flare-induced HF absorption. The first issue affecting the HIDIVE data discussed here is local interference. An example of local HF interference is shown in Figure 6.2.1, which shows daytime HF signal strengths received at the BLO HIDIVE receiver on 26 February 2004 for a 5 MHz and 10 MHz signal transmitted from the U.S. Standard Time station in Kekaha, Kauai, Hawaii (WWVH). The signals transmitted from the WWVH are monitored by HIDIVE receivers; however, due to the previously mentioned interference and limited signal availability, the WWVH transmissions are not analyzed here. Local interference is present occasionally in the WWV transmissions; however, the WWVH data collected by the BLO HIDIVE receiver on 26 February 2004 is shown here because the interference in the WWVH data is periodic and easily discerned and serves as a good visual example of how interference can affect signal strength. In Figure 6.2.1, interference occurs periodically at 45 minutes after the hour and on the hour throughout the day.

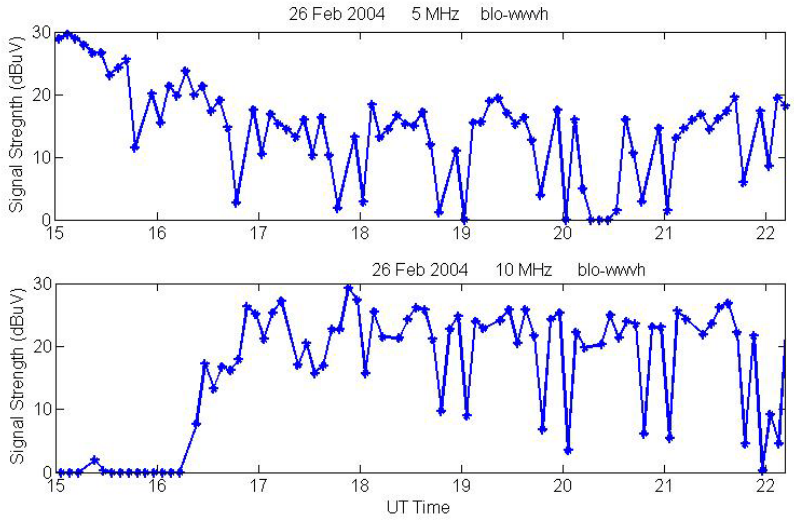

Figure 6.2.1. HF signal strength data collected at the BLO HIDIVE receiver on 26 February 2004 show local interference at 45 minutes after the hour and on the hour periodically throughout the day.

6.2.3 Propagation Mode Changes.

Another issue affecting the ability to determine flare-induced absorption is propagation mode changes during the day. Recall from §2.4.5 the altitude at which an HF signal refracts back towards the earth is dependent on the signal frequency, the N_e profile, and the signal elevation angle. When a ray refracts close to a boundary between ionospheric regions, subtle changes in the ionosphere and the N_e profile can lead to drastic changes in the ray's propagation path, resulting in either not allowing the ray to make it to the receiver, additional absorption of ray energy, or allowing the ray to penetrate the ionosphere. Figure 2.4.2 demonstrates there are usually multiple propagation paths available for a transmission; however, the geometry of the paths will determine the amount of absorption the signal will suffer traveling from the transmitter to the receiver so some modes will dominate the signal strength observations. Figure 6.2.2 shows some examples of what are believed to be propagation mode changes captured in the HIDIVE data. Shown in the top plot of each panel are the daytime HIDIVE data, and the arrows point to data obtained when there has been a change in the propagation modes for the transmission. In the bottom plot of each panel are GOES hard and soft X-ray flux observations.

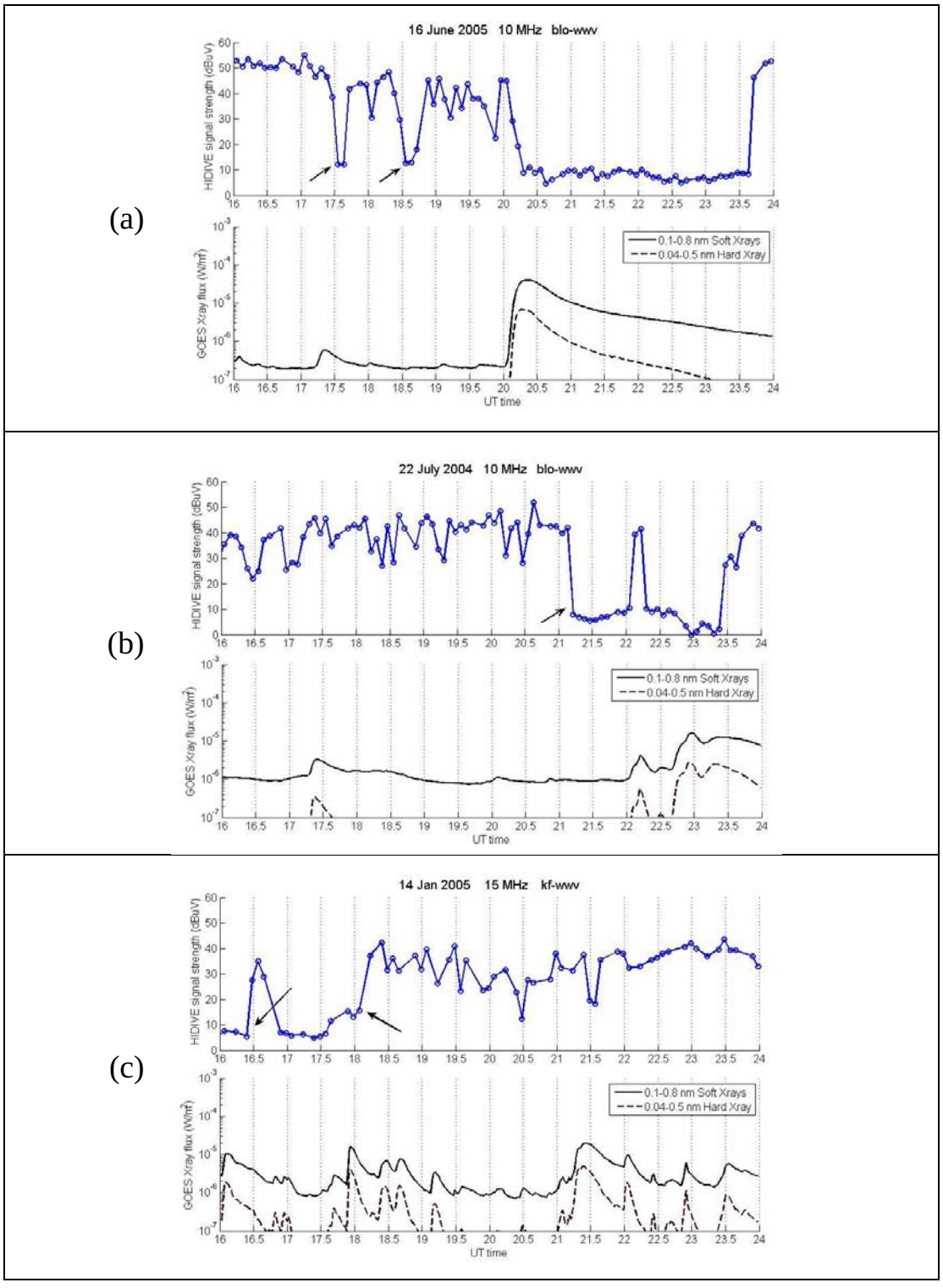

Figure 6.2.2. Change in propagation modes is seen in daytime HIDIVE data, which are shown in the top plot of each panel. The arrows point to data obtained when there has been a change in the propagation modes. In the bottom plot of each panel are GOES hard and soft X-ray flux observations.

The problem of determining flare-induced absorption in the presence of propagation mode changes can be seen in Figure 6.2.2. Presently, there is no way to distinguish during a flare if the loss of signal strength is due to the flare-enhanced solar X-ray flux or if it is due to a change in signal propagation. Thus, an additional criterion is used to select X-ray flares and HIDIVE data obtained during these flares to be used here. If the HIDIVE data suggests changes in propagation modes are occurring during a given day, X-ray flares occurring on that day and the data obtained during those flares are not used here.

6.2.4 Lag in Flare-Induced Absorption.

Another criterion used to select X-ray flares and the HIDIVE data obtained during the flares is there must not be apparent lag between the onset or peak of the flare and flare-induced HF absorption. The D-region ionospheric N_e density is typically assumed to respond immediately to changes in solar radiation; however, there are cases in which flare-induced absorption lags the onset of X-ray flares or the peak of flares by two to 15 minutes. Figure 6.2.3 shows the case on 16 January 2005 in which the flare-induced absorption of the 5 MHz blo-wwv HIDIVE transmission lags the peak of the M2.4 flare at 22:00 UT by six minutes. The HIDIVE data is shown in top panel of Figure 6.2.3, and GOES soft (solid line) and hard (dashed line) X-ray flux is shown in the bottom panel. The vertical green line in the figure represents the time of flare peak, 22:00 UT.

For the 5 MHz blo-wwv HIDIVE data on 16 January 2005, shown in Figure 6.2.3, the average magnitude of noise is approximately 7 dBuV, which could account for the apparent lag in flare-induced absorption. However, Figure 6.2.4 shows a lag in flare-induced absorption for three of the HIDIVE transmissions 10 MHz kf-wwv, and 15 MHz kf-wwv) for the M1.7 X-ray flare on 23 July. The data for the 5 MHz blo-wwv transmission are shown in panel a, data for the 10 MHz kf-wwv transmission are shown in panel b, data for the 15 MHz kf-wwv transmission are shown in panel c. In each panel, the HIDIVE data are shown in the top plot and the GOES data are shown in the bottom plot. The vertical lines in the panels mark the time of flare peak at 21:23 UT. For all three transmissions shown in Figure 6.2.4, the peak of flare-induce absorption lags the peak of the flare by about five minutes. Noise still is a possible cause of the apparent

delay in flare-effects; however, since the lag in seen in all three transmissions, there is most likely another reason for the delay.

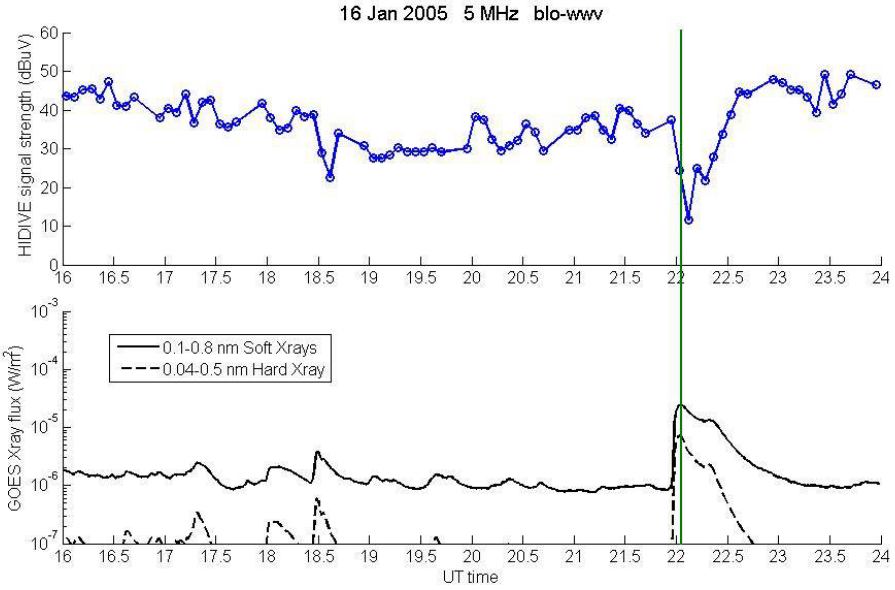

Figure 6.2.3. Flare-induced absorption of the 5 MHz blo-wwv HIDIVE transmission lags the peak of the M2.4 flare at 22:00 UT by six minutes on 16 January 2005. The HIDIVE data is shown in top panel of Figure 6.2.3, and GOES soft (solid line) and hard (dashed line) X-ray flux is shown in the bottom panel. The vertical green line in the figure represents the time of flare peak, 22:00 UT.

Although the exact cause of the apparent delay is unknown, it is believed the photons driving HF absorption in the D-region are of slightly longer wavelength than the 0.1-0.8 nm X-ray photons monitored by the GOES satellites. Hence, the GOES soft X-ray flux may not be an adequate proxy for the solar photons affecting HF propagation and absorption in the D-region during all conditions. During the investigation into the cause of the lag between the flare-enhanced X-ray flux and the observed flare-induced absorption, various other solar flux datasets and radio signal strength datasets were evaluated in hopes of determining if the cause is a processing issue related to the time stamps used in the datasets or if the cause is related to the flare spectrum. According to Vince Eccles via private communication on 9 August 2007, signal strength data from an instrument monitoring very low frequency (VLF) radio signals were compared to the signal strength data from HIDIVE transmission during a 2006 M-class flare during which

there was a lag between the onset of the flare and the start of flare-induced absorption. Interestingly, both the VLF data and HIDIVE data showed a delay in flare-induced absorption of approximately five minutes; thus, the cause of the lag does not appear to be related to a dataset time tag issue.

The data in Figures 6.2.4, 6.2.5, and 6.2.6 also support the case that the cause of the lag is due to something more than noise in the data or dataset time tag issues. HIDIVE data for the 5 MHz blo-wwv, 10 MHz kf-wwv, and 15 MHz kf-wwv transmission on 23 July 2004 are shown in the top panel of Figures 6.2.4, 6.2.5, and 6.2.6, respectively, and GOES data are shown in the bottom panel of Figure 6.2.4 and the middle panel of Figures 6.2.5 and 6.2.6. All three transmissions show a five minute delay between the peak of the M1.7 flare at 21:24 UT and the peaks of flare-induced absorption. Thus, the delay seen in the data on 23 July 2004 is most likely not due to noise.

To further investigate flare spectrum as being the source of the apparent lag, data from the Solar EUV Monitor (SEM) instrument onboard the Solar and Heliospheric Observatory (SOHO) were evaluated. Since the EUV photons responsible for the majority of HF absorption in the D-region may be of wavelength slightly longer than the 0.1-0.8 nm photons monitored by GOES, the SEM data, which report solar flux in the 0.1-50 nm band, might be a better proxy for the radiation affecting HF propagation in the ionosphere [*Judge et al.*, 1998]. However, as seen by the dashed blue line in the bottom panel of Figures 6.2.5 and 6.2.6, the SOHO/SEM data does not seem to shed light on the issue of lag between the start of a flare and the onset of flare-induced absorption. In Figures 6.2.5 and 6.2.6, as for the other cases in which there is a lag, the lag in the absorption of the HIDIVE data is the same with respect to the GOES data as it is to the SOHO/SEM data. The solid green line in the bottom panels of Figures 6.2.5 and 6.2.6 are the hardness ratios, which are the ratios of the soft X-ray flux to the hard X-ray flux. The flare-time hardness ratios were also examined as a possible cause of the lag. Currently, however, no trend with respect to flare hardness has been identified. Without a means of determining the actual source of the lag, data during a flare in which there is

an apparent lag of five minutes or more between flare-enhanced X-ray flux and flare-induced absorption are not used.

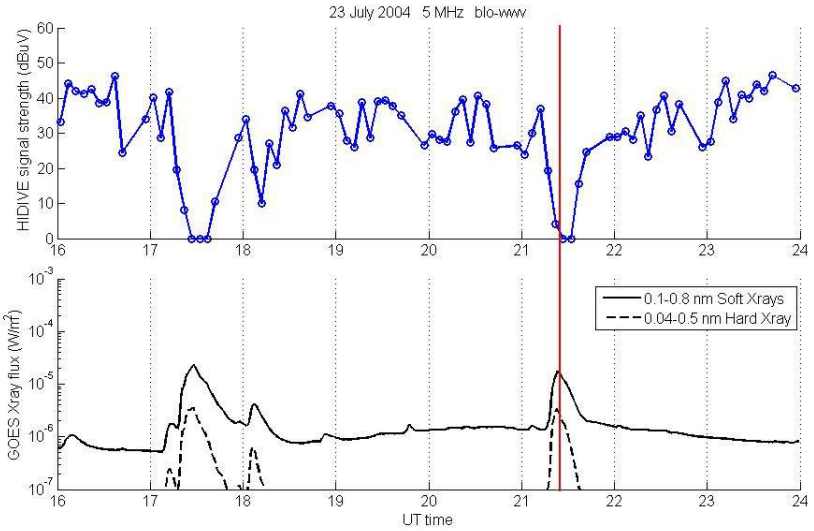

Figure 6.2.4. HIDIVE data for the 5 MHz blo-wwv signal on 23 July 2004 are shown in the top panel, and shown in the bottom panel are the GOES soft (solid) and hard (dashed) X-ray flux data.

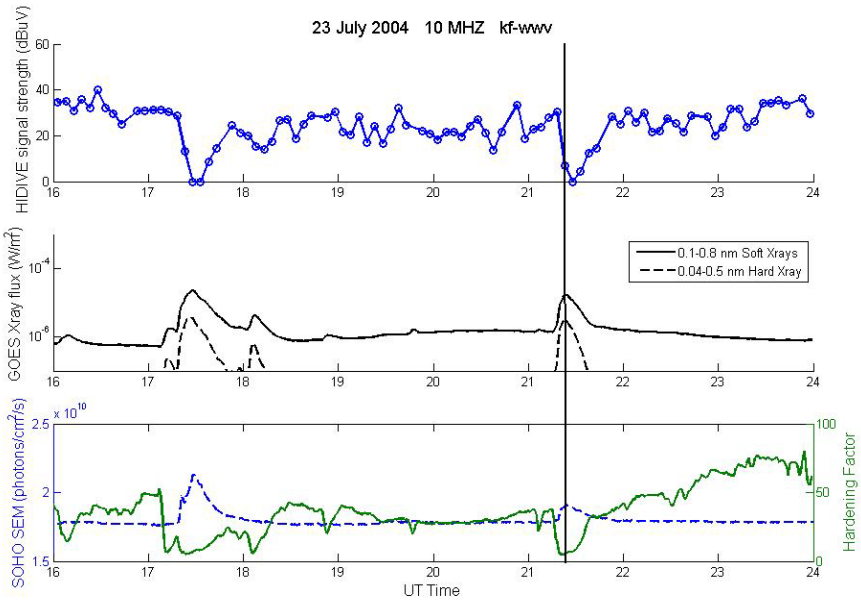

Figure 6.2.5. HIDIVE data for the 10 MHz kf-wwv signal on 23 July 2004 are shown in the top panel, and shown in the middle panel are the GOES soft (solid) and hard (dashed) X-ray flux data. SOHO SEM 0.1-50 nm flux data (dashed blue) are shown in the bottom panel along with the hardness factor (solid green).

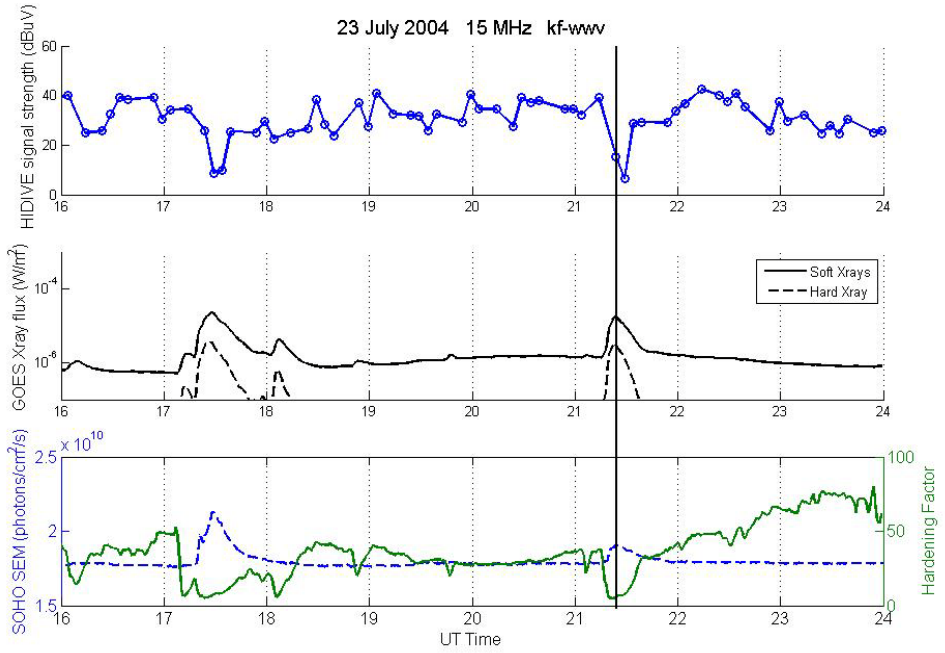

Figure 6.2.6. HIDIVE data for the 15 MHz kf-wwv signal on 23 July 2004 are shown in the top panel, and shown in the middle panel are the GOES soft (solid) and hard (dashed) X-ray flux data. SOHO SEM 0.1-50 nm flux data (dashed blue) are shown in the bottom panel along with the hardness factor (solid green).

6.2.5 Sporadic Signal Strength Enhancements.

The last problematic issue affecting the ability to measure flare-induced absorption during a flare is sporadic signal strength enhancements during a flare. Examples of the sporadic enhancements in signal strength are shown in Figure 6.2.7 in which HIDIVE data for the 5 MHz blo-wwv transmission on 9 September 2005 are shown along with the soft and hard GOES X-ray flux. On this date, two signal strength enhancements are observed during an X6.2 flare, at 20:00 UT and 22:34 UT. An HF signal of only 5 MHz is completely attenuated during an X-class flare; however, in Figure 6.2.7, spikes in the HIDIVE signal strength data are present when the signal is expected to be completely absorbed. Local interference contributing to the signal intensity may be the cause of the sudden spikes in signal strength, or the signal strength enhancements may be due to the propagation mode changes due to the enhanced flare-time N_e.

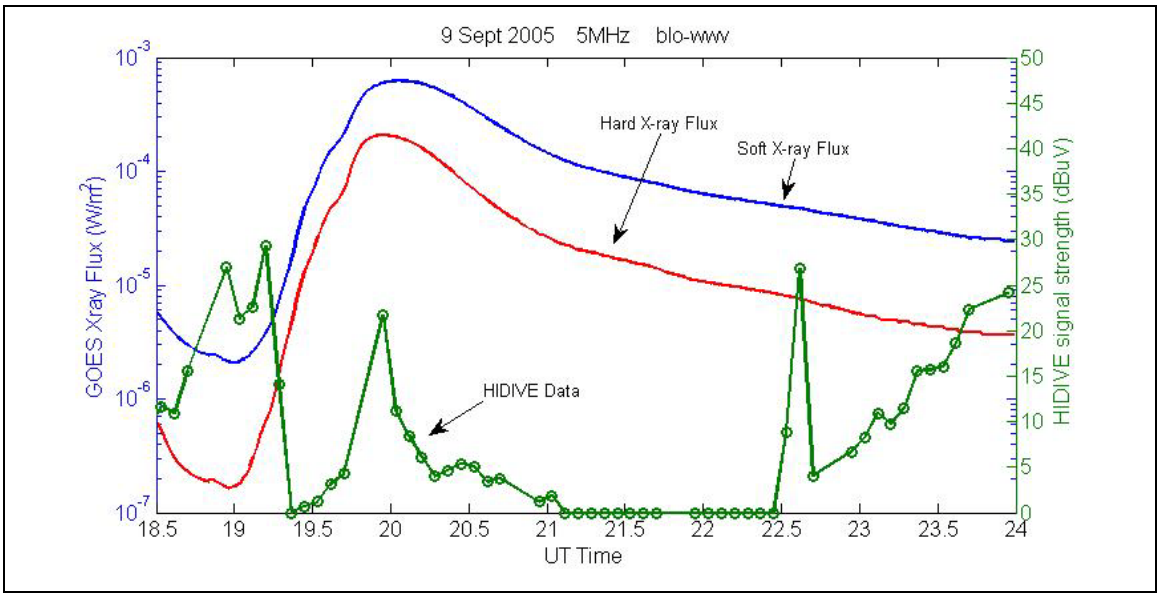

Figure 6.2.7. HIDIVE data for the 5 MHz blo-wwv transmission on 9 September 2005 are shown along with the soft and hard GOES X-ray flux. On this date, two signal strength enhancements are observed during the X6.2 flare, one at 20:00 UT and the other at 22:34 UT.

Since there is currently no method for determining the source of a sudden signal strength enhancement, flare cases for which the corresponding HIDIVE data exhibits significant increases in signal strength during a flare are not used. Here, a significant increase in signal strength is defined as that of magnitude greater than the average noise on a given date.

6.2.6 The "Premier" Flares.

With a list of problematic issues affecting the flare-induced absorption measurements during an X-ray flare, each absorption case is individually examined, and fewer cases are analyzed here. Flare-induced absorption events selected for further analysis are limited to only those for which none of the previously mentioned problematic issues are present. As a result, this research focuses on a "premier" set of 61 flare-induced absorption cases from the 5 MHz blo-wwv, the 10 MHz kf-wwv, and the 15 MHz kf-wwv transmissions. This set of premier flares is listed in Table G.2 in Appendix G and is a subset of the flares initially selected given the criteria in §6.1, and in addition to adhering to the criteria in §6.1, the premier flares also fit the following criteria.

- No local interference is suspected during the day of the flare
- HIDIVE data show no apparent delay between flare onset and the start of flare-induced absorption
- HIDIVE data show no delay between flare peak and maximum flare-induced absorption
- No suspected propagation mode changes are occurring on the day of the flare

6.3 Normalization of Flare-Induced Absorption Data

6.3.1 Normalization Scheme.

Since the propagation paths of the HIDIVE transmissions differ in the number of passes through the D-region, elevation angle, and reflection altitude, flare-induced absorption measurements must be normalized to a common solar zenith angle (χ), and elevation angle (ϕ) in order to make comparisons between the data and to investigate the frequency dependence of absorption. Here the absorption measurements are normalized to a sun directly overhead ($\chi = 0°$) and to a vertically incident signal ($\phi = 90°$) passing through the D-region only once.

Let L_i be the absorption suffered by a HIDIVE signal during a single pass through the D-region when the local solar zenith angle is χ_i. L_i normalized to a sun directly overhead is

$$L_{\chi=0} = \frac{L_i}{Cos^{0.9}(\chi_i)} \tag{6.3.1}$$

where χ_i is the local solar zenith angle during the signal's i^{th} pass through the D-region before reaching the receiver, and i goes from one to the total number of times a given signal passes through the D-region (N). The $Cos^{0.9}(\chi_i)$ term comes from the relation between absorption and solar zenith angle determined in §5.4 and equation 5.4.1.

Applying the horizontal slab approximation for the ionosphere introduced in §2.1.2, L_V is the loss expected during the i^{th} pass through the D-region if propagation is vertical and is given by

$$L_V = L_i \cdot Sin(\phi_i) \tag{6.3.2}$$

where ϕ_i is the elevation angle of the signal as it enters the ith pass as shown in Figure 6.3.1.

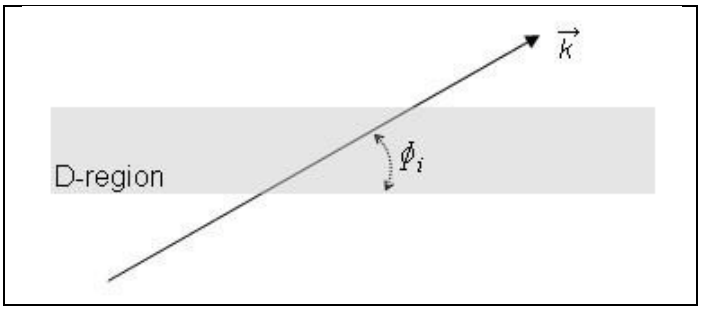

Figure 6.3.1. Local signal elevation angle during its ith pass through the D-region, ϕ_i .

Combining equations 6.3.1 and 6.3.2, we obtain the normalized signal absorption L_i^{norm} for a single pass through the D-region,

$$L_i^{norm} = \frac{L_i \cdot Sin(\phi_i)}{Cos^{0.9}(\chi_i)} \tag{6.3.3}$$

The flare-induced HIDIVE absorption data give the total loss suffered by a signal over an entire propagation path (L_{tot}). Thus,

$$L_{tot} = \sum_{i=1}^{N} L_i = \sum_{i=1}^{N} \frac{L_i^{norm} \cdot Cos^{0.9}(\chi_i)}{Sin(\phi_i)} \tag{6.3.4}$$

The elevation angles for each pass through the D-region and the distances traveled within the D-region for each pass are approximately equal according to the ray tracing programs used here (see §6.3.2). Thus, equation 6.3.4 can be simplified and rewritten as

$$L_{norm} = \frac{L_{tot} \cdot Sin(\phi)}{\sum_{i=1}^{N} Cos^{0.9}(\chi_i)}) \qquad (6.3.5)$$

which is the expression for the normalized loss expected for a signal passing through the D-region once when $\chi = 0°$, $\phi = 90°$, and total observed loss is L_{tot}. Normalization of the observed loss data to a common zenith angle, elevation angle, and number of D-region passes allows for signal frequency and solar X-ray flux to be the only variables in the comparisons between the flare-induced absorption data. This allows for the determination of HF absorption dependence on signal frequency (see §6.4).

6.3.2 Normalization Scheme Validation.

Validation of the normalization scheme outlined in §6.3.1 requires two or more signals of the same frequency but different propagation paths. Here the 10 MHz blo-wwv and 10 MHz kf-wwv HIDIVE transmissions are used since flare-induced absorption measurements can be obtained for both transmissions during given flares and the propagation paths for both signals can be modeled. The 5 MHz HIDIVE transmissions are not used to validate the normalization scheme since, for any of the flare cases examined here, at least one of the 5 MHz signals is completely attenuated. Furthermore, the 15 MHz signals are not used for validation since the HASEL [*Coleman*, 1993] and the Hausman-Nickisch codes [*Huang and Reinisch*, 2006; *Nickisch*, 1988] both predict the signal for the 15 MHz blo-wwv propagation path to penetrate the ionosphere and not make it to the Bear Lake receiver. Without the ability to model the propagation path, elevation angle and number of D-region passes are not known for the 15 MHz blo-wwv transmission, and the normalization scheme cannot be applied.

The characteristics of the 10 MHz transmission propagation path predicted by the Hausman-Nickisch ray tracing code are used here to validate the normalization scheme and are given in Table 6.3.1.

Table 6.3.1. The propagation path characteristics for the predicted 10 MHz kf-wwv and 10 MHz blo-wwv HIDIVE signals.

Signal	Elevation Angle (ϕ)	Number of D-region Passes (N)
10 MHz kf-wwv	33.8°	4
10 MHz blo-wwv	47.4°	2

Here, results of the normalization of the flare-induced absorption data for the 10 MHz blo-wwv and the 10 MHz kf-wwv signals during flares on 24 October 2004 and 17 July 2004 are shown in Figures 6.3.2 and 6.3.3, respectively. The top panel in Figure 6.3.2 shows the normalized flare-induced absorption data for both 10 MHz transmissions during the M2.4 and C5.6 flares on 24 October 2004. The middle panel shows the raw flare-induced absorption measurements, and GOES 0.1-0.8 nm X-ray flux data are shown in the bottom panel.

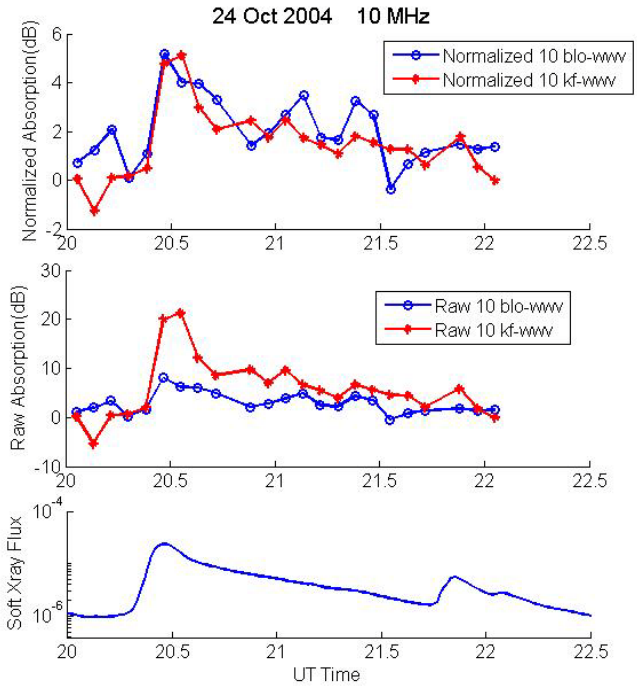

Figure 6.3.2. Normalized flare-induced absorption data for the 10 MHz blo-wwv and 10 MHz kf-wwv HIDIVE transmissions during the M2.4 and C5.6 flares on 24 October 2004 are shown in the top panel. The middle panel shows the raw flare-induced absorption measurements, and GOES 0.1-0.8 nm X-ray flux data are shown in the bottom panel.

The normalized flare-induced absorption for the10 MHz signals during the C2.5 flare on 17 July 2004 are shown in the top panel of Figure 6.3.3. The raw absorption data are shown in the middle panel, and GOES 0.1-0.8 nm X-ray flux data during the 17 July 2004 flare are shown in the bottom panel.

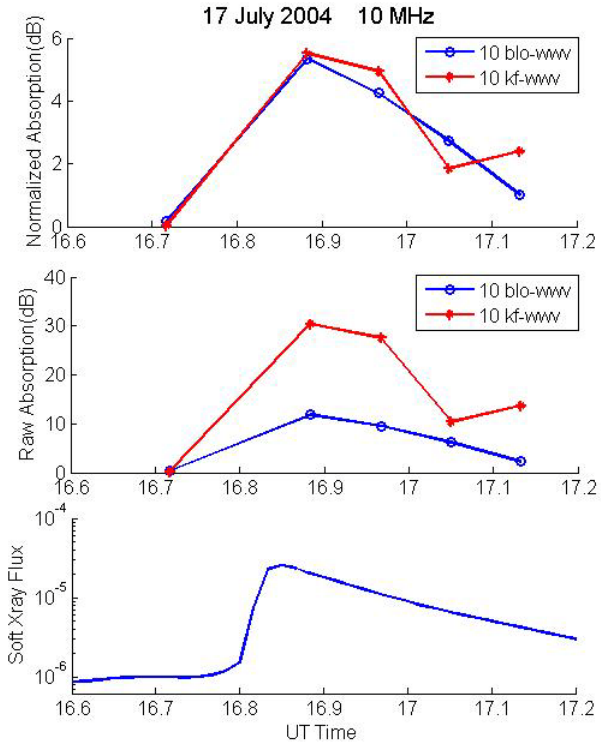

Figure 6.3.3. Normalized flare-induced absorption data for the 10 MHz blo-wwv and 10 MHz kf-wwv HIDIVE transmissions during the C2.5 flare on 17 July 2004 are shown in the top panel. The middle panel shows the raw flare-induced absorption measurements, and GOES 0.1-0.8 nm X-ray flux data are shown in the bottom panel.

The validity of the normalization scheme discussed in §6.3.1 is supported by the top panels of Figures 6.3.2 and 6.3.3. For the same X-ray flux, normalized absorption data from signals of the same frequency should be equal, and as expected, the normalized data in the top panels of Figures 6.3.2 and 6.3.3 overlay each other. This shows the normalization scheme discussed here can be used to compare flare-induced absorption

data observed from signals of different propagation paths and obtained at different times of the day and year.

6.4 Absorption Dependence on Signal Frequency

6.4.1 HIDIVE Absorption Dependence of Frequency.

The two previous sections described the criteria of selecting "premier" flare-induced absorption events and the proven method for normalizing the data. With the selection of those events thought to best capture the relation between flare-enhanced solar X-ray flux and HF absorption and a normalizing method to enable comparisons of those events, a method is developed in this section to quantify the dependence of flare-induced absorption on signal frequency. The relation between signal frequency and flare-induced absorption is then used in §7 during the development of the Empirical HIDIVE D-region Absorption (EHA) model. Recall from equation 2.4.18 HF absorption within the D-region, where ω and ν are of similar orders of magnitude, is determined by the term, $\left(\omega^2 + \nu^2\right)^{-1}$. However, the dependence of non-deviative absorption on signal frequency can be simplified to f^{-2}, where $\omega = 2\pi f$, in the upper ionosphere where ν ranges from 10^2-10^3 s^{-1} and $\omega >> \nu$.

The investigation into the signal frequency dependence of the HIDIVE and riometer flare-induced absorption data begins with plotting the normalized absorption data with respect to the square-root of the GOES soft X-ray flux ($U^{1/2}$) as shown in Figure 6.4.1. Recall from equation 2.5.5, absorption is proportional to the square root of ionizing radiation flux. Also shown in Figure 6.4.1 are the least squares (LS) lines fitted to the scatter plots for each of the HIDIVE and riometer signals. The black asterisks in Figure 6.4.1 represent the normalized absorption versus the square root of solar X-ray flux data for the 5 MHz blo-wwv HIDIVE signal, the red circles represent the data for the 10 MHz kf-wwv signal, the blue diamonds represent the data for the 15 MHz kf-wwv signal, and the green dots represent the normalized absorption versus the square root of solar X-ray flux 30 MHz riometer data. The LS lines fitted to each dataset in Figure 6.4.1 are fitted such that the sum of the root mean squared distances from the line to each data point in the dataset is minimized and the line passes through the origin.

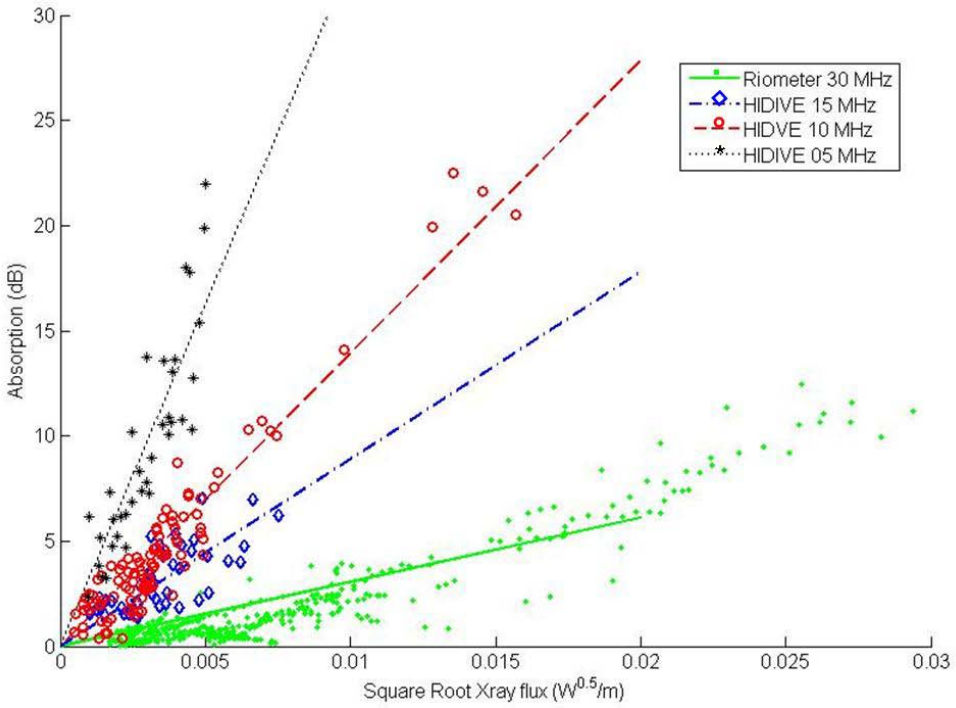

Figure 6.4.1. The normalized absorption data for the HIDIVE and riometer signals are plotted with respect to the square root of the GOES soft X-ray flux. The lines are least squares lines fitted to the data for a given signal.

The equations for the LS lines shown in Figure 6.4.1 are given in Table 6.4.1, and the data given in Table 6.4.2 and shown in Figures 6.4.2 through 6.4.5 quantify the goodness of the LS line fits to the normalized absorption versus X-ray flux data. For a given absorption versus square root X-ray flux dataset, the residuals are the differences between observed absorption and the absorption modeled by the LS line, and analyzing the distribution of the residuals with respect to zero sheds light on how well the LS line fits the data. If an LS line fits data well, the residuals should be randomly and evenly distributed about zero. Such distributions can be seen in the bottom panels of Figures 6.4.2, 6.4.3, and 6.4.4 for the residuals of the 5 MHz blo-wwv, 10 MHz kf-wwv, and 15 MHz kf-wwv transmissions, respectively. The bottom panels of Figures 6.4.2 through 6.4.5 show the residuals for a given signal, where the residuals are plotted with respect to the solar X-ray flux at the time of the observation. The dashed black lines in the figures represents the mean value of the residuals, and the blue dotted lines represent one

standard deviation from the mean of the residuals. The top panels of Figures 6.4.2 through 6.4.5 show the absorption versus flux datasets for a given transmission and the best fitting LS line.

Table 6.4.2 lists the values for the means, the standard deviations of the residuals, and the root-mean-squared error of the best fitting LS line for each dataset. The standard deviation of the residuals captures the variance of the residuals about the mean, and the mean value of the residuals gives insight into whether or not the data is evenly distributed about the LS line. The magnitude of the mean residual for the 30 MHz riometer dataset is the largest of the four datasets at -0.40 dB, which indicates the absorption versus flux data for the riometer is not evenly distributed about the LS line. This can be seen in the bottom panel of Figure 6.4.5, which shows the first 330 flare-induced riometer data points are often below the mean value of the residuals, while the majority of the last 70 data points are above the mean and have a larger spread in their values than the previous data points. The standard deviation of the residuals for the first 330 riometer data points is 0.65 dB, and the standard deviation of the residuals for the last 70 riometer data points is 1.6 dB. These results suggest the LS line used to model the 30 MHz riometer absorption data may be a poor fit.

Recall from §4.2 the absorption data for the 30 MHz riometer are calculated by the University of Calgary staff managing the Pinawa riometer with a method independent of the method used in this research to calculate the flare-induced absorption of the HIDIVE signals (§5). The method used to calculate the riometer 30 MHz signal SQ reference curve may be the reason the normalized riometer absorption versus flux data for $\sqrt{U} < 0.006^{W^{0.5}}/_{m}$ in Figure 6.4.5 appears to be nonlinear and the data for $\sqrt{U} > 0.006^{W^{0.5}}/_{m}$ appears to be linear. Since the frequency of the signal monitored by the riometer is two to six times larger than the HIDIVE transmissions, the amount of X-ray flux needed for a measurable loss of signal strength for the 30 MHz signal would be higher than for that of a HIDIVE signal. Also, there are instances for which the technique to produce the riometer SQ reference curve provides a “poor fit [to quiet time data] due to instrument fluctuations on a day-to-day basis” [*CANOPUS*, 2008]. For these reasons and in order to investigate how sensitive the calculations, outlined below, are to

the slope of the LS line best fitting the riometer data, an LS line is fitted to the riometer data for which $\sqrt{U} > 0.006^{W^{0.5}/_m}$. The resulting LS line is for this case is also given in Table 6.4.1.

Table 6.4.1. The equations for the LS lines that best fit the normalized absorption versus square root solar X-ray flux data shown in Figure 6.4.1.

Signal	LS Line Equation
5 MHz blo-wwv	$L(dB) = 3256\sqrt{U}$
10 MHz kf-wwv	$L(dB) = 1391\sqrt{U}$
15 MHz kf-wwv	$L(dB) = 889\sqrt{U}$
30 MHz riometer	$L(dB) = 305\sqrt{U}$
30 MHz riometer data when $\sqrt{U} > 0.006^{W^{0.5}/_m}$	$L(dB) = 479.2\sqrt{U}$

Table 6.4.2. The mean residual, standard deviation of the residuals, and the RMS error for each absorption versus flux dataset.

Signal	Mean residual (dB)	Standard deviation of residuals (dB)	RMS Error (dB)
5 MHz blo-wwv	-0.15	2.3	2.3
10 MHz kf-wwv	-0.20	1.2	1.2
15 MHz kf-wwv	+0.13	1.1	1.1
30 MHz riometer	-0.40	1.2	1.1

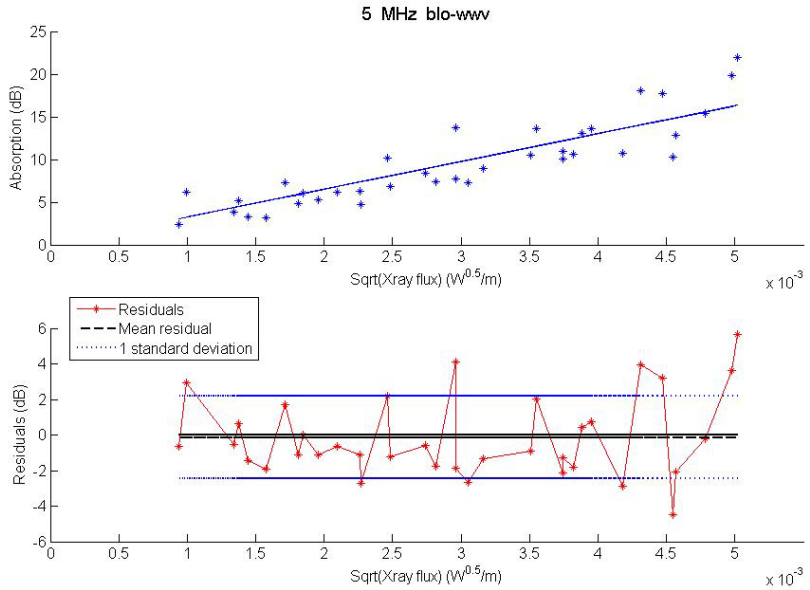

Figure 6.4.2. An LS line fit to the normalized absorption versus square root of solar X-ray flux data for the 5 MHz blo-wwv HIDIVE signal (top). The residuals (bottom) for the LS line fit are randomly distributed about a mean of -0.15 dB with a standard deviation of 2.3 dB, suggesting a relatively decent fit to the data.

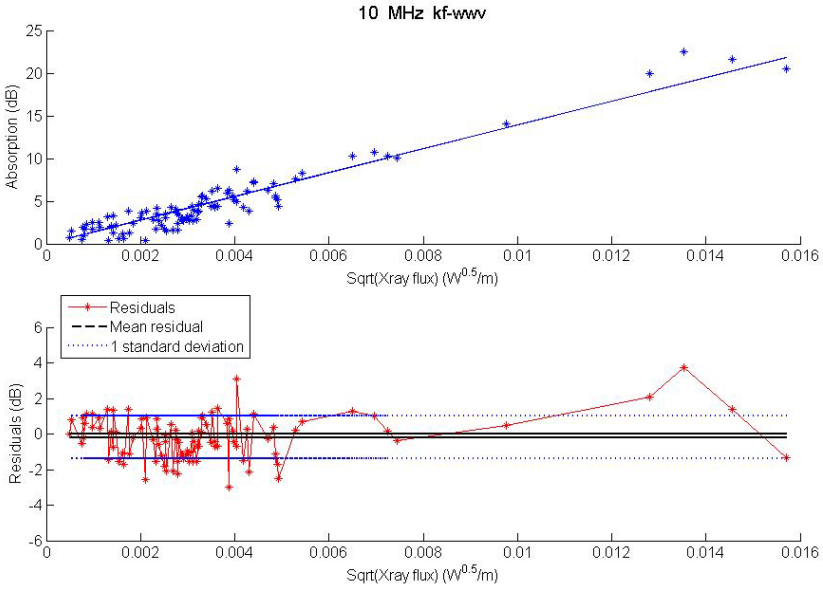

Figure 6.4.3. An LS line fit to the normalized absorption versus square root of solar X-ray flux data for the 10 MHz kf-wwv HIDIVE signal (top). The residuals (bottom) for the LS line fit are randomly distributed about a mean of -0.2 dB with a standard deviation of 1.2 dB, suggesting a relatively decent fit to the data.

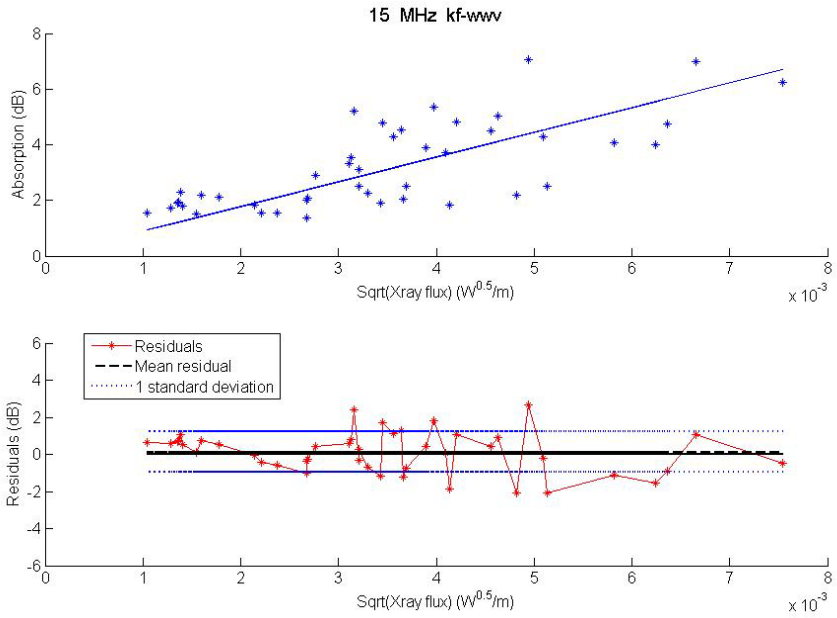

Figure 6.4.4. An LS line fit to the normalized absorption versus square root of solar X-ray flux data for the 15 MHz kf-wwv HIDIVE signal (top). The residuals (bottom) for the LS line fit are randomly distributed about a mean of +0.13 dB with a standard deviation of 1.1 dB, suggesting a relatively decent fit to the data.

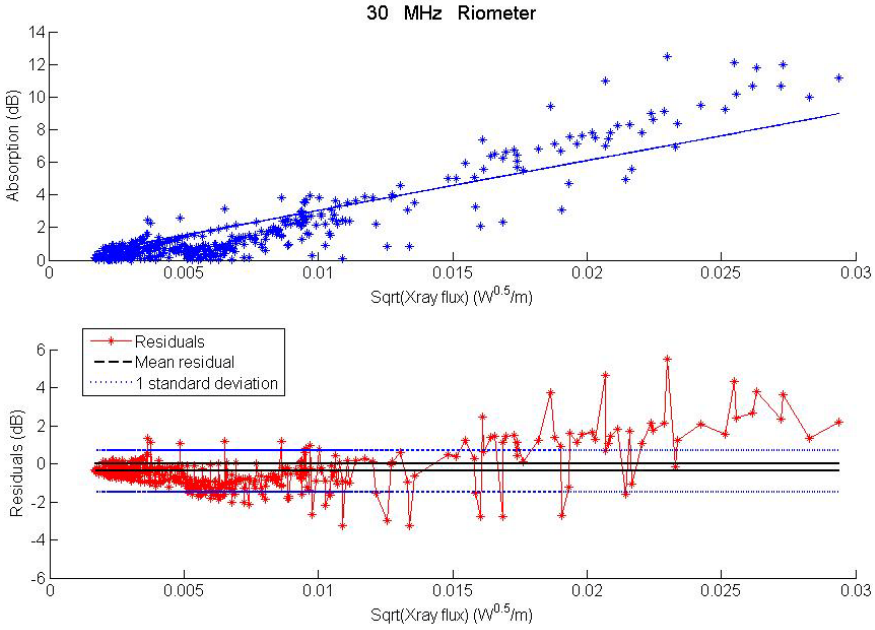

Figure 6.4.5. An LS line fit to the normalized absorption versus square root of solar X-ray flux data for the 30 MHz riometer signal (top). The residuals (bottom) for the LS line fit are not randomly distributed about the mean of -0.4 dB. The spread of the residuals about the mean increases significantly with increasing X-ray flux.

The slopes of the LS lines, shown in the top panels of Figures 6.4.2 through 6.4.5, characterize the amount of decibel loss a signal of a given frequency will experience for a given value of X-ray flux, and by fitting the equation,

$$s = C_1 * f^{C_2} \tag{6.4.1}$$

to the scatter plot of LS line slopes versus signal frequencies, the frequency dependence of absorption is determined. Here *s* is the LS line slope and C_1 and C_2 are fit parameters to be determined simultaneously. The red dashed line Figure 6.4.6 is the curve,

$$s = 2.4E4 * f^{-1.24} \tag{6.4.2}$$

which results from fitting equation 6.4.1 to the LS line slope versus signal frequency data given in Table 6.4.1. The blue circles in Figure 6.4.6 are the data with the error of the LS line slopes determined by the standard deviation of the residuals given in Table 6.4.2.

As noted in the discussion above, non-deviative absorption should follow an f^{-2} dependence when $\omega >> \nu$, such as in the E- and F-regions. Also recall from §3.3, the SWPC D-region absorption model uses an f^{-2} dependence for HF absorption. The black dotted line in Figure 6.4.6 represents the best fitting curve to the LS line slope versus signal frequency data when the exponent in equation 6.4.1 to signal frequency is set to -2. The RMS errors for the curves in Figure 6.4.6 are given in Table 6.4.3.

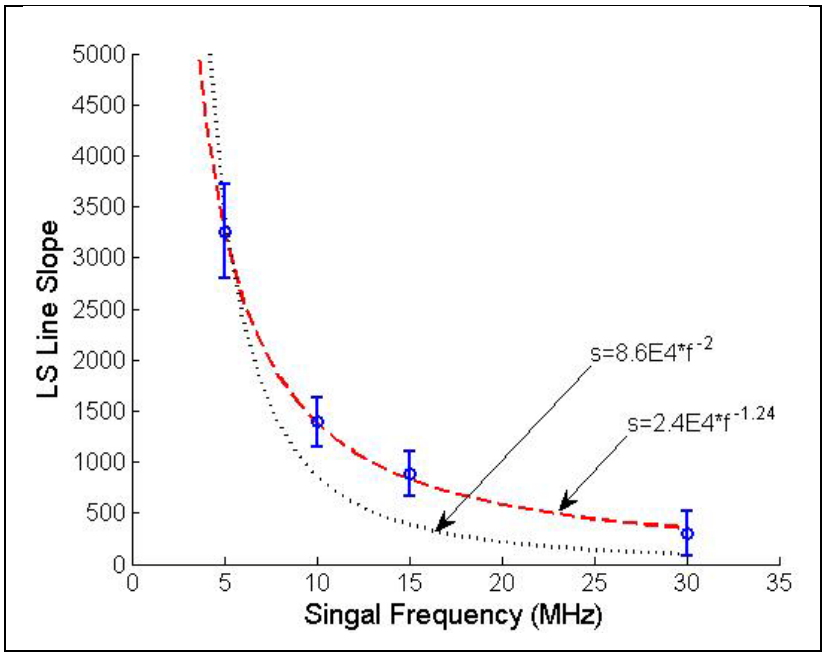

Figure 6.4.6. Equation 6.4.1 fitted to the LS line slope versus signal frequency data suggests the HIDIVE and riometer absorption dependence on signal frequency is best represented by an $f^{-1.24}$ dependence.

Several cases of fitting equation 6.4.1 to the data when C_2 is set to -2 are examined and are shown in Figure 6.4.7. The red dashed line in Figure 6.4.7 represents the best fit to the data when the 5 MHz blo-wwv dataset is omitted and C_2 = -2 in equation 6.4.1. This case is examined since the 5 MHz signal had the greatest standard deviation of the residuals and the largest RMS error with respect to the LS line. The black dotted line in Figure 6.4.7 represents the case when the 30 MHz riometer data is not included in the fit. This case is examined since the previous analysis of the residuals suggested the resulting LS line fitted to the 30 MHz data may be a poor representation of the data. Note from Figure 6.4.7 the best fitting curve when C_2 = -2 and the 30 MHz data point is omitted is the same as that found above when all four data points were included. The best fitting curve also is unchanged when the LS line slope of 479.2 is used for the 30 MHz datapoint. Recall 479.2 is the slope of the LS line fitted to the 30 MHz data corresponding to $\sqrt{U} > 0.006^{W^{0.5}}/_{m}$. Thus, the slope of the LS line modeling the 30 MHz absorption versus flux data has little effect on the curve when we are fitting for an f^{-2}

dependence. RMS errors for the curves given in Figure 6.4.7 are also given in Table 6.4.3, and based on RMS errors, equation 6.4.2 is the best fit and an f^{-2} dependence is unlikely for flare-induced absorption of the HIDIVE and riometer signals.

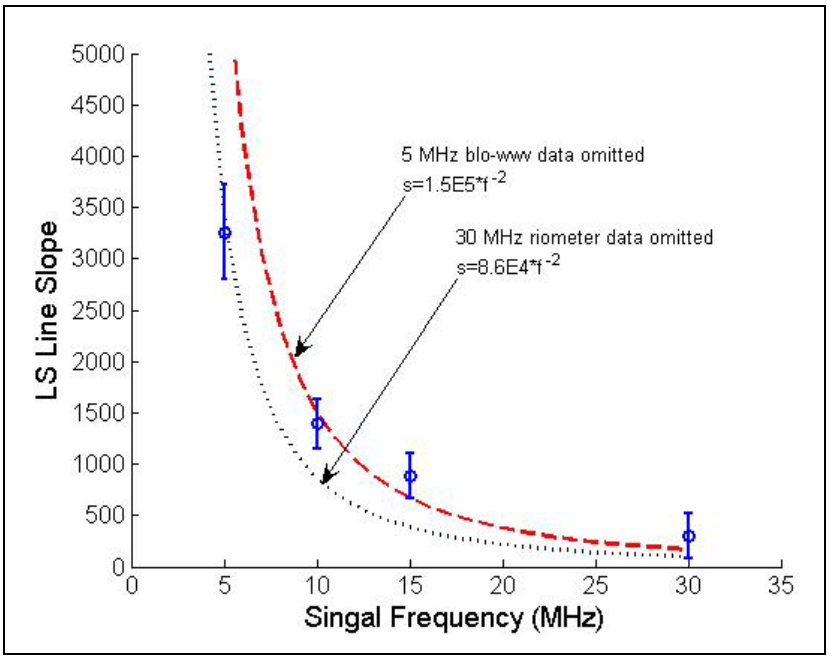

Figure 6.4.7. Equation 6.4.1 fitted to the LS line slope versus signal frequency data when C_2 is set to -2 suggests the HIDIVE and riometer absorption dependence on signal frequency is not best modeled by an f^{-2} dependence.

Table 6.4.3. The RMS errors for the curves fitting the LS line slope versus signal frequency data.

LS Line Slope versus Signal Frequency Curve	RMS Error
$s = 2.4E4 * f^{-1.24}$	1.3*E*3
$s = 8.6E4 * f^{-2}$	1.5*E*5
$s = 1.5E5 * f^{-2}$	1.9*E*6

As mentioned above, the theoretical f^{-2} dependence of absorption is valid in regions where absorption is purely non-deviative and $\omega >> \nu$ [*Davies*, 1990 ;

McNamara,1991], and the most likely explanation for the observed deviation of the absorption dependence of the HIDIVE and riometer data from the f^{-2} dependence is deviative absorption is occurring for some HIDIVE signals, especially for those signals not completely passing through the region of maximum absorption between 70 km and 110 km. To investigate the possibility HIDIVE signals are suffering deviative absorption within the lower ionosphere and the possibility some signals are being refracted back towards the earth within the D-region, the ray path predictions of the HASEL and the Hausman-Nickisch raytracing codes are examined.

Figure 6.4.8 shows the raypaths predicted by the HASEL raytracing code for the 5 MHz blo-wwv and 15 MHz kf-wwv HIDIVE transmissions during solar quiet conditions on 1 November 2003. The red dashed line in Figure 6.4.8 is the predicted ray path for the 5 MHz blo-wwv signal, the black solid line is the predicted path for the 15 MHz kf-wwv signal, and the blue asterisks represent the AbbyNormal model predictions for absorption (dB) per kilometer as a function of altitude. The AbbyNormal model predicts the region of maximum absorption on 1 November 2003 to be between 110 km and 125 km. AbbyNormal also predicts deviative absorption for the 15 MHz signal between these altitudes as can be seen in Figure 6.4.8 by the refraction, or change in propagation direction, of the signal between 110 km and 125 km. The ray path predicted by HASEL for the 5 MHz signal does not take it into the region of maximum absorption predicted by AbbyNormal and has the 5 MHz ray refracting back towards the earth at approximately 105 km, just past the upper boundary of the D-region. Thus, on 1 November 2003 the 5 MHz is not predicted to travel in to regions in which $\omega >> \nu$ and non-deviative absorption can be represented by an f^{-2} dependence.

The raytracing code developed by Mark Hausman and L.J. Nickisch of NWRA [*Huang and Reinisch*, 2006; *Nickisch*, 1988], which is based upon the Jones-Stephenson raytracing algorithm [*Jones and Stephenson*, 1975], also predicts instances in which the 5 MHz blo-wwv HIDIVE transmission fails to completely pass through the region of maximum absorption and is refracted back towards the earth within the D-region. Both raytracing codes also predict multiple-hop ray paths for the 10 MHz kf-wwv and 15 MHz kf-wwv signals which are refracted back towards below 110 km. These paths also fail to

enter regions in which an f^{-2} dependence of absorption is valid. Furthermore, the data used in Figures 6.4.1 through 6.4.7 and in the analysis of the dependence of absorption on signal frequency are flare-time observations when N_e is elevated. Thus, the signals in Figure 6.4.8 would be expected to reflect at even lower altitudes and suffer additional deviative absorption during solar active conditions, which would lead to greater deviation from the f^{-2} dependence of absorption.

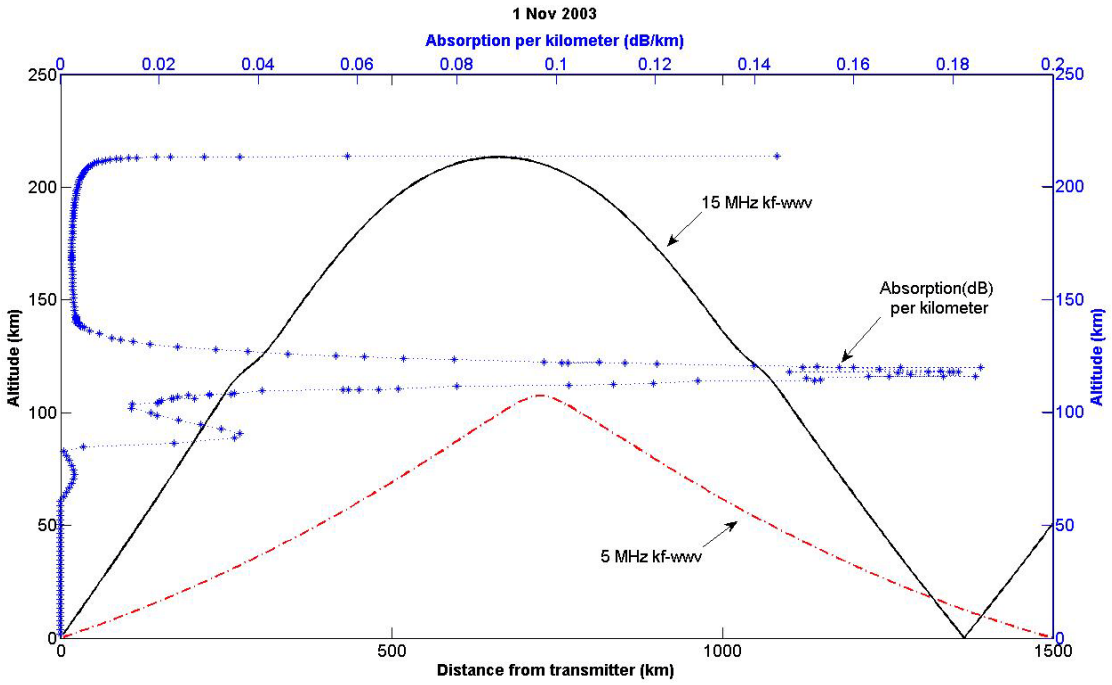

Figure 6.4.8. HASEL ray path predictions for the 5 MHz blo-wwv (red dashed line) and the 15 MHz kf-wwv (black solid line) HIDIVE transmissions and the AbbyNormal model predictions for dB absorption per kilometer (blue asterisks) on 1 November 2003 during solar quiet conditions are shown.

From the analysis of the normalized flare-time absorption data, the frequency dependence of absorption for the HIDIVE and riometer data is best described as an $f^{-1.24}$ dependence. This dependence is used in the devolvement of the Empirical HIDIVE D-region Absorption (EHA) model discussed in Chapter 7.

7. Empirical HIDIVE D-region Absorption (EHA) Model

7.1 EHA Model

From the theory of D-region HF absorption discussed in §2.5 and the empirical relations determined in §5.1 and §6.4.1, a simple model, the Empirical HIDIVE D-region Absorption Model (EHA), is presented for prediction of HIDIVE signal strength and a method for applying the EHA model to any HF transmission is outlined. As stated in §2.2, the primary sources for free electrons in the D-region are ionization of the major neutral constituents, N_2 and O_2, by solar X-rays (0.1-0.8 nm) and Lyman-α (121.6 nm) ionization of the minor constituent, nitric oxide (NO), and from equation 2.5.8 and equation 2.5.9, decibel loss is a function of the square root of the ionizing radiation flux. Rewriting equation 2.5.9 and equation 6.3.5 to solve for the decibel loss, $L_r(f, N, \chi, \phi)$, of a signal of frequency, f, due to the ionizing radiation, U_r, propagating over a path with N passes through the D-region, an elevation angle of ϕ, and a solar zenith angle of χ gives the result,

$$L_r(U_r, f, N, \chi, \phi) = G(N, \chi, \phi) \cdot C_r(f) \cdot \sqrt{U_r} \tag{7.1.1}$$

$C_r(f)$ is a frequency dependent multiplicative constant unique to the ionizing radiation. The propagation path component, $G(N, \chi, \phi)$, given in equation 7.1.2, scales the absorption according to number of passes through the D-region (N), signal elevation angle (ϕ), and solar zenith angle (χ). See §6.3.1.

$$G(N, \chi, \phi) = \frac{\sum_{i}^{N} Cos^{0.9}(\chi_i)}{Sin(\phi)} \tag{7.1.2}$$

where the term, $Cos^{0.9}(\chi)$, is determined from SQ curve fits discussed in §5.4.

D-region absorption of a HIDIVE signal due to ionization by solar X-ray flux, U_{Xray}, can now be expressed as

$$L_{Xray}(U_{Xray}, f, N, \chi, \phi) = 2.4E4 \cdot f^{-1.24} \sqrt{U_{Xray}} \left(\frac{\sum_{i}^{N} Cos^{0.9}(\chi_i)}{Sin(\phi)} \right) \tag{7.1.3a}$$

where
$$C_{Xray}(f) = 2.4E4 \cdot f^{-1.24} \tag{7.1.3b}$$

is the empirical relation ascertained in §6.4.1. Loss due to ionization of NO via Lyman-α flux, U_α, for a vertically propagating signal when $\chi = 0°$ passing only once through the D-region is given by

$$L_\alpha(U_\alpha, f, N = 1, \chi = 0°, \phi = 90°) = C_\alpha(f) \sqrt{U_\alpha} \tag{7.1.4}$$

Section 10.2 discusses the potential for future work on defining C_α and determining the frequency dependence of L_α.

Thus, the EHA Model for prediction of HIDIVE signal decibel loss within the D-region is

$$L(U_{Xray}, U_\alpha, f, N, \chi, \phi) = \frac{\sum_{i}^{N} Cos^{0.9}(\chi_i)}{Sin(\phi)} \left(2.4E4 \cdot f^{-1.24} \sqrt{U_{Xray}} + C_\alpha \sqrt{U_\alpha} \right) \tag{7.1.5}$$

With equation 7.1.5, the signal strengths, $A(f)$, of the HIDIVE signals can be predicted once the baseline signal strength, $B(f)$, is known.

$$A(f) = B(f) - L(U_{Xray}, U_\alpha, f, N, \chi, \phi) \tag{7.1.6}$$

The baseline signal strength is the expected strength of a given signal in the absence of any absorption, and baseline signal strength for a given HIDIVE signal is determined by averaging the signal strength data near sunrise and sunset during quiet conditions when the signal strength is maximized. The baseline signal strengths for the HIDIVE data are given in Table 7.1.1, and the EHA predicted signal strength is calculated by subtracting the loss calculated from equation 7.1.5 from the baseline strength.

Table 7.1.1: HIDIVE baseline signal strengths

HIDIVE Signal	Baseline Signal Strength (dBuV)
5 MHz blo-wwv	60
10 MHz kf-wwv	48
15 MHz kf-wwv	48

7.2 Operational EHA Model

The EHA model can be used operationally to predict absorption in near-real time when real-time ionizing radiation flux is used. For real time signal strength predictions, the primary raypaths and the baseline signal strength must be known and $C_\alpha(f)$ must be fitted. Without real-time measurements of local NO density, a signal strength prediction for a specific time on a given day relies on earlier signal strength observation from the same day to determine the appropriate value of $C_\alpha(f)$. The value of $C_\alpha(f)$ is determined by scaling $C_\alpha(f)$ until the predicted signal strengths, given in equation 7.1.6, best fit observed data for the given day.

Figure 7.2.1 shows the EHA model prediction of the strength of the 10 MHz kf-wwv HIDIVE signal on 15 January 2005 agrees well with observations when $C_\alpha(f) =$ 0.49. On this date, the EHA model could be used operationally to predict in real time the strength of the 10 MHz kf-wwv signal during the X2.6 flare lasting from 22:25 UT to 23:31 UT. As signal strength data are obtained, equation 7.1.6 is fitted to the data with

only the term, $C_\alpha(f)$, allowed to vary. The best fitting $C_\alpha(f)$ value is continuously adjusted throughout the day as new data are observed. The fit of equation 7.1.6 to the signal strength data on 15 January 2005 from 16:00 UT to 22:20 UT, just prior to the X2.6 flare, results in a $C_\alpha(f)$ value of 0.49, which allows for good signal strength predictions during the X2.6 flare. Also shown in Figure 7.2.1 are predictions when $C_\alpha(f)$=0.01 and $C_\alpha(f)$=1.0. The possibility of fitting equation 7.1.6 to HIDIVE data and using the resulting $C_\alpha(f)$ value as a means of measuring local NO density is discussed in §10.1, and a method of determining the frequency dependence of $C_\alpha(f)$ is suggested in §10.2.

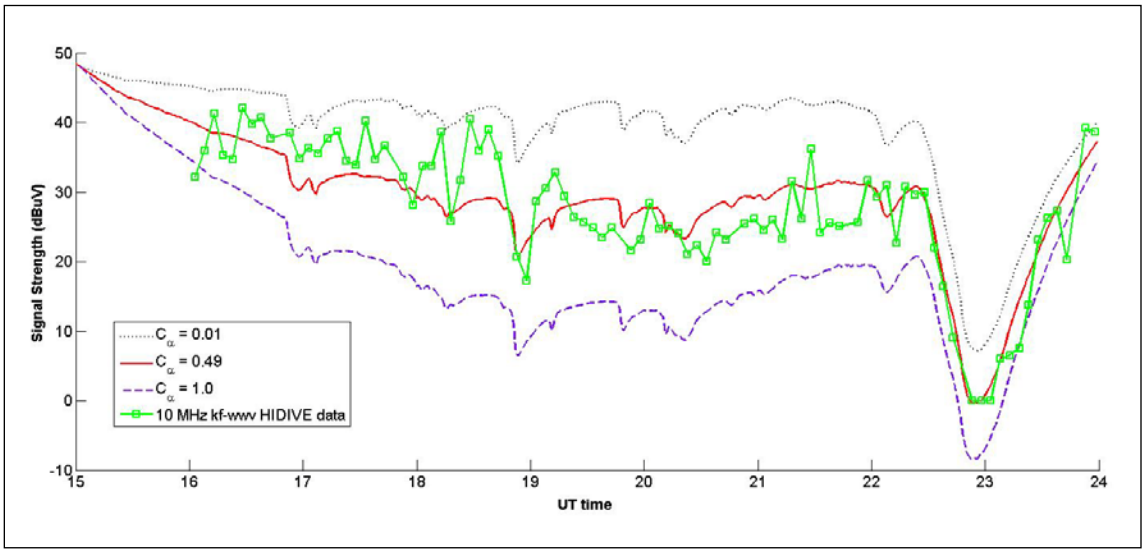

Figure 7.2.1. HIDIVE data and EHA model predictions for the 10 MHz kf-wwv signal on 15 January 2005 on which date an X2.6 flare occurred are shown. The EHA model signal strength predictions shown result from equation 7.1.6 when $C_\alpha(f)$ equals 0.01, 0.49, and 1.0. $C_\alpha(f)$=0.49 results in the best fit of equation 7.1.6 to the HIDIVE data with respect to minimizing RMS error and allows for a relatively accurate prediction of flare-time signal strength.

8. Validation of AbbyNormal, SWPC, and EHA Model Performances

8.1 Validation of Model Performances

Flare-induced absorption cases captured in the HIDIVE dataset that were not used in the development of the EHA model are used here to validate and compare the performances of the AbbyNormal, SWPC, and EHA models for the 5 MHz blo-wwv, 10 MHz kf-wwv, and 15 MHz kf-wwv HIDIVE transmissions. The dates and times of the flare-induced absorption cases used to validate the models are given in Table 8.1.1. Two metrics are used to compare and quantify the performances of the models. The first metric is the root-mean-squared (RMS) error of model daytime signal strength (DSS) predictions on days when solar flares occur, which quantifies how well a model predicts the intensity of the HIDIVE transmission. The second metric, referred to here as the flare-time absorption (FTA) RMS, is a relative RMS error of the predicted signal absorption due to solar X-ray flux during a flare.

A model's FTA RMS for a given flare-induced absorption event is the RMS error of the model prediction of absorption during the flare, normalized by the maximum observed absorption during the event. The FTA RMS is normalized so comparisons of model performance at different frequencies can be made. Since the 5 MHz blo-wwv signal suffers greater absorption than the 15 MHz kf-wwv signal for a given X-ray flux, a prediction error of 5 dBuV is more significant for the 15 MHz signal than the 5 MHz signal.

To determine the DSS RMS for the SWPC model, diurnal absorption due to Lyman-α radiation must be modeled. Recall from §3.3, the SWPC model only predicts absorption due to X-ray flux and does not produce signal strength predictions. However, from equation 7.1.5 and §2.1, there are two primary sources of loss for HF signals needed to determine the daytime signal strength deviation from the optimum baseline signal strengths given in Table 7.1.7. The first is loss due to ionization by solar X-rays and the second is loss due to ionization by Lyman-α radiation. To obtain comparable SWPC signal strength predictions for model validation, loss due to daytime ionization via Lyman-α radiation must be added to the X-ray flux induced absorption predicted by the

SWPC model. The absorption due to Lyman-α radiation for the SWPC signal strength prediction is determined by fitting the SQ reference curve equation,

$$I_{SWPC,Lyman_\alpha}(t) = A - B \cdot Cos^{0.75}(\chi_t) \tag{8.1.1}$$

to quiet time signal strength data. $I_{SWPC,Lyman_\alpha}(t)$ is the SQ curve signal strength value, A is the optimum baseline signal strength given in Table 7.1.7 for a given signal frequency, B is a fit parameter, and χ_t is the solar zenith angle at time t. The zenith angle dependence of equation 8.1.1 differs from that of equation 5.4.1 since the SWPC model (§ 3.3) suggests diurnal HF absorption varies with time as $Cos^{0.75}(\chi_t)$.

The SWPC signal strength predictions are given by

$$I_{SWPC}(f, N, \chi, \phi, U_{Xray}, t) = B(f) - G_{SWPC}(N, \chi, \phi) \cdot L_{SWPC,Xray}(U_{Xray}, f) - L_{SWPC,Lyman_\alpha}(t) \tag{8.1.1}$$

where, $G_{SWPC}(N, \chi, \phi)$ is the geometric factor suggested by the SWPC model to scale absorption predictions for propagation path elevation angle (ϕ), time of day, and number of hops (N),

$$G_{SWPC} = \frac{\sum_{i}^{N} Cos^{0.75}(\chi_i)}{Sin(\phi)} \tag{8.1.2}$$

$I_{SWPC}(f, N, \chi, \phi, U_{Xray}, t)$ is the SWPC signal strength prediction, $L_{SWPC,Xray}$ is the normalized X-ray induced absorption predicted by the SWPC model given by equations 3.4.1 and 3.4.2,

$$L_{SWPC,Xray}(U_{Xray}, f) = \frac{\left(10 \cdot \log_{10}(U_{Xray}) + 65\right)^2}{f^2} \tag{8.1.2}$$

Table 8.1.1. Dates and flare peak times for the flare-induced absorption cases used to validate the AbbyNormal, SWPC, and EHA models for the 5 MHz blo-wwv, 10 MHz kf-wwv, and 15 MHz kf-wwv HIDIVE transmissions.

5 MHz blo-wwv		10 MHz kf-wwv		15 MHz kf-wwv	
Date	Peak Time (UT)	Date	Peak Time (UT)	Date	Peak Time (UT)
26 Feb 2004	20:18	24 Mar 2004	20:18	24 Mar 2004	20:18
26 Feb 2004	22:30	24 Mar 2004	23:29	24 Mar 2004	23:29
24 Mar 2004	20:18	15 Jul 2004	22:01	15 Jul 2004	18:24
24 Mar 2004	23:29	17 Jul 2004	16:51	15 Jul 2004	22:01
15 Jul 2004	18:24	17 Jul 2004	21:31	17 Jul 2004	16:51
15 Jul 2004	22:01	17 Jul 2004	22:39	17 Jul 2004	21:31
17 Aug 2004	18:14	23 Jul 2004	17:28	17 Jul 2004	22:39
17 Aug 2004	19:37	23 Jul 2004	21:23	17 Aug 2004	18:14
17 Aug 2004	22:28	15 May 2005	22:36	17 Aug 2004	19:37
2 Aug 2005	18:31			17 Aug 2004	22:28
2 Aug 2005	20:16				

In order to determine FTA RMS for the AbbyNormal model, model predictions of flare-time absorption due to solar X-rays must be known. The AbbyNormal model output currently provides predictions of deviative and non-deviative absorption but does not specify the amount of absorption due solely to X-ray flux or Lyman-α flux. To determine the AbbyNormal prediction for flare-time absorption due to enhanced solar X-ray radiation, the method described in §5.1 for fitting a SQ reference curve to quiet time signal strength data is used. The best fit SQ curve represents the AbbyNormal predicted diurnal absorption due to Lyman-α radiation and is determined for a given date and transmission by fitting equation 5.1.4 to AbbyNormal signal strength predictions during solar quiet times. The squares in the top panel of Figure 8.1.1 are examples of AbbyNormal signal strength predictions coinciding with flares which are omitted during the fit of the SQ signal strength curve. Figure 8.1.1 shows HIDIVE data along with the AbbyNormal signal strength predictions for the 5 MHz blo-wwv transmission on 24

March 2004. The dotted line in Figure 8.1.1 is the SQ curve resulting from fitting equation 5.1.4 to the quiet-time AbbyNormal predictions. The SQ curve represents the signal strength predicted by AbbyNormal in the absence of flares and significant ionizing solar X-ray radiation. Thus, the AbbyNormal predicted absorption due to X-rays during a flare is the difference between the fitted SQ curve and the AbbyNormal predicted signal strength during the time of the flare. The procedure to determine AbbyNormal predicted X-ray induced absorption is the same method used to calculate flare-induced absorption of the HIDIVE transmissions described in §5.

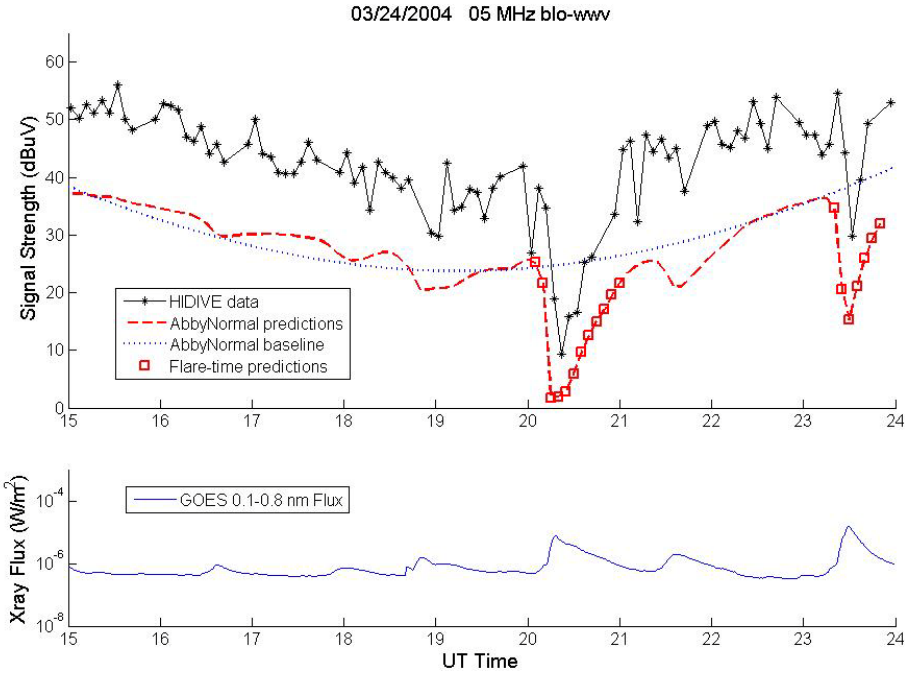

Figure 8.1.1. The baseline signal strength curve for the AbbyNormal prediction for the 5 MHz blo-wwv transmission on 24 March 2004 is used to determine absorption due to solar X-ray flux during the flares on that date.

The AbbyNormal, EHA, and SWPC model signal strength predictions for the 5 MHz blo-wwv, 10 MHz kf-wwv, and 15 MHz kf-wwv HIDIVE transmissions for 24 March 2004 are shown in Figures 8.1.2, 8.1.3, and 8.1.4, respectively, along with the DSS RMS errors. Recall the signal strength predictions for the EHA and SWPC models

begin by first fitting a baseline to the HIDIVE data and then subtracting from that the absorption predicted by the models. The AbbyNormal model, on the other hand, predicts a baseline from which flare-induced absorption is subtracted. The comparisons between the predicted signal strengths are done here to demonstrate the EHA and SWPC models could be used to predict daytime signal strengths once enough data is obtained on a given day to which a baseline could be fitted (see §7.2). The comparison also aids in highlighting problems in AbbyNormal predictions of baseline signal strength. Inaccurate NO modeling within AbbyNormal is shown in §9 to be the cause of the AbbyNormal baseline problem and is discussed in detail in §9.

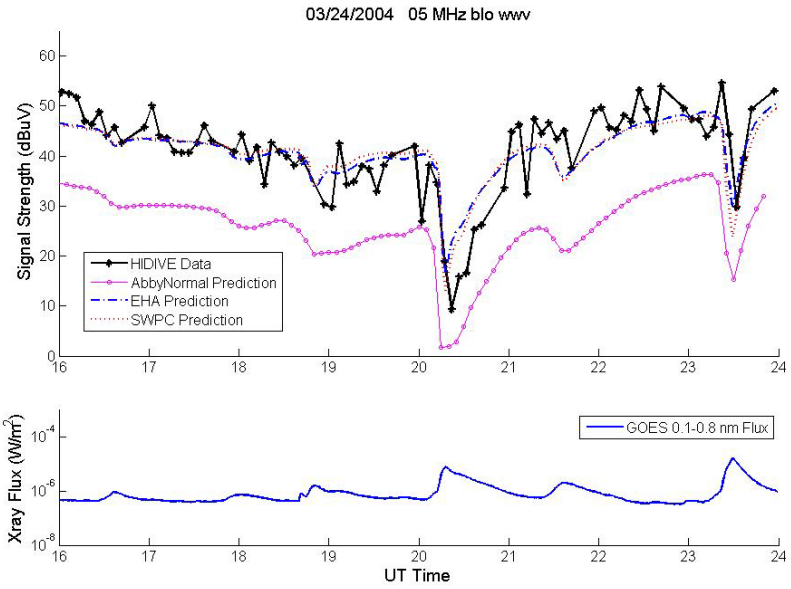

DSS RMS (dBuV)

AbbyNormal… 15.7

EHA……. **4.0**

SWPC……... 4.3

Figure 8.1.2. The AbbyNormal, EHA, and SWPC predictions for signal strength for the 5 MHz blo-wwv HIDIVE transmission on 24 March 2004.

The predicted and observed absorption due to X-ray flux during the flares on 24 March 2004 are shown in Figures 8.1.5, 8.1.6, and 8.1.7 with model FTA RMS errors for each flare. Figures of the predictions and data for the other absorption events listed in Table 8.1.1 are shown in Appendix A. Table 8.1.2 lists the DSS RMS errors for the dates listed in Table 8.1.1, and Tables 8.1.3, 8.1.4, and 8.1.5 list the FTA RMS errors for the

flares listed in Table 8.1.1 for the AbbyNormal, EHA, and SWPC models, respectively. The following section, §8.2, provides further analysis of model predictions and performances.

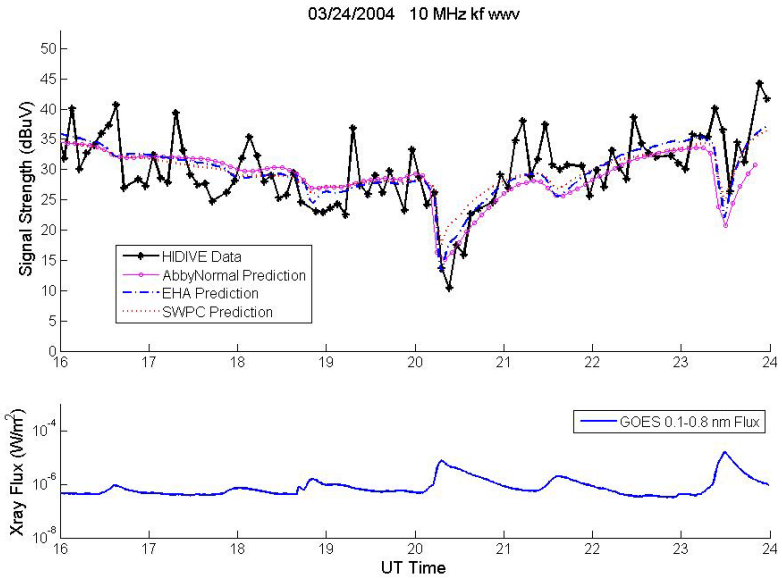

DSS RMS (dBuV)

AbbyNormal… 4.0

EHA……. **3.2**

SWPC…….. 3.3

Figure 8.1.3. The AbbyNormal, EHA, and SWPC predictions for signal strength for the 10 MHz kf-wwv HIDIVE transmission on 24 March 2004.

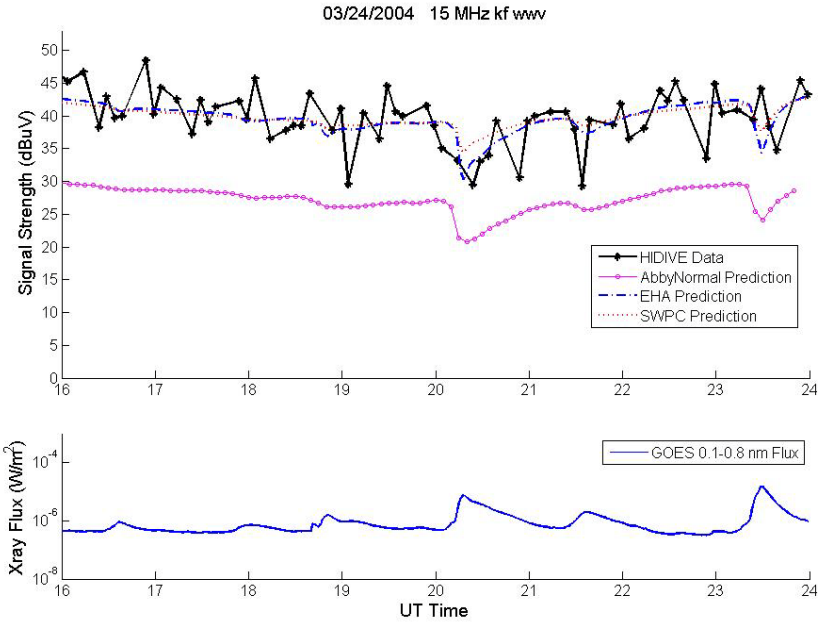

DSS RMS (dBuV)

AbbyNormal… 12.8

EHA……. **2.7**

SWPC…….. 2.8

Figure 8.1.4. The AbbyNormal, EHA, and SWPC predictions for signal strength for the 15 MHz kf-wwv HIDIVE transmission on 24 March 2004.

Table 8.1.2. DSS RMS values for the 5 MHz blo-wwv, 10 MHz kf-wwv, and 15 MHz kf-wwv HIDIVE transmission.

Model	Signal	26 Feb 2004	24 Mar 2004	15 Jul 2004	17 Jul 2004	23 Jul 2004	17 Aug 2004	15 May 2005	2 Aug 2005
AbbyNormal DSS RMS (dBuV)	5 MHz blo-wwv	12.8	15.7	16.6	-	-	16.8	-	12.1
	10 MHz kf-wwv	-	4.0	12.0	7.4	6.6	-	5.9	-
	15 MHz kf-wwv	-	12.8	8.8	10.7	-	8.7	-	-
EHA DSS RMS (dBuV)	5 MHz blo-wwv	3.5	4.0	6.8	-	-	5.6	-	4.6
	10 MHz kf-wwv	-	3.3	4.2	3.8	4.0	-	4.3	-
	15 MHz kf-wwv	-	2.7	5.2	9.0	-	6.1	-	-
SWPC DSS RMS (dBuV)	5 MHz blo-wwv	3.0	6.6	6.3	-	-	4.7	-	4.9
	10 MHz kf-wwv	-	5.0	3.4	4.1	4.5	-	4.1	-
	15 MHz kf-wwv	-	3.7	6.0	8.7	-	6.5	-	-

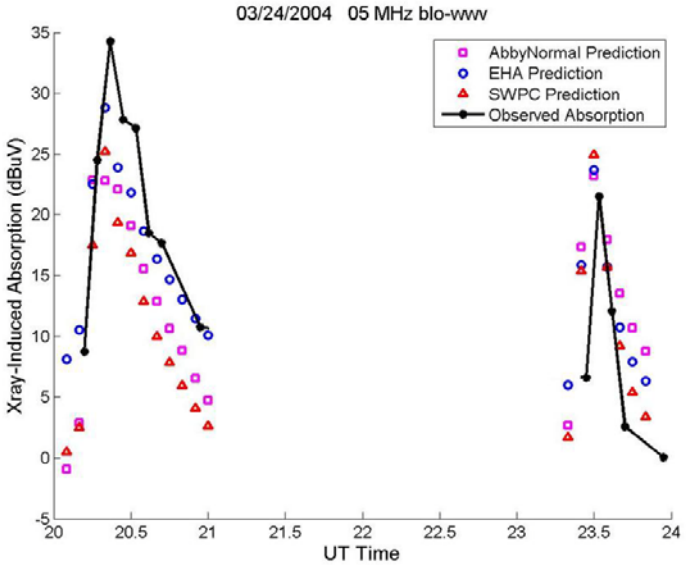

FTA RMS @ 20.1 UT
AbbyNormal… 18.7
EHA……. **13.9**
SWPC…….. 25.1

FTA RMS @ 23.3 UT
AbbyNormal… 60.3
EHA……. 31.0
SWPC…….. **28.1**

Figure 8.1.5. The AbbyNormal, EHA, and SWPC predictions for absorption due to solar X-ray flux for the 5 MHz blo-wwv HIDIVE transmission during two flares on 24 March 2004.

Table 8.1.3. FTA RMS values for AbbyNormal predictions of flare-induced absorption of the 5 MHz blo-wwv, 10 MHz kf-wwv, and 15 MHz kf-wwv HIDIVE transmissions. The values in bold font identify the lowest FTA RMS values of the three models for a given flare.

5 MHz blo-wwv			10 MHz kf-wwv			15 MHz kf-wwv		
Date	Peak Time (UT)	FTA RMS	Date	Peak Time (UT)	FTA RMS	Date	Peak Time (UT)	FTA RMS
26 Feb 2004	20:18	**12.7**	24 Mar 2004	20:18	**20.8**	24 Mar 2004	20:18	**24.1**
26 Feb 2004	22:30	34.1	24 Mar 2004	23:29	**31.5**	24 Mar 2004	23:29	40.3
24 Mar 2004	20:18	18.7	15 Jul 2004	22:01	72.3	15 Jul 2004	18:24	**32.5**
24 Mar 2004	23:29	60.3	17 Jul 2004	16:51	**10.9**	15 Jul 2004	22:01	33.4
15 Jul 2004	18:24	**40.1**	17 Jul 2004	21:31	**15.2**	17 Jul 2004	16:51	48.8
15 Jul 2004	22:01	22.7	17 Jul 2004	22:39	27.2	17 Jul 2004	21:31	38.9
17 Aug 2004	18:14	27.8	23 Jul 2004	17:28	**19.4**	17 Jul 2004	22:39	39.0
17 Aug 2004	19:37	42.3	23 Jul 2004	21:23	41.5	17 Aug 2004	18:14	**21.4**
17 Aug 2004	22:28	28.4	15 May 2005	22:36	54.3	17 Aug 2004	19:37	36.4
2 Aug 2005	18:31	**52.5**				17 Aug 2004	22:28	18.4
2 Aug 2005	20:16	27.1						

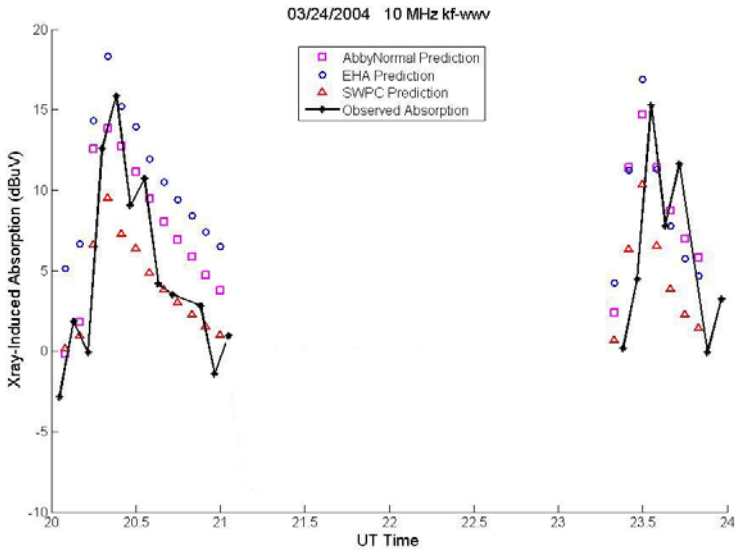

FTA RMS @ 20.1 UT
AbbyNormal… **20.8**
EHA……. 47.0
SWPC…….. 26.8

FTA RMS @ 23.3 UT
AbbyNormal… **31.5**
EHA……. 48.9
SWPC…….. 33.0

Figure 8.1.6. The AbbyNormal, EHA, and SWPC predictions for absorption due to solar X-ray flux for the 10 MHz kf-wwv HIDIVE transmission during two flares on 24 March 2004.

Table 8.1.4. FTA RMS values for EHA model predictions of flare-induced absorption of the 5 MHz blo-wwv, 10 MHz kf-wwv, and 15 MHz kf-wwv HIDIVE transmissions. The values in bold font identify the lowest FTA RMS values of the three models for a given flare.

5 MHz blo-wwv			10 MHz kf-wwv			15 MHz kf-wwv		
Date	Peak Time (UT)	FTA RMS	Date	Peak Time (UT)	FTA RMS	Date	Peak Time (UT)	FTA RMS
26 Feb 2004	20:18	20.7	24 Mar 2004	20:18	47.0	24 Mar 2004	20:18	36.7
26 Feb 2004	22:30	13.8	24 Mar 2004	23:29	48.9	24 Mar 2004	23:29	**38.1**
24 Mar 2004	20:18	**13.9**	15 Jul 2004	22:01	85.5	15 Jul 2004	18:24	54.4
24 Mar 2004	23:29	31.0	17 Jul 2004	16:51	20.1	15 Jul 2004	22:01	**19.8**
15 Jul 2004	18:24	73.5	17 Jul 2004	21:31	24.0	17 Jul 2004	16:51	**26.3**
15 Jul 2004	22:01	19.7	17 Jul 2004	22:39	30.8	17 Jul 2004	21:31	**30.8**
17 Aug 2004	18:14	30.9	23 Jul 2004	17:28	31.1	17 Jul 2004	22:39	**32.3**
17 Aug 2004	19:37	13.7	23 Jul 2004	21:23	**37.2**	17 Aug 2004	18:14	42.9
17 Aug 2004	22:28	17.7	15 May 2005	22:36	37.2	17 Aug 2004	19:37	**22.8**
2 Aug 2005	18:31	84.8				17 Aug 2004	22:28	32.3
2 Aug 2005	20:16	**21.7**						

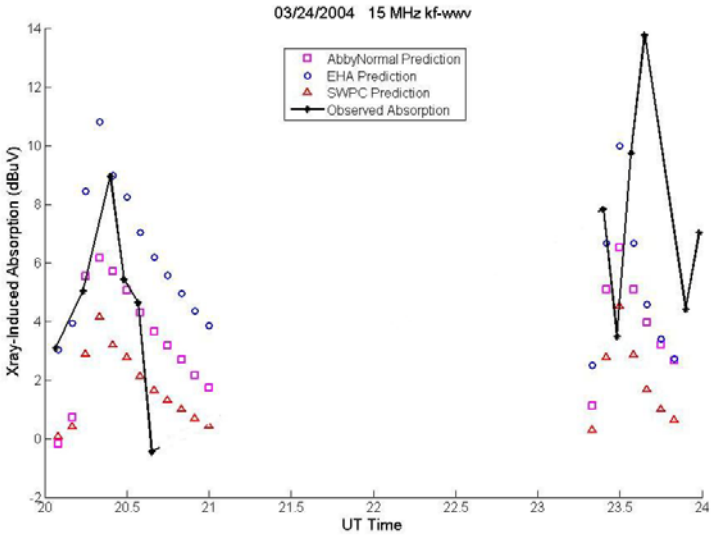

FTA RMS @ 20.1 UT
AbbyNormal… **24.1**
EHA……. 36.7
SWPC…….. 37.7

FTA RMS @ 23.3 UT
AbbyNormal… 40.3
EHA……. **38.1**
SWPC…….. 49.8

Figure 8.1.7. The AbbyNormal, EHA, and SWPC predictions for absorption due to solar X-ray flux for the 15 MHz kf-wwv HIDIVE transmission during two flares on 24 March 2004.

Table 8.1.5. FTA RMS values for SWPC model predictions of flare-induced absorption of the 5 MHz blo-wwv, 10 MHz kf-wwv, and 15 MHz kf-wwv HIDIVE transmissions. The values in bold font identify the lowest FTA RMS values of the three models for a given flare.

5 MHz blo-wwv			10 MHz kf-wwv			15 MHz kf-wwv		
Date	Peak Time (UT)	FTA RMS	Date	Peak Time (UT)	FTA RMS	Date	Peak Time (UT)	FTA RMS
26 Feb 2004	20:18	20.0	24 Mar 2004	20:18	26.8	24 Mar 2004	20:18	37.7
26 Feb 2004	22:30	**11.2**	24 Mar 2004	23:29	33.0	24 Mar 2004	23:29	49.8
24 Mar 2004	20:18	25.1	15 Jul 2004	22:01	**25.3**	15 Jul 2004	18:24	33.1
24 Mar 2004	23:29	**28.1**	17 Jul 2004	16:51	23.4	15 Jul 2004	22:01	52.6
15 Jul 2004	18:24	58.0	17 Jul 2004	21:31	31.8	17 Jul 2004	16:51	48.4
15 Jul 2004	22:01	**18.8**	17 Jul 2004	22:39	**22.2**	17 Jul 2004	21:31	46.3
17 Aug 2004	18:14	**19.3**	23 Jul 2004	17:28	24.2	17 Jul 2004	22:39	47.6
17 Aug 2004	19:37	**2.0**	23 Jul 2004	21:23	37.6	17 Aug 2004	18:14	30.2
17 Aug 2004	22:28	**15.4**	15 May 2005	22:36	21.9	17 Aug 2004	19:37	52.3
2 Aug 2005	18:31	85.7				17 Aug 2004	22:28	37.2
2 Aug 2005	20:16	32.9						

8.2 Analysis of Model Daytime Signal Strength Performance

The comparison of the models' predictions for daytime signal strengths show the EHA and SWPC models could be used to produce signal strength predictions throughout the day. Recall from §7.1 and §8.1 the EHA model absorption dependence on solar zenith angle goes as $Cos^{0.9}(\chi)$, and the SWPC model uses a $Cos^{0.75}(\chi)$ relation. From the comparison here of signal strength predictions, which are summarized in Table 8.1.2, there is no noticeable advantage of one zenith angle dependence over the other when the method of producing signal strength predictions begins with fitting baseline signal strength to solar quiet data.

The comparison does, however, highlight problems with AbbyNormal's signal strength baseline for the 5 MHz blo-wwv, 10 MHz kf-wwv, and 15 MHz kf-wwv HIDIVE transmissions. These problems can be seen in Figures 8.1.2 through 8.1.4 and

the figures in Appendix A. For the dates used in the comparison, AbbyNormal consistently under-predicts signal strength by as much as 15 dBuV for the 5 MHz blo-wwv signal and 10 dBuV for the 15 MHz kf-wwv signal. Furthermore, there seems to be a seasonal trend in AbbyNormal signal strength predictions. During the summer months, AbbyNormal under-predicts the signal strength of the 10 MHz kf-wwv signal by approximately 5 dBuV, while AbbyNormal signal strength predictions for the 10 MHz signal on 24 March 2004 are comparable to the EHA and SWPC model predictions. AbbyNormal's method of modeling atmospheric NO densities are examined in §9 as a possible cause for the low baseline signal strength predictions and the seasonal trend in model performance.

8.3 Analysis of Model Flare-Induced Absorption Performance

Unlike the signal strength predictions, direct comparisons of the three models' flare-induced absorption predictions can be made, see the summary of FTA RMS errors in Table 8.1.3. The absorption predictions of the three models are comparable on the dates analyzed here for the 5 MHz blo-wwv HIDIVE signal. However, the EHA model consistently out-performs the other two models in predicting the maximum absorption observed during a flare for the 15 MHz kf-wwv transmission, as can be seen in Figure 8.1.7 and Figures A.6.1 through A.6.3 in Appendix A.

The ability for the SWPC model to predict maximum absorption during a flare degrades as signal frequency increases. This can be seen by comparing the SWPC model FTA RMS errors in Table 8.1.5 for the three HIDIVE frequencies during a given flare. The reason for AbbyNormal's change in performance is likely due to the propagation paths the model predicts for the 10 MHz and 15 MHz signals and to the method by which it predicts atmospheric NO profiles. The AbbyNormal method for predicting NO profiles, how the NO profiles affect ray propagation predictions, and suggestions on how to improve the modeling of NO profiles are discussed in §9.

The degradation of SWPC model performance with increasing signal frequency is most likely due to the model's f^{-2} frequency dependence for absorption. Recall from §6.4.1, the frequency dependence of absorption observed for the HIDIVE data is better characterized by a $f^{-1.24}$ dependence. From the FTA RMS values in Table 8.1.3 for the

SWPC model, we see SWPC model performance for predicting flare-induced absorption degrades as signal frequency increases. Also, Figures A.1 through A.10 in Appendix A show as signal frequency increases, the amount by which the SWPC model under-predicts flare-induced absorption increases. These trends in SWPC model performance are consistent with the model not adequately characterizing the frequency dependence of absorption.

The frequency dependence of SWPC model performance can be traced to its development. Recall from §3.3 and §3.4, the SWPC model is based on Stonehocker's work which produced an empirical relationship between flare optical class and dB loss of a 5 MHz signal. From this relationship, an automated method of predicting flare-induced absorption at any frequency was suggested by scaling the expected absorption of a 5 MHz signal by f^{-2}. Thus, the SWPC model performs well for the 5 MHz blo-wwv HIDIVE signal but begins to under-predict absorption as signal frequency increases. Figures 8.3.1 through 8.3.4 show the SWPC predicted X-ray induced absorption for several dates listed in Table 8.1.1 for the 5 MHz blo-wwv signal, 10 MHz kf-wwv signal, 15 MHz kf-wwv signal, and 30 MHz riometer signal along with the observed flare-induced absorption data. Note the margin by which the SWPC model under-predicts flare-induced absorption increases with increasing signal frequency.

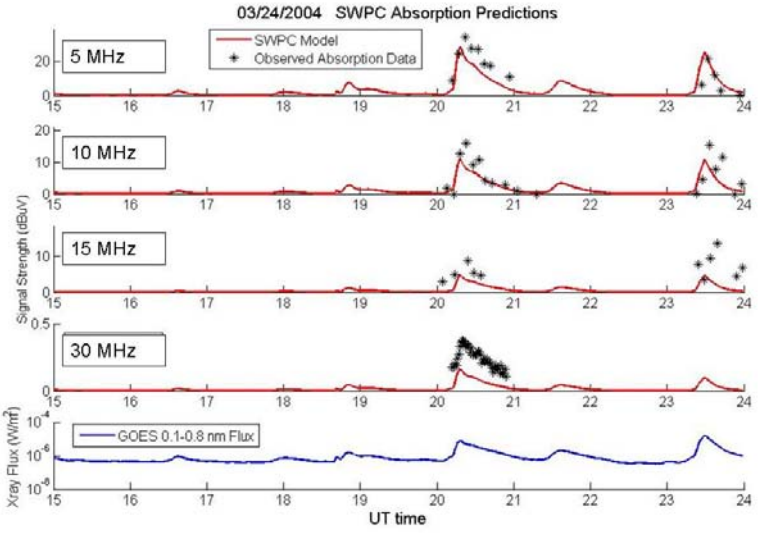

Figure 8.3.1. SWPC model predictions for X-ray induced absorption on 24 March 2004 for the 5 MHz blo-wwv signal, 10 MHz kf-wwv signal, 15 MHz kf-wwv signal, and 30 MHz riometer signal are shown along with flare-time observed absorption data.

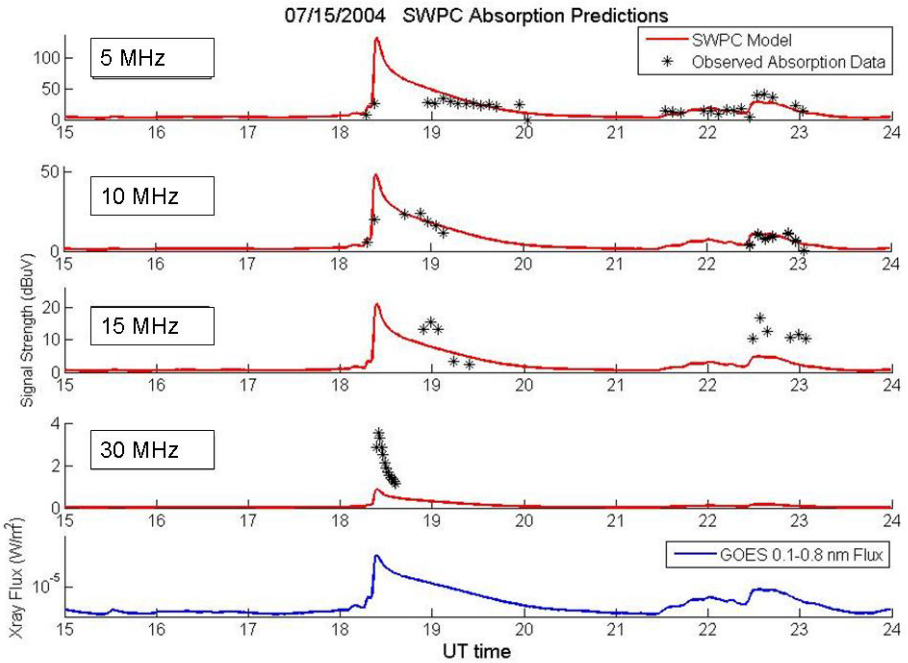

Figure 8.3.2. SWPC model predictions for X-ray induced absorption on 15 July 2004 for the 5 MHz blo-wwv signal, 10 MHz kf-wwv signal, 15 MHz kf-wwv signal, and 30 MHz riometer signal are shown along with flare-time observed absorption data.

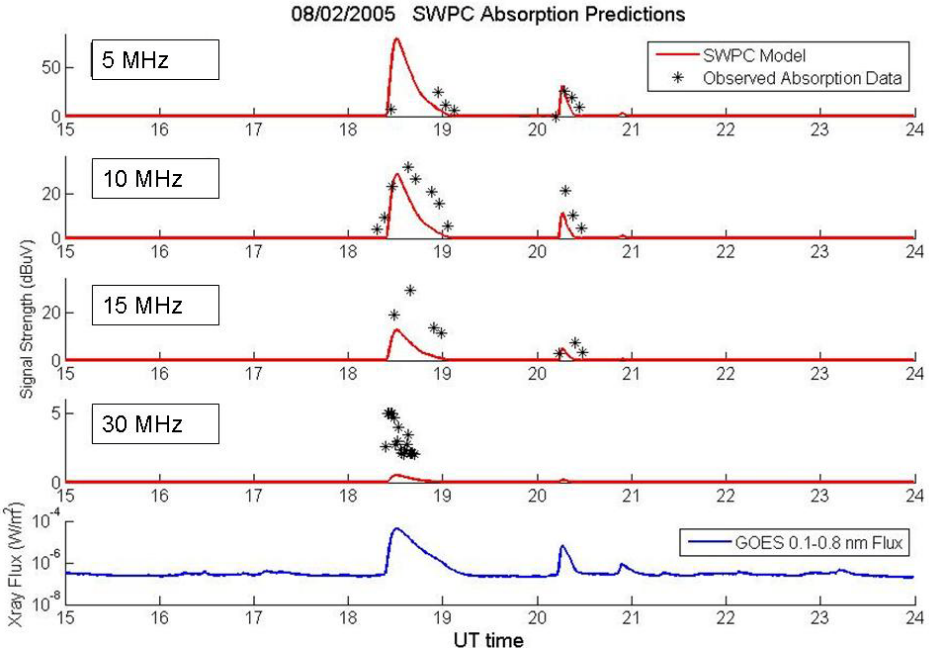

Figure 8.3.3. SWPC model predictions for X-ray induced absorption for 17 August 2004 for the 5 MHz blo-wwv signal, 10 MHz kf-wwv signal, 15 MHz kf-wwv signal, and 30 MHz riometer signal are shown along with flare-time observed absorption data.

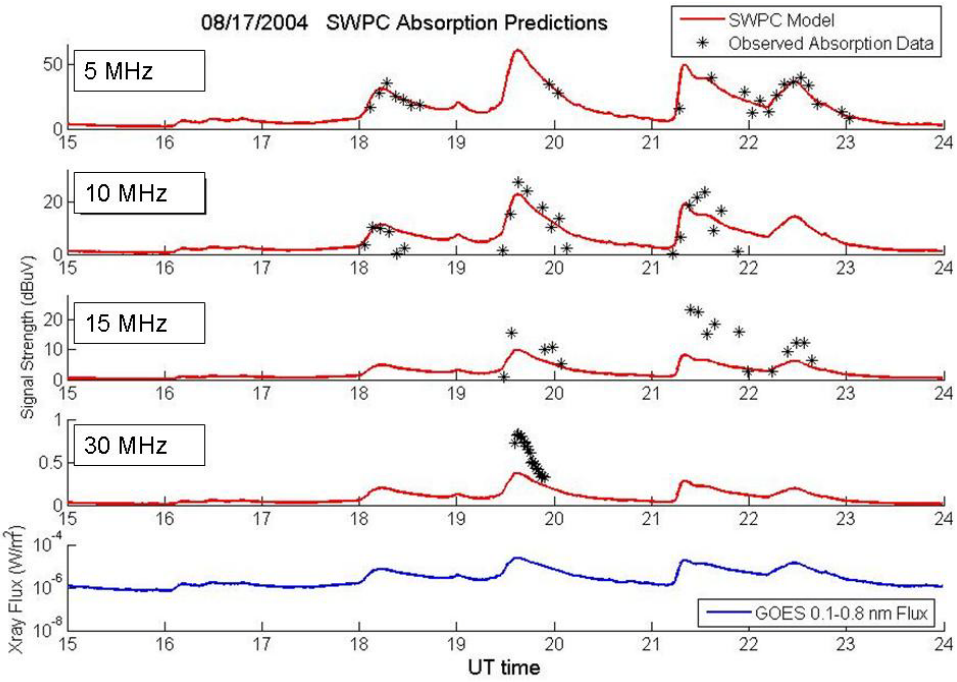

Figure 8.3.4. SWPC model predictions for X-ray induced absorption for 2 August 2005 for the 5 MHz blo-wwv signal, 10 MHz kf-wwv signal, 15 MHz kf-wwv signal, and 30 MHz riometer signal are shown along with flare-time observed absorption data.

9. AbbyNormal Analysis

9.1 AbbyNormal Validation Analysis

The validation of the AbbyNormal model in §8.1 brought to light some trends in the model signal strength predictions of the 5 MHz blo-wwv and 15 MHz kf-wwv HIDIVE transmissions. On the dates for which validation of the SWPC and AbbyNormal models is conducted in §8.1, the AbbyNormal model consistently under-predicts the 5 MHz blo-wwv and 15 MHz kf-wwv signals by approximately 15 dBuV and 10 dBuV, respectively, as can be seen in the figures in Appendix A and Figures 8.1.2 and 8.1.4. The author of the model suggests the cause of the consistently low signal strength predictions may be due to an inaccurate nitric oxide (NO) atmospheric profile [*Eccles, private communication*, 17 Jan 2008]. AbbyNormal uses NO densities produced by the MODerate spectral resolution atmospheric TRANSsmittance (MODTRAN) neutral atmospheric model [*Anderson et al.*, 1986] to create the AbbyNormal NO profiles; however, AbbyNormal's author acknowledges MODTRAN NO densities "are not sufficient to provide for a proper D-region model" and this shortfall should "be addressed in future [model] versions" [*Eccles et al.*, 2005]. This section explores methods to improve AbbyNormal NO profiles and analyzes the resulting signal strength predictions.

Further investigation of AbbyNormal performance in §9.2 shows the under-prediction trends mentioned above are seasonal, occurring most often during summer months. The under-prediction of baseline signal strengths means may be due to an over-prediction of absorption, and since AbbyNormal absorption predictions are dependent on the product, $N_e\nu$, as discussed in §2.5, a closer look is taken at AbbyNormal N_e profiles. Analysis in §9.2 suggests AbbyNormal is over-predicting N_e during summer months. The dependence of N_e on NO densities within the ionosphere is discussed in §2.2.4, and AbbyNormal predicted NO profiles are investigated as a possible avenue for improving model performance. In §9.3, the AbbyNormal NO profiles are compared to NO ionospheric density data collected by the Student Nitric Oxide Explorer (SNOE) [*Barth and Bailey*, 2004; *Marsh et al.*, 2004] and the Halogen Occultation Experiment (HALOE) [*Marsh and Russell*, 2000]. From the comparisons of NO data, alternate methods of

producing AbbyNormal NO profiles are explored and used to create three versions of the AbbyNormal model in §9.4. The model versions and their predictions for each HIDIVE transmission are then compared in §9.5.

9.2 AbbyNormal Seasonal Variation of N_e Profiles

The dates listed in Table 8.1.1 and used for the initial validation of AbbyNormal include one winter date, two spring dates, and five summer dates. Recall from §8.2, AbbyNormal signal strength performance for the 10 MHz kf-wwv HIDIVE signal worsened for summer dates. The amount by which the model under-predicted signal strength was significantly greater for summer dates, and this suggests a seasonal trend to AbbyNormal performance. Given only one winter date was used for validation in §8.2, further analysis of AbbyNormal predictions for winter dates, 11-16 January 2004 and 27-31 January 2004, is done in this section.

AbbyNormal under-prediction of signal strengths for non-winter dates is seen in Appendix A and Figures 8.1.2 and 8.1.4; however, AbbyNormal did not under-predict the signal strengths for the January 2004 dates. HIDIVE data and AbbyNormal predictions for the 5 MHz blo-wwv (top panels), 10 MHz kf-wwv (middle panels), and 15 MHz kf-wwv (bottom panels) signals for 16 January 2004 (left column) and 28 January 2004 (right column) are shown in Figure 9.2.1. AbbyNormal seasonal behavior is due to the changing N_e profiles predicted by AbbyNormal throughout the year, as seen in Figure 9.2.2. Figure 9.2.2 shows the AbbyNormal N_e profiles for several dates during 2004 near local noon at 19:00 UT. These dates include 15 January 2004, 31 January 2004, 24 March 2004, 15 July 2004, 17 July 2004, and 17 August 2004. Note two of the dates are during the winter, one during the spring, and three during summer. As shown in the figure, there is more than an order of magnitude increase in AbbyNormal N_e densities in the D-region from winter to summer, which is several times more than the seasonal changes seen in rocket, radar, and satellite measurements [*Bilitza et al.*, 2007; *Chau and Woodman*, 2006; *Friedrich et al*., 2001; *Friedrich and Torkar*, 2001].

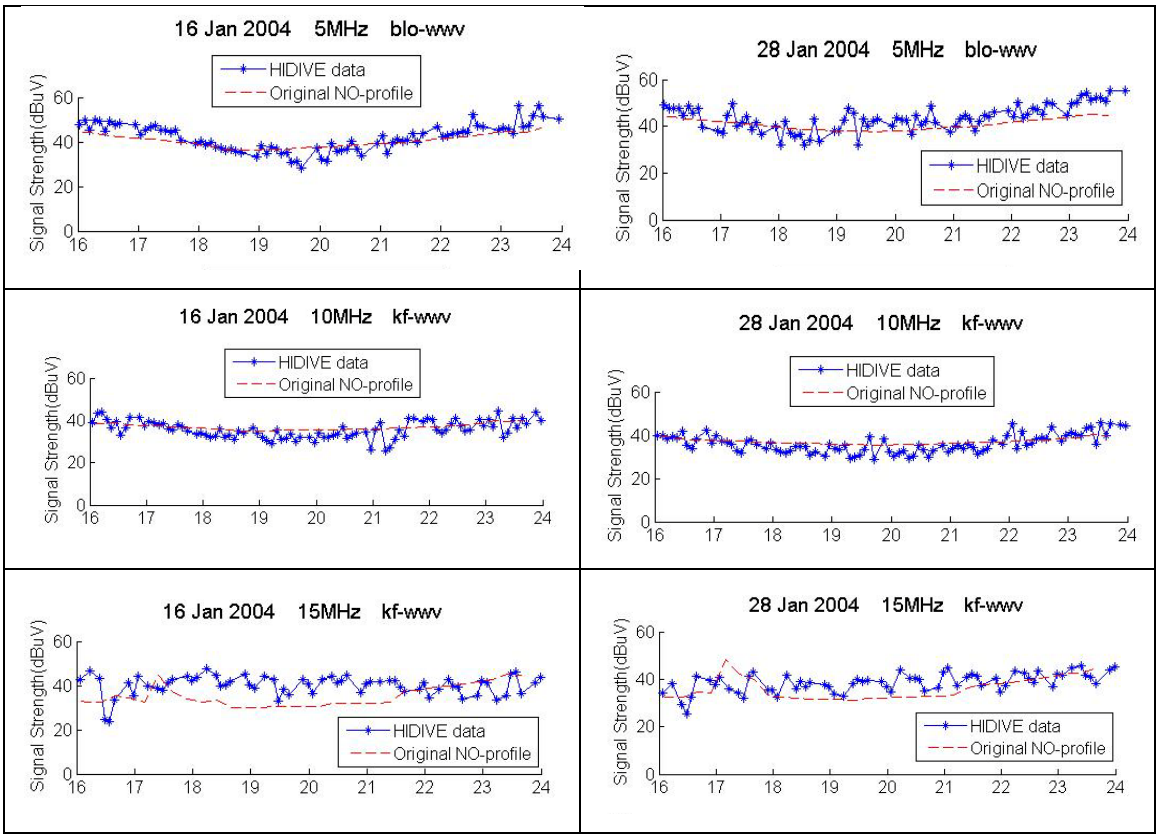

Figure 9.2.1. HIDIVE data and AbbyNormal predictions for the 5 MHz blo-wwv (top panels), 10 MHz kf-wwv (middle panels), and 15 MHz kf-wwv (bottom panels) signals for 16 January 2004 (left column) and 28 January 2004 (right column).

The drastic change in AbbyNormal predicted N_e profiles from winter to summer explains the seasonal trend in model performance in predicting 5 MHz blo-wwv signal strength. RMS errors of AbbyNormal signal strength predictions for the validation dates used here are given in Table 9.2.1. The mean RMS error for the 5 MHz blo-wwv signal strength predictions for winter dates is 8.7 dBuV, compared to a mean RMS error of 15.4 dBuV for summer dates. As shown by the RMS errors, AbbyNormal signal strength predictions for the 5 MHz transmission are better for winter dates than summer dates.

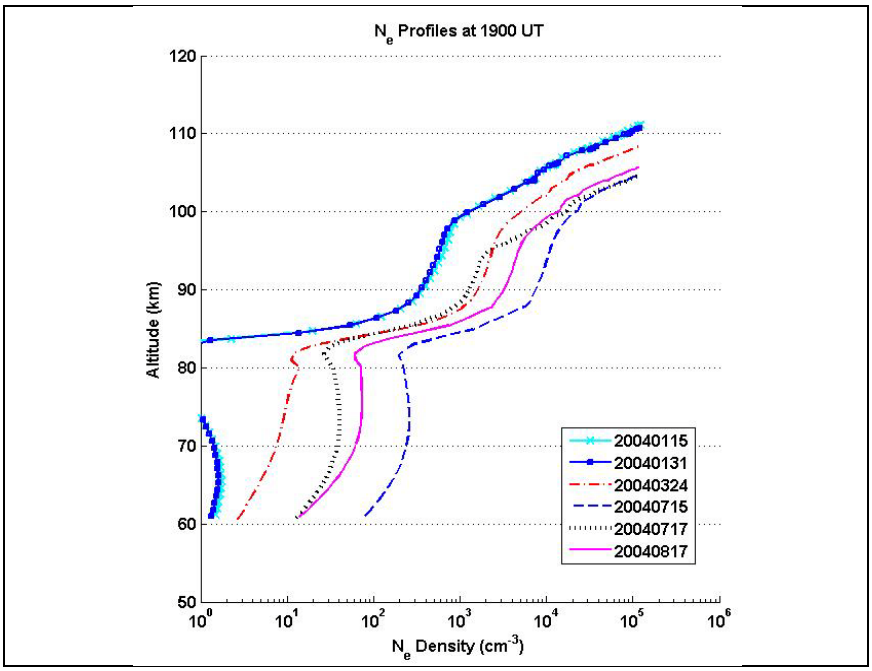

Figure 9.2.2. Electron densities predicted by AbbyNormal for several dates throughout 2004 show how model predictions for electron density increase from winter to summer months.

The larger summertime AbbyNormal N_e values lead to absorption predictions for summer dates that are as much as ten times that for winter dates. Figure 9.2.3 depicts how AbbyNormal N_e profiles affect ray path and signal absorption predictions for the 5 MHz blo-wwv transmission. Figure 9.2.3 shows noon-time AbbyNormal predicted ray paths and parameters for six dates throughout 2004. The top left panel of Figure 9.2.3 shows the predicted E-mode ray paths for the 5 MHz blo-wwv signal on the six dates. The middle left panel shows N_e along the ray path, and the bottom left panel shows the total running absorption of the signal. The plot in the upper right-hand side of Figure 9.2.3 shows the $N_e\nu$ product predicted along the ray path. Recall from equations 2.4.18 and equation 2.5.1, absorption is proportional to $N_e\nu$ when $\omega^2 >> \nu^2$. Figure 9.2.3 shows the increase of N_e of more than an order of magnitude within the D- and E-regions from winter to summer did not noticeably change the propagation paths, but it did change the amount of non-deviative absorption within the D-region and the value of $N_e\nu$ by more than an order of magnitude. Hence, AbbyNormal under-predicts summer time

signal strengths for the 5 MHz blo-wwv HIDIVE transmission due to over-predicting $N_e\nu$ and non-deviative absorption. Plots of AbbyNormal predictions and observed 5 MHz blo-wwv HIDIVE signal strength data for the validation dates listed in Table 8.1.1 are found in Appendix A, and the data for the January 2004 validation dates are found in Appendix B.

Table 9.2.1. RMS errors for daytime AbbyNormal signal strength predictions

DATE	5 BLO (dBuV)	10 KF (dBuV)	15 KF (dBuV)
11 Jan 2004	7.8	5.9	13.0
12 Jan 2004	8.8	8.8	11.7
13 Jan 2004	8.5	6.0	7.7
14 Jan 2004	5.6	11.2	6.4
15 Jan 2004	13.9	9.4	7.4
16 Jan 2004	4.0	7.3	11.8
27 Jan 2004	7.7	2.6	12.0
28 Jan 2004	4.4	2.9	5.3
29 Jan 2004	6.6	3.9	10.0
30 Jan 2004	12.5	12.4	11.7
31 Jan 2004	11.9	8.5	9.6
26 Feb 2004	12.8	4.3	9.2
24 Mar 2004	15.7	4.0	12.8
15 May 2005	6.1	5.9	12.8
21 May 2004	-	7.6	7.1
15 Jul 2004	16.6	12.0	8.7
17 Jul 2004	14.1	7.4	10.7
23 Jul 2004	17.5	6.6	11.8
2 Aug 2005	12.1	6.1	10.3
17 Aug 2004	16.8	15.3	8.7

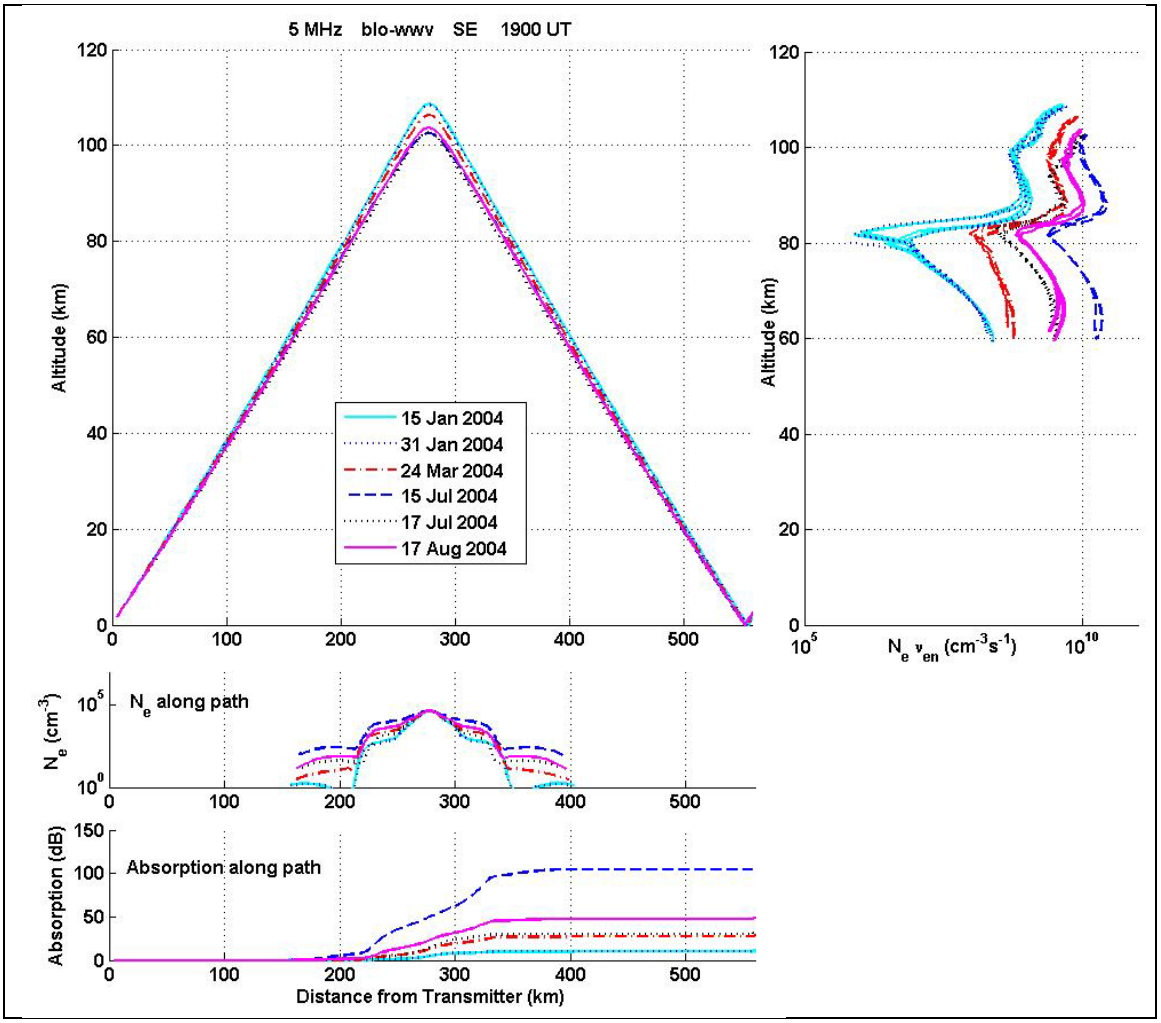

Figure 9.2.3. Shown in the left top panel are the AbbyNormal predicted E-mode ray paths for the 5 MHz blo-wwv signal for the dates throughout 2004. The middle left panel shows the prediction of N_e along the ray paths, and the bottom left panel shows the predicted total running absorption of the signal along the ray paths. Shown in the upper right-hand side is the AbbyNormal prediction for the product, $N_e\nu$, along the ray paths.

The summer-time AbbyNormal N_e profiles are also the cause of the model under-predicting the signal strength of the 15 MHz kf-wwv transmission during summer months. However, the cause of under-predicting summertime 15 MHz signal strength is not over-prediction of N_e and non-deviative absorption, as it is for the 5 MHz signal. Instead, AbbyNormal under-predicts summertime 15 MHz kf-wwv signal strength

because it predicts a different set of available propagation paths for the 15 MHz signal in the summer than in the winter. For winter dates, AbbyNormal predicts two paths are available for the 15 MHz kf-wwv transmission: a single-hop F2-mode and a single-hop E-mode, which are shown in the top panel of Figure 9.2.4. The blue dashed line in the top panel of Figure 9.2.4 represents the AbbyNormal predicted F2-mode ray path at 19:00 UT, and the solid red line is the predicted E-mode ray path at 19:00 UT. The enhanced N_e profile predicted during summer months leads to the model predicting rays to refract at lower altitudes, which results in a different set of predicted available propagation paths. During summer AbbyNormal predicts a single-hop E-mode path and a double-hop E-mode path are available for the 15 MHz kf-wwv transmission, as shown in the bottom panel of Figure 9.2.4. The blue dashed line in the bottom panel of Figure 9.2.4 is the predicted single-hop E-mode ray path, and the solid red line is the double-hop E-mode ray path. Significantly lower signal strengths are predicted for the 15 MHz kf-wwv signal in the summer since one of the ray paths predicted is a double-hop path which passes through the D-region four times and suffers approximately twice the absorption as the single-hop path.

The summer 15 MHz kf-wwv transmissions suffer additional losses due to the enhanced value of the product, $N_e\nu$, as shown in Figure 9.2.5. The right panel of Figure 9.2.5 shows predicted $N_e\nu$ increasing from winter to summer, and the bottom left panel shows how absorption also increases as a direct result of the increasing $N_e\nu$ values. Shown in the left top panel of Figure 9.2.5 are the predicted single-hop E-mode ray paths for the 15 MHz kf-wwv signal for the six dates in 2004 near local noon at 19:00 UT.

The cause of the consistent under-prediction of summertime signal strengths for the 5 MHz blo-wwv and 15 MHz kf-wwv HIDIVE transmissions seem to lie with the AbbyNormal predicted N_e profiles. The change in AbbyNormal N_e profiles from winter to summer is many times greater than the seasonal changes seen in rocket and satellite data. Summertime AbbyNormal N_e values lead to over-prediction of non-deviative absorption of the 5 MHz signal and lead to a different set of propagation paths predicted for the 15 MHz signal.

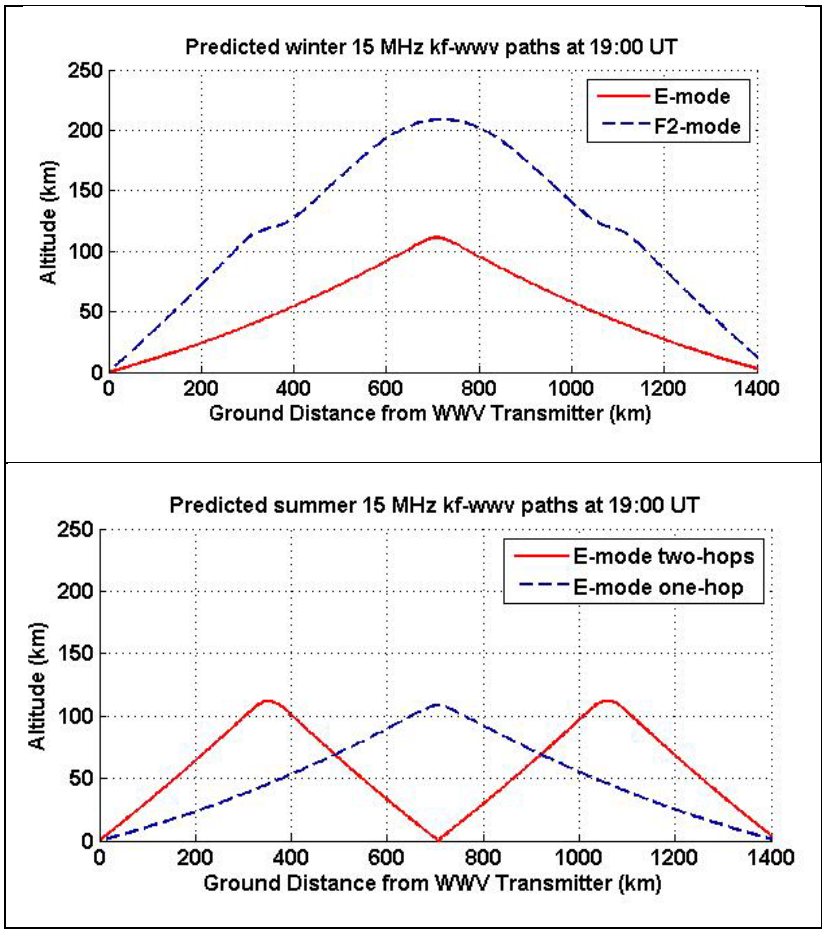

Figure 9.2.4. (Top) During winter months, AbbyNormal predicts two paths available for the 15 MHz kf-wwv transmission, a single-hop F2-mode (dashed blue) and a single-hop E-mode (solid red). (Bottom) During summer months, AbbyNormal predicts a single-hop E-mode (dashed blue) and a double-hop E-mode (solid red) are available propagation path for the 15 MHz kf-wwv HIDIVE signal.

In previous sections, N_e values and baseline signal strengths are shown to be directly dependent on local NO densities and Lyman-α flux. This research and the next section focus on AbbyNormal NO profiles as possible areas for improving model performance. As mentioned earlier in this chapter, AbbyNormal NO profiles based on MSIS O and O_2 density predictions are likely inadequate at D- and E-region altitudes according to the model author, and this likely degrades AbbyNormal baseline predictions. AbbyNormal NO profiles are shown in §9.3 to not agree well with NO satellite observations, and this research and the following sections investigate whether or not

more accurate NO profiles improve model performance and correct the seasonal trend seen in baseline signal strength predictions.

Results obtained in §9.5 show more accurate NO profiles provide better baseline signal strength predictions in some, but not all, cases. Work to further improve NO profiles is discussed in §9.5, and other areas to investigate to correct AbbyNormal seasonal trends and improve baseline signal strengths predictions are discussed in chapter 11. For example, AbbyNormal dependence of N_e on the F10.7 index, which serves as a proxy for solar Lyman-α flux, should be investigated.

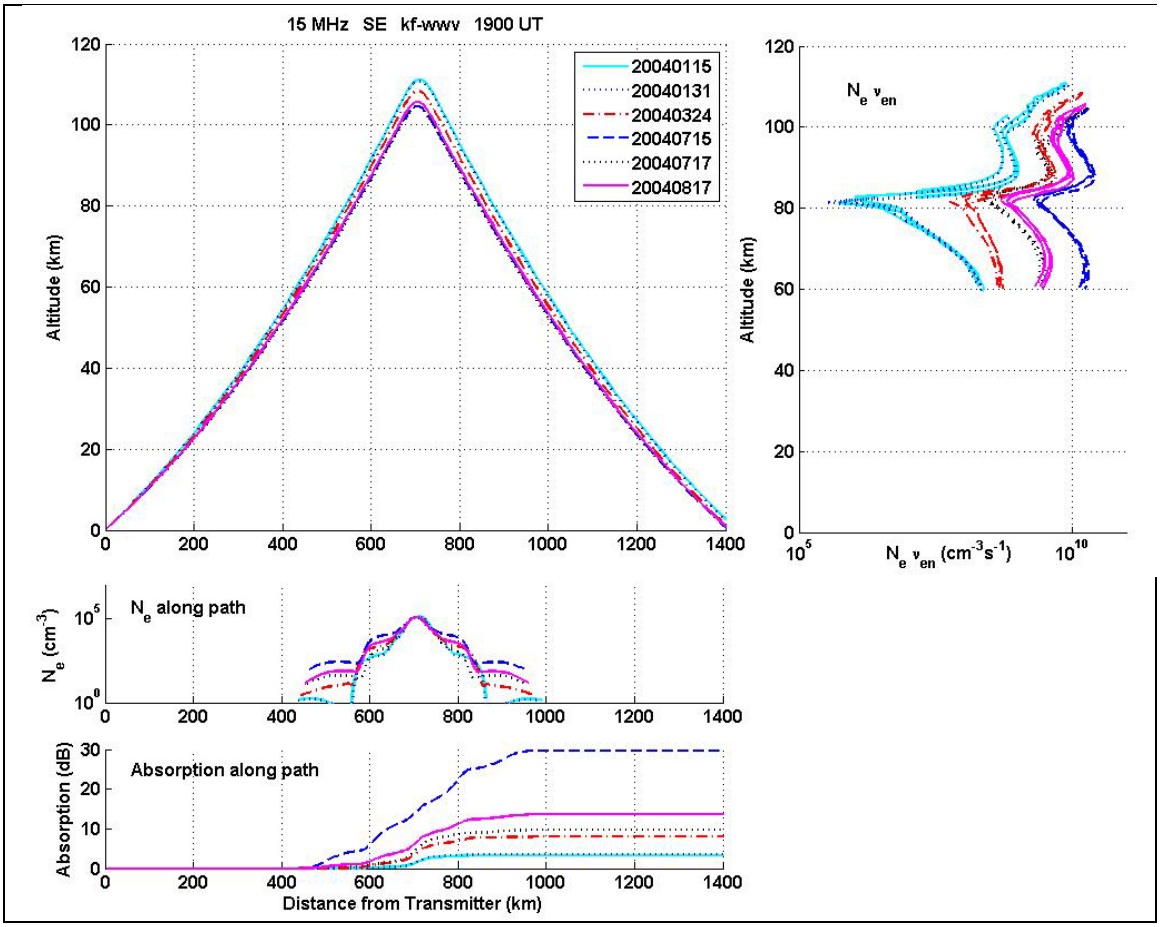

Figure 9.2.5. Shown in the left top panel are the AbbyNormal predicted E-mode ray paths for the 15 MHz kf-wwv signal for six dates throughout 2004 near local noon at 19:00 UT. The middle left panel shows the prediction of N_e along the ray paths, and the bottom left panel shows the predicted total running absorption of the signal along the ray paths. Shown in the upper right-hand side is the AbbyNormal prediction for the product, $N_e\nu$, along the ray paths.

9.3 Original AbbyNormal NO Profile Compared to Data

This investigation into whether or not more accurate AbbyNormal NO profiles improve baseline signal strength predictions begins by comparing AbbyNormal predicted NO profiles to satellite data. The original AbbyNormal NO profile is defined using the atomic oxygen (O) and molecular oxygen (O_2) densities produced by the MSIS model [*Hedin*, 1991]. Based on mixing ratios published in MODTRAN [*Anderson et. al.*, 2000; *Minschwaner et al*, 1995], AbbyNormal models the NO density profile *NO(h)* at a given altitude (*h*) as

$$NO(h) = \frac{O(h)}{2\times10^{4} cm^{-3}} + \frac{O_2(h)}{2\times10^{7} cm^{-3}} \tag{9.3.1}$$

where the number densities are given in cm^{-3}. The profiles produced by equation 9.3.1 are compared in this section to SNOE and HALOE satellite NO density observations.

The HALOE experiment was launched aboard the Upper Atmosphere Research Satellite (UARS) spacecraft on 12 September 1991 and began observations on 11 October 1991 [*Marsh and Russell*, 2000]. HALOE NO densities are measured via solar occultation at sunrise and sunset, and data are available from 11 October 1991 to 21 November 2005, allowing for some HALOE observations to temporally coincide with HIDIVE data.

The SNOE dataset is comprised of nearly continuous NO density satellite observations from 11 March 1998 to 30 Sept 2000 and between the altitudes of 90 km and 150 km [*Barth et al.*, 2004; *Marsh et al.*, 2004]. The SNOE satellite orbited the earth 14 times a day in a nearly circular orbit at an altitude of 556 km [*Barth*, 1999] and made observations in the HIDIVE region of interest around 17:45 UT on the dates considered here. SNOE NO density observations are deduced from on-board spectrometer measurements of NO gamma band emissions at 237 nm. Unfortunately, the time periods for which SNOE data and HIDIVE data are available do not overlap; however, SNOE data can still be used to validate AbbyNormal NO profiles with the use of an empirical model.

Aside from observational data, an empirical NO model based on SNOE data was developed by *Marsh, Soloman, and Reynolds* [2004] for the altitude range of 100 km to 150 km using eigenanalysis to determine the three orthogonal functions that best characterize the data. The Marsh, Soloman, and Reynolds empirical model (MSR model) calculations of NO begin by defining NO densities according to a latitude and altitude grid. Then the inputs (day of year, F10.7 flux, and the Kp planetary index) are used to determine the value of the three orthogonal eigenfunctions, which modify the initial mean NO density grid. The first function is closely related to enhancements in aurorally-produced NO and is modified by a parameter based on the average of the eight reported geomagnetic Kp indices from the prior day. The second function is associated with solar declination angle and is modified by an expression dependent on the day of the year. The third function correlates highly with long term solar radiation flux variations, such as changes seen throughout a solar cycle and solar rotation. The third function is scaled by an expression dependent on the 10.7 cm solar flux reported for the previous day [*Marsh et al.*, 2004]. The sum of the mean and three scaled functions results in the model prediction of NO densities from -80° latitude to +80° latitude and from 100 km to 150 km.

AbbyNormal NO profiles, SNOE data, Empirical NO Model predictions, and HALOE data are shown for three consecutive days in July 1998 in Figures 9.3.1a, 9.3.1b, and 9.3.1c. As seen from the plots in Figure 9.3.1, the AbbyNormal profile does not agree well with observations above 80 km. It is important AbbyNormal NO profiles are accurate within the altitude range of 80 km to 120 km since this is the region in which significant absorption occurs and the N_e profile above 80 km determines predicted ray paths and reflection altitudes. Table 9.3.1 lists the observed SNOE and HALOE NO densities and the MSR and AbbyNormal predicted densities at 100 km and 140 km. As seen in Table 9.3.1, satellite observations at 140 km are greater than predicted AbbyNormal values by more than an order of magnitude. To better model NO density, three alternate methods for producing NO profiles to be used by the AbbyNormal model are investigated and described in §9.4.

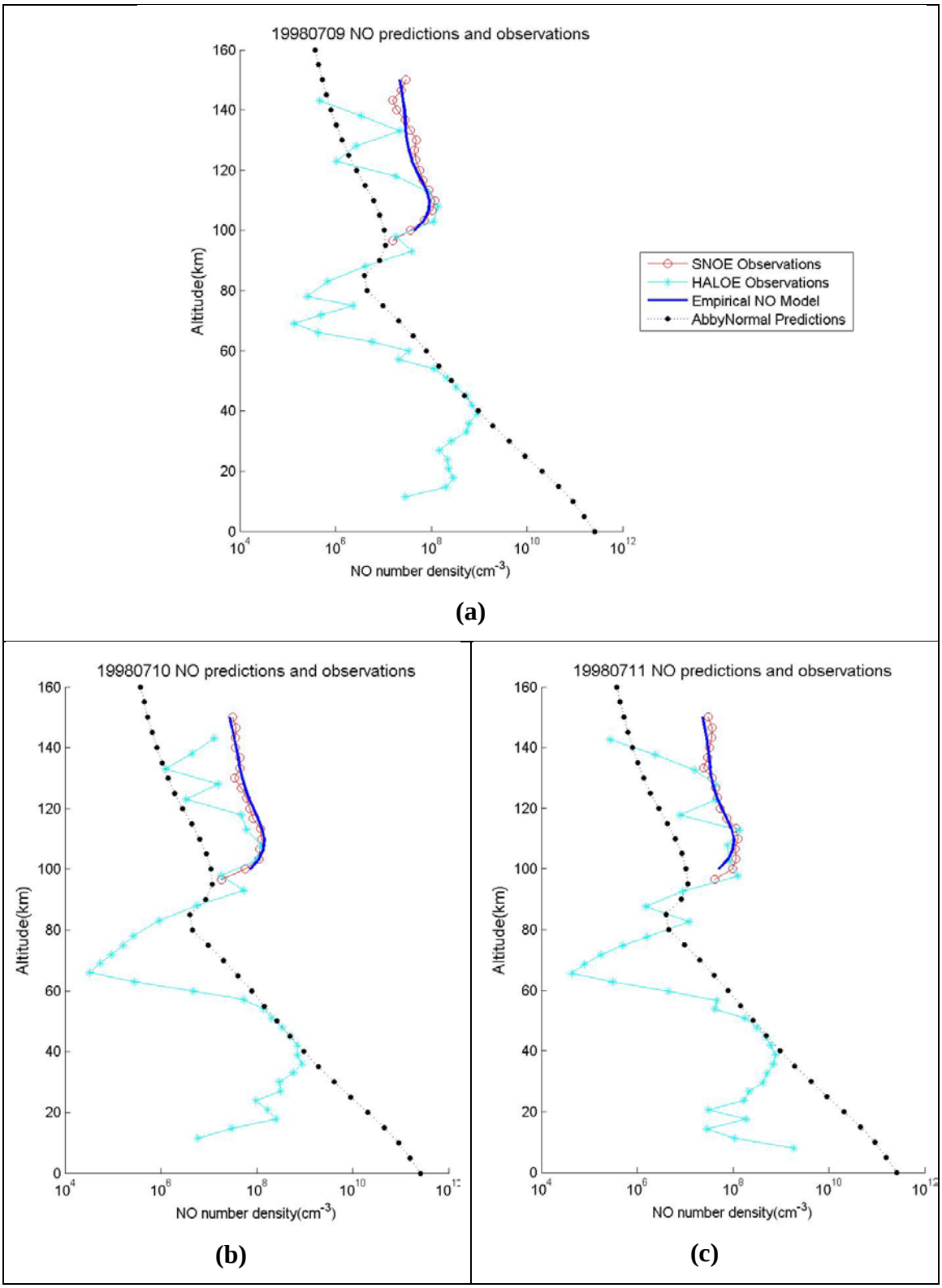

Figure 9.3.1. AbbyNormal and MRS model NO density predictions for and SNOE and HALOE observations on three consecutive days, 9 July, 10 July, and 11 July 1998.

Table 9.3.1. NO densities (cm^{-3}) observed by the SNOE and HALOE satellites and predicted by the MSR empirical and AbbyNormal models on 9, 10 , and 11 July 1998 at the altitudes of 100 km and 140 km.

	9 July 1998		10 July 1998		11 July 1998	
	100 km	140 km	100 km	140 km	100 km	140 km
SNOE	3.6e7	1.9e7	5.8e7	3.5e7	9.9e7	3.2e7
HALOE	3.6e7	3.5e6	3.9e7	4.5e6	1.1e8	8.1e5
MSR	4.4e7	2.7e7	7.2e7	3.7e7	5.0e7	3.0e7
AbbyNormal	1.0e7	8.1e5	1.1e7	8.2e5	1.1e7	8.1e5

9.4 New Methods for Defining AbbyNormal NO Profiles

In light of the poor agreement between AbbyNormal defined NO profiles and observed NO densities shown in §9.3, several alternative methods for defining the NO profile within AbbyNormal are investigated in order to improve AbbyNormal performance in predicting NO profiles, N_e profiles, and HF absorption. The first method, discussed in §9.4.1, is to recalibrate equation 9.3.1 by changing the scaling of *O* so the profile more closely matches the SNOE and HALOE data. This method of producing NO profiles results in improved signal strength predictions for the 5 MHz blo-wwv and, occasionally, the 10 MHz blo-wwv signals; however, the NO densities predicted by this method are approximately an order of magnitude greater than SNOE and HALOE observations between the altitudes of 80 km and 100 km. Two other methods of producing AbbyNormal NO profiles are investigated in §9.4.2 and §9.4.3. In §9.4.2 the second method, which uses the MSR empirical NO model to produce NO profiles, is outlined, and the third model, which incorporates actual HALOE NO density data, is discussed in §9.4.3. The signal strength predictions resulting from the MSR model-based and HALOE-based NO profiles are analyzed in §9.5.

9.4.1 Rescaling MSIS Densities.

The first method investigated to improve AbbyNormal NO profiles is to recalibrate equation 9.3.1 by changing the scaling of *O* so the profile more closely matches the SNOE and HALOE data. *O* dominates the AbbyNormal profile above 100 km and in the region of maximum absorption, shown in Figures 9.2.2 and 9.2.4 to be

between 80 km and 110 km. Thus, scaling *O* to match the peak NO density seen in data is sufficient. 87 dates were identified for which both SNOE and HALOE data were available for the geographical region in which HIDIVE data are collected, and on these dates, the following equation is fitted to SNOE and HALOE data in order to determine the appropriate scale for *O*,

$$NO(h) = C \cdot O(h) + \frac{O_2(h)}{2 \times 10^7 \, cm^{-3}} \tag{9.4.1}$$

where *C* is the parameter to be determined and the number densities are given in cm^{-3}. The result of fitting equation 9.4.1 to the data for the 87 dates is an average value for *C* of $(6.0 \pm 1.8) \times 10^{-4}$. The modified equation for predicting AbbyNormal NO profile is

$$NO(h) = 6 \times 10^{-4} \cdot O(h) + \frac{O_2(h)}{2 \times 10^7} \tag{9.4.2}$$

Figure 9.4.1 shows the original AbbyNormal NO profile given by equation 9.2.1 along with the modified profile, given by equation 9.4.2, in which *O* is scaled by 6×10^{-4}. The figure also shows the NO density predictions of the MSR model and SNOE and HALOE observations.

Figure 9.4.1 shows the modified scaling of *O* results in a better fit to observations above 100 km; however, the modified NO profile does not agree well with observations between 80 km and 110 km and is approximately an order of magnitude greater than observations.. Figures 9.4.2 and 9.4.3 show the general trend of the AbbyNormal predictions for the 5 MHz and 10 MHz blo-wwv signals using the modified NO profile. The figures show HIDIVE data and signal strength predictions produced when equation 9.3.1 is used to model NO densities (original AbbyNormal model) and when equation 9.4.2 is used (modified AbbyNormal model) for 10 July 2004 and 27 December 2003. Increasing the NO density profile above 80 km did not increase absorption in the 5 MHz signal; it instead resulted in higher predicted signal strengths. The modified NO profile

also led to changes in the 5 MHz and 10 MHz blo-wwv predicted propagation paths, namely higher reflection altitudes. Higher predicted reflection altitudes and higher predicted signal strengths are also seen in the kf-wwv signals when equation 9.4.2 is used to define AbbyNormal NO profiles.

Figures 9.4.4 and 9.4.5 show the AbbyNormal predicted propagation paths for the 5 MHz and 10 MHz blo-wwv signals on 10 July 2004 and 27 December 2003, respectively. The reason for higher predicted signal strengths is the modified model predicts the signals to travel a shorter distance within the altitude range of maximum absorption, refracts at a higher altitude where deviative losses are less, and predicts the signals to have a more vertical elevation angle when passing through the D-region. Signal strength RMS errors for the 10 July 2004 and 27 December 2003 predictions are given in Table 4.4.1. In Table 4.4.1 RMS errors are used to compare the predictions produced of the original AbbyNormal model and the modified AbbyNormal model. RMS errors for the 10 MHz blo-wwv signal, shown in the bottom panels of Figures 9.4.2 and 9.4.3, are calculated during the time period the modified AbbyNormal model predicts a non-zero signal strength. The time period used to calculate the 10 MHz blo-wwv signal strength RMS error on 10 July 2004 is from 16:18 UT to 22:45 UT, and the time period for the signal on 27 December 2003 is from 18:15 UT to 22:05 UT.

Other methods of defining the NO profile within AbbyNormal are investigated since the NO profile given in equation 9.4.2 yields predicted signal strengths for the 5 MHz blo-wwv signal that continue to be to too low and since no signal is often predicted for the 10 MHz blo-wwv and 15 MHz kf-wwv transmissions at hours close to sunrise and sunset.

Table 9.4.1. Signal strength RMS errors for the Original AbbyNormal and Modified AbbyNormal models.

	10 July 2204		27 December 2003	
	Original AbbyNormal	Modified AbbyNormal	Original AbbyNormal	Modified AbbyNormal
5 MHz blo-wwv	12.1	9.7	7.7	7.2
10 MHz blo-wwv	7.5	6.0	4.0	9.7

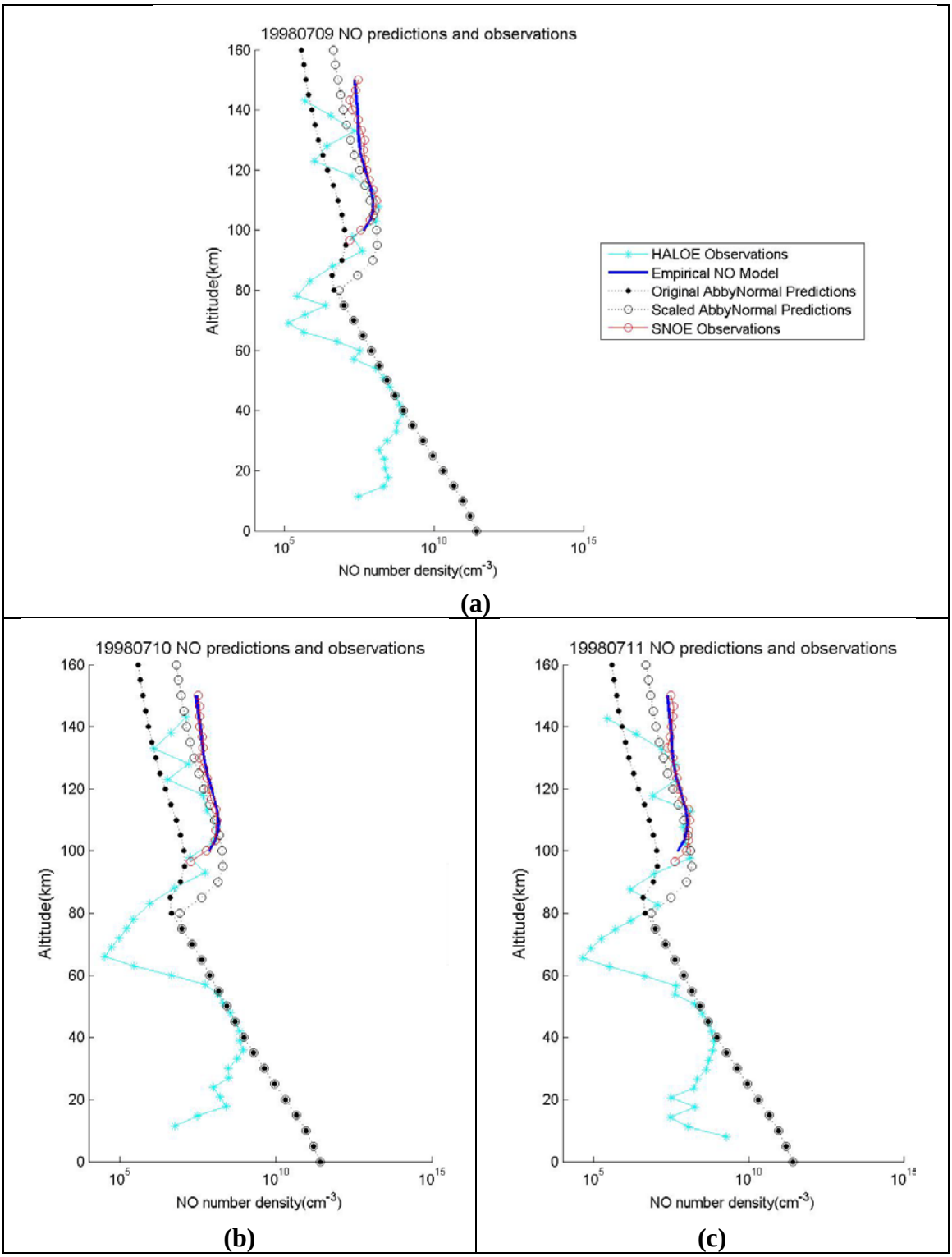

Figure 9.4.1. Shown are NO density predictions and observations for three consecutive days, 9 July (a), 10 July (b), and 11 July 1998 (c). Here the original AbbyNormal NO profile which uses the mixing ratio of 5E-5 to scale atomic oxygen is shown (black closed circles) along with the modified NO profile defined by scaling atomic oxygen by 6.02E-4 (black open circles).

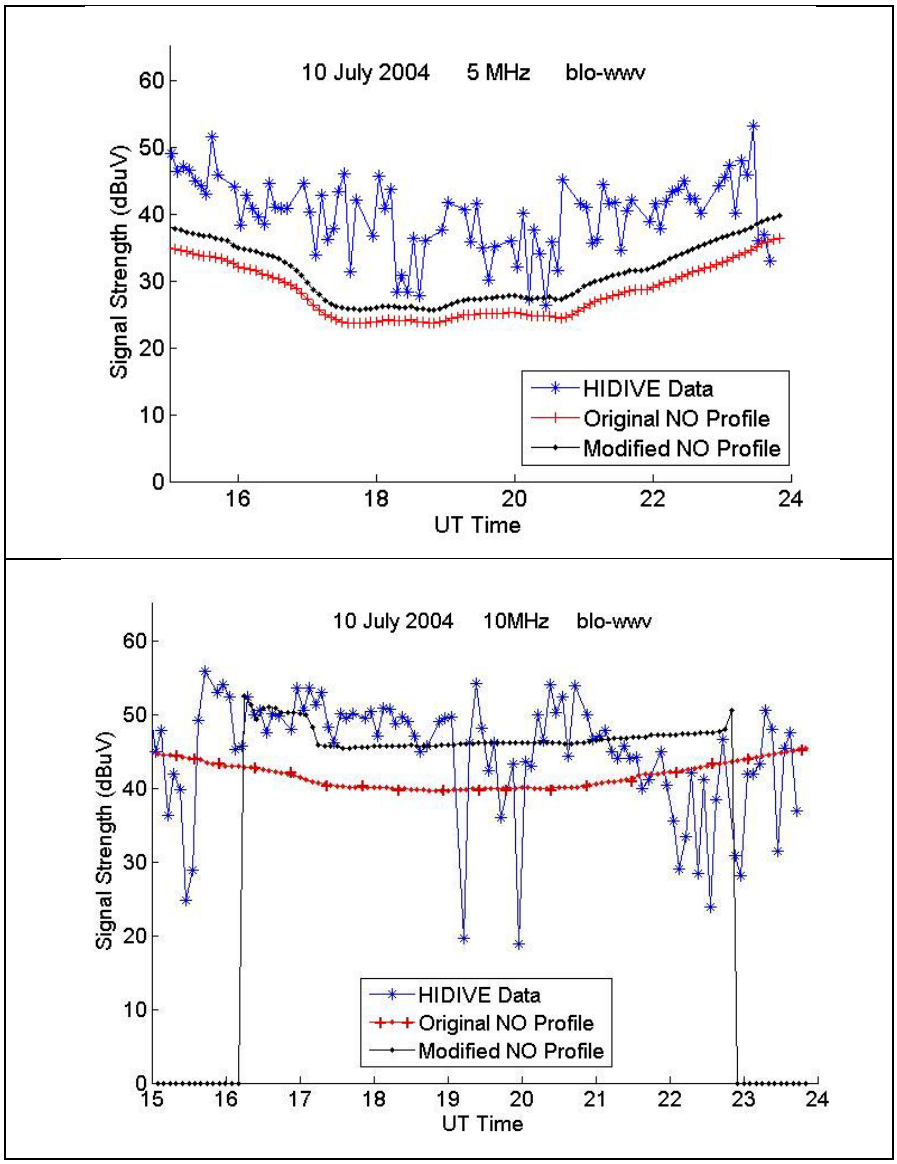

Figure 9.4.2. HIDIVE data for the 5 MHz (top) and 10 MHz blo-wwv (bottom) signals on 10 July 2004 are shown along with the signal strength predictions of the original and modified versions of the AbbyNormal model. The signal strength predictions using the original AbbyNormal version of producing NO profiles, which is given in equation 9.2.1, are shown by the black dotted line in the above panels. The predictions of the version which uses equation 9.4.2 to define AbbyNormal NO profiles are shown by the red line marked with crosses.

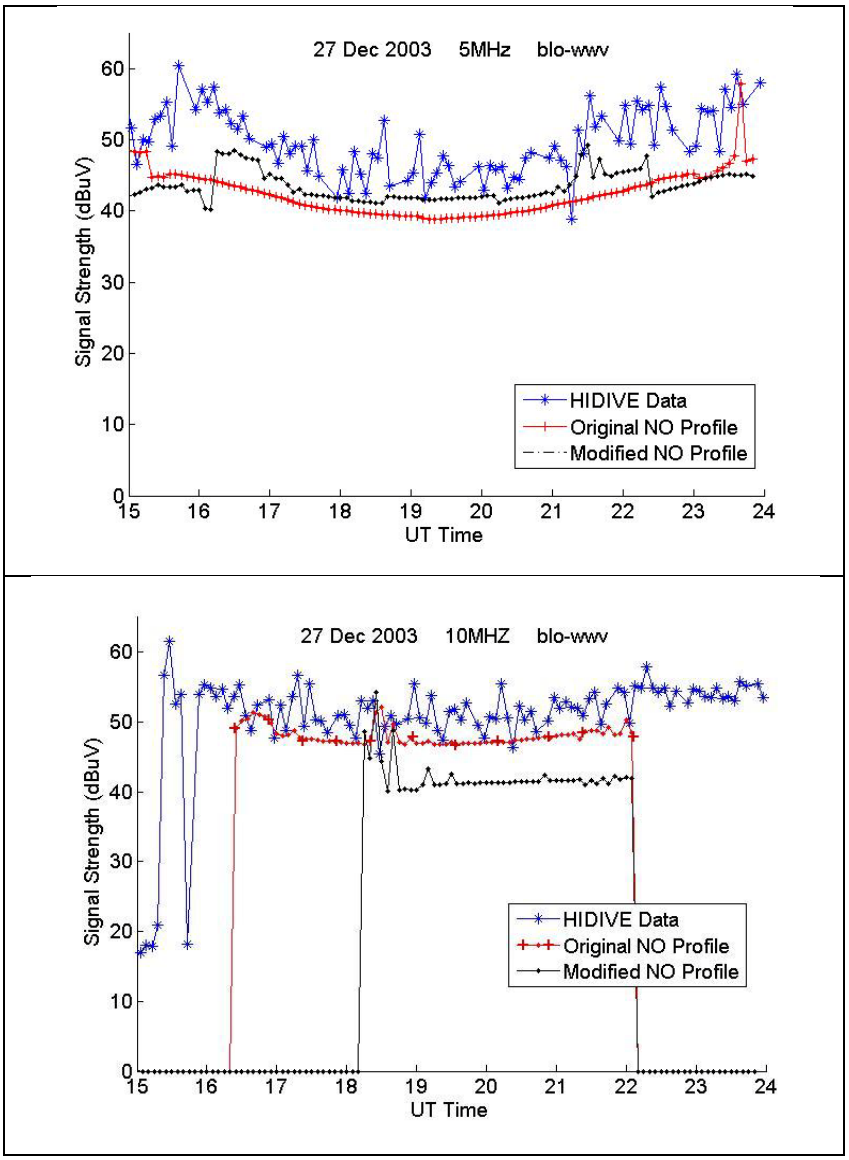

Figure 9.4.3. HIDIVE data for the 5 MHz (top) and 10 MHz blo-wwv (bottom) signals on 27 December 2003 are shown along with the signal strength predictions of the original and modified versions of the AbbyNormal model. The signal strength predictions using the original AbbyNormal version of producing NO profiles, which is given in equation 9.2.1, are shown by the black dotted line in the above panels. The predictions of the version which uses equation 9.4.2 to define AbbyNormal NO profiles are shown by the red line marked with crosses.

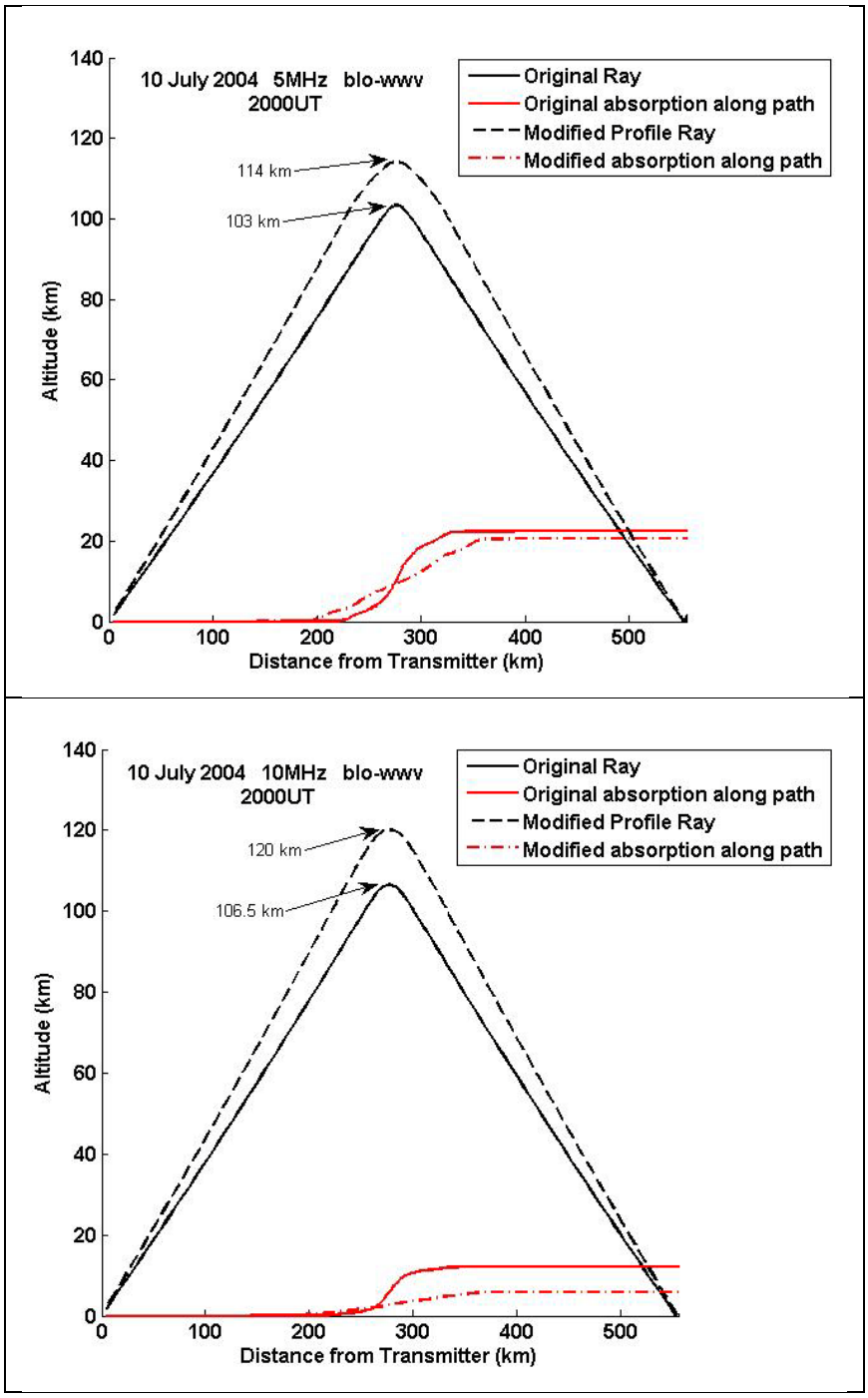

Figure 9.4.4. AbbyNormal predicted propagation paths for the 5 MHz (top) and 10 MHz (bottom) blo-wwv signals on 10 July 2004 show the originally defined NO profile, given in equation 9.2.1, results in lower reflection altitudes and more total absorption than the model using the modified scaling of atomic oxygen, given in equation 9.4.2.

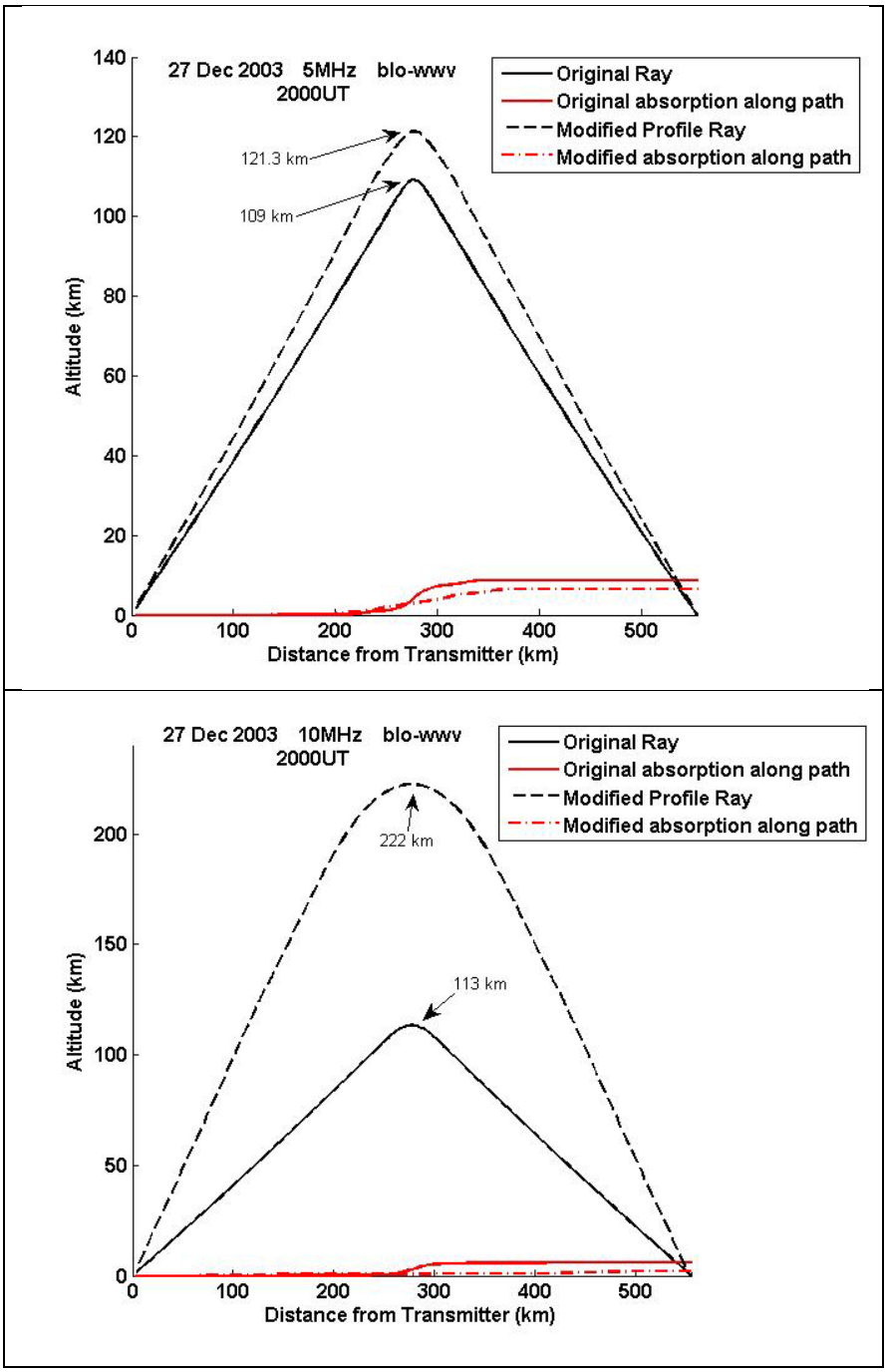

Figure 9.4.5. AbbyNormal predicted propagation paths for the 5 MHz (top) and 10 MHz (bottom) blo-wwv signals on 27 December 2003 show the originally defined NO profile, given in equation 9.2.1, results in lower reflection altitudes and more total absorption than the model using the modified scaling of atomic oxygen, given in equation 9.4.2.

9.4.2 Empirical NO Model Profile.

To further improve AbbyNormal NO profiles, a method for producing NO profiles based on the predictions of the MSR empirical NO model is investigated. Recall from §9.3 the MSR model only produces NO density predictions between the altitudes of 100 km and 150 km. Thus, the MSR model-based NO profile incorporates the original AbbyNormal NO profile given by equation 9.2.1 and the predictions of the MSR model to produce a profile that spans the altitude range of 50 km to 350 km. The MSR model is used to determine NO densities between 100 km and 150 km, and the original AbbyNormal NO profile is used to determine NO densities from 50 km to 90 km. Linear interpolation is then used to smoothly combine the NO profile between 90 km and 100 km. In order to define the NO profile above 150 km and to smoothly transition from the MSR model profile, equation 9.2.1 is scaled so that its value at 150 km is equal to that of the MSR model at 150 km. This scaled version of equation 9.2.1 is then used to define NO above 150 km. The NO profiles based on the MSR model for the dates, 10 July 2004 and 9 September 2000, are shown in Figure 9.4.6 and are good representations of the majority of profiles created using this method. For a comparison to data, HALOE NO observations for 9 September 2000 are shown in the bottom panel of Figure 9.4.6. No SNOE data are available on 9 September, and no satellite NO density observations are available for 10 July 2004 for comparison. Figure 9.4.6 shows the MSR model-based profile is in good agreement with HALOE observations between 85 km and 130 km on 9 September 2000. Recall from §2.2 it is within this altitude range NO is ionized by Lyman-α. Analysis and figures of AbbyNormal predictions using the MSR model-based method for producing NO profiles are presented in §9.5.

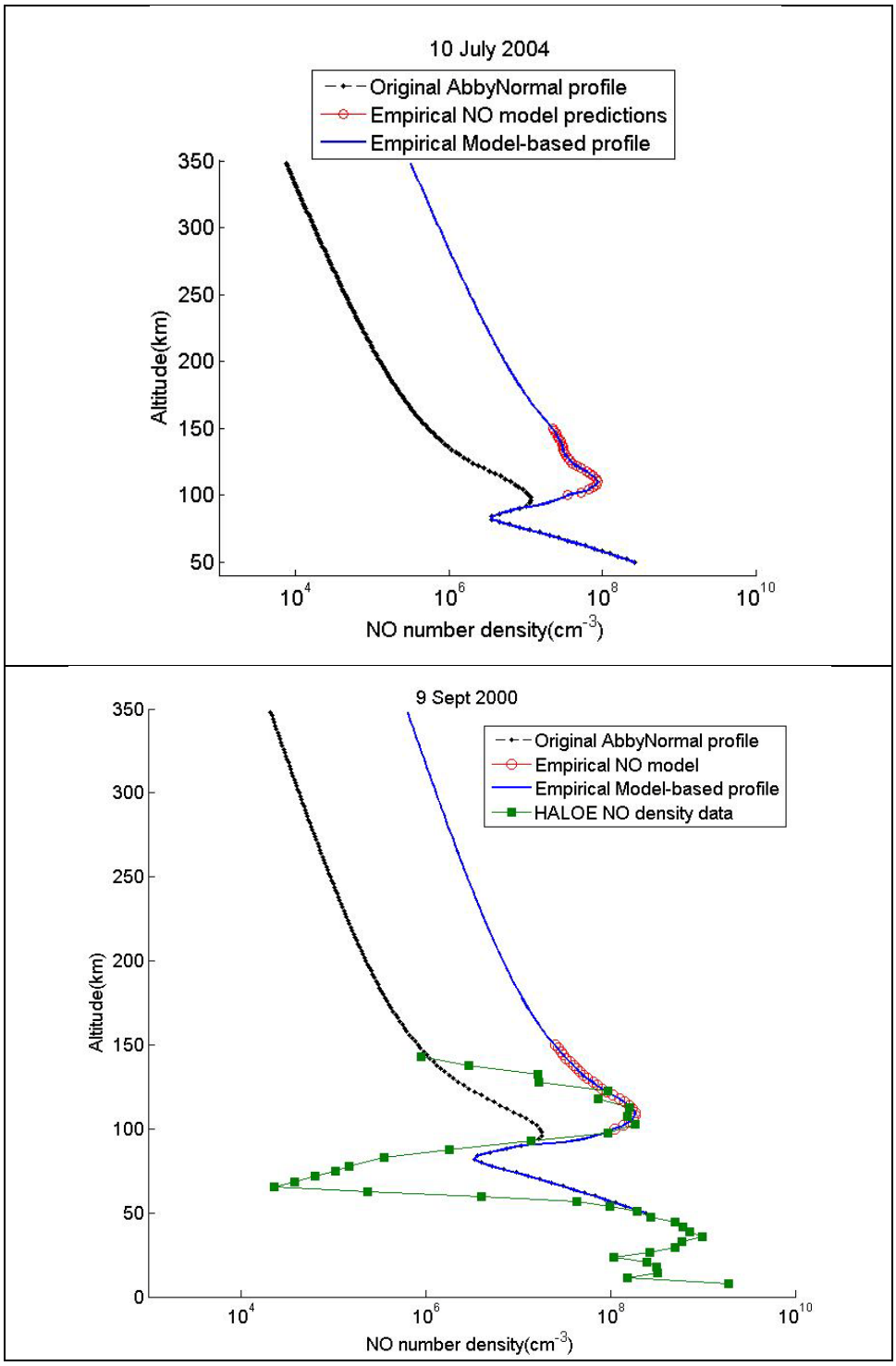

Figure 9.4.6. The NO profiles based on the MSR empirical NO model for the dates, 10 July 2004 (top) and 9 September 2000 (bottom), are shown along with the original AbbyNormal NO profiles

and MSR model predictions. HALOE NO density data are available on 9 Sept 2000 and are shown by green squares for comparison.

9.4.3 HALOE Data Profile.

A version of AbbyNormal which uses HALOE data to define the NO profile is also created in order to compare how AbbyNormal performs when actual NO density data are used versus when the NO profile is modeled. On all dates, the lowest altitude a HALOE NO density measurement is taken at is 50 km. However, the highest altitude for a measurement (h_{max}) on a given date can range from 140 km to 150 km. The lower half of the HALOE-based NO profile is defined as the HALOE data from 50 km to h_{max} interpolated to an altitude stepsize of 2 km, since the AbbyNormal model reads in the NO profile at a 2 km altitude step. Above h_{max} the profile is given by a linear extrapolation of the data points observed at the two highest altitudes, h_{max} and ($h_{\max} - 2km$). AbbyNormal predictions using HALOE data to produce NO profiles are presented and are compared to the results of other AbbyNormal versions in §9.5.

The signal variations of several orders of magnitude present in the HALOE NO profile seen in Figure 4.3.1 are due to aerosols in the instrument line of sight and to limb cloud cover. Since HALOE NO data are obtained using solar occultation, aerosols in the local area and cloud cover can result in erroneously low measurements of NO and any NO densities below $5\times10^{6} cm^{-3}$ "should be treated with caution" and densities above $5\times10^{6} cm^{-3}$ can be used with confidence [*Beaver et al*., 1994]. We can also see from Figure 4.3.1 peak HALOE NO densities between 80 km and 120 km are consistent with other observations and predictions [*Hervig et al.,* 1995]. As will be shown in the following section, it is the peak NO density value between the altitudes of 80 km and 120 km which mostly effect HF absorption and propagation paths. HALOE NO densities below $5\times10^{6} cm^{-3}$ do not significantly affect absorption calculations. A problem with accurately predicting absorption would arise if at the altitudes where HALOE reported densities to be below $5\times10^{6} cm^{-3}$, actual NO densities were significantly greater than the reported peak densities within the D- and E-regions. In this situation, absorption

predictions would be less than those observed. Assuming peak NO densities within the D- and E-regions are adequately captured in the HALOE data, HALOE data can be used here confidently for validation and to produce AbbyNormal NO profiles.

9.5 MSR model-based and SNOE-based AbbyNormal Results

Section 9.1 discusses trends in the original AbbyNormal model's performance in predicting baseline signal strengths for HIDIVE transmissions. These trends led to an investigation of the model's predicted N_e and NO profiles and to the development of two additional versions of the AbbyNormal model. In this section, the signal strength predictions of the three model versions are analyzed with respect to predicted N_e and NO profiles. In each of the following subsections, the signal strength predictions of the three AbbyNormal versions for a specific HIDIVE transmission are reviewed in detail in order to determine the affect of the different methods of defining NO profiles on signal strength predictions and if any improvements were made to the original AbbyNormal model.

Each subsection begins with comparing observed HIDIVE signal strength data for a specific transmission on a given date to the signal strength predictions of the three AbbyNormal versions. Each version's N_e and NO profiles are then examined in order to provide some insight into how the profiles affect signal strength predictions and into whether or not AbbyNormal trends in baseline prediction are caused solely by inaccurate NO profiles.

9.5.1 Predictions for 5 MHz blo-wwv transmission.

This subsection analyzes the results of the three AbbyNormal versions and their signal strength predictions for the 5 MHz blo-wwv transmission. The predictions for eleven dates in January 2004 along with HIDIVE and GOES data are shown in Appendix B. These eleven dates are chosen for analysis due to the availability of HALOE NO data. From the figures in Appendix B, we see baseline signal strengths predicted by the original AbbyNormal version and the MSR model-based version do not vary from day to day, and only the HALOE-based version predictions show any significant variation in baseline signal strengths from one day to the next. This can also be seen in Figures 9.5.1 and 9.5.2 in which the 5 MHz blo-wwv transmission HIDIVE data and GOES data are

shown along with the signal strength predictions of the three AbbyNormal versions for 15 January 2004 and 27 January 2004.

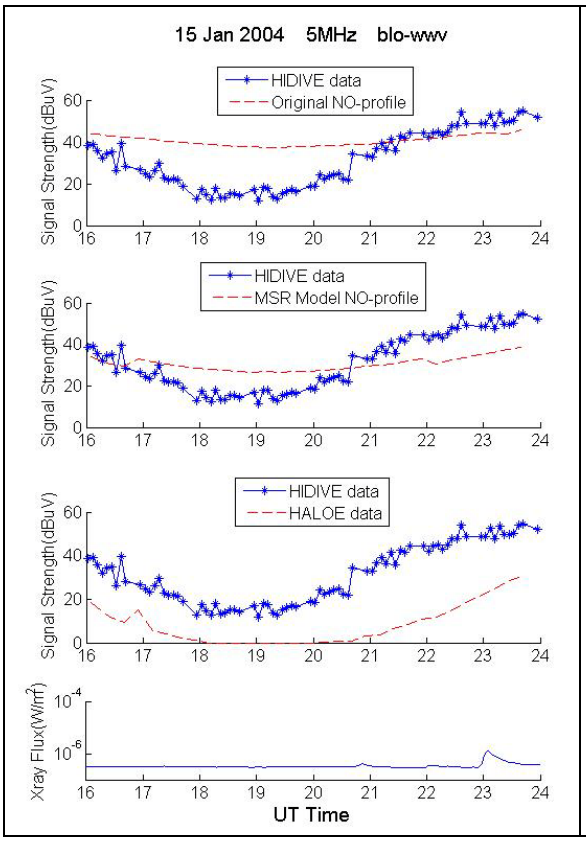

Figure 9.5.1. HIDIVE signal strength data for 15 January 2004 for the 5 MHz blo-wwv transmission are shown along with signal strength predictions of the original AbbyNormal version (top panel), the MSR model-based version (second to top panel), and the HALOE-based version (second to bottom panel), and GOES data (bottom panel).

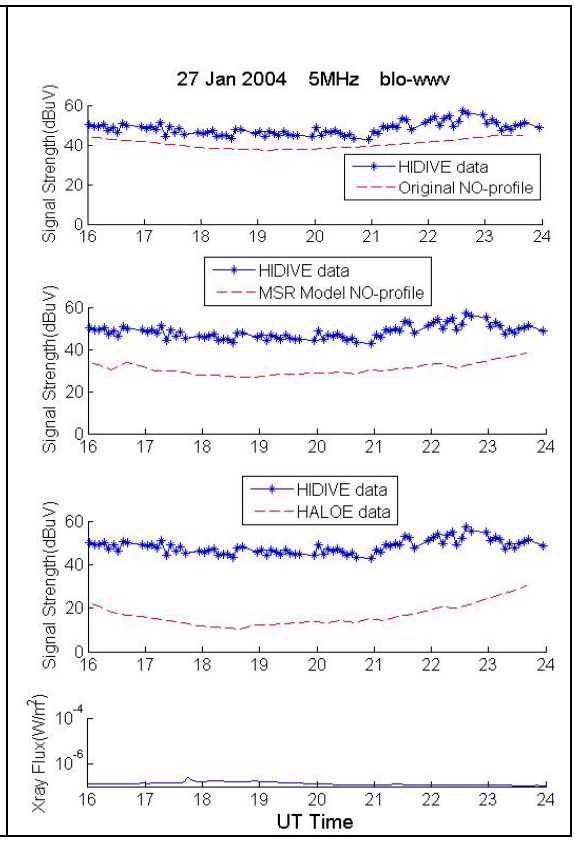

Figure 9.5.2. HIDIVE signal strength data for 27 January 2004 for the 5 MHz blo-wwv transmission are shown along with signal strength predictions of the original AbbyNormal version (top panel), the MSR model-based version (second to top panel), and the HALOE-based version (second to bottom panel), and GOES data (bottom panel).

This section focuses on understanding how the various methods of defining AbbyNormal NO profiles affect baseline signal strength predictions for the 5 MHz blo-wwv transmission by analyzing in detail how NO profiles affect N_e and $N_e\nu$ profiles. N_e and $N_e\nu$ profiles are of interest because N_e profiles determine refraction of an HF wave

and available propagation paths and $N_e\nu$ profiles determine loss of signal strength, as discussed in §2.4 and §2.5. Analysis of the results for 15 January 2004 provides a good representation of how the three methods of producing NO profiles influence signal strength predictions.

The HASEL ray tracing program within AbbyNormal, discussed in §3.4, calculates the raypaths available to an HF signal and the loss suffered by the signal based on the ionosphere predicted by AbbyNormal. On 15 January 2004, HASEL predicts several propagation paths available to the 5 MHz blo-wwv transmission for all three AbbyNormal versions; however, HASEL does not predict the same set of paths for each AbbyNormal version. It does predict a single-hop E-mode path as a primary path for all versions. A primary path is one that contributes significantly to a transmission's received signal strength. Thus, analysis of the single-hop E-mode is sufficient to provide insight into how the three versions of producing NO profiles influence baseline signal strength predictions. The single-hop E-mode path shared by all versions is shown in the top panel of Figure 9.5.3. Also shown in Figure 9.5.3 are N_e along the raypath (second panel from top), total absorption suffered by the wave as it propagates (second panel from bottom), and $N_e\nu$ along the raypath (bottom panel).

The top panel of Figure 9.5.3 shows the single-hop E-mode propagation paths resulting from the original AbbyNormal version and the MSR model-based version are very similar with both having an elevation angle (ϕ) of 21°, while the HALOE-base version produces a path of $\phi = 33°$. The reason for the differing propagation paths is the various N_e profiles produced by the AbbyNormal versions, shown on the left in Figure 9.5.4. As seen in the top panel of Figure 9.5.3, the paths predicted by the original and MSR model-based versions are refracted back towards earth above 100 km and reach a maximum altitude of approximately 110 km. Compared to the HALOE-based path, the original and MSR model-based paths are refracted towards earth over a shorted ground distance. This is due to the gradients of the N_e profiles. The original and MSR model-based N_e profiles have a steeper gradient than the HALOE-based profile above 100 km where N_e values for all three versions are large enough to refract the 5 MHz wave. Thus, the steeper N_e gradient leads to different propagation paths and elevation angles.

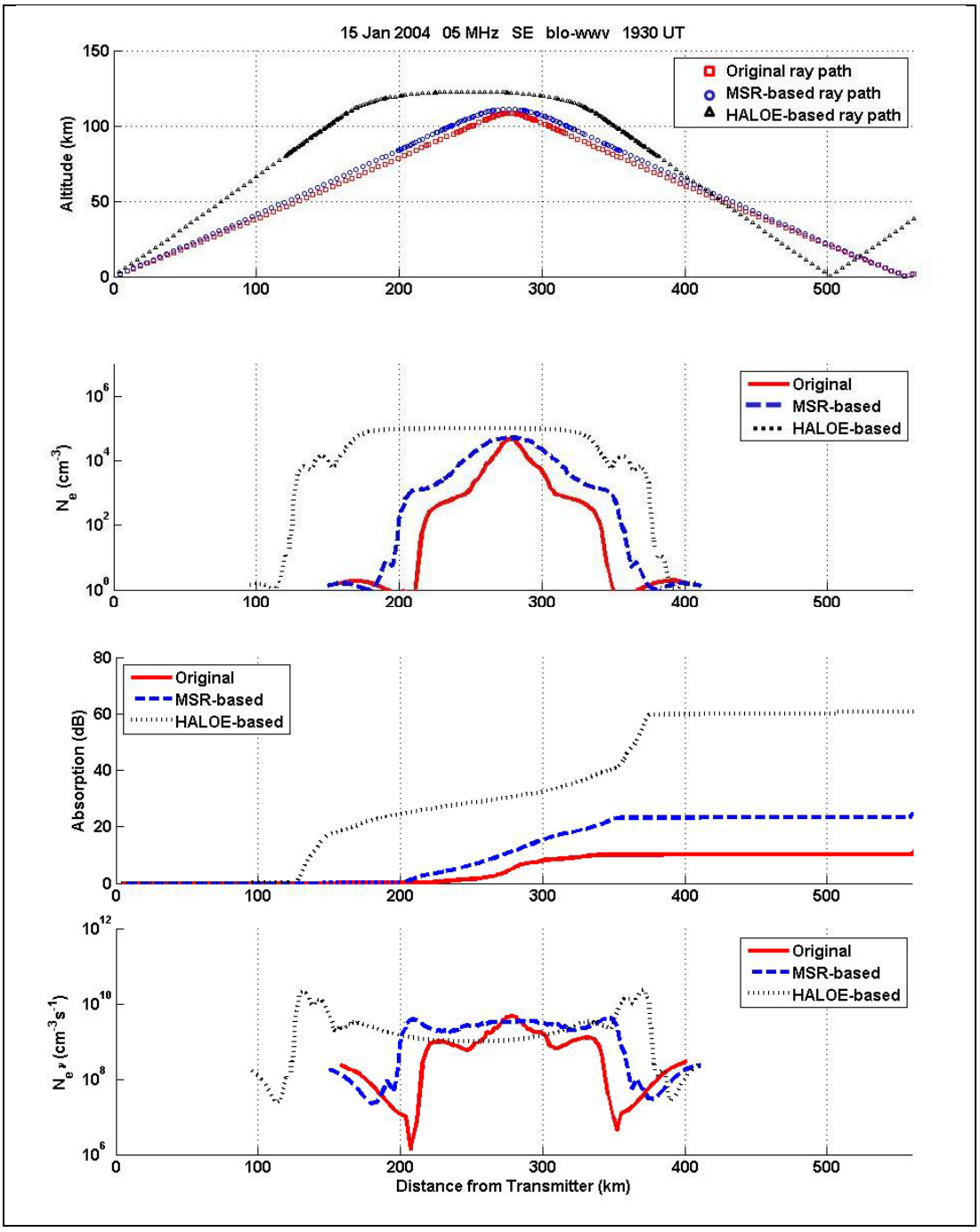

Figure 9.5.3. Dominant propagation paths predicted by HASEL for the 5 MHz blo-wwv transmission on 15 January 2004 at 19:30 UT are shown in the top panel. Also shown are the predictions of the three AbbyNormal versions for N_e along the raypath (second panel from top), total absorption suffered by the wave as it propagates (second panel from bottom), and $N_e\nu$ along the raypath (bottom panel).

The different propagation paths do not, however, explain the variance in baseline signal strengths between the three AbbyNormal versions seen in Figure 9.5.1.

The variance in baseline signal strengths can best be explained by examining the $N_e\nu$ values along the raypath, shown on the right in Figure 9.5.4 and in the bottom panel of Figure 9.5.3. Loss of signal strength is shown in §2.4 to be directly proportional to $N_e\nu$, and from the right panel of Figure 9.5.4, we see the HALOE-based $N_e\nu$ values are more than an order of magnitude greater than the original and MSR model-based values in the altitude range where significant non-deviative absorption occurs, between 80 km and 100 km. As seen in the panel second from the bottom in Figure 9.5.3, it is within this altitude range the majority of absorption occurs for the 5 MHz blo-wwv transmission. The $N_e\nu$ values predicted by the three AbbyNormal versions are direct results of their NO profiles, which are shown in Figure 9.5.5.

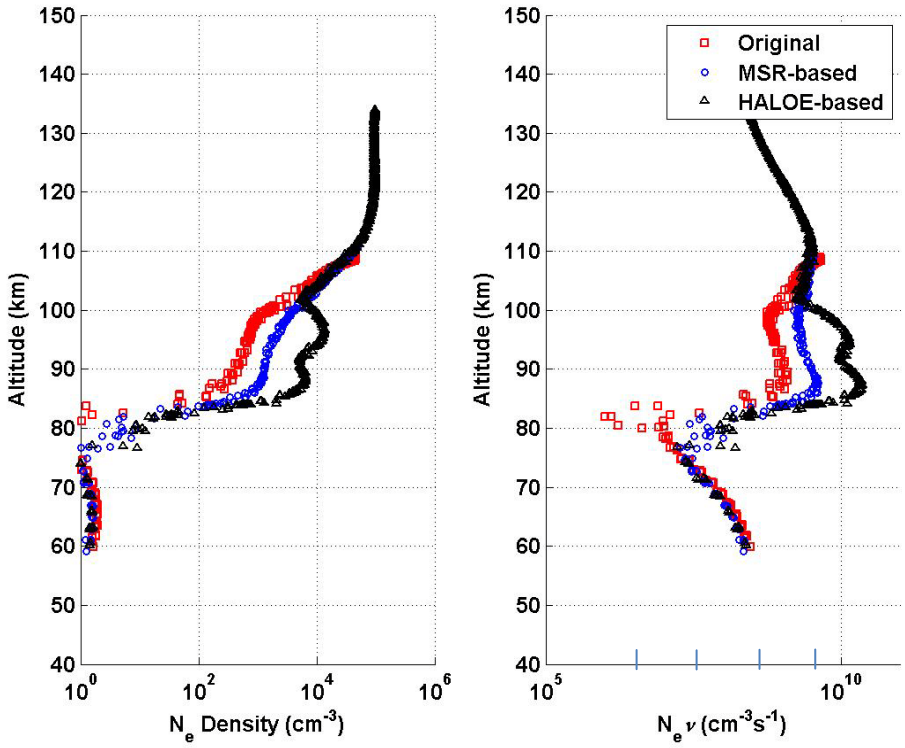

Figure 9.5.4. N_e along the raypath (left) and $N_e\nu$ along the raypath (right) predicted by the three AbbyNormal versions on 15 January 2004 at 19:30 UT.

On 15 January HALOE NO observations between 80 km and 100 km are at times more than an order of magnitude greater than the NO densities predicted by the original and MSR model-based versions. Thus, for the 5 MHz blo-wwv transmission, the greatest impact the various methods of producing NO profiles have on baseline signal strengths is determining the amount of non-deviative absorption the signal will suffer. The algorithm employed by the original AbbyNormal model to produce NO profiles provides for profiles that are fairly constant from day to day; thus, we see original AbbyNormal baseline signal strengths that are also fairly constant one day to another. However, as discussed in §2.2.4, NO densities can fluctuate daily by several orders of magnitude.

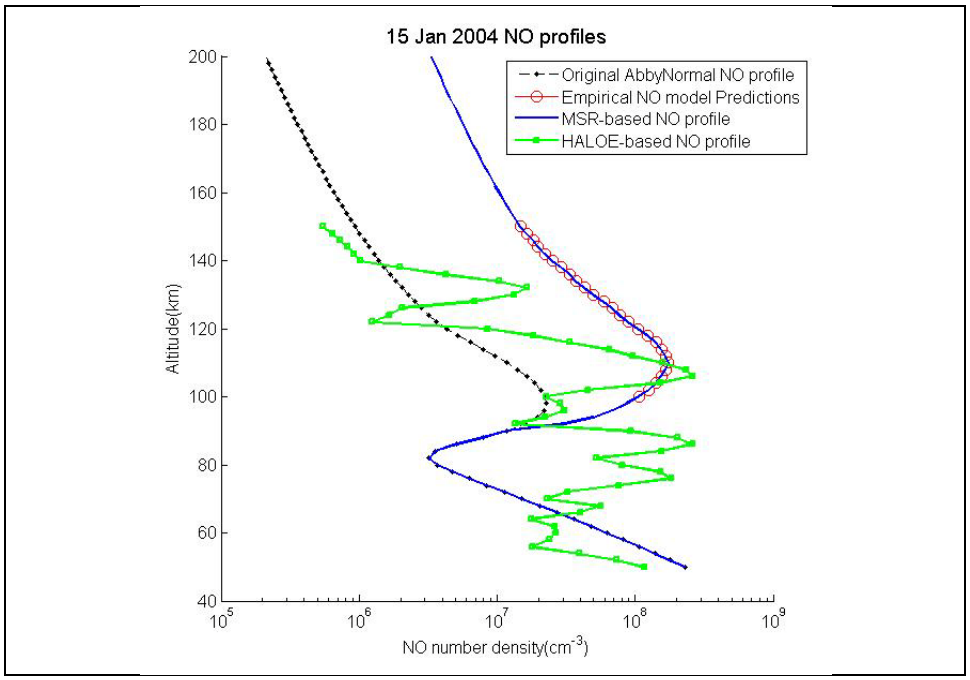

Figure 9.5.5. NO profiles produced by the original version of AbbyNormal, the MSR-based version, and the HALOE-based version for 15 January 2004.

Thus, HALOE-based NO profiles allow for realistic variations in baseline signal strengths for the 5 MHz blo-wwv transmission. As seen from the figures in Appendix B, however, more work is needed to determine why the HALOE-based AbbyNormal version

under-predicts the baseline on some dates and if the cause is due to a poor representation of NO density along the raypath. As is discussed in §9.6, local NO enhancements at times may only measure tens of kilometers horizontally and HALOE observations, which are limited temporally and spatially, may not adequately describe NO densities along the raypath.

9.5.2 Predictions for 10 MHz blo-wwv transmission.

The last section shows NO profiles greatly influence the predicted $N_e v$ values and the amount of non-deviative absorption the 5 MHz blo-wwv signal is predicted to suffer. In this section, the same is shown for NO profiles and the 10 MHz blo-wwv transmission; however, this section also shows NO profiles influence the types of propagation paths AbbyNormal predicts to be available to the 10 MHz blo-wwv transmission. This can be seen in Figure 9.5.6 and the figures in Appendix C. The figures in Appendix C show signal strength predictions of the three AbbyNormal versions for the 10 MHz blo-wwv transmission for eleven dates in January 2004 along with HIDIVE and GOES data. Figure 9.5.6 shows the HIDIVE signal strength data for the 10 MHz blo-wwv transmission on 15 January 2004 along with signal strength predictions of the original AbbyNormal version (top panel), the MSR model-based version (second to top panel), the HALOE-based version (second to bottom panel), and GOES data (bottom panel). The HIDIVE data shown in the figures of Appendix C show many instances in which the 10 MHz blo-wwv signal is not received, and the three AbbyNormal versions differ in when they predict the signal to be received, which can be seen in Figure 9.5.6. The differences in signal availability and in baseline signal strengths are shown in this section to be a direct result of the different NO profiles predicted by the three model versions, and detailed analysis of model results for 15 January provides a good representation of how the NO profiles of the three versions influence the predictions for the 10 MHz blo-wwv transmission.

Both the HALOE-based and MSR model-based AbbyNormal versions predict no 10 MHz blo-wwv signal to be received prior to 19:00 UT on 15 January, while the original AbbyNormal version does. The reason for this can be seen by examining the N_e values predicted by the three model versions in Figure 9.5.7.

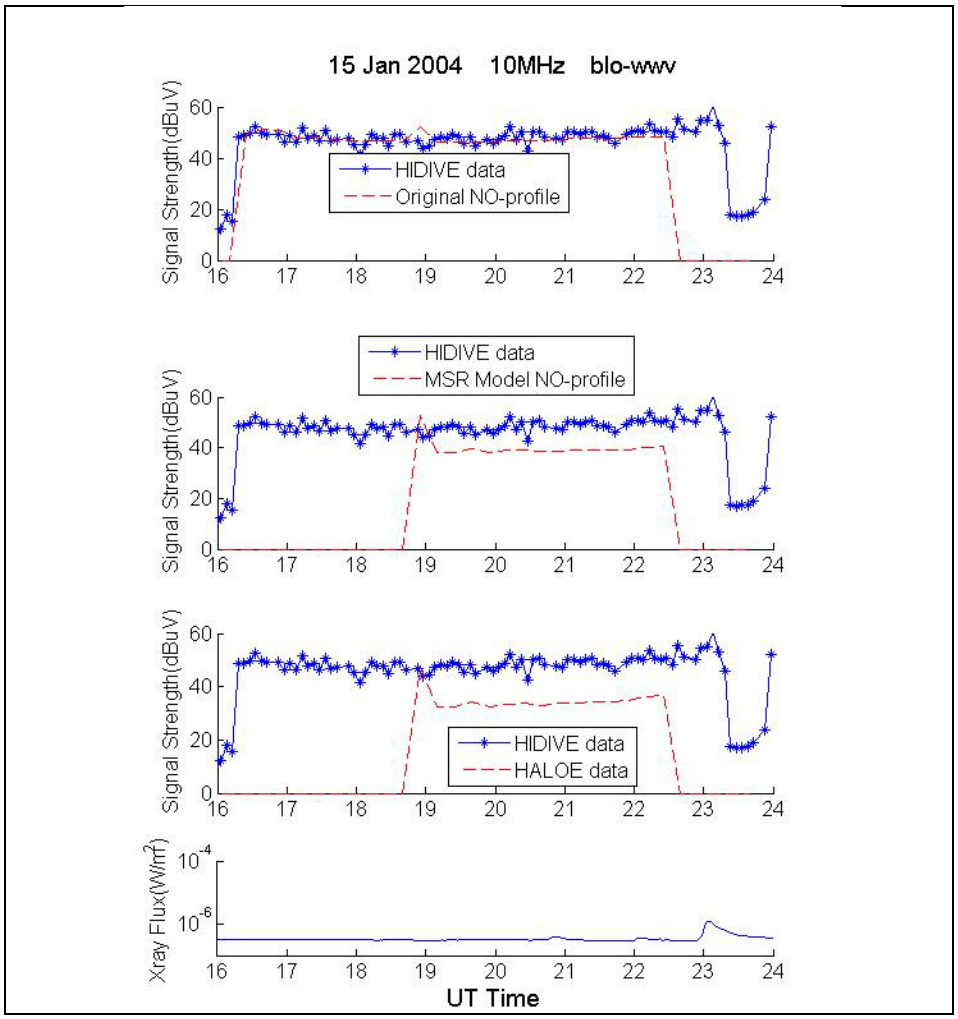

Figure 9.5.6. HIDIVE signal strength data for 15 January 2004 for the 10 MHz blo-wwv transmission are shown along with signal strength predictions of the original AbbyNormal version (top panel), the MSR model-based version (second to top panel), the HALOE-based version (second to bottom panel), and GOES data (bottom panel).

Figure 9.5.7 shows the N_e values along the raypath predicted by the three AbbyNormal versions (left) and the resulting $N_e v$ values along the raypath (right) on 15 January 2004 at 19:00 UT. The local N_e peak at 120 km in the original AbbyNormal N_e values is a result of the method by which the original model defines the local ionosphere. As discussed in §3.4, AbbyNormal merges the results of two ionospheric models to produce N_e profiles. For the altitude range of 50 km to 110 km, AbbyNormal uses the DDDR model to define the ionosphere, and above 130 km, the IRI model is used to define the

ionosphere. Model outputs are then blended together to define the ionosphere between 110 km and 130 km, which results in the nonphysical N_e peak at 120 km.

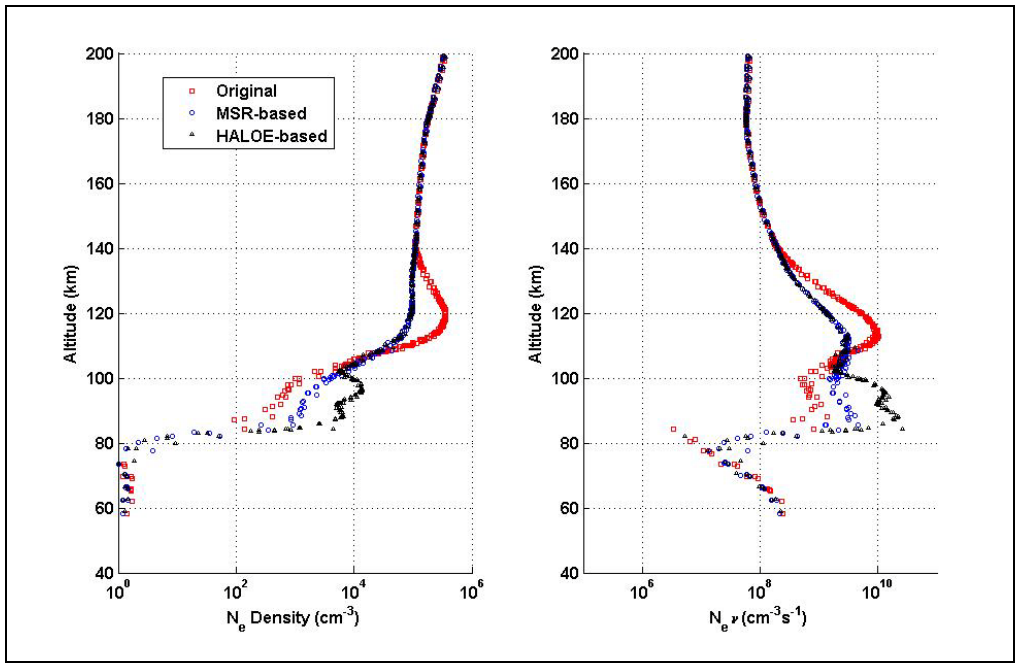

Figure 9.5.7. N_e values along the raypath predicted by the three AbbyNormal versions (left) and the resulting $N_e\nu$ values along the raypath (right) at 19:00 UT on 15 January 2004.

This nonphysical peak allows for the original AbbyNormal model to predict an E-mode propagation path to be available earlier in the day which the other two model versions do not predict. Prior to 19:00 UT, the N_e densities predicted by the HALOE-based and MSR-based versions are not large enough to refract to 10 MHz signal back towards earth and the models predict the signal to penetrate the ionosphere. However, the local N_e peak at 120 km in the original AbbyNormal profile provides densities large enough to refract the signal within the E-region; thus, the original model predicts an E-mode path and an F-mode path to be available prior to 19:00 UT and, thus, predicts a signal to be received. After 19:00 UT, the local N_e peak at 120 km also is responsible for two additional available propagation paths for the original version that are not supported by the other two AbbyNormal versions, leading to differences in baseline signal

strengths. Consequently, when HIDIVE data for the 10 MHz blo-wwv transmission shows a sudden loss in signal strength, such between 23:00 UT and 24:00 UT in Figure 9.5.6, only an E-mode path is being received while the F-mode paths are penetrating the ionosphere. This suggests the F-mode paths are refracted back towards earth near the F2-peak. As discussed in §2.1.1, the F2-peak located at approximately 250 km is the location of maximum electron density within the ionosphere. Above the F2-peak N_e begins to decline with altitude; thus, if a wave is not refracted back towards earth by the F2-peak, it will penetrate the ionosphere and will not be received.

After 19:00 UT, HASEL predicts only one available propagation path for the HALOE-based and MSR-based versions and predicts three available paths for the original version. Table 9.5.1 lists the available propagation paths predicted for each AbbyNormal version. The availability of two additional propagation paths for the original AbbyNormal versions partially explains the higher baseline signal strength predictions for the 10 MHz blo-wwv transmission. Another reason for the higher baseline can be found by examining the $N_e v$ values along the raypath predicted by the three AbbyNormal versions, shown on the right in Figure 9.5.7.

Table 9.5.1. Available propagation paths predicted for the 10 MHz blo-wwv transmission on 15 January 2004 for the three versions of AbbyNormal.

AbbyNormal Version	Propagation paths available after 19:00 UT
Original	E-mode $\phi = 22°$ F-mode $\phi = 31°$ F-mode $\phi = 46°$
MSR model-based	F-mode $\phi = 45°$
HALOE-based	F-mode $\phi = 45°$

Once again HALOE-based $N_e\nu$ values are more than an order of magnitude greater than those of the original and MSR model-based versions between 80 km and 100 km where significant non-deviative absorption occurs, and as seen in the second to bottom panel of Figure 9.5.6, $N_e\nu$ values between 80 km and 100 km for the three AbbyNormal versions determine the amounts of absorption the 10 MHz blo-wwv signal will suffer. The original AbbyNormal version predicts the highest baseline signal strength because it predicts the lowest $N_e\nu$ values between 80 km and 100 km, while the HALOE-based version predicts the lowest baseline signal strengths because it predicts the highest $N_e\nu$ values and signal absorption between 80 km and 100 km. The predicted $N_e\nu$ values along the raypath and absorption are a direct result of the NO profiles produced by the three AbbyNormal versions on 15 January 2004, shown in Figure 9.5.5. As mentioned previously, HALOE NO observations on 15 January 2004 between 80 km and 100 km are at times more than an order of magnitude greater than the NO densities predicted by the original and MSR model-based versions. Thus, for the 10 MHz blo-wwv transmission, the greatest impacts the various methods of producing NO profiles have on baseline signal strengths are determining $N_e\nu$ values and the amount of non-deviative absorption the signal will suffer and determining available propagation paths.

9.5.3 Predictions for 5 MHz kf-wwv transmission.

Unlike the 10 MHz blo-wwv signal, the signal strength of the 5 MHz kf-wwv transmission is rarely above the noise, as can be seen in the figures of Appendix D. This is due to substantial absorption of the signal along the few E-mode propagation paths available to the 5 MHz kf-wwv transmission. Although the 5 MHz kf-wwv transmission is rarely available, the original AbbyNormal model on most dates predicts a strong signal to be received. This unrealistic baseline signal strength prediction, which is seen in Figure 9.5.8 and the figures in Appendix D, is due to the original AbbyNormal model's under-prediction of NO between the altitudes of 80 km and 100 km, which in turn leads to an under-prediction of signal absorption.

Figure 9.5.8 shows the 5 MHz kf-wwv HIDIVE data on 13 January 2004 along with the signal strength predictions of the three AbbyNormal versions. The results for 13 January 2004 are chosen for analysis here since this is one of the few dates on which

HALOE data are available, the 5 MHz kf-wwv signal is above the noise, and the signal strength predictions of the three AbbyNormal versions are good representations of their predicted baselines.

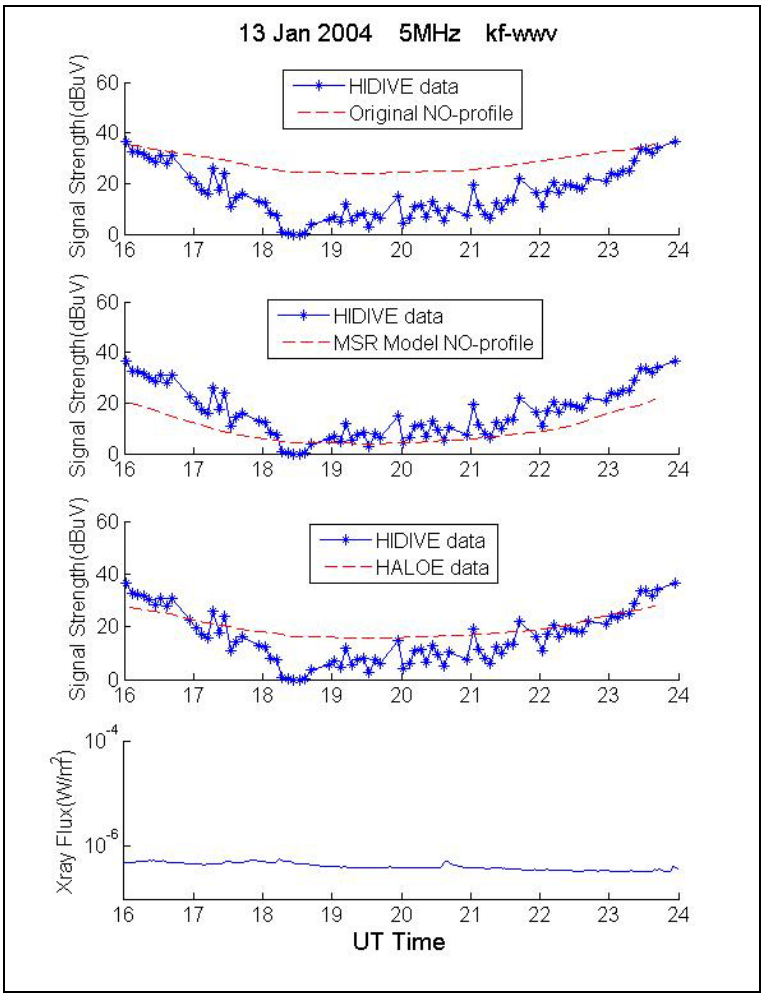

Figure 9.5.8. HIDIVE signal strength data for 13 January 2004 for the 5 MHz kf-wwv signal are shown along with signal strength predictions of the original AbbyNormal (top panel), the MSR model-based (second to top panel), and the HALOE-based versions (second to bottom panel), and GOES data (bottom panel).

The figures in Appendix D show there is little to no variation in the original AbbyNormal baselines and the MSR model-based baselines from day to day even though NO densities can vary by orders of magnitude from one day to another and the availability of the 5 MHz kf-wwv signal varies. Appendix D also shows HALOE-based baseline predictions

do vary from day to day, although the HALOE-based version under-predicts signal strength at times. The underlying causes for these trends in baseline predictions are the NO profiles produced by the three AbbyNormal versions shown in Figure 9.5.9.

Figure 9.5.9 shows the NO profiles produced by the three AbbyNormal versions for 13 January 2004. From these NO profiles, N_e and $N_e v$ values along the raypath are produced, which are shown in Figure 9.5.10. From the given N_e values, the HASEL raytracing code within AbbyNormal predicts propagation paths available to the 5 MHz kf-wwv transmission, and for most dates, HASEL predicts a signal-hop E-mode to be the dominant path for the 5 MHz kf-wwv transmission. Details of the dominant E-mode path are shown in Figure 9.5.11.

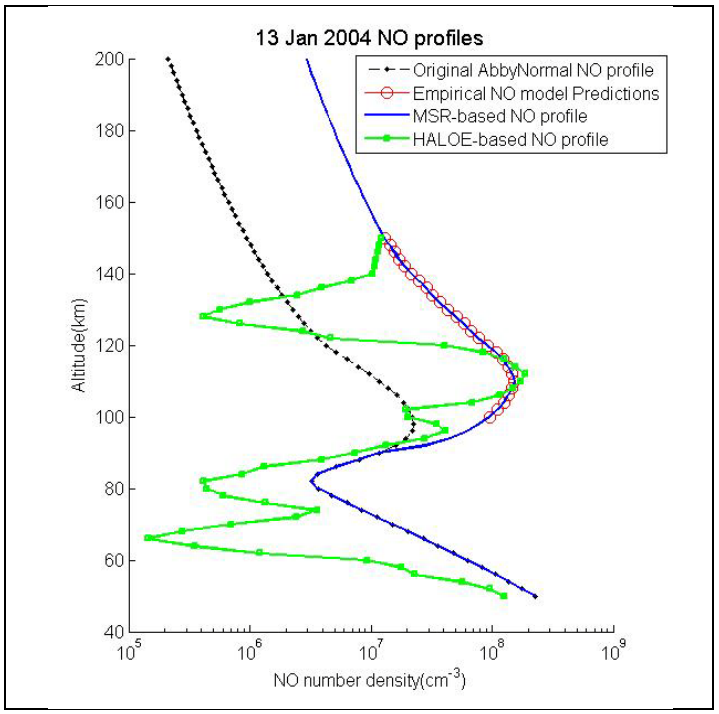

Figure 9.5.9. The NO profiles produced by the three AbbyNormal versions for 13 January 2004.

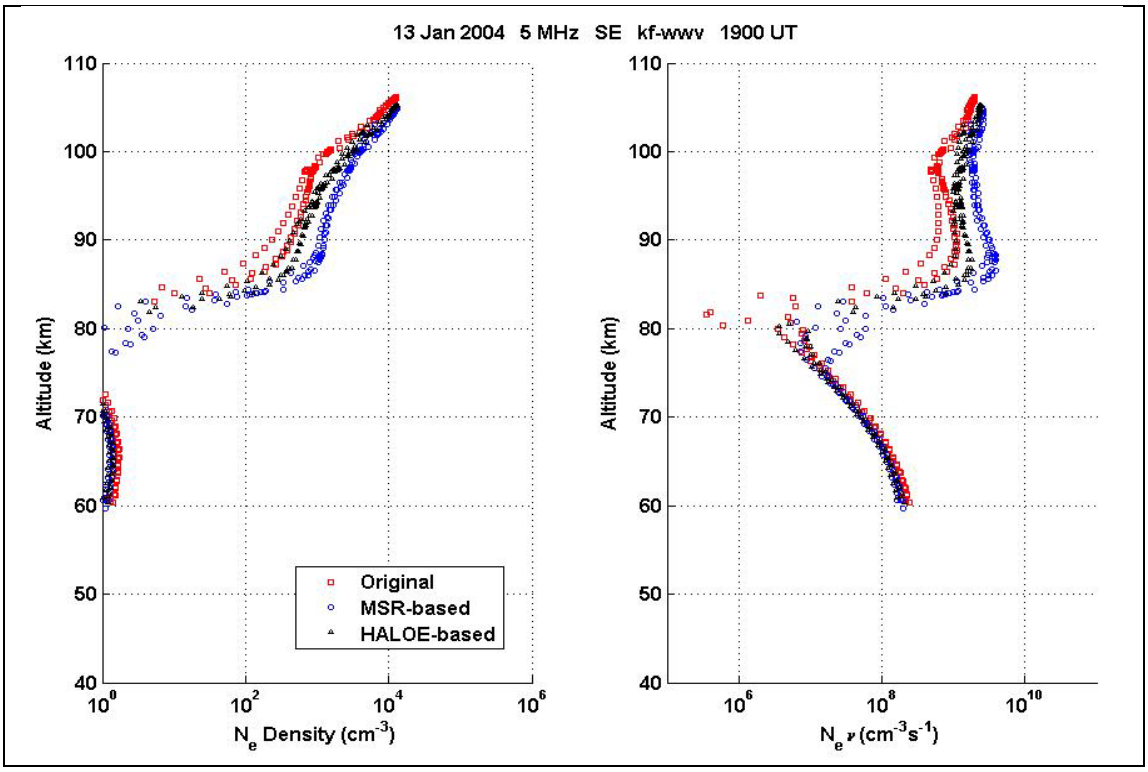

Figure 9.5.10. N_e and $N_e\nu$ values along the raypath predicted by the three AbbyNormal versions for 13 January 2004.

All three versions predict a similar dominant propagation path as a result of their N_e profiles which have comparable gradients and values above 100 km. Above 100 km, the three profiles obtain values of N_e capable of refracting the radio wave back towards earth. However, the three N_e profiles differ significantly between the altitudes of 80 km and 100 km where the majority of signal absorption occurs. The differences are a direct result of the NO profiles produced by the versions, and as seen in Figure 9.5.9, the MSR model-based NO values between 80 km and 100 km are at times an order of magnitude greater than the values of the original AbbyNormal version and several times those of the HALOE-based version. These disparities are reflected in the $N_e\nu$ values between 80 km and 100 km, which explains the differences in predicted signal absorption and the resulting baseline signal strengths.

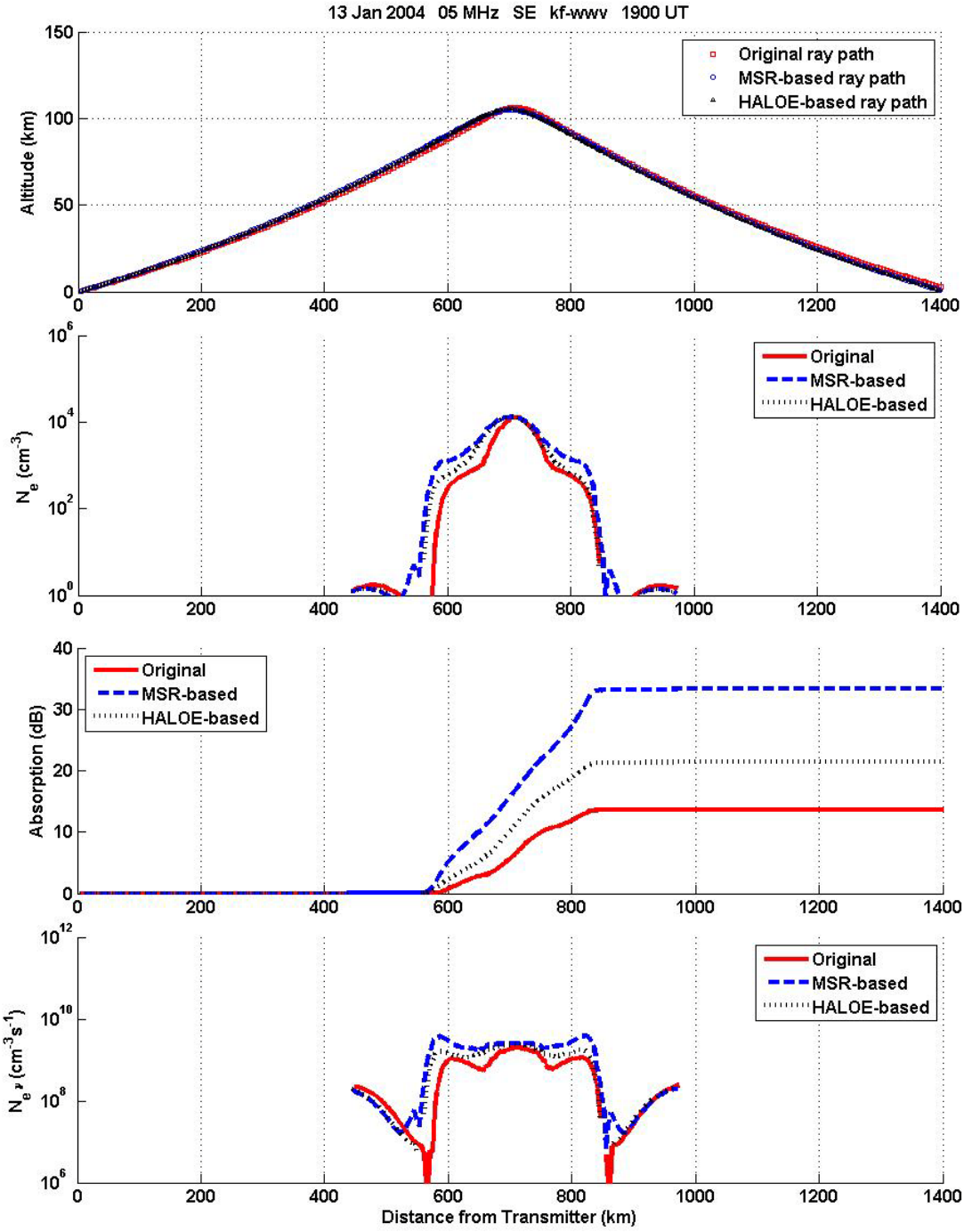

Figure 9.5.11. Dominant propagation paths predicted by HASEL for the 5 MHz kf-wwv transmission on 13 January 2004 at 19:00 UT are shown in the top panel. Also shown are the predictions of the three AbbyNormal versions of N_e along the raypath (second panel from top), total absorption suffered by the wave as it propagates (second panel from bottom), and $N_e v$ along the raypath (bottom panel).

Between 80 km and 100 km MSR-based $N_e\nu$ values are an order of magnitude greater than the values of the original AbbyNormal version and several times those of the HALOE-based version, leading to the differences in predicted signal absorption, shown in the second to last panel of Figure 9.5.11, and the differences in the signal baselines in Figure 9.5.8. Although MSR model-based NO values are only a few times that of the HALOE-based values between 80 km and 100 km, significant differences in predicted signal absorption arise due to the low signal frequency of 5 MHz and the low signal elevation angle of 6°. The low elevation angle means the wave spends a significant portion of its path within the region of maximum absorption, and a low signal frequency means the wave is more susceptible to absorption given the frequency dependence of wave absorption discussed in sections 2.5 and 6.4.

Thus, for the 5 MHz kf-wwv transmission, the original AbbyNormal model's over-prediction of signal strength baselines is due to its unrealistic NO profile which is consistently too low within the altitude range of maximum signal absorption. Given the dominant path for the 5 MHz kf-wwv transmission refracts below 110 km, as shown in Figure 9.5.11, the MSR model-based and HALOE-based versions are better able to predict baseline signal strengths since they produce more realistic NO profiles between 80 km and 110 km where the majority of signal absorption and refraction of the wave occur.

9.5.4 Predictions for 10 MHz kf-wwv transmission.

Of the five HIDIVE transmissions reviewed in §9.5, the original AbbyNormal model performs best at predicting baseline signal strengths for the 10 MHz kf-wwv transmission. Interestingly, altering the method by which AbbyNormal produces NO profiles did not noticeably alter baseline predictions; however, changes to the NO profile do result in significantly different sets of predicted available propagation paths for the 10 MHz kf-wwv transmission. The figures in Appendix E show HIDIVE and GOES data and the signal strength predictions of the three AbbyNormal model versions for eleven dates in January 2004, and Figure 9.5.12 shows the data for 13 January 2004, which is analyzed here in detail in order to see how the various methods of producing NO profiles affect AbbyNormal predictions.

From the figures in Appendix E, one can see all three model versions predict baseline signal strengths well. Figure 9.5.12 also shows adequate baseline predictions even though the NO profiles for the three versions on 13 January 2004, which are shown again in Figure 9.5.13, are significantly different. As is the case for the 10 MHz blo-wwv transmission discussed in §9.5.2, the dissimilarities between the three NO profiles lead to the AbbyNormal versions predicting different sets of available propagation paths for the 10 MHz kf-wwv transmission. Table 9.5.2 lists the available paths predicted by each AbbyNormal version along with the elevation angle of the path and the total absorption along each path.

Table 9.5.2. The available propagation paths predicted by the AbbyNormal versions at 17:45 UT on 13 January 2004.

AbbyNormal Version	Ray Path Type	ϕ (deg)	Total loss (dB)
Original	Single-hop E-mode	6	4
	Double-hop E-mode	17	8
	Double-hop F2-mode	39	9
MSR model-based	Single-hop E-mode	7	10
	Single-hop F1-mode	10	11
	Single-hop F2-mode	17	7
	Double-hop F2-mode	38	7
HALOE-based	Single-hop E-mode	7	7
	Single-hop F1-mode	10	9
	Single-hop F2-mode	17	5
	Double-hop F2-mode	38	5

Even though the original AbbyNormal version predicts only three available paths while the other two versions predict four, the original version predicts similar baseline signal strengths due to the amount of absorption predicted for each path. The cause for the disparity among the sets of predicted available paths can be seen in Figure 9.5.14, which shows the N_e and $N_e\nu$ values along the arypath predicted by each AbbyNormal

version at 17:45 UT on 13 January 2004. The figure also shows the local peak at 120 km within the original AbbyNormal N_e profile.

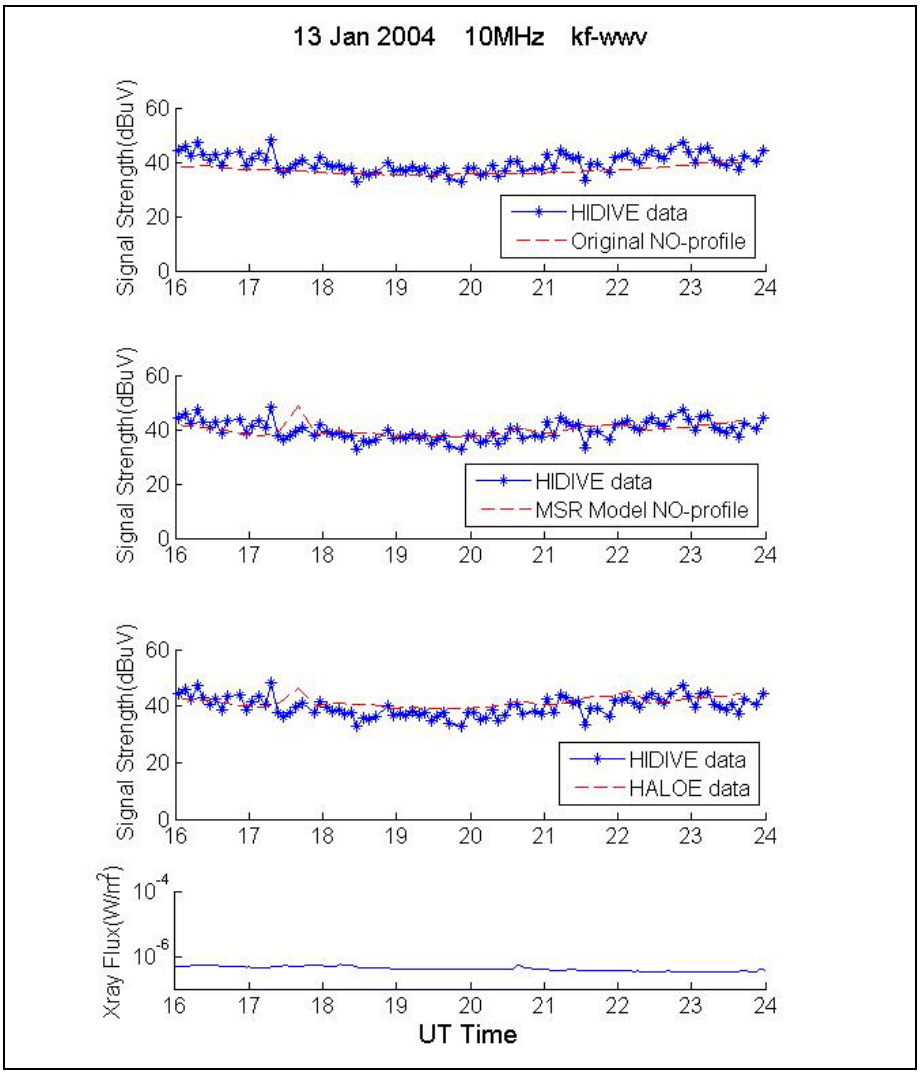

Figure 9.5.12. HIDIVE signal strength data are shown for 13 January 2004 for the 10 MHz kf-wwv transmission along with signal strength predictions of the original AbbyNormal (top panel), the MSR model-based (second to top panel), and the HALOE-based models (second to bottom panel), and GOES data (bottom panel).

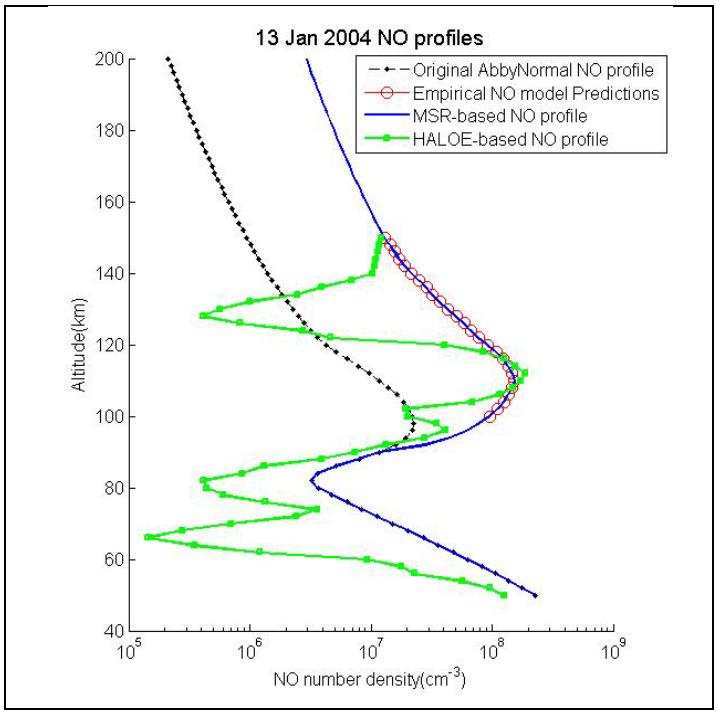

Figure 9.5.13. The NO profiles produced by the three AbbyNormal versions for 13 January 2004.

As discussed in §9.5.2, the local peak at 120 km in the original AbbyNormal N_e profile is due to the method by which the original AbbyNormal version builds the ionosphere by blending together the IRI and DDDR ionospheric models between the altitudes of 110 km and 130 km. A result of the local peak at 120 km is the original version predicts N_e values capable of refracting the 10 MHz kf-wwv wave back towards earth at a lower altitude than the other versions. This can be seen in the top panel of Figure 9.5.15 which shows the single-hop E-mode paths predicted by the three AbbyNormal versions. Also contributing to the different sets of predicted paths is the gradient of the original N_e profile between 100 km and 120 km. At these altitudes the original version's gradient is greater than the those of the HALOE-based and MSR model-based profiles, which means the original AbbyNormal model predicts waves to be refracted back towards earth over a shorter ground distance than the other model versions. This can also be seen in Figure 9.5.15.

There are two paths which are predicted by all three AbbyNormal versions to be available to the 10 MHz kf-wwv transmission. One is the E-mode path shown in Figure

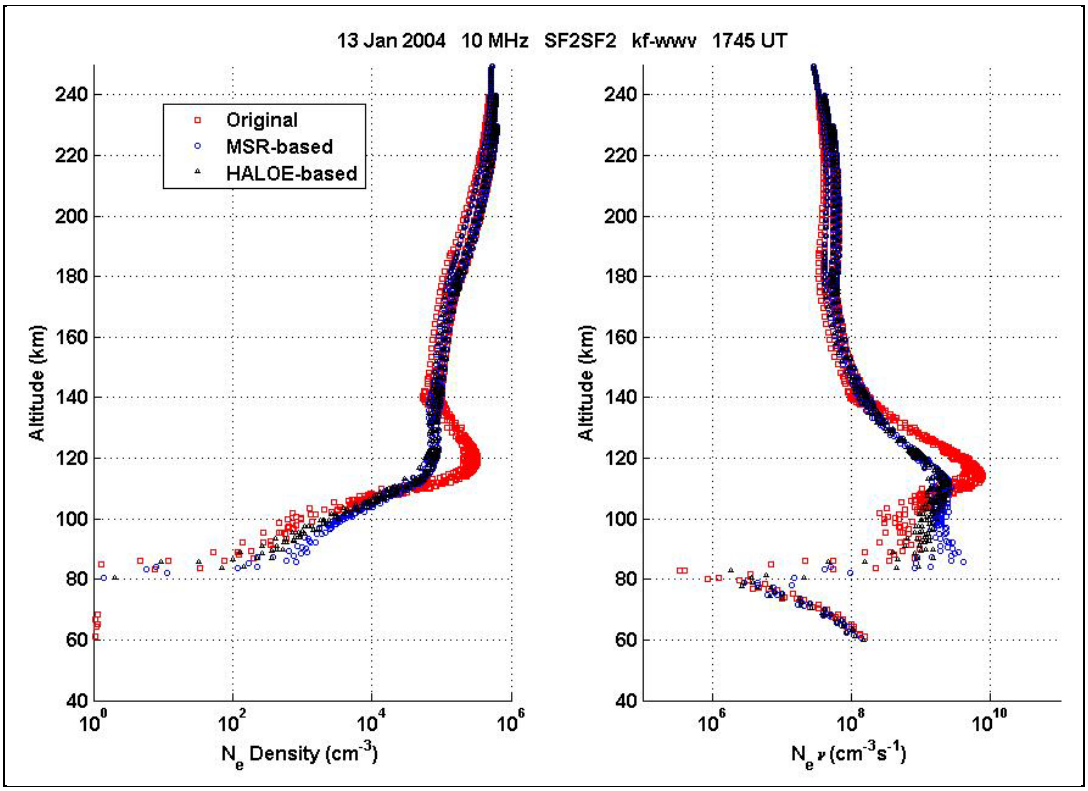

Figure 9.5.14. N_e **and** $N_e\nu$ **values along the raypath predicted by the AbbyNormal versions at 17:45 UT on 13 January 2004.**

9.5.15, and the other is a double-hop F-mode path shown in Figure 9.5.16. The affect of the various NO profiles on the single-hop E-mode path discussed above is the altitude and degree at which the wave is refracted. The principal affect of the NO profiles on the double-hop F-mode path is the amount of absorption suffered by the signal as it passes through the D- and E-regions. The local N_e peak at 120 km predicted by the original version results in a local peak in the original version $N_e\nu$ profile which leads to significant absorption of the signal as the wave passes through the altitudes range of 110 km to 130 km. As seen in the right panels of Figure 9.5.14 and Figure 9.5.17, the original version's peak $N_e\nu$ value at 118 km is nearly an order of magnitude greater than the peak $N_e\nu$ values of the other two versions at 88 km. Figure 9.5.17 is a zoomed-in view of the N_e and $N_e\nu$ values along the raypath shown in Figure 9.5.14 and better displays the values within the D- and E-regions. Consequently, the original version predicts greater signal losses for the double-hop F-mode signal than the other versions.

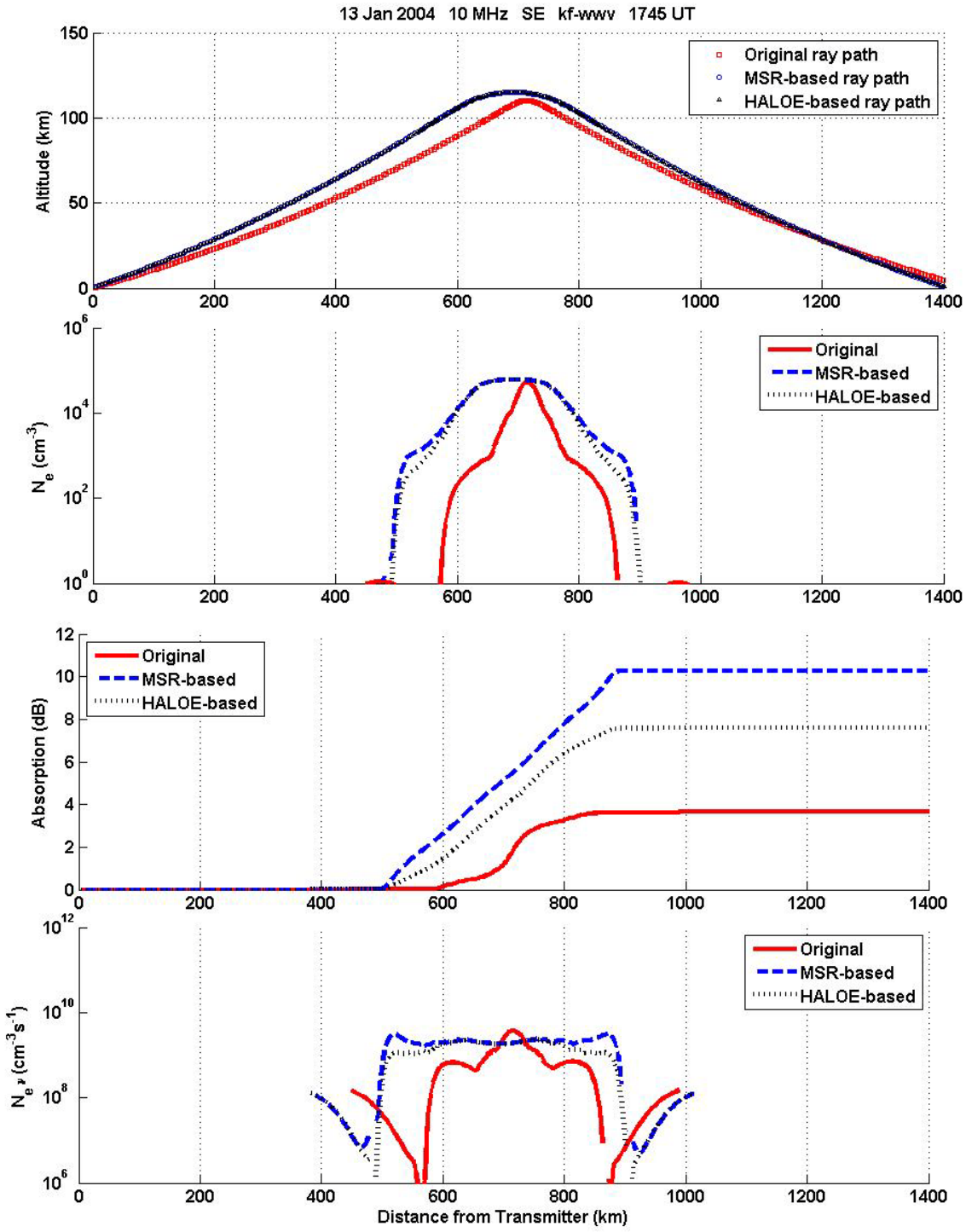

Figure 9.5.15. E-mode propagation paths predicted by HASEL for the 10 MHz kf-wwv transmission on 13 January 2004 at 17:45 UT are shown in the top panel. Also shown are the predictions of the three AbbyNormal versions of N_e along the raypath (second panel from top), total absorption suffered by the wave as it propagates (second panel from bottom), and $N_e\nu$ along the raypath (bottom panel).

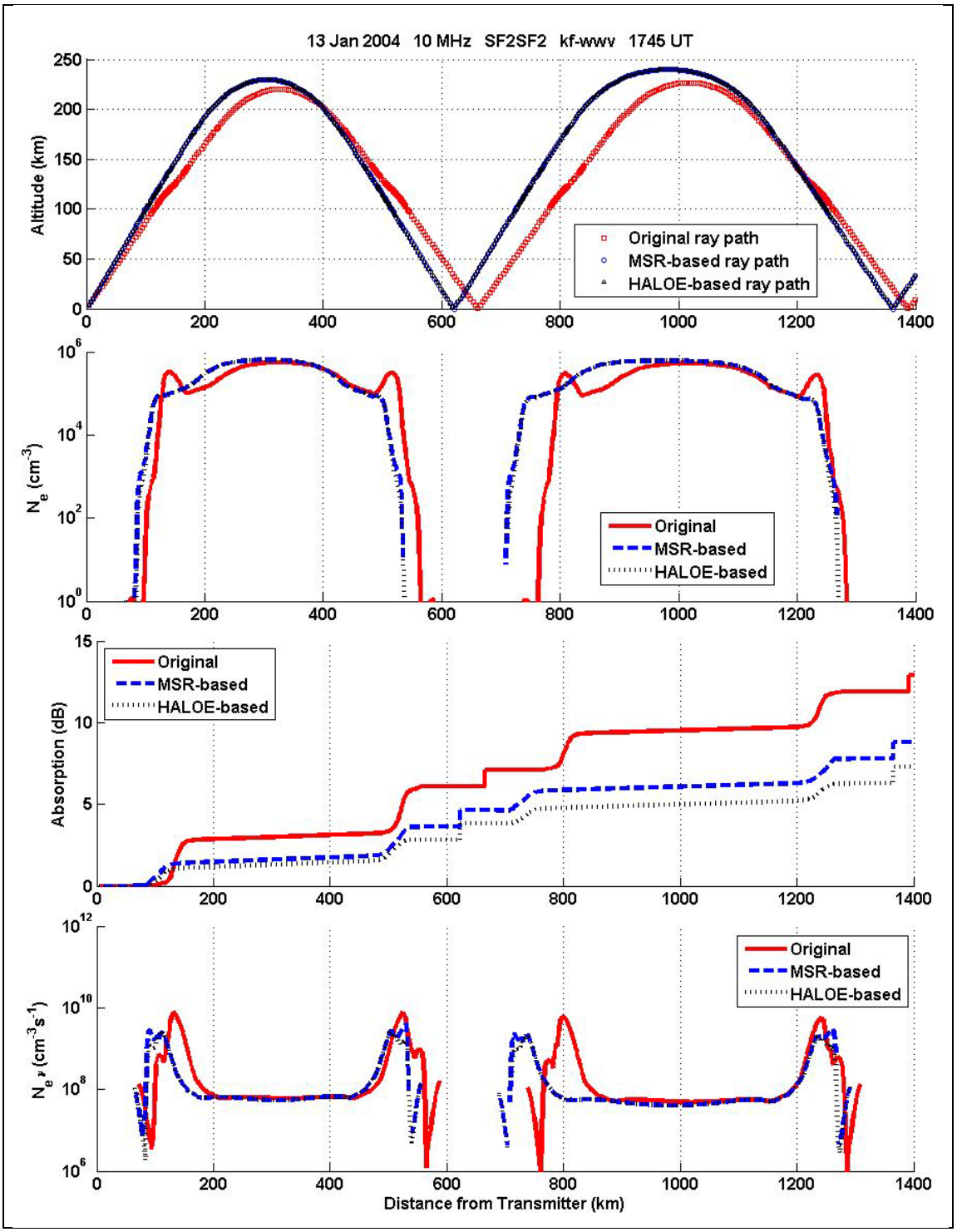

Figure 9.5.16. F-mode propagation paths predicted by HASEL for the 10 MHz kf-wwv transmission on 13 January 2004 at 17:45 UT are shown in the top panel. Also shown are the predictions of the three AbbyNormal versions of N_e along the raypath (second panel from top), total absorption suffered by the wave as it propagates (second panel from bottom), and $N_e\nu$ along the raypath (bottom panel).

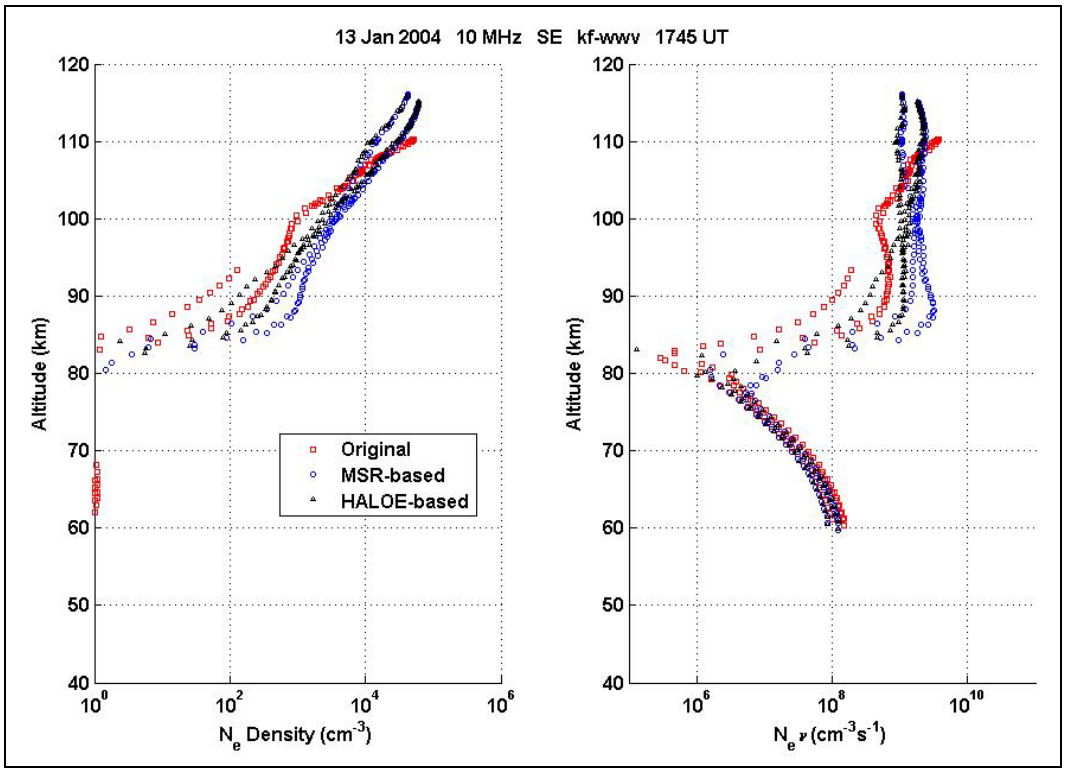

Figure 9.5.17. N_e and $N_e\nu$ values along the raypath predicted by the AbbyNormal versions at 17:45 UT on 13 January 2004 within the D- and E-regions.

Although the original AbbyNormal version predicts baseline signal strengths well for the 10 MHz kf-wwv transmission, closer examination of predicted ionospheric profiles reveals the original version's predicted available propagation paths and signal losses result from a non-realistic N_e profile. Thus, the original version's signal strength predictions are questionable. The other methods of defining NO profiles produce realistic and credible results for the 10 MHz kf-wwv transmission.

9.5.5 AbbyNormal Performances for 15 MHz kf-wwv Transmission.

As discussed in §9.1, the original AbbyNormal version baseline predictions for the 15 MHz kf-wwv transmission show a trend of under-predicting signal strengths during the summer by approximately 10 dB, and this trend prompted the investigation into AbbyNormal's method of defining ionospheric NO densities. Figures in Appendix F show signal strength predictions for the 15 MHz kf-wwv transmission for eleven dates in

January 2004 along with HIDIVE and GOES data and the predictions of the MSR model-based and HALOE-based AbbyNormal versions. Figure 9.5.18 shows the data and predictions on 15 January 2004 which will be examined here in detail. As can be seen from the figures in Appendix F, the AbbyNormal versions do not always predict the 15 MHz kf-wwv signal to be available; however, when the versions do predict an available signal, they do well in predicting baseline signal strengths. The HIDIVE data for these dates also show sudden changes in signal availability, such as that seen in Figure 9.5.18 between 16:00 UT and 16:10 UT.

The cause for the sudden loss in signal strength and availability for the 15 MHz kf-wwv transmission is the radio wave is refracted back towards earth at an altitude close to the F2-peak. As discussed in §2.1.1, the F2-peak located at approximately 250 km is the location of maximum electron density within the ionosphere. Above the F2-peak N_e begins to decline with altitude; thus, if a wave is not refracted back towards earth by the F2-peak, it will penetrate the ionosphere and will not be received, which is the situation responsible for the sudden loss in signal availability seen in the 15 MHz kf-wwv transmission. Figure 9.5.19 shows the single-hop F-mode propagation path available to the 15 MHz kf-wwv transmission, which is the only path predicted by the MSR model-based and HALOE-based versions to be available, and Figure 9.5.20 shows the N_e and $N_e v$ values along the raypath predicted by the three AbbyNormal versions. From Figures 9.5.19 and 9.5.20, we see all three versions predict an N_e value large enough to refract the 15 MHz wave back towards earth at 210 km. Unlike the other two versions, the original AbbyNormal version predicts more than one available propagation path for the 15 MHz kf-wwv transmission. As seen in Figure 9.5.20, the original version N_e values predict an N_e large enough to refract the 15 MHz wave back towards earth at two altitudes, 210 km and 120 km. As discussed in previous sections, the source of the local N_e peak is the method by which the original AbbyNormal model blends two ionospheric models together between 110 km and 130 km.

Unlike the other two versions, the original AbbyNormal version predicts more than one available propagation path for the 15 MHz kf-wwv transmission. As seen in Figure 9.5.20, the original version N_e values predict an N_e large enough to refract the 15

MHz wave back towards earth at two altitudes, 210 km and 120 km. As discussed in previous sections, the source of the local N_e peak is the method by which the original AbbyNormal model blends two ionospheric models together between 110 km and 130 km.

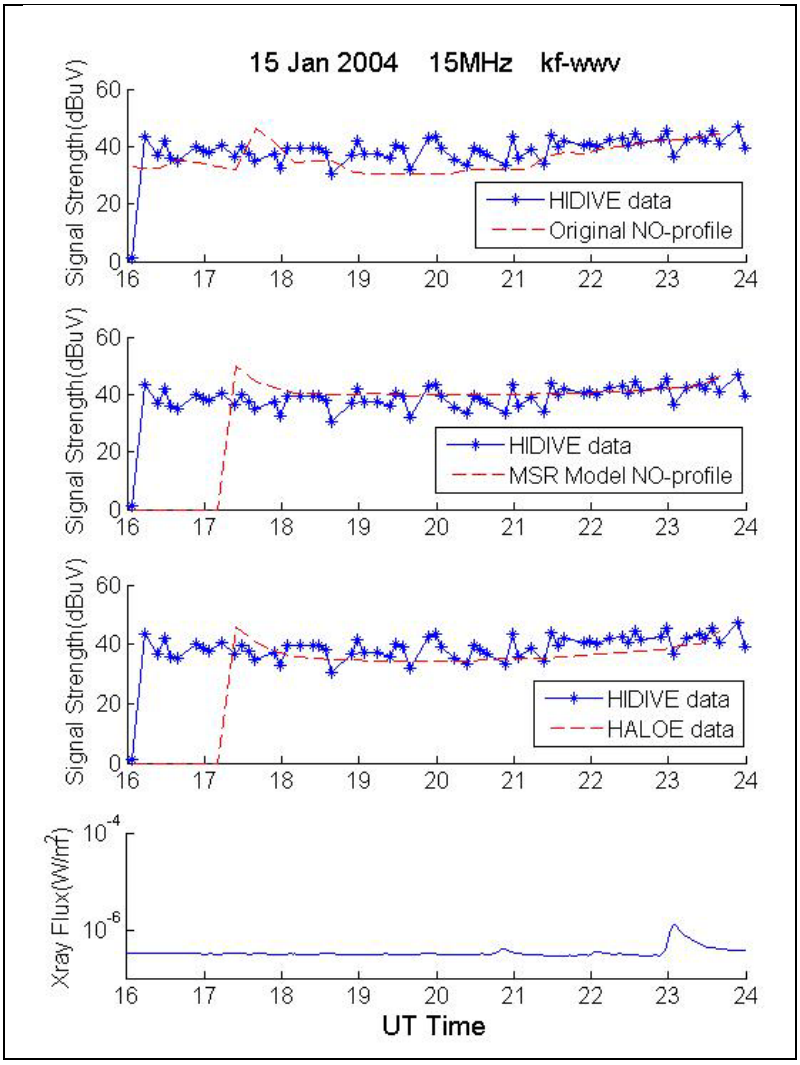

Figure 9.5.18. HIDIVE signal strength data are shown for 15 January 2004 for the 15 MHz kf-wwv transmission along with signal strength predictions of the original AbbyNormal version (top panel), the MSR model-based version (second to top panel), the HALOE-based version (second to bottom panel), and GOES data (bottom panel).

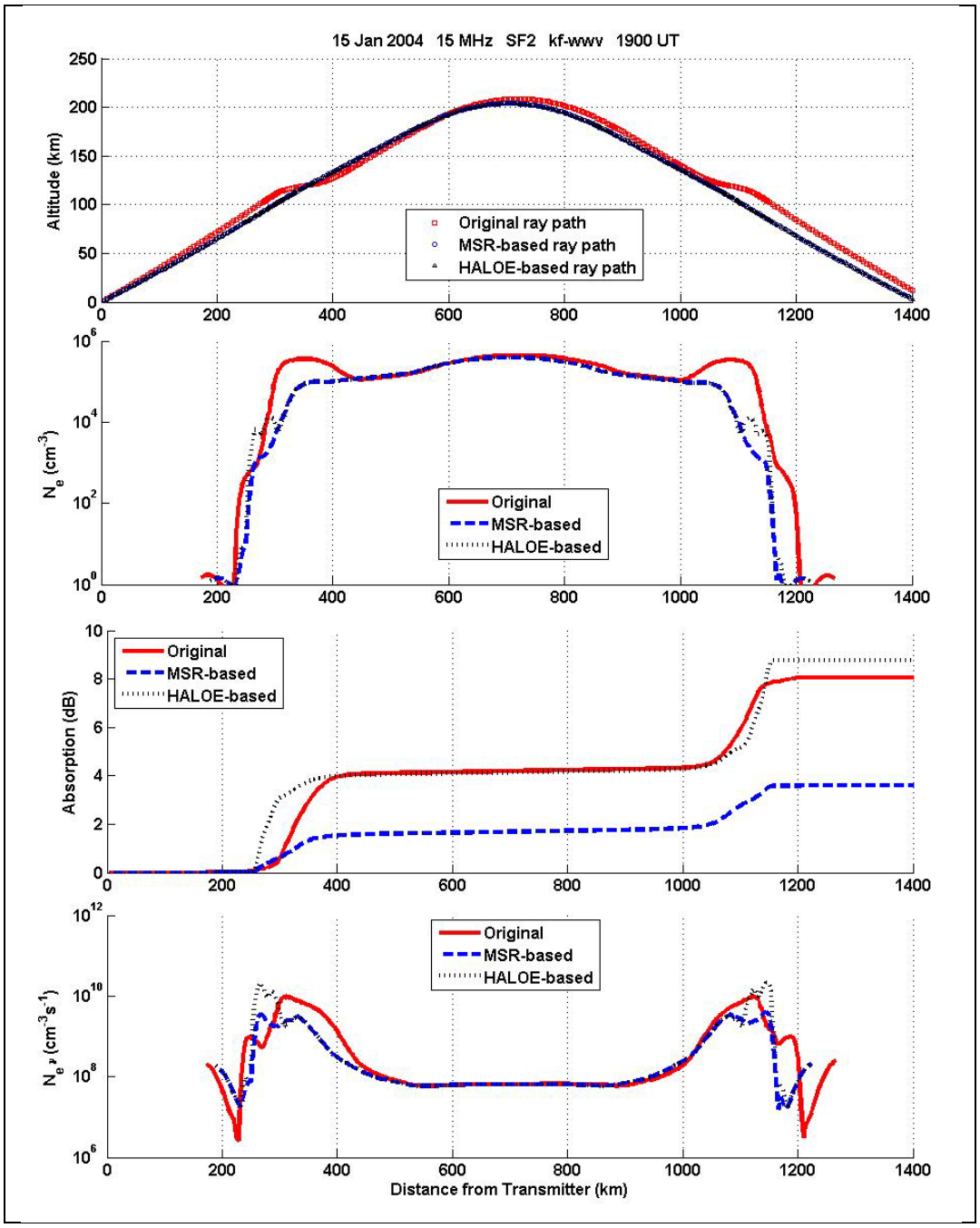

Figure 9.5.19. F-mode propagation paths predicted by HASEL for the 15 MHz kf-wwv transmission on 15 January 2004 at 19:00 UT are shown in the top panel. Also shown are the predictions of the three AbbyNormal versions of N_e along the raypath (second panel from top), total absorption suffered by the wave as it propagates (second panel from bottom), and $N_e\nu$ along the raypath (bottom panel).

Once again the results of the original AbbyNormal model are called into question due to the unrealistic N_e peak at 120 km. Not only does the N_e peak lead to two additional predicted propagation paths, it also leads enhanced $N_e\nu$ values and signal absorption between 110 km and 130 km. The MSR model-based and HALOE-based versions produce more realistic NO and N_e profiles and perform well at predicting baseline signal strengths for the 15 MHz kf-wwv transmission.

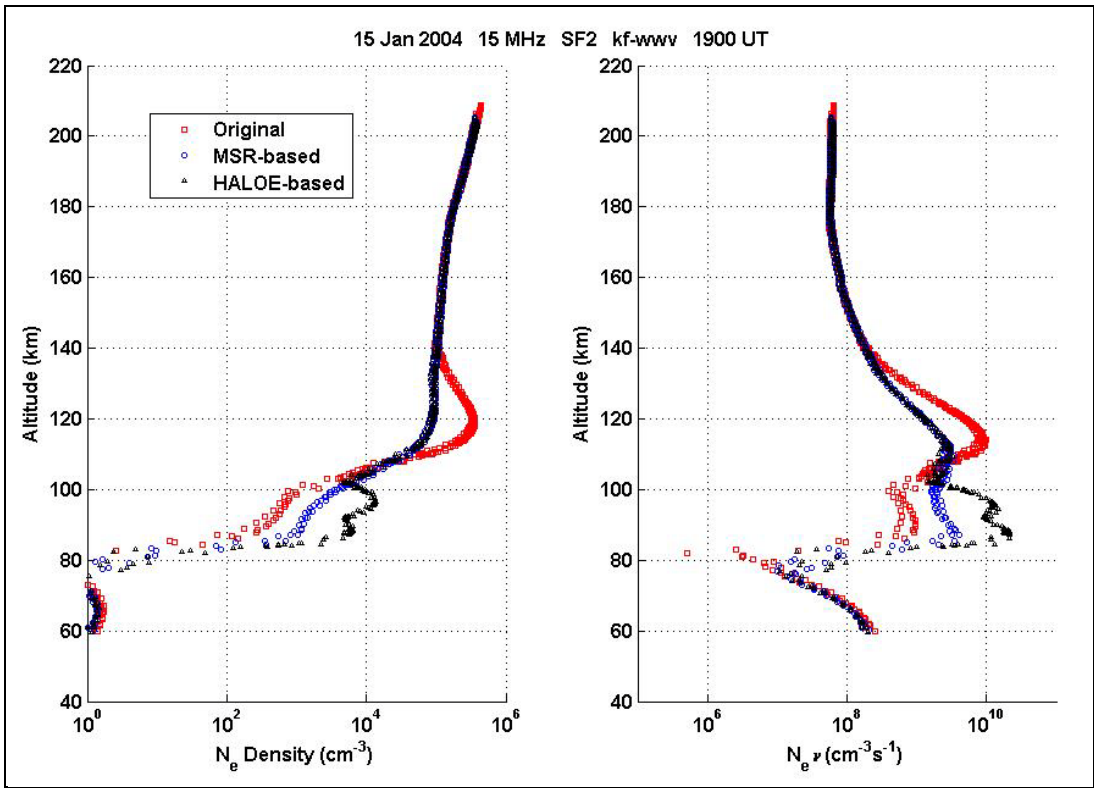

Figure 9.5.20. N_e and $N_e\nu$ values along the raypath predicted by the three AbbyNormal versions at 19:00 UT on 15 January 2004.

9.6 AbbyNormal Results Summary

The comparison of the three AbbyNormal versions provided valuable insight into how significantly NO profiles affect model signal strength predictions. Unfortunately, no one method of producing AbbyNormal NO profiles clearly out-performed the other two, and no performance trends existed across all five HIDIVE transmissions. The

performances of the three AbbyNormal versions were different for each HIDIVE transmission, and even for a single transmission, version performance was not always consistent. Below is a summary of the comparison of the three AbbyNormal versions for each HIDIVE transmission.

9.6.1 Summary of 5 MHz blo-wwv Analysis

Only the baseline signal strength predictions of the HALOE-based AbbyNormal version showed daily variation, while the baseline signal strength predictions of the original and MSR model-based versions were consistent from day to day. Although the HALOE-based version consistently under-predicted baseline signal strengths, it had the ability to capture variations in local NO densities and baseline signal strengths. Neither the original nor the MSR model-based versions consistently out-performed the other, and neither consistently predicted baseline signal strengths adequately. The signal strengths predictions of the original and MSR model-based versions did not change from day to day even though observed signal strengths varied daily. The same primary path was predicted for all three versions, a single hop E-mode. Thus, the differences seen in the predictions of baseline signal strengths were due to differences in the NO profiles, which lead to differences in $N_e\nu$ profiles and non-deviative absorption.

9.6.2 Summary of 10 MHz blo-wwv Analysis

The MSR model-based and the HALOE-based versions consistently under-predicted the baseline signal strengths for the 10 MHz blo-wwv HIDIVE transmission, while the original AbbyNormal version consistently predicted the baseline well when the signal was available. However, closer inspection revealed the baseline predictions of the original model, although accurate, resulted from non-realistic N_e profiles and were fundamentally flawed. The method used by the original model of blending together the ionospheric DDDR and IRI models to generate N_e profiles resulted in a nonphysical peak at 120 km. Due to this nonphysical peak the raytracing program, HASEL, predicted additional available propagation paths for the original AbbyNormal version that it did not predict for the other two versions, resulting in the original version predicting higher signal strengths.

9.6.3 Summary of 5 MHz kf-wwv Analysis

All three AbbyNormal versions prediced similar dominate propagation paths for the 5 MHz kf-wwv transmission; however, they differed greatly in their prediction of the signal's availability and baseline signal strength. Although the 5 MHz kf-wwv transmission is rarely above the noise, the original AbbyNormal model consistently predicted the signal to be available and over predicted the baseline signal strengths. This is due to the model under-predicting NO densities between the altitudes of 80 km and 100 km, where the 5 MHz kf-wwv suffers the majority of its absorption. The MSR model-based and HALOE-based AbbyNormal versions produced more realistic NO profiles between 80 km and 100 km and were better able to predict day-to-day variations in NO and baseline signal strengths for the 5 MHz kf-wwv transmission.

9.6.4 Summary of 10 MHz kf-wwv Analysis

All three AbbyNormal versions predictd the baseline signal strengths of the 10 MHz kf-wwv transmission well; however, upon closer examination, the predictions of the original AbbyNormal version were questionable due to the unrealistic local peak in its N_e profile at 120 km. Due to the local peak at 120 km, the original AbbyNormal version predicted a set of propagation paths that differed from the sets predicted by the other two versions. Although the original AbbyNormal version predicted fewer available propagation paths for the 10 MHz kf-wwv transmission, its baseline signal strength predictions were as good as the other two versions. This is due to the original version under-predicting NO densities between 80 km and 100 km and under-predicting the absorption suffered by the dominate E-mode paths.

9.6.5 Summary of 15 MHz kf-wwv Analysis

Initial results of model performance showed AbbyNormal summertime baseline predictions for the 15 MHz kf-wwv transmission were consistently too low due to over-prediction of N_e and absorption. However, the original AbbyNormal model, the MSR model-based version, and the HALOE-based version all performed well at predicting the baseline signal strengths of the 15 MHz kf-wwv transmission for the winter dates examined here. The analysis done in chapter nine did not uncover the reason for the disparity between model performance for summer and winter. The analysis did show the

predictions of the original version were questionable due to the model's unrealistic local N_e peak at 120 km. The local N_e peak resulted in the original version predicting two additional available propagation paths the other two AbbyNormal versions did not predict. Even though the original version predicted more available paths, all three versions had similar baseline signal strength predictions since the original version's local N_e peak also results in greater predicted absorption of those paths passing through 120 km.

9.7. AbbyNormal Analysis Summary

Initial validation of the physical AbbyNormal model revealed problems with model baseline signal strength predictions, where the model consistently under-predicted signal strengths for the 5 MHz and 15 MHz HIDIVE signals, and suggested AbbyNormal's under-prediction of signal strength baselines had a seasonal trend and was worse during summer months. Further investigation into the apparent seasonal trend revealed significant increases in model predicted N_e profiles from winter to summer that were orders of magnitude greater than observations. In an attempt to improve AbbyNormal baseline signal strength predictions and to correct the problem of over-prediction of summer time N_e profiles, areas within the model which affect N_e predictions and which could be improved were investigated. One area of AbbyNormal known to the model's author to be inconsistent with observations was model predictions of atmospheric nitric oxide (NO) densities.

The strength of a received HIDIVE signal is dependent on the free electron density it encounters along its propagation path, and N_e between 80 km and 140 km is directly related to local NO density. Thus, to accurately predict HIDIVE signal strengths, local NO profiles must be correctly modeled. It was shown in §9.3 AbbyNormal NO profiles did not agree with observations and severely under-predicted NO densities above 80 km, where the majority of HF absorption occurs and where N_e profiles determine available propagation paths. Thus, two alternative methods for producing AbbyNormal NO profiles were developed, and signal strength predictions for the five HIDIVE transmissions produced by the three AbbyNormal versions were compared.

Unfortunately, of the three AbbyNormal versions; the original version, the HALOE-based version, and the MSR model-based version, no one version consistently outperformed the other two at predicting baseline signal strengths for all five HIDIVE transmissions. This is due to the baseline signal strengths being dependent on the characteristics of the propagation path, including signal elevation angle, refraction altitudes, and percentage of travel within the D-region. The HASEL model within AbbyNormal was used here to determine the available propagation paths for each of the HIDIVE transmissions and the characteristics of each path. However, HASEL's ability to predict propagation paths and the amount of absorption suffered by a signal is only as accurate as the NO profile provided to it since NO profiles are used to determine N_e and $N_e\nu$ profiles, which determine available propagation paths and non-deviative absorption, respectively.

Both propagation paths and the amount of non-deviative absorption suffered must be examined when analyzing an AbbyNormal version's performance. For example, the NO profiles of the original AbbyNormal version were orders of magnitude lower than observations above 80 km, and one would expect the original version's performance in predicting baseline signal strengths to be consistently poor. However, in §9.5.4 it was shown the original version predicted the baseline signal strengths of the 10 MHz kf-wwv transmission well due to addition available propagation paths predicted by HASEL as a result of a nonphysical local N_e peak near 120 km. This case highlighted a problem with AbbyNormal's method of building the local ionosphere and an area in which the model can be improved.

The local N_e peak near 120 km was not present in the predictions of the MSR model-based and HALOE-based versions; however, neither of these versions consistently outperformed the other versions in predicting HIDIVE baseline signal strengths. The work in chapter 9 showed improvements can and need to be made to the AbbyNormal method of producing NO profiles for improved model performance. The changes made to obtain the MSR model-based and HALOE-based versions are just the first steps in providing AbbyNormal with more realistic NO profiles and better model performance. More work is needed to further improve the accuracy of the modeled NO profiles, and

additional ways to improve AbbyNormal model performance are discussed in §10.4 and include obtaining NO observations along the raypath and performing model validation while holding F10.7 constant.

10. Discussion

10.1 Data

Coupling space weather observations with HF signal strength data, this research set out to characterize flare-induced HF absorption and to validate and suggest improvements for current HF absorption models. The data used here were signal strength observations at 5 MHz, 10 MHz, and 15 MHz and were obtained from the HF Investigation of D-region Ionospheric Variation Experiment (HIDIVE). Signal strength data at 30 MHz obtained from the NORSTAR Pinawa riometer were also used to expand the frequency range of the data. The HF signal strength data were selected based on the following criteria.

- No local interference was suspected the day of the flare
- HIDIVE data showed no apparent delay between flare onset and the start of flare-induced absorption
- HIDIVE data showed no delay between flare peak and maximum flare-induced absorption
- Propagation mode changes were not suspected on the day of the flare

These criteria were established in order to provide a reproducible method of selecting signal strength data to be used for calculation of flare-induced absorption of HF signals.

Although the three HIDIVE transmissions and the riometer datasets spanned the HF frequency realm from 5 MHz to 30 MHz, additional transmissions of frequencies between 15 MHz and 30 MHz would have helped decrease the uncertainty of the frequency dependence of absorption calculated in §6.4. Figure 6.4.6 showed how the position of the 30 MHz data point greatly influenced the fit of the LS line slope versus signal frequency curve. Additional datapoints between 15 MHz and 30 MHz would have greatly aided in reducing the uncertainty in fitting the curve and in determining the frequency dependence of HF absorption.

Future work should also address the issue of standardizing the type of raw data used. Unlike the initial HIDIVE data used here which were raw signal strengths, the 30 MHz riometer data obtained online from the NORSTAR Pinawa riometer were

absorption measurements calculated by the University of Calgary staff managing the Pinawa riometer. The riometer absorption measurements were calculated using a method of determining baseline riometer signal strengths created by the University of Calgary staff, which differs from the method used here and discussed in §5.3 to determine HIDIVE baseline signal strengths. It would have been better for consistency and reproducibility if raw riometer signal strength data were obtained and the same method used for calculating the baseline signal strengths and absorption of the HIDIVE signals was applied to the raw riometer signal strength data.

10.2 Solar Quiet Curves

10.2.1 Flare-Induced Absorption

After the selection of signal strength data was complete, expected signal strength curves were determined to calculate flare-induced absorption. A reproducible and automated method of producing daily solar quiet curves (SQ curves) was established to calculate the expected quiet time diurnal absorption of a given HIDIVE transmission.

The functional form of the SQ curves used here was given in equation 5.4.1, $I(t) = A \cdot Cos^{0.9}(\chi_t) + B$. The cosine term was consistent with the findings discussed in §2.2.3 which showed photoionization rates and electron densities within the D-region are proportional to $Cos^r(\chi)$. Since D-region HF absorption is dependent on local electron densities, it was reasonable the strength of an HF transmission during solar quiet times also depended on the cosine of the solar zenith angle. The power of that dependence, r = 0.9, was also consistent with previous studies which suggested the power of the cosine dependence of D-region absorption at midlatitudes was between 0.6 and 1.0 [*Davies*, 1990; *McNamara*, 1991; *Rishbeth and Garriott*, 1969, *Oyinloye*, 1978].

10.2.2 Local NO Density

Daily SQ curves provide a baseline from which flare-induced absorption can be calculated and may also provide information about local NO densities. The parameter, *B*, in equation 5.4.1 represented the received strength of the HF signal in the absence of any loss, and the parameter, *A*, was a scaling factor which contained information about ionizing Lyman-α flux, local NO densities, and background solar X-ray flux. As discussed in §2.2.1, D-region electron densities and absorption of HF signals during solar

quiet-time depend on photoionization of NO via solar Layman-α radiation. Since the F10.7 index serves as a proxy for Layman-α radiation, future work may be able to determine local NO densities on a given day if the value of the F10.7 index, the background solar X-ray flux, and the value of the fit parameter, *A*, are known. In order to determine NO densities based on the fit parameter, *A*, future work must determine the empirical relations between *A* and the factors determining quiet-time diurnal absorption (Lyman-α flux, neutral densities, and background solar X-ray flux). Of the factors listed, all but NO density can currently be determined by direct observations. Once the empirical relations have been determined for a given transmission, future work should be able to calculate local NO densities given the SQ curve for that day.

Figures 10.2.1 and 10.2.2 showed the signal strength data for the 5 MHz blo-wwv and the 10 MHz kf-wwv HIDIVE transmissions, respectively, for dates during December 2003 when there was no significant solar activity and background solar X-ray flux was fairly constant. Also given in the figures were the average F10.7 indices for each day. The HIDIVE data for dates during December 2003 were shown to illustrate winter anomalies, which are discussed in §2.3.1 and are enhanced HF absorption in the absence of high levels of solar ionizing radiation flux. Winter absorption anomalies are likely explained by significant increases in local NO densities. The figures showed drastic daily variations in signal strength that cannot be easily explained by fluctuations in Lyman-α or background X-ray flux. A promising avenue for future work is to apply SQ curves to signal strength data and use the resulting fit parameter, *A*, and known F10.7 indices and background solar X-ray flux values to determine local NO densities.

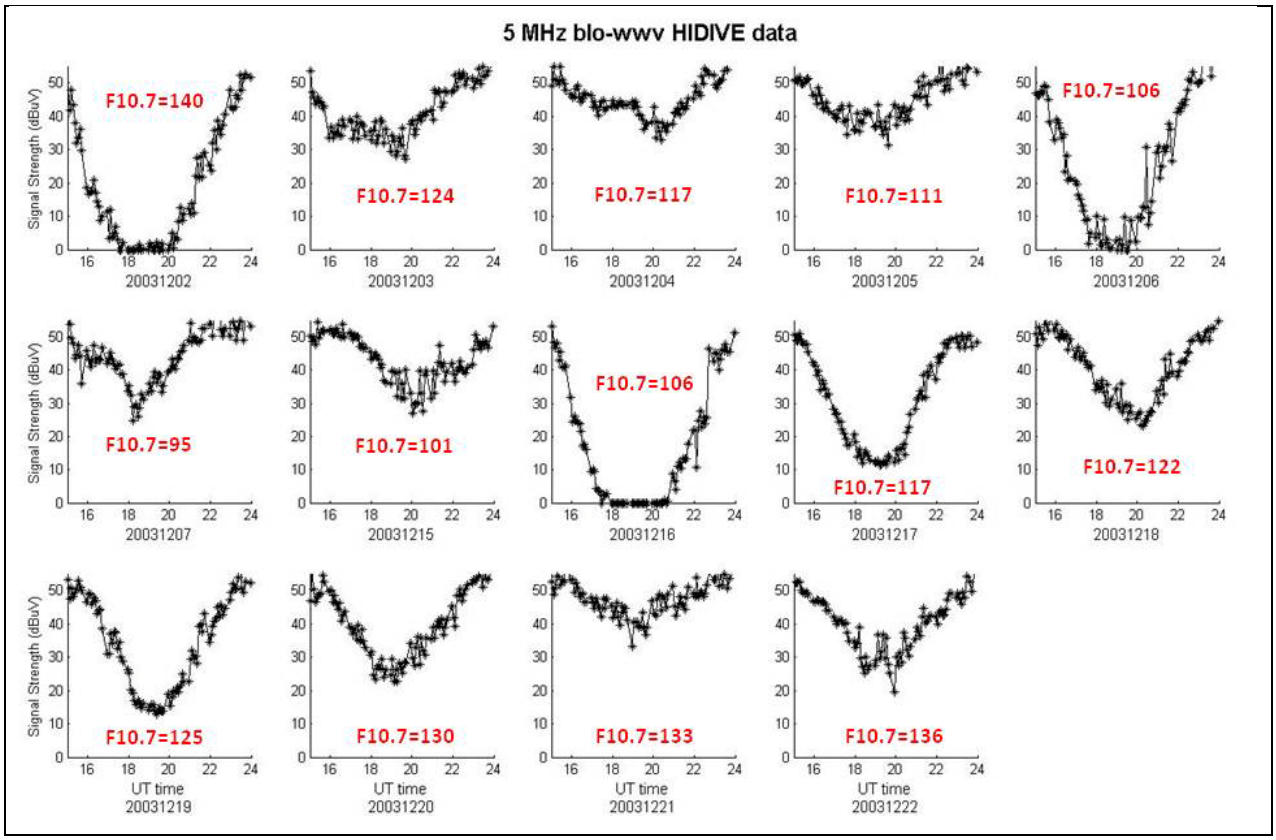

Figure 10.2.1. Signal strength data for the 5 MHz blo-wwv HIDIVE transmission and daily average F10.7 values are shown during solar quiet conditions during December 2003.

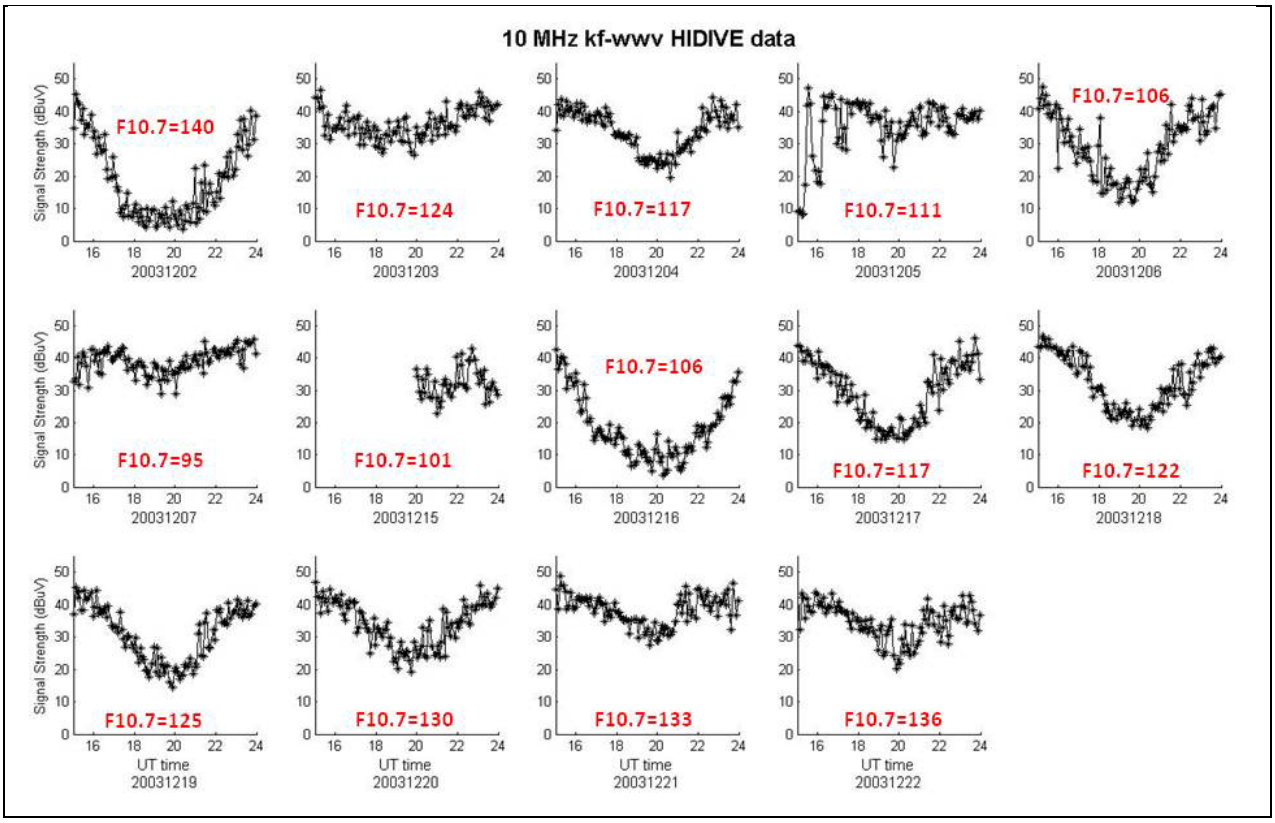

Figure 10.2.2. Signal strength data for the 10 MHz kf-wwv HIDIVE transmission and daily average F10.7 values are shown during solar quiet conditions during December 2003.

10.3 Frequency Dependence of Midlatitude HF Absorption

The procedure for producing SQ curves developed here provided an automated and reproducible method for calculating flare-induced HF absorption during 61 "premier" events discussed in §6.2.6. Normalization of the raw flare-induced absorption data from the 61 premier events to a common solar zenith angle (χ) and propagation path allowed for the investigation of the dependence of HF absorption on signal frequency.

The normalized flare-induced absorption data revealed an $f^{-1.24}$ dependence of absorption on signal frequency, which differed from the f^{-2} dependence commonly used in HF absorption models, such as the SWPC D-region absorption model published by the National Weather Service. An f^{-2} dependence for non-deviative absorption of HF waves is valid in the F-region and upper E-region where $\omega \gg \nu$. When $\gg \nu$, the equation for the absorption coefficient given in equation 2.4.18 reduces to

$$\kappa = \left(\frac{N_e e^2}{2\mu c \varepsilon_o m} \right) \frac{\nu}{\omega^2} = \left(\frac{N_e e^2}{8\pi^2 \mu c \varepsilon_o m} \right) \frac{\nu}{f^2} \qquad (10.3.1).$$

However, within the D-region $\omega \sim \nu$ and the simple f^{-2} dependence does not apply.

The HF absorption dependencies on solar zenith angle and signal frequency within the D-region, $Cos^{0.9}(\chi)$ and $f^{-1.24}$, were used to develop the Empirical HIDIVE Absorption (EHA) model for prediction of D-region HF absorption. The EHA model and the $f^{-1.24}$ empirical relation can be further refined in future work by obtaining the raw riometer signal strength data and applying the method developed here and discussed chapters 5 an 6 to calculate flare-induced absorption.

10.4 Future Work for AbbyNormal Improvement

The investigation into the apparent seasonal trend in model performance and into ways to improve AbbyNormal model performance in chapter 9 led to two additional versions of AbbyNormal, with each version employing a different method for defining NO profiles. Unfortunately, of the three AbbyNormal versions; the original version, the HALOE-based version, and the MSR model-based version, no one version was best at predicting baseline signal strengths for all five HIDIVE transmissions. Thus, future work should continue to investigate the cause of AbbyNormal's apparent seasonal trend in baseline signal strength predictions and should continue to refine model NO profiles.

Since the original AbbyNormal model bases NO profiles on MSIS *O* and O_2 densities and MODTRAN mixing ratios, as discussed in §9.3, AbbyNormal NO profiles are fairly constant throughout the year. This does not explain the significant increase seen in AbbyNormal N_e densities from winter to summer or the seasonal trends in baseline signal strength predictions. For the goal of tracking down the source of the seasonal trends, future work should include running AbbyNormal for dates throughout the year while keeping the input for the F10.7 index constant. AbbyNormal uses the published F10.7 index as a proxy for ionizing Lyman-α radiation, which can vary significantly from day to day. Thus, by holding the input for the F10.7 index constant, one factor contributing to AbbyNormal N_e densities is removed.

Another issue future work should consider for improving AbbyNormal performance is to use NO observations along the raypath to build NO profiles. Currently, HALOE observations used here to build NO profiles were obtained either at sunrise or sunset and did not necessarily coincide temporally or spatially with the HIDIVE transmissions. Given the limited temporal and spatial availability of HALOE observations, HALOE data were used if the satellite pass was within 1500 km of the midpoint of the HIDIVE transmissions. The midpoint is located at 41 N latitude and 113 W longitude, which is the mean latitude and longitude between the WWV transmitter in Fort Collins, CO and the furthest receiver in Klamath Falls, OR. Local NO enhancements due to NO transport from polar regions by thermospheric winds can be on the order of tens or hundreds of kilometers wide horizontally; thus, HALOE data used here were not always an accurate measure of NO along the HIDIVE raypaths. The HALOE-based AbbyNormal version showed NO data can be used to build NO profiles within AbbyNormal. However, observations of NO obtained closer to actual HIDIVE raypaths are needed for more realistic modeling of the local ionosphere.

In the absence of local NO observations, an NO model can be used to build AbbyNormal NO profiles for near-real time predictions of HIDIVE signal strengths. Since accurate baseline signal strength predictions depend on accurate NO density predictions at D-region and lower E-region altitudes, future work should seek out or develop a model which produces NO profiles that cover D-, E-, and F-region altitudes. As mentioned in §9.3, the MSR empirical NO model used here only predicts NO between the altitudes of 100 km and 150 km. Thus, MSR model-based AbbyNormal NO profiles below 100 km were the same as those of the original AbbyNormal model. With more accurate modeling of NO within the D-region, future work should be able to improve baseline signal strength predictions.

Although no one AbbyNormal version clearly outperformed the others, valuable insight into how the three different methods of producing NO profiles influenced N_e and $N_e\nu$ profiles and, thus, the predictions of non-deviative absorption and available propagation paths was obtained. The HALOE-based and MSR model-based AbbyNormal versions showed improved predictions of baseline signal strengths are

possible with more accurate AbbyNormal NO profiles; however, these AbbyNormal versions were just the first steps in improving model performance.

10.5 Conclusion

This research addressed the need for better characterization of flare-induced HF absorption within the D-region and the need for a reliable, easily implemented, near-real-time, operational HF absorption model. Unlike within the ionospheric E- and F-regions, collisions between free electrons and neutrals within the D-region are significant and cannot be ignored. As a result, the function describing the absorption of HF waves as they travel through a plasma cannot be simplified to a f^{-2} relation, which many current HF absorption models use. The SWPC D-region Absorption Model published by the National Weather Service is one such operational model which is widely used by both the military and private sectors.

Analysis of HF signal strength data obtained by the HIDIVE experiment and analysis of Pinawa riometer absorption data provided by the University of Calgary revealed a $f^{-1.24}$ dependence for flare-induced D-region HF absorption on signal frequency. Further analysis of the data during solar quiet periods also indicated diurnal absorption of HF transmissions has a $Cos^{0.9}(\chi)$ dependence on solar zenith angle. This was also in disagreement with the SWPC model which scales absorption as $Cos^{0.75}(\chi)$. These empirical relations were used to develop the EHA model, which was shown to be able to provide HIDIVE signal strengths predictions in near-real time. A method for adapting the EHA model to other HF transmissions was also outlined here.

Validation of the EHA and SWPC models showed the EHA model performed well at predicting signal strengths for HIDIVE transmissions and the SWPC model f^{-2} absorption dependence on signal frequency was inappropriate for HIDIVE transmissions. Validation also showed SWPC model performance degraded with increasing signal frequency. Thus, this work established a methodology for developing an operational model for predicting D-region flare-induced HF absorption which out-performed the SWPC model, can be used in near-real-time, and can be customized to specific HF transmissions.

Validation of the physical AbbyNormal model was also done in order to satisfy another research goal, which was to improve AbbyNormal model performance. The performance of the physical AbbyNormal model is directly related to our understanding of the physics governing the ionosphere and the propagation of HF transmissions through the ionosphere. Unfortunately, validation revealed problematic issues concerning AbbyNormal baseline signal strength predictions and seasonal trends in model performance. Initial work into correcting these issues started with addressing known problems with AbbyNormal NO profiles, and alternative ways for producing AbbyNormal NO profiles that better agree with satellite NO observations were presented. Unfortunately, no one method explored here of defining NO profiles resulted in an AbbyNormal version that clearly outperformed the other versions.

Even though, improvements to AbbyNormal NO profiles were not enough to solve the baseline signal strength issues identified during initial model validation, this research was able to improve AbbyNormal NO profiles and highlighted possible ways to improve AbbyNormal performance in the future. This research also revealed absorption dependencies which lead to the development of an easily implemented methodology for establishing a near-real-time operational model for prediction of HF communication availability. More work must be done, but this work has laid the foundation for improved modeling of D-region flare-induced HF absorption.

Appendix A. Signal Strengths and Absorption Predictions of the Abby Normal, EHA, and SWPC Models

A.1 Signal Strength Predictions for the 5 MHz blo-wwv HIDIVE transmission

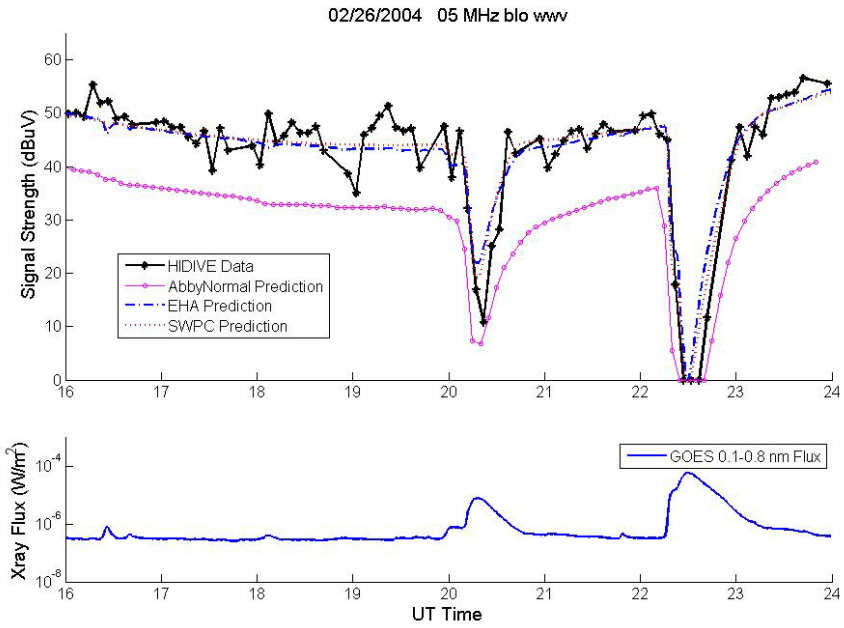

Figure A.1.1. AbbyNormal model prediction, EHA model prediction, and SWPC model prediction for the 5 MHz blo-wwv transmission on 26 February 2004 compared to HIDIVE signal strength data and GOES 0.1-0.8 nm flux data.

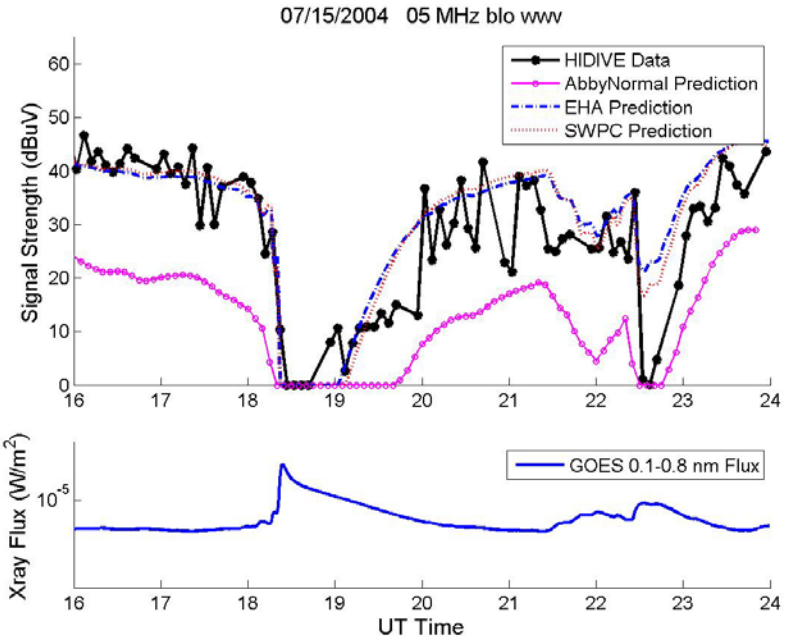

Figure A.1.2. AbbyNormal model prediction, EHA model prediction, and SWPC model prediction for the 5 MHz blo-wwv transmission on 15 July 2004 compared to HIDIVE signal strength data and GOES 0.1-0.8 nm flux data.

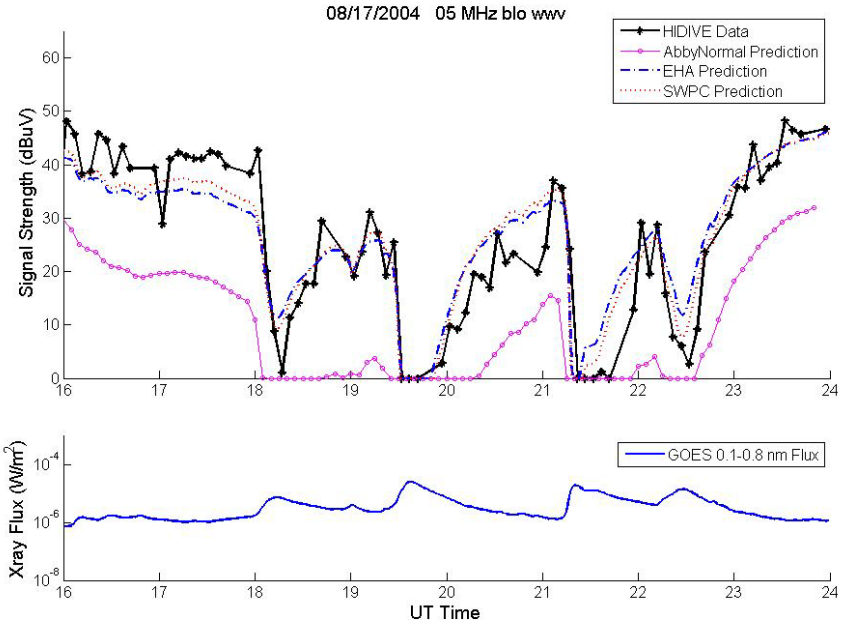

Figure A.1.3. AbbyNormal model prediction, EHA model prediction, and SWPC model prediction for the 5 MHz blo-wwv transmission on 17 August 2004 compared to HIDIVE signal strength data and GOES 0.1-0.8 nm flux data.

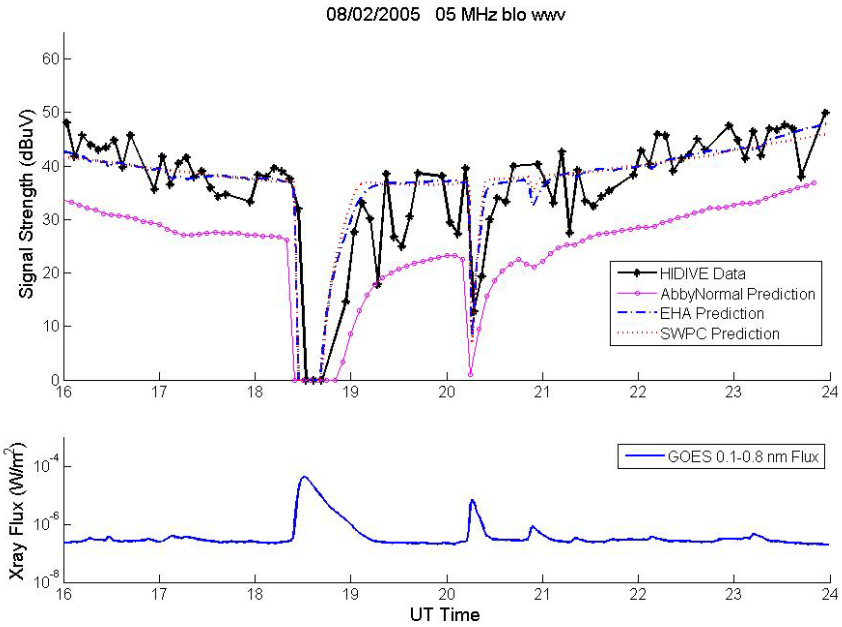

Figure A.1.4. AbbyNormal model prediction, EHA model prediction, and SWPC model prediction for the 5 MHz blo-wwv transmission on 2 August 2005 compared to HIDIVE signal strength data and GOES 0.1-0.8 nm flux data.

A.2 X-ray Flare Induced Absorption Predictions for the 5 MHz blo-wwv Signal

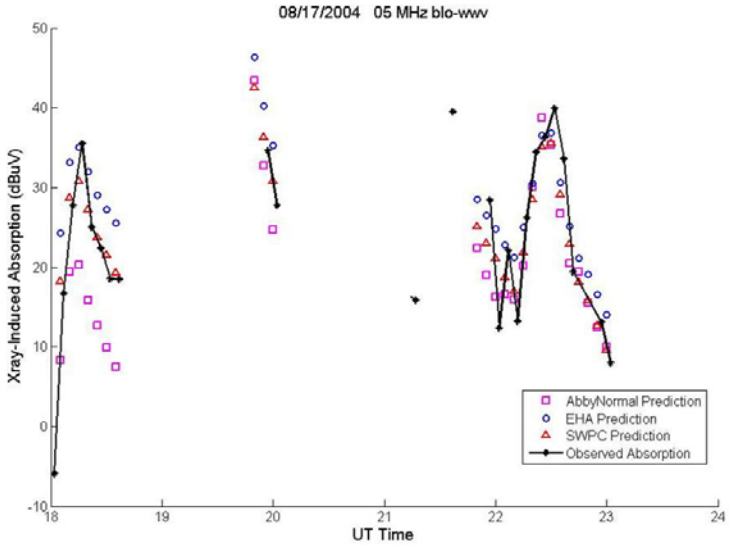

Figure A.2.1. X-ray flare-induced absorption of the 5 MHz blo-wwv signal on 17 August 2004 as observed with respect to the HIDIVE data compared to the flare-induced absorption predicted by the AbbyNormal model, EHA model, and SWPC model.

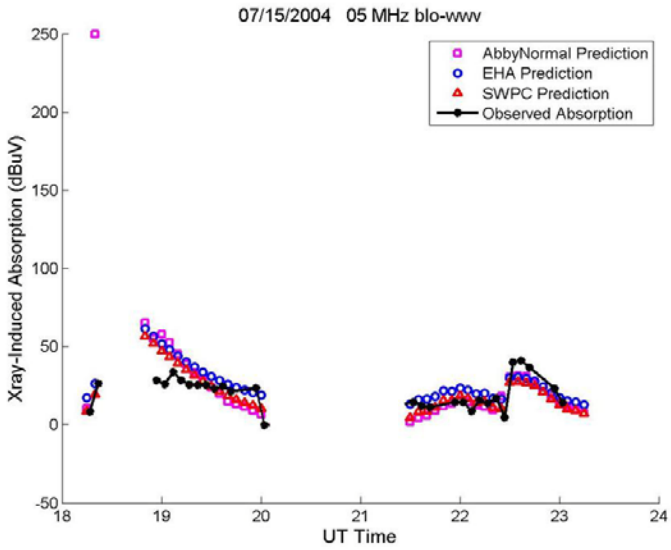

Figure A.2.2. X-ray flare-induced absorption of the 5 MHz blo-wwv signal on 15 July 2004 as observed with respect to the HIDIVE data compared to the flare-induced absorption predicted by the AbbyNormal model, EHA model, and SWPC model.

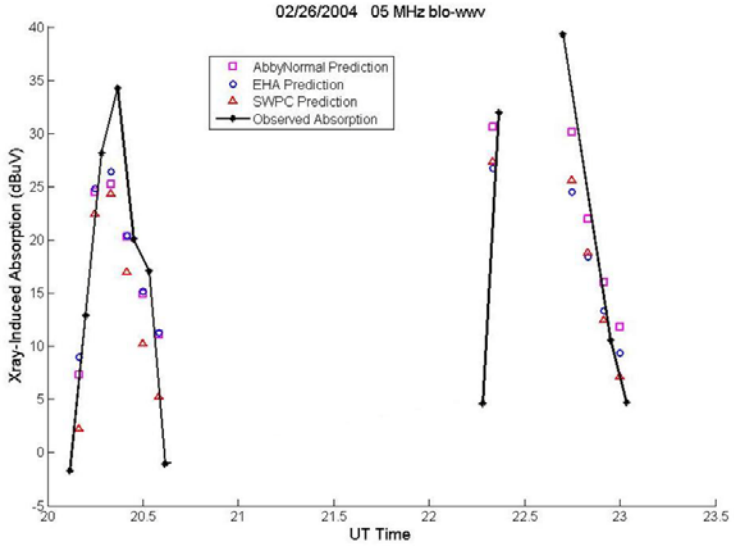

Figure A.2.3. X-ray flare-induced absorption of the 5 MHz blo-wwv signal on 26 February 2004 as observed with respect to the HIDIVE data compared to the flare-induced absorption predicted by the AbbyNormal model, EHA model, and SWPC model.

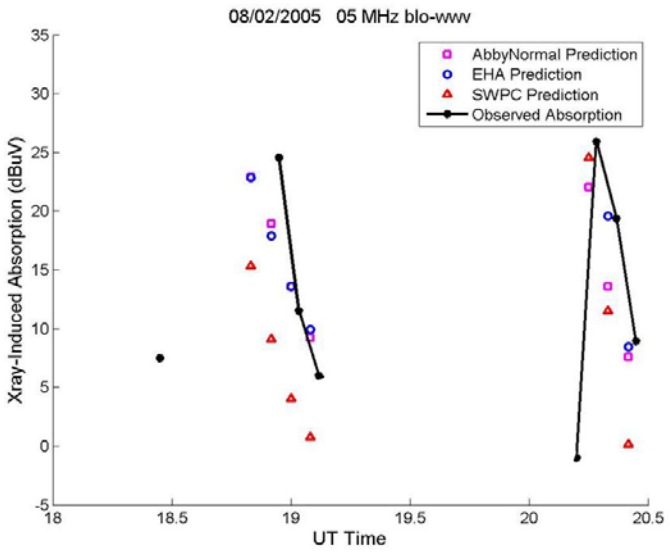

Figure A.2.4. X-ray flare-induced absorption of the 5 MHz blo-wwv signal on 2 August 2005 as observed with respect to the HIDIVE data compared to the flare-induced absorption predicted by the AbbyNormal model, EHA model, and SWPC model.

A.3 Signal Strength Predictions for the 10 MHz kf-wwv HIDIVE transmission

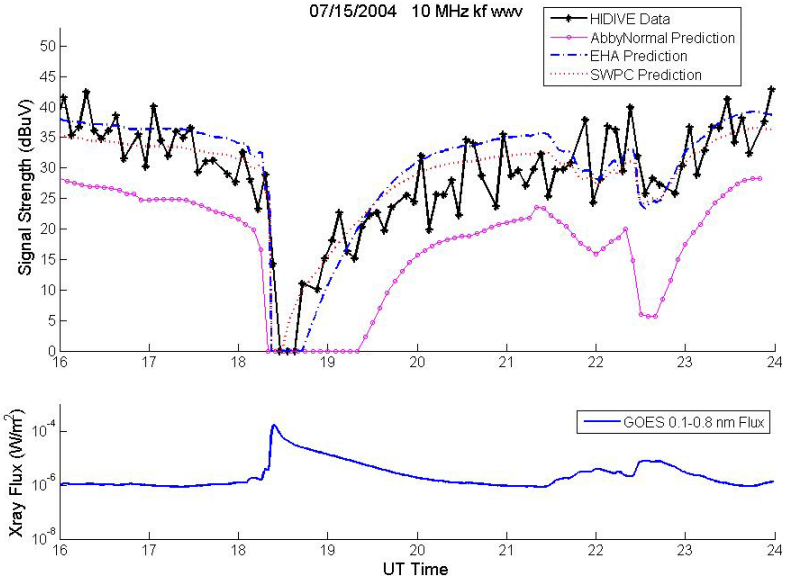

Figure A.3.1. AbbyNormal model prediction, EHA model prediction, and SWPC model prediction for the 10 MHz kf-wwv transmission on 15 July 2004 compared to HIDIVE signal strength data and GOES 0.1-0.8 nm flux data.

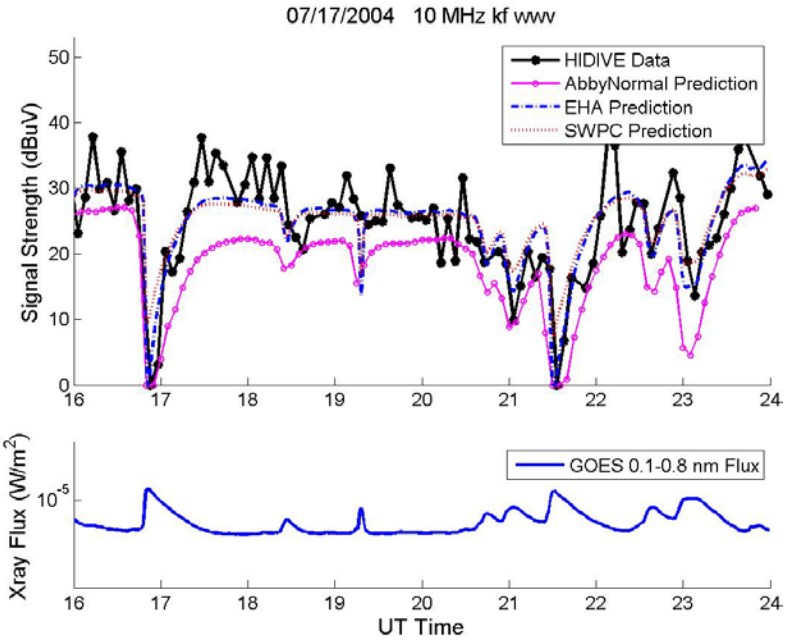

Figure A.3.2. AbbyNormal model prediction, EHA model prediction, and SWPC model prediction for the 10 MHz kf-wwv transmission on 17 July 2004 compared to HIDIVE signal strength data and GOES 0.1-0.8 nm flux data.

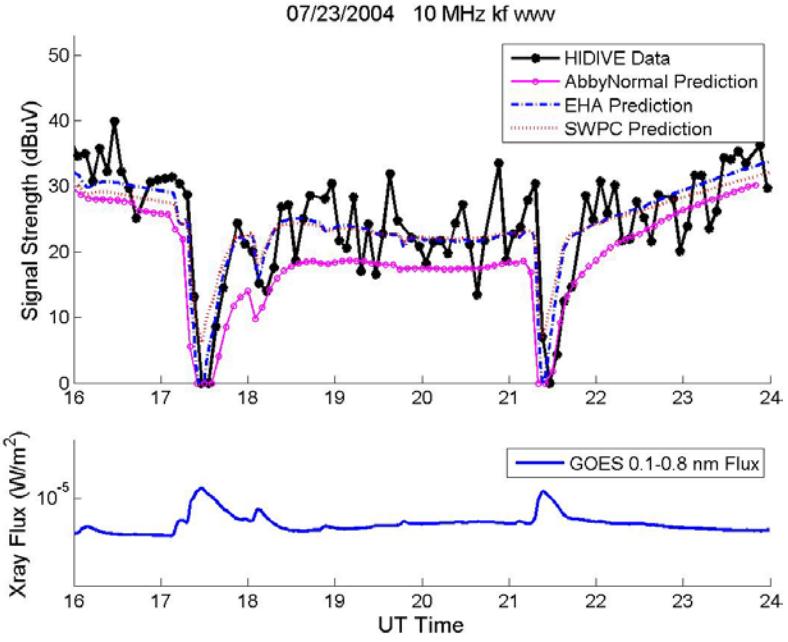

Figure A.3.3. AbbyNormal model prediction, EHA model prediction, and SWPC model prediction for the 10 MHz kf-wwv transmission on 23 July 2004 compared to HIDIVE signal strength data and GOES 0.1-0.8 nm flux data.

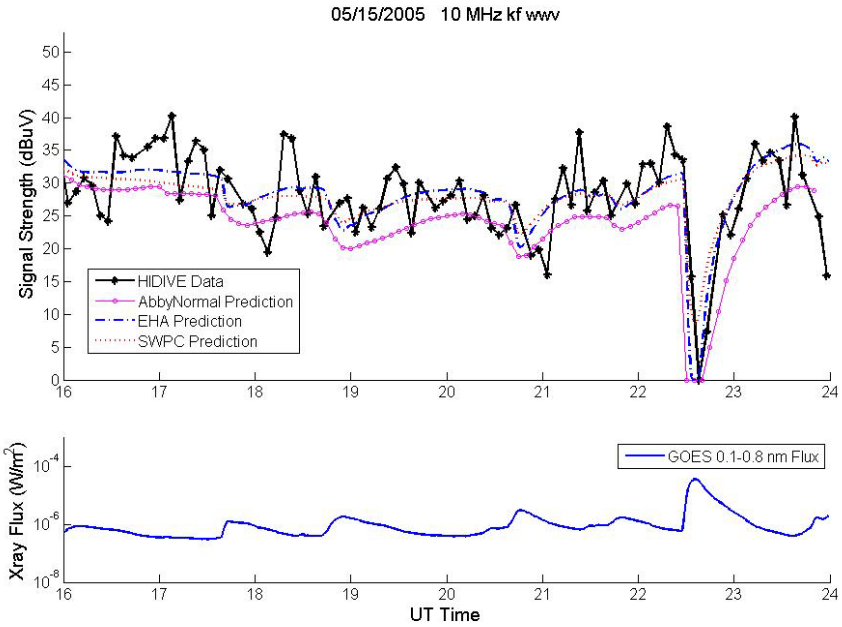

Figure A.3.4. AbbyNormal model prediction, EHA model prediction, and SWPC model prediction for the 10 MHz kf-wwv transmission on 15 May 2005 compared to HIDIVE signal strength data and GOES 0.1-0.8 nm flux data.

A.4 X-ray Flare Induced Absorption Predictions for the 10 MHz kf-wwv Signal

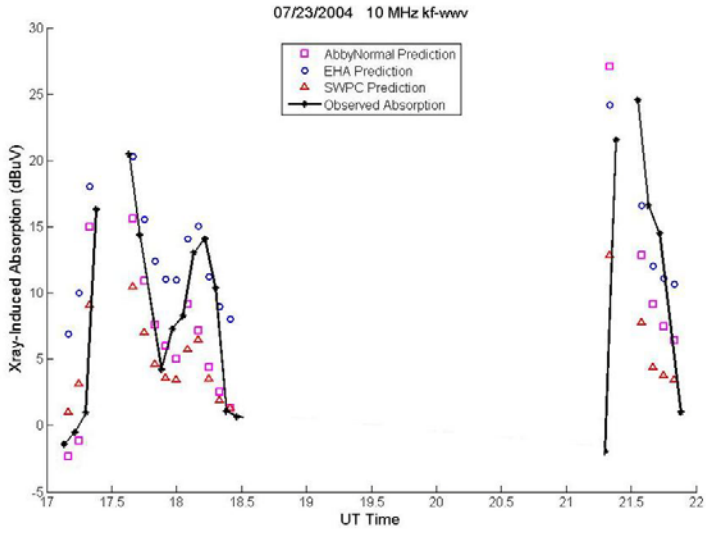

Figure A. 4.1. X-ray flare-induced absorption of the 10 MHz kf-wwv signal on 23 July 2004 as observed with respect to the HIDIVE data compared to the flare-induced absorption predicted by the AbbyNormal model, EHA model, and SWPC model.

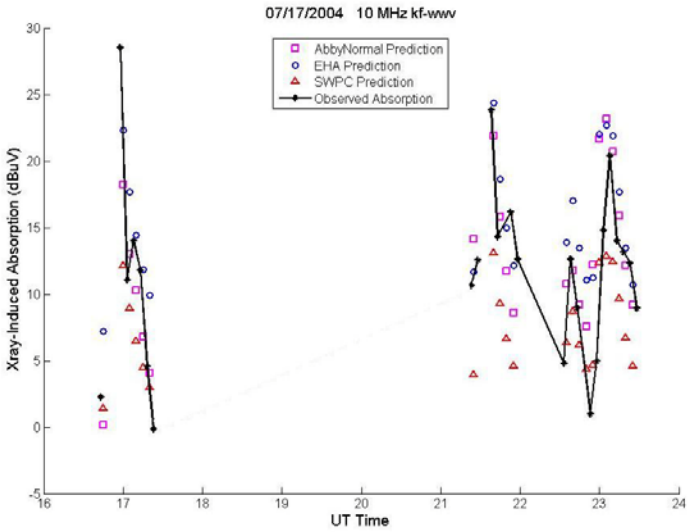

Figure A. 4.2. X-ray flare-induced absorption of the 10 MHz kf-wwv signal on 17 July 2004 as observed with respect to the HIDIVE data compared to the flare-induced absorption predicted by the AbbyNormal model, EHA model, and SWPC model.

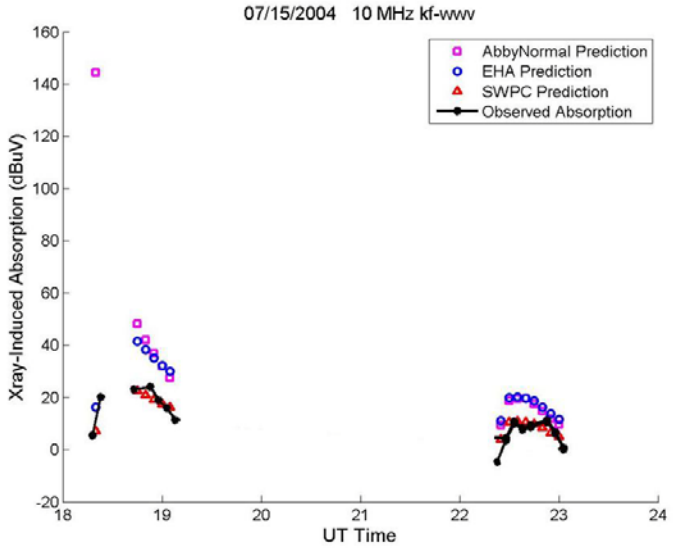

Figure A. 4.3. X-ray flare-induced absorption of the 10 MHz kf-wwv signal on 15 July 2004 as observed with respect to the HIDIVE data compared to the flare-induced absorption predicted by the AbbyNormal model, EHA model, and SWPC model.

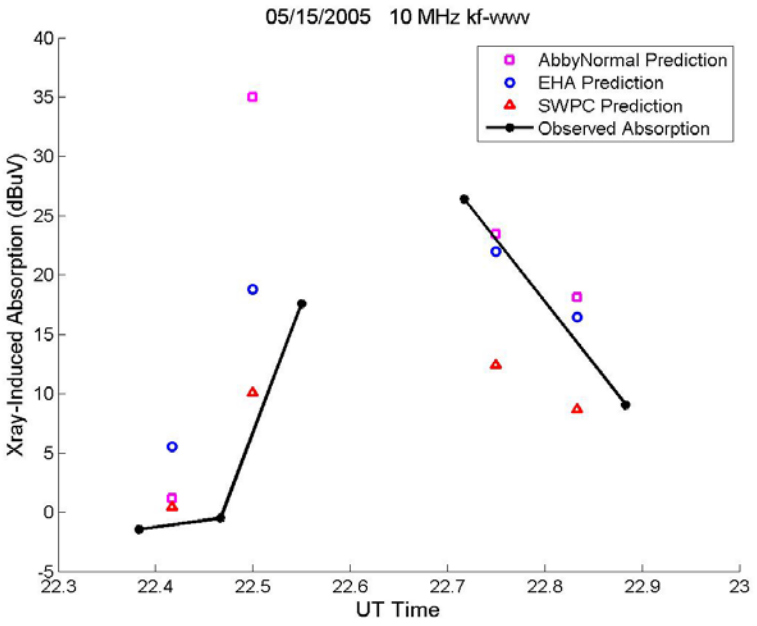

Figure A. 4.4. X-ray flare-induced absorption of the 10 MHz kf-wwv signal on 5 May 2005 as observed with respect to the HIDIVE data compared to the flare-induced absorption predicted by the AbbyNormal model, EHA model, and SWPC model.

A.5 Signal Strength Predictions for the 15 MHz kf-wwv HIDIVE transmission

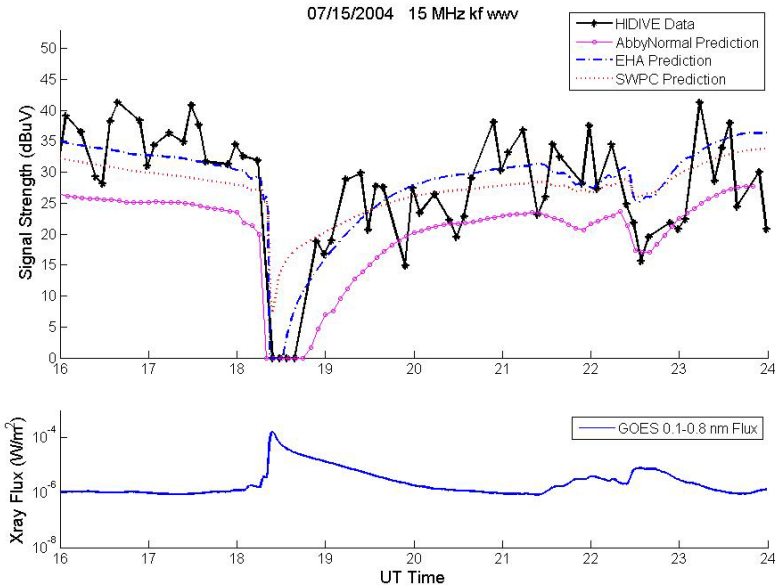

Figure A.5.1. AbbyNormal model prediction, EHA model prediction, and SWPC model prediction for the 15 MHz kf-wwv transmission on 15 July 2004 compared to HIDIVE signal strength data and GOES 0.1-0.8 nm flux data.

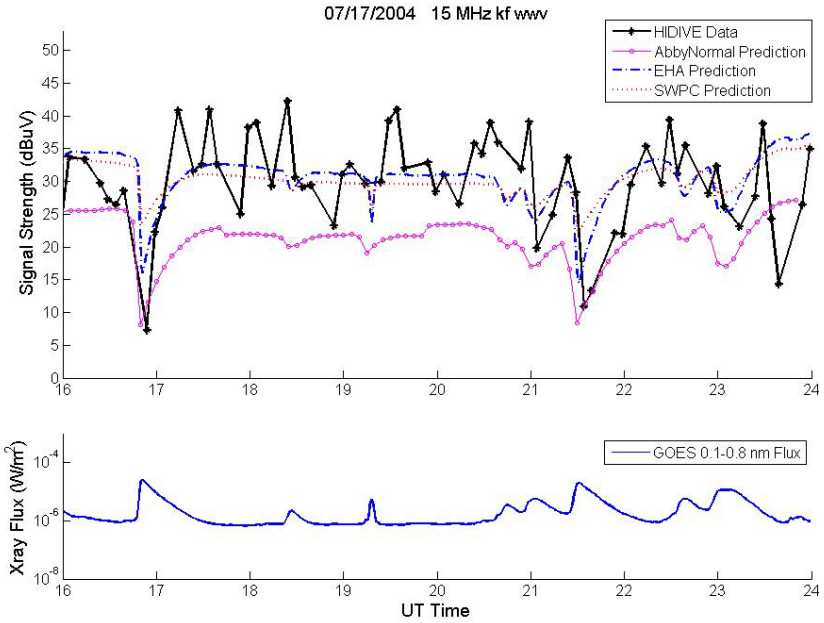

Figure A.5.2. AbbyNormal model prediction, EHA model prediction, and SWPC model prediction for the 15 MHz kf-wwv transmission on 17 July 2004 compared to HIDIVE signal strength data and GOES 0.1-0.8 nm flux data.

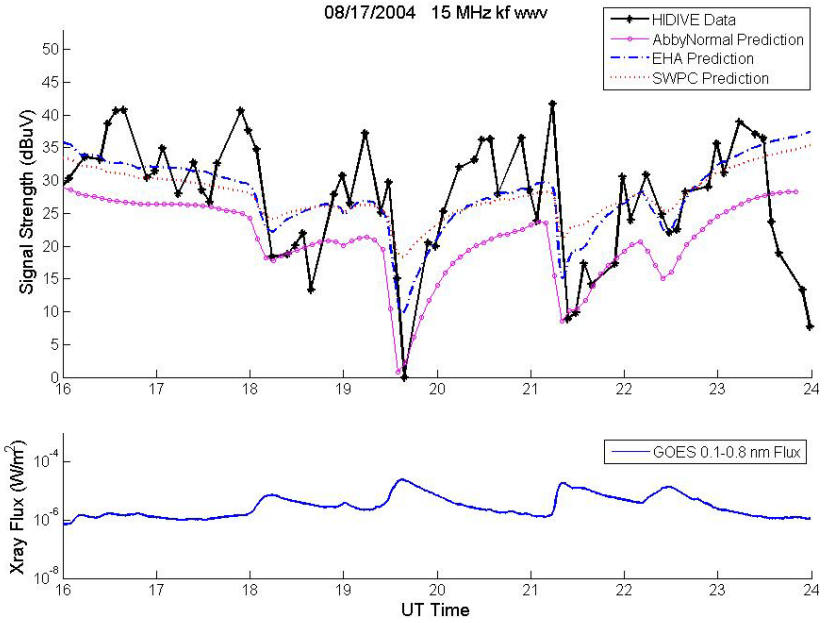

Figure A.5.3. AbbyNormal model prediction, EHA model prediction, and SWPC model prediction for the 15 MHz kf-wwv transmission on 17 August 2004 compared to HIDIVE signal strength data and GOES 0.1-0.8 nm flux data.

A.6 X-ray Flare Induced Absorption Predictions for the 15 MHz kf-wwv Signal

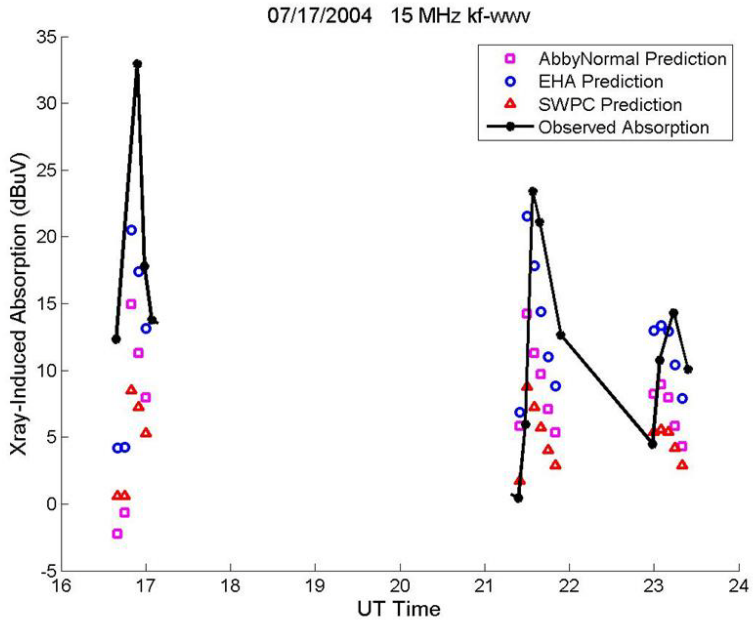

Figure A.6.1. X-ray flare-induced absorption of the 15 MHz kf-wwv signal on 17 July 2004 as observed with respect to the HIDIVE data compared to the flare-induced absorption predicted by the AbbyNormal model, EHA model, and SWPC model.

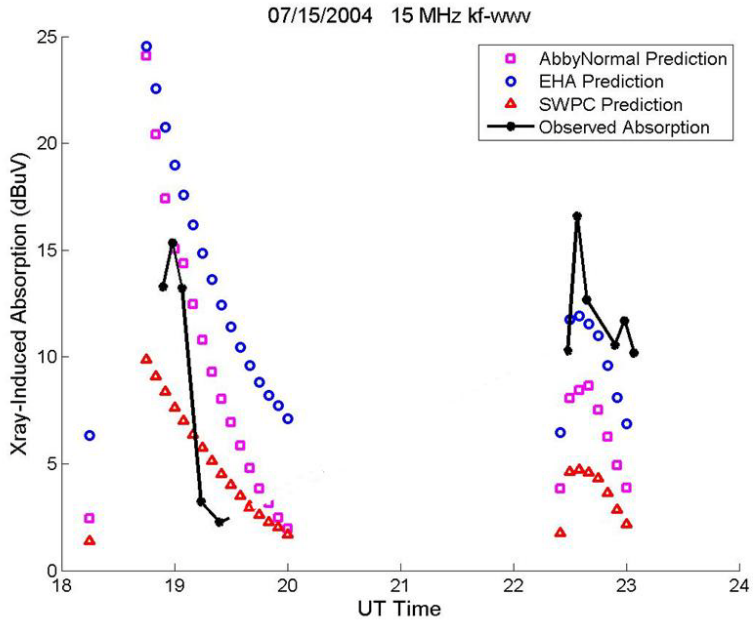

Figure A.6.2. X-ray flare-induced absorption of the 15 MHz kf-wwv signal on 15 July 2004 as observed with respect to the HIDIVE data compared to the flare-induced absorption predicted by the AbbyNormal model, EHA model, and SWPC model.

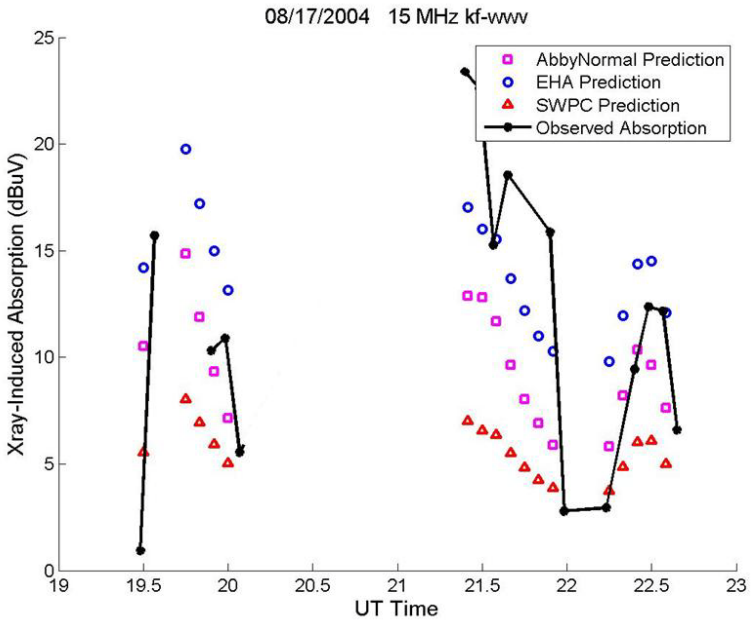

Figure A.6.1. X-ray flare-induced absorption of the 15 MHz kf-wwv signal on 17 August 2004 as observed with respect to the HIDIVE data compared to the flare-induced absorption predicted by the AbbyNormal model, EHA model, and SWPC model.

Appendix B. AbbyNormal model versions predictions of 5 MHz blo-wwv transmission

The figures in this section show the predictions obtained from three versions of the AbbyNormal model (§9.4) for the 5 MHz blo-wwv HIDIVE transmission on eleven nearly consecutive dates in January 2004, and each figure shows the signal strength predictions of the three AbbyNormal versions, HIDIVE data, and GOES data for a given date. The three AbbyNormal versions all differ in how the NO profile is defined within the model. The top panel in each figure shows the prediction produced by the original AbbyNormal version in which the NO density profile is defined by equation 9.3.1. The second panel in each figure shows the prediction from the AbbyNormal version in which the NO profile is defined by the Empirical NO Model [*Marsh et al.*, 2004], and the third panel shows the prediction from the version in which HALOE data are used to define atmospheric NO densities. Also, GOES 0.1-0.8 nm flux data for the given date are shown in the bottom panel of each figure.

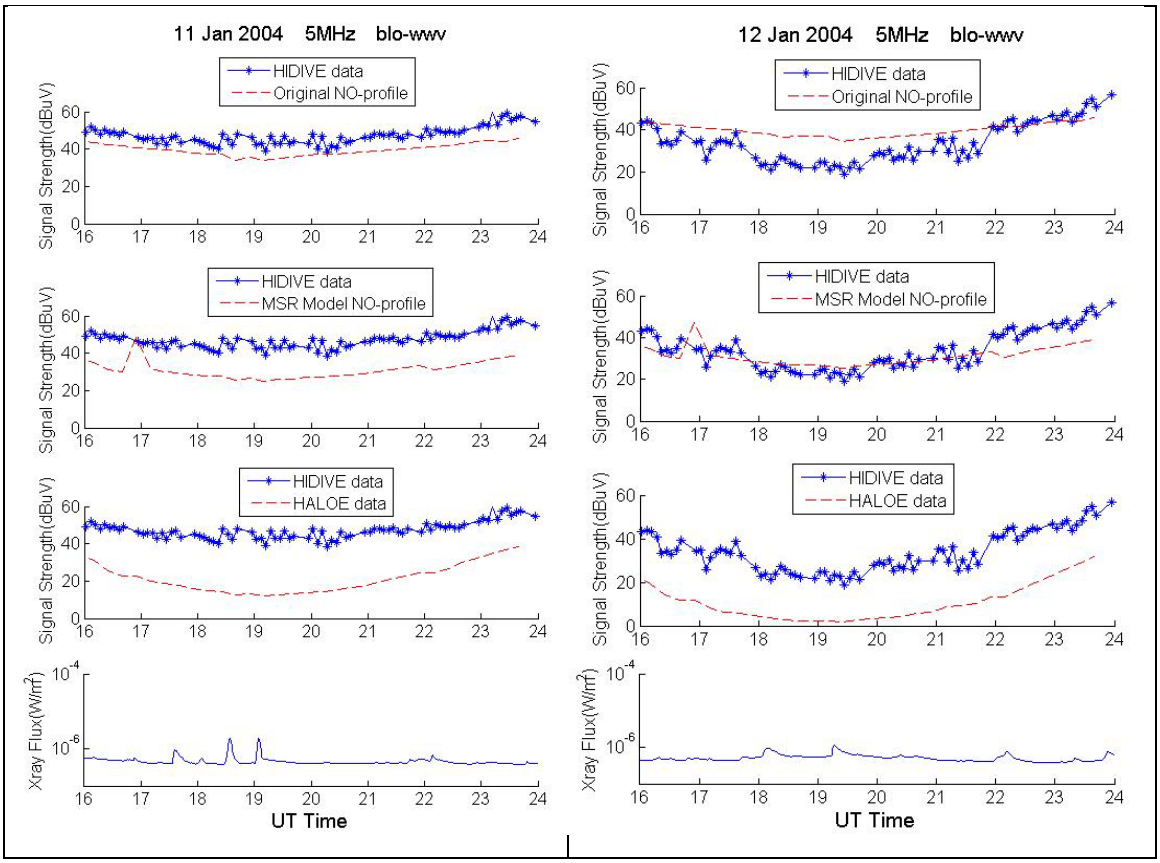

Figure B.1. HIDIVE data, GOES data, and AbbyNormal version predictions for the 5 MHz blo-wwv transmission on 11 January 2004.

Figure B.2. HIDIVE data, GOES data, and AbbyNormal version predictions for the 5 MHz blo-wwv transmission on 12 January 2004.

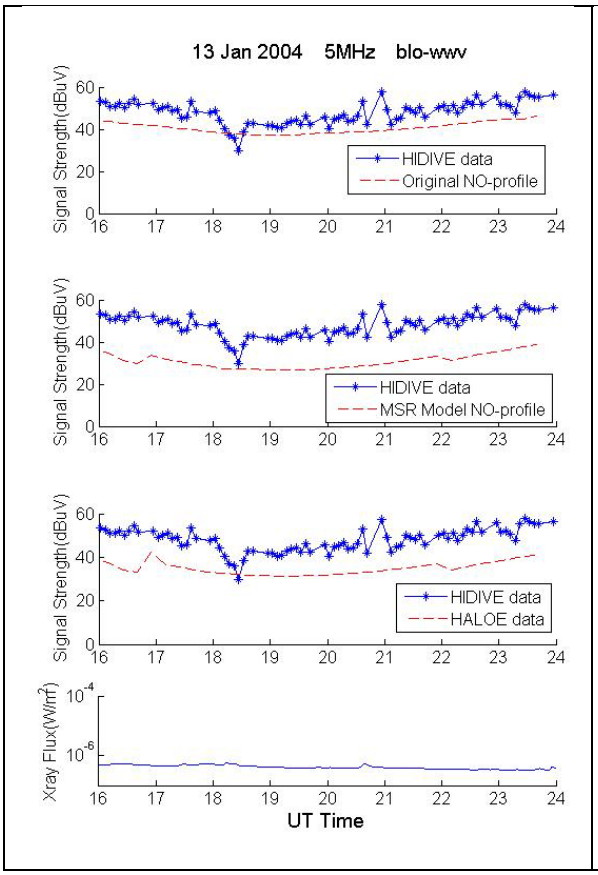

Figure B.3. HIDIVE data, GOES data, and AbbyNormal version predictions for the 5 MHz blo-wwv transmission on 13 January 2004.

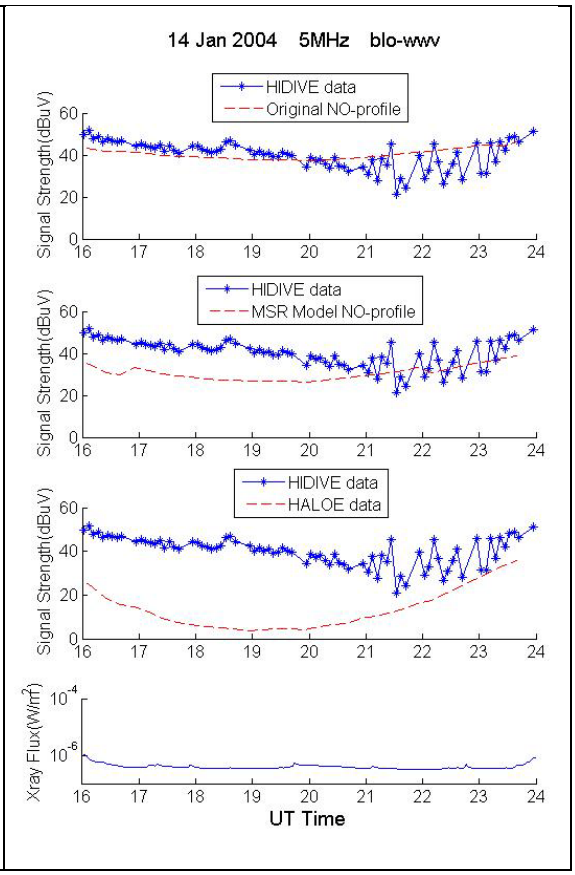

Figure B.4. HIDIVE data, GOES data, and AbbyNormal version predictions for the 5 MHz blo-wwv transmission on 14 January 2004.

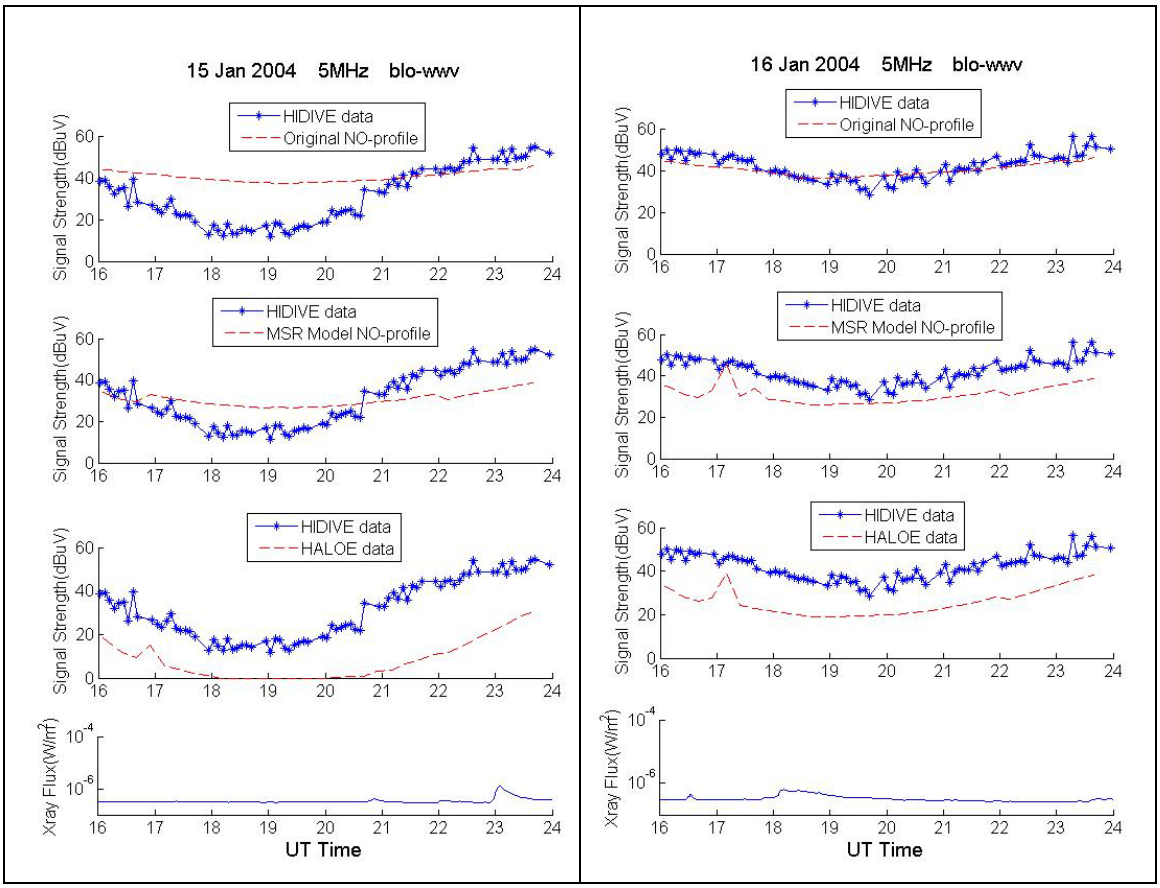

Figure B.5. HIDIVE data, GOES data, and AbbyNormal version predictions for the 5 MHz blo-wwv transmission on 15 January 2004.

Figure B.6. HIDIVE data, GOES data, and AbbyNormal version predictions for the 5 MHz blo-wwv transmission on 16 January 2004.

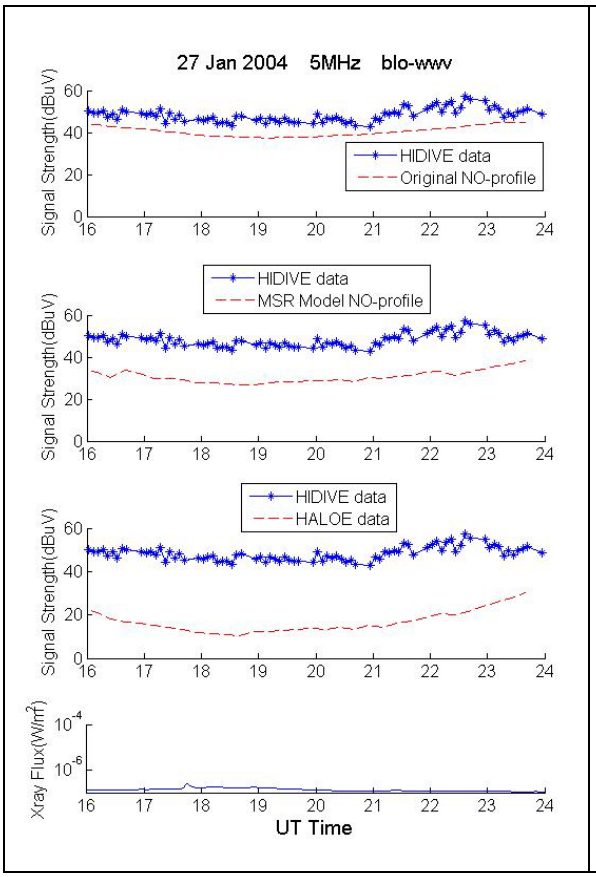

Figure B.7. HIDIVE data, GOES data, and AbbyNormal version predictions for the 5 MHz blo-wwv transmission on 27 January 2004.

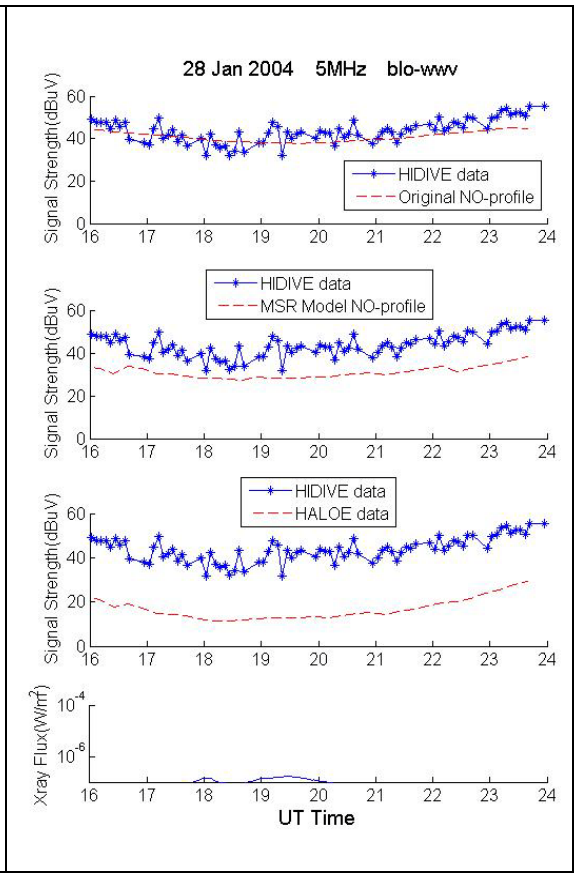

Figure B.8. HIDIVE data, GOES data, and AbbyNormal version predictions for the 5 MHz blo-wwv transmission on 28 January 2004.

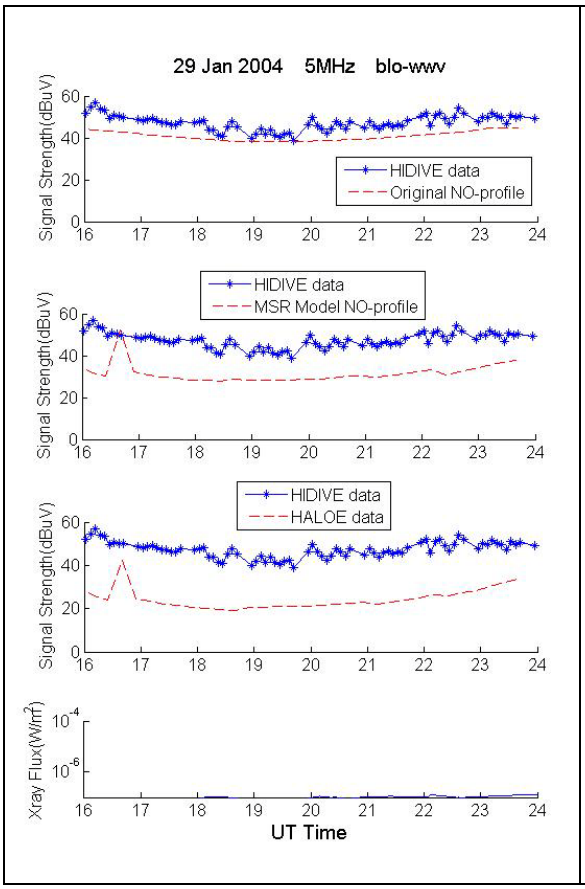

Figure B.9. HIDIVE data, GOES data, and AbbyNormal version predictions for the 5 MHz blo-wwv transmission on 29 January 2004.

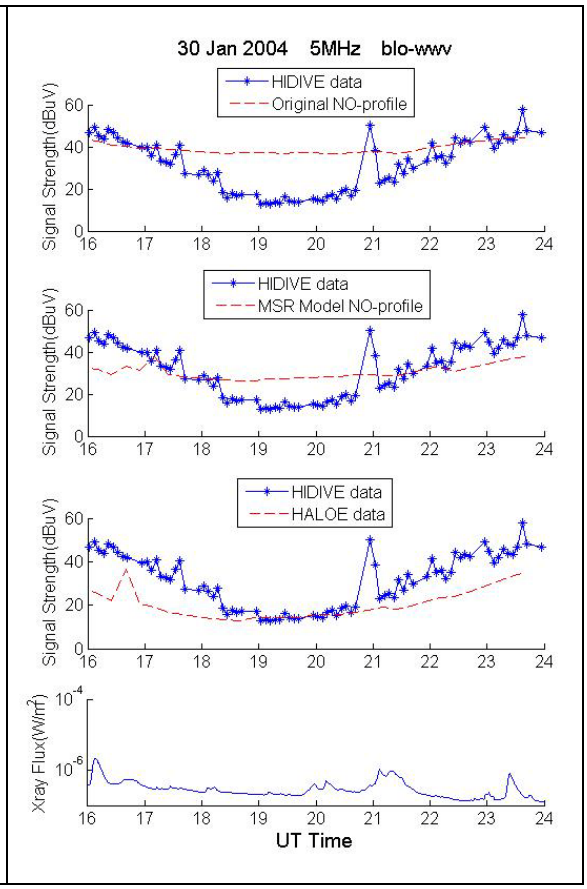

Figure B.10. HIDIVE data, GOES data, and AbbyNormal version predictions for the 5 MHz blo-wwv transmission on 30 January 2004.

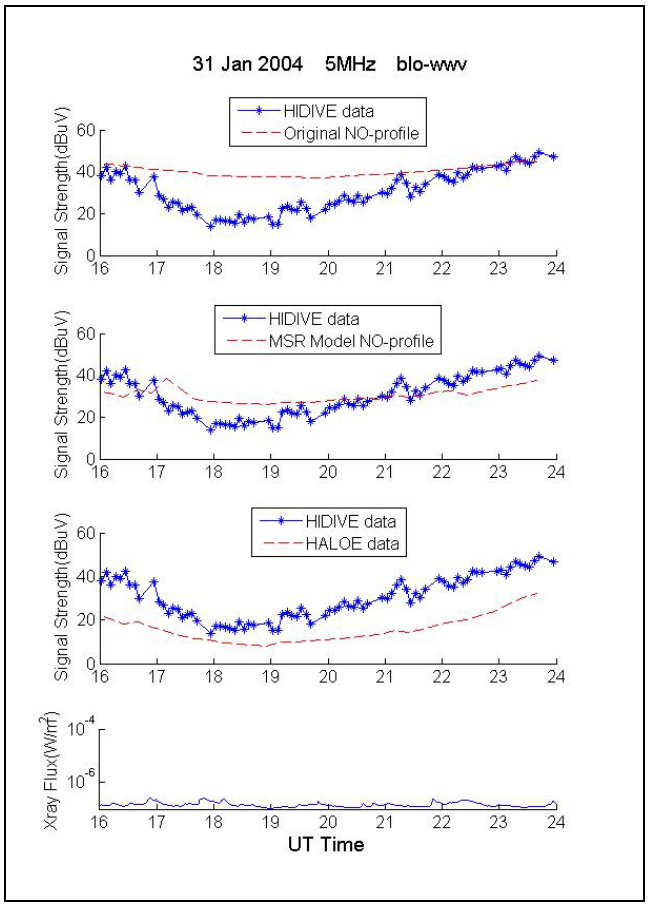

Figure B.11. HIDIVE data, GOES data, and AbbyNormal version predictions for the 5 MHz blo-wwv transmission on 31 January 2004.

Appendix C. AbbyNormal model versions predictions of 10 MHz blo-wwv transmission

The figures in this section show the predictions obtained from three versions of the AbbyNormal model (§9.4) for the 10 MHz blo-wwv HIDIVE transmission on eleven nearly consecutive dates in January 2004, and each figure shows the signal strength predictions of the three AbbyNormal versions, HIDIVE data, and GOES data for a given date. The three AbbyNormal versions all differ in how the NO profile is defined within the model. The top panel in each figure shows the prediction produced by the original AbbyNormal version in which the NO density profile is defined by equation 9.3.1. The second panel in each figure shows the prediction from the AbbyNormal version in which the NO profile is defined by the Empirical NO Model [*Marsh et al.*, 2004], and the third panel shows the prediction from the version in which HALOE data are used to define atmospheric NO densities. Also, GOES 0.1-0.8 nm flux data for the given date are shown in the bottom panel of each figure.

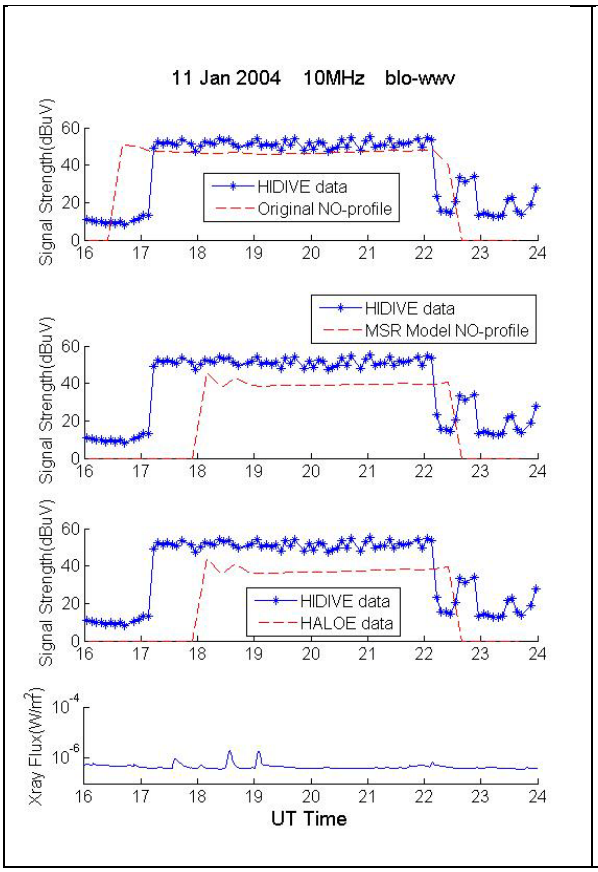

Figure C.1. HIDIVE data, GOES data, and AbbyNormal version predictions for the 10 MHz blo-wwv transmission on 11 January 2004.

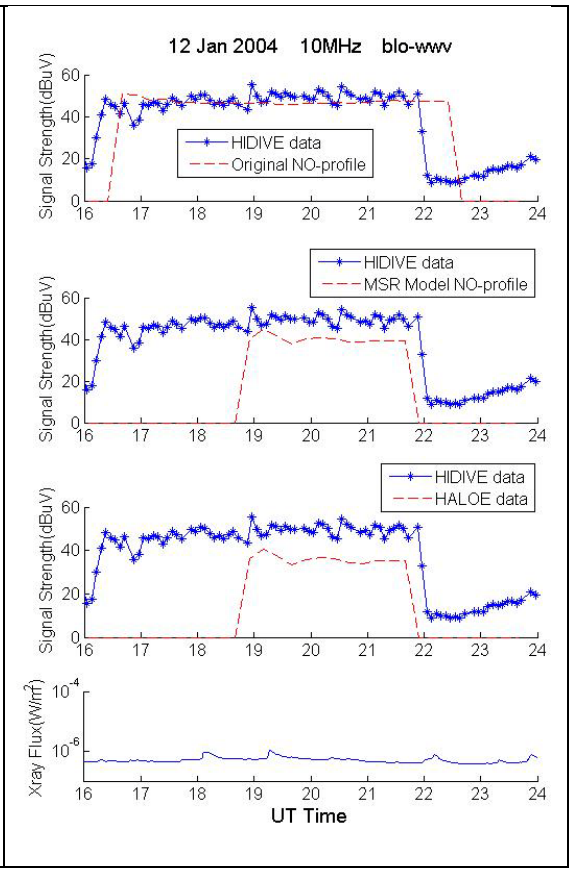

Figure C.2. HIDIVE data, GOES data, and AbbyNormal version predictions for the 10 MHz blo-wwv transmission on 12 January 2004.

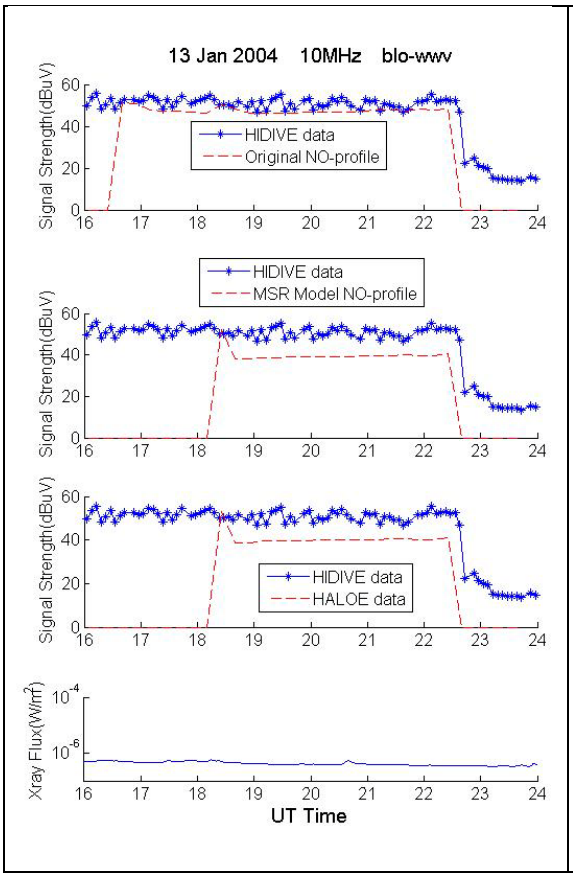

Figure C.3. HIDIVE data, GOES data, and AbbyNormal version predictions for the 10 MHz blo-wwv transmission on 13 January 2004.

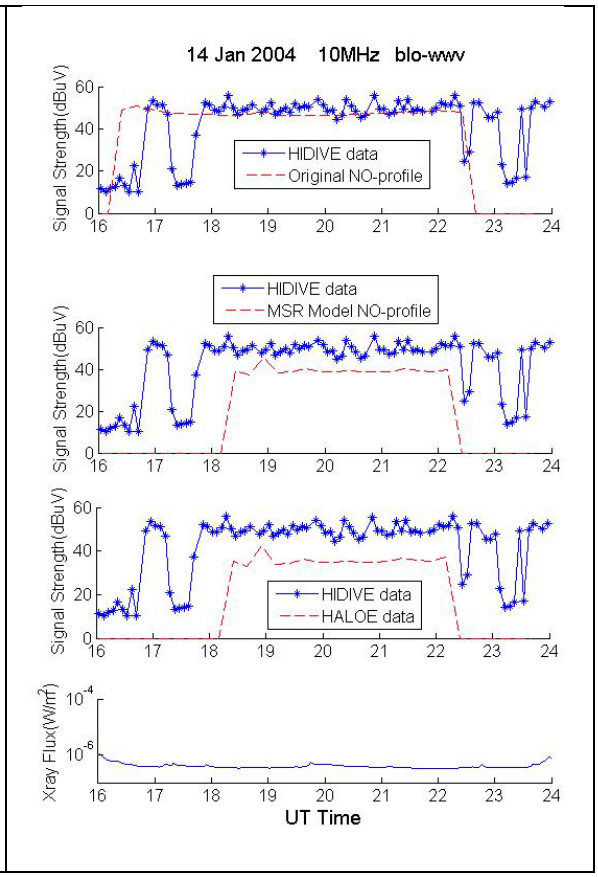

Figure C.4. HIDIVE data, GOES data, and AbbyNormal version predictions for the 10 MHz blo-wwv transmission on 14 January 2004.

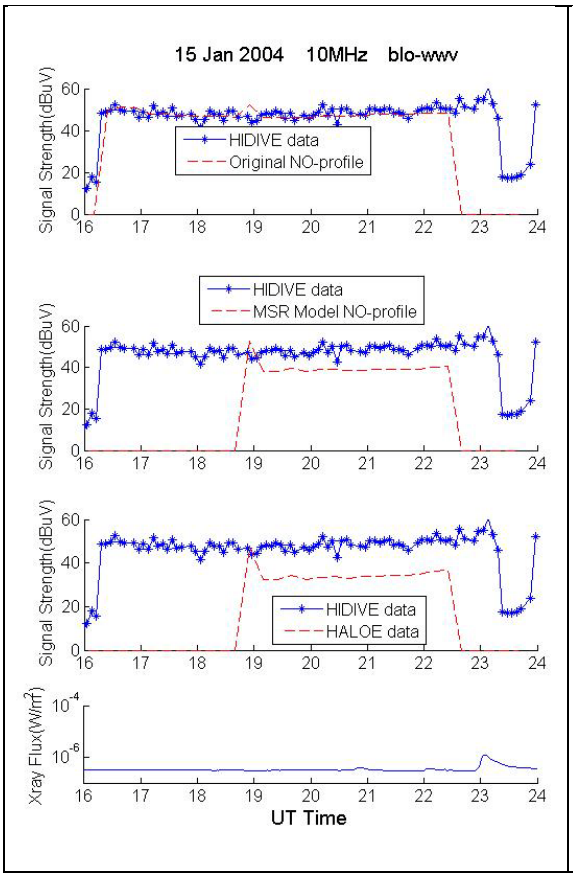

Figure C.5. HIDIVE data, GOES data, and AbbyNormal version predictions for the 10 MHz blo-wwv transmission on 15 January 2004.

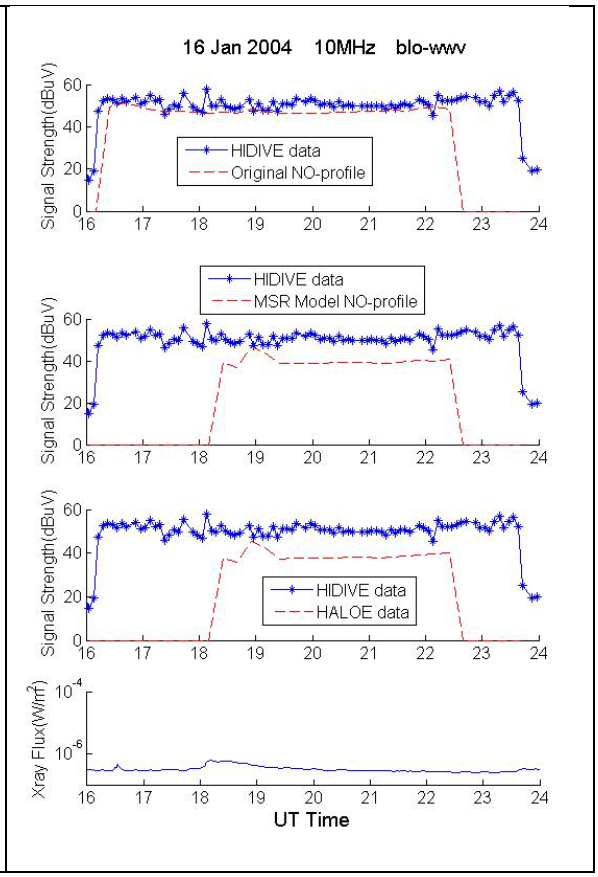

Figure C.6. HIDIVE data, GOES data, and AbbyNormal version predictions for the 10 MHz blo-wwv transmission on 16 January 2004.

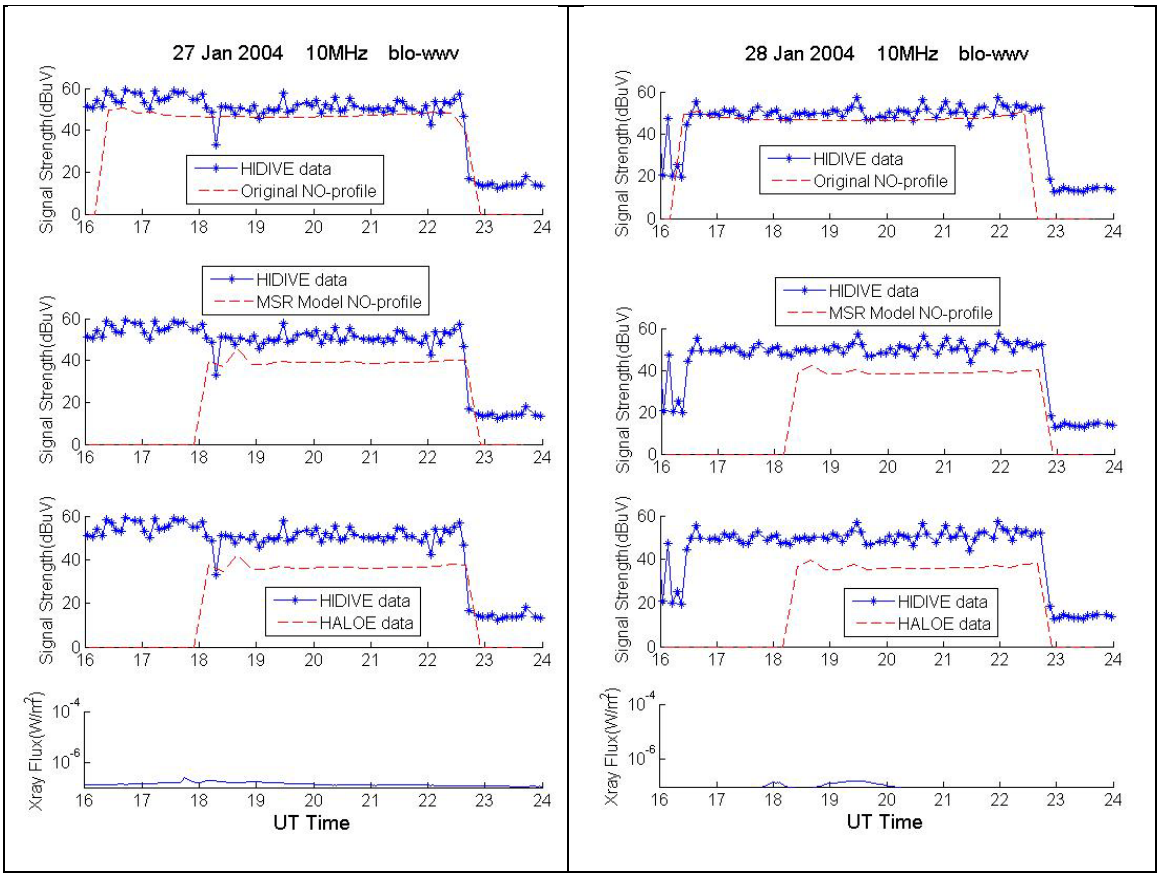

Figure C.7. HIDIVE data, GOES data, and AbbyNormal version predictions for the 10 MHz blo-wwv transmission on 27 January 2004.

Figure C.8. HIDIVE data, GOES data, and AbbyNormal version predictions for the 10 MHz blo-wwv transmission on 28 January 2004.

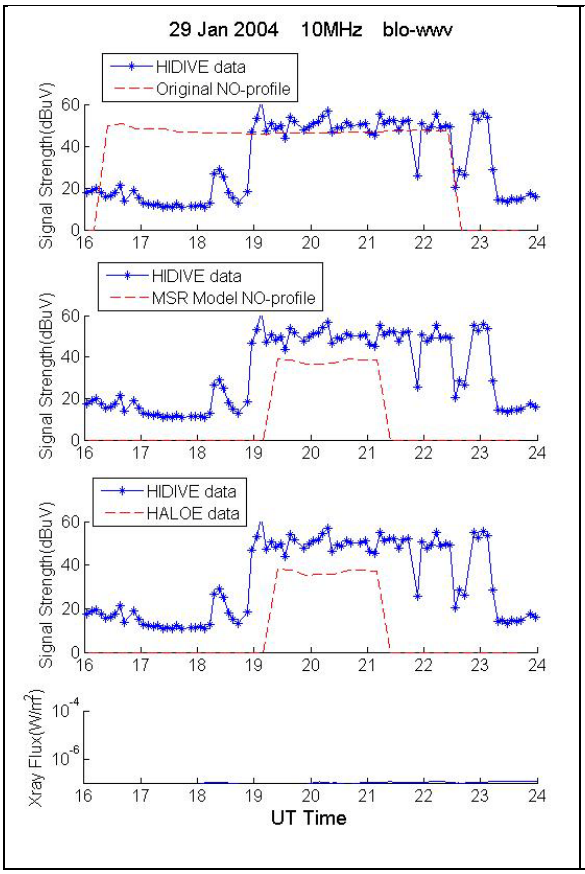

Figure C.9. HIDIVE data, GOES data, and AbbyNormal version predictions for the 10 MHz blo-wwv transmission on 29 January 2004.

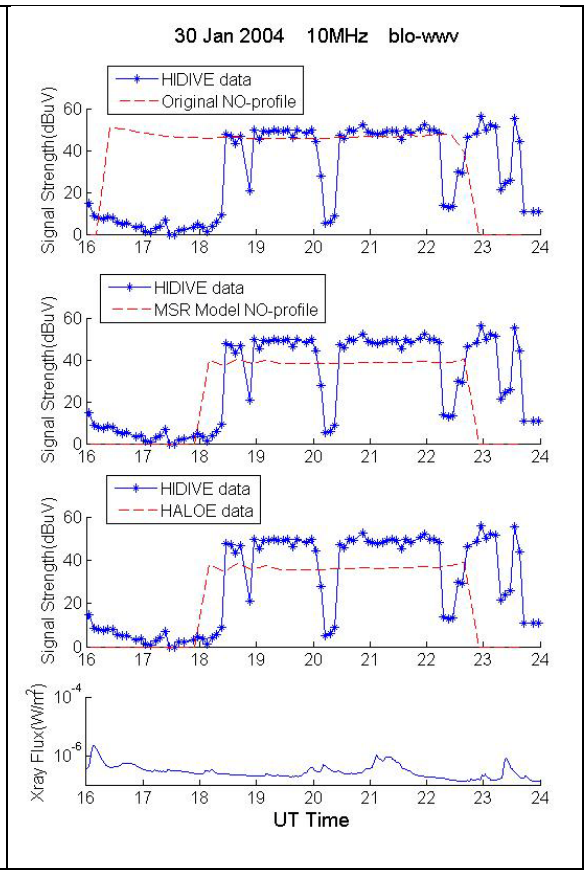

Figure C.10. HIDIVE data, GOES data, and AbbyNormal version predictions for the 10 MHz blo-wwv transmission on 30 January 2004.

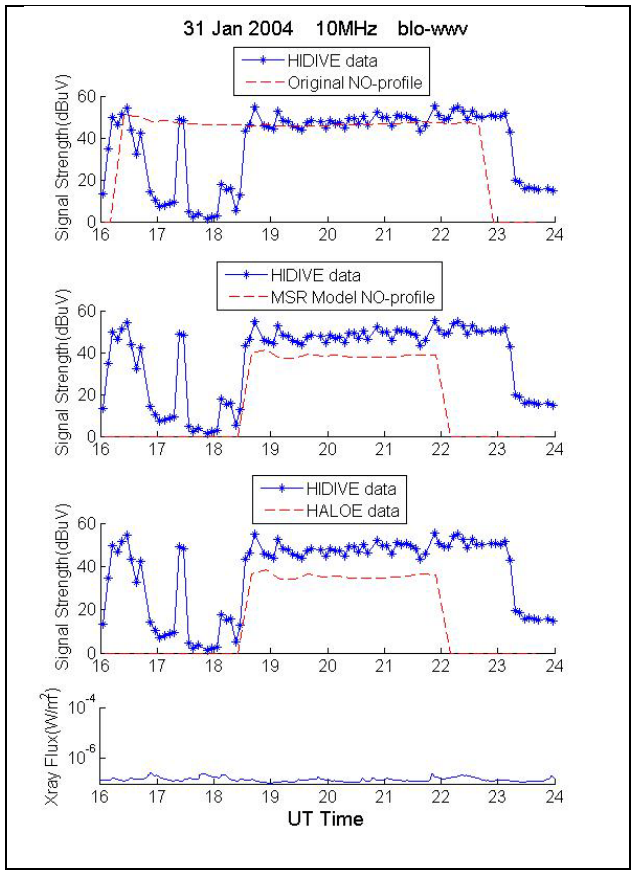

Figure C.11. HIDIVE data, GOES data, and AbbyNormal version predictions for the 10 MHz blo-wwv transmission on 31 January 2004.

Appendix D. AbbyNormal model versions predictions of 5 MHz kf-wwv transmission

The figures in this section show the predictions obtained from three versions of the AbbyNormal model (§9.4) for the 5 MHz kf-wwv HIDIVE transmission on eleven nearly consecutive dates in January 2004, and each figure shows the signal strength predictions of the three AbbyNormal versions, HIDIVE data, and GOES data for a given date. The three AbbyNormal versions all differ in how the NO profile is defined within the model. The top panel in each figure shows the prediction produced by the original AbbyNormal version in which the NO density profile is defined by equation 9.3.1. The second panel in each figure shows the prediction from the AbbyNormal version in which the NO profile is defined by the Empirical NO Model [*Marsh et al.*, 2004], and the third panel shows the prediction from the version in which HALOE data are used to define atmospheric NO densities. Also, GOES 0.1-0.8 nm flux data for the given date are shown in the bottom panel of each figure.

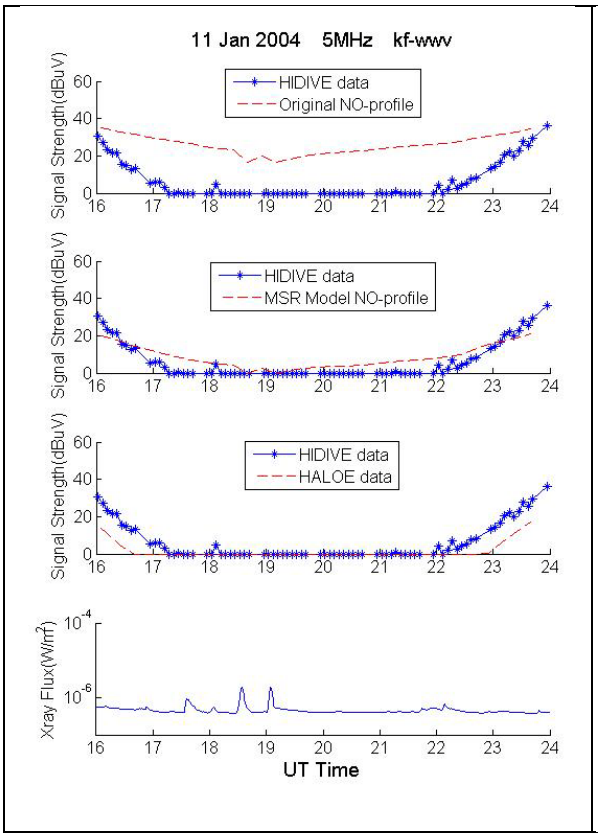

Figure D.1. HIDIVE data, GOES data, and AbbyNormal version predictions for the 5 MHz kf-wwv transmission on 11 January 2004.

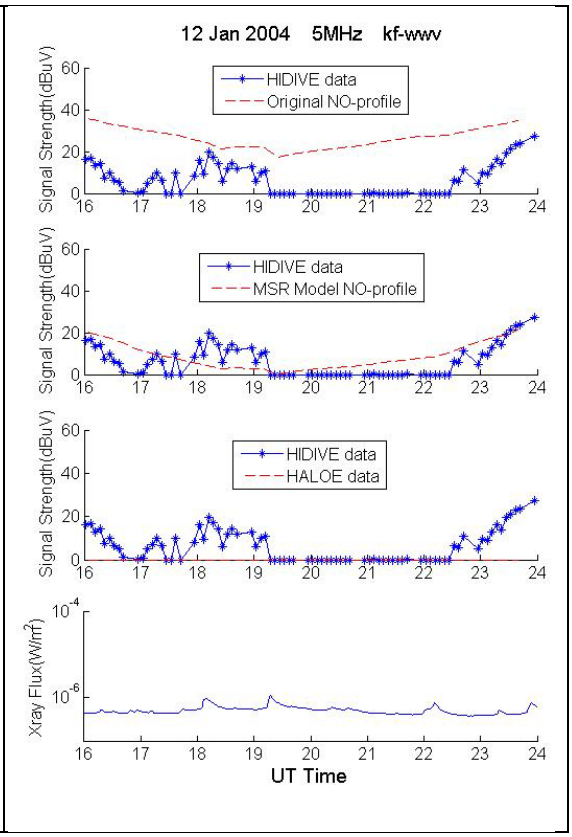

Figure D.2. HIDIVE data, GOES data, and AbbyNormal version predictions for the 5 MHz kf-wwv transmission on 12 January 2004.

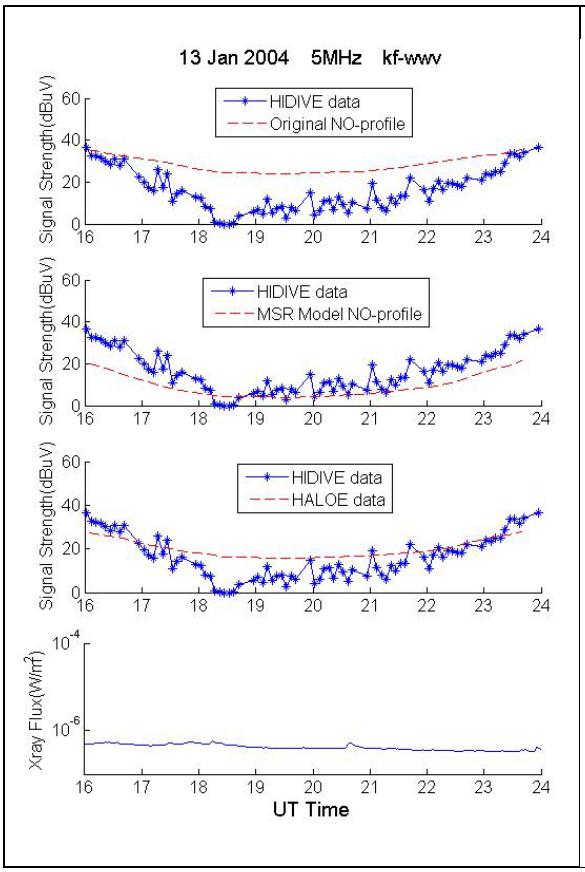

Figure D.3. HIDIVE data, GOES data, and AbbyNormal version predictions for the 5 MHz kf-wwv transmission on 13 January 2004.

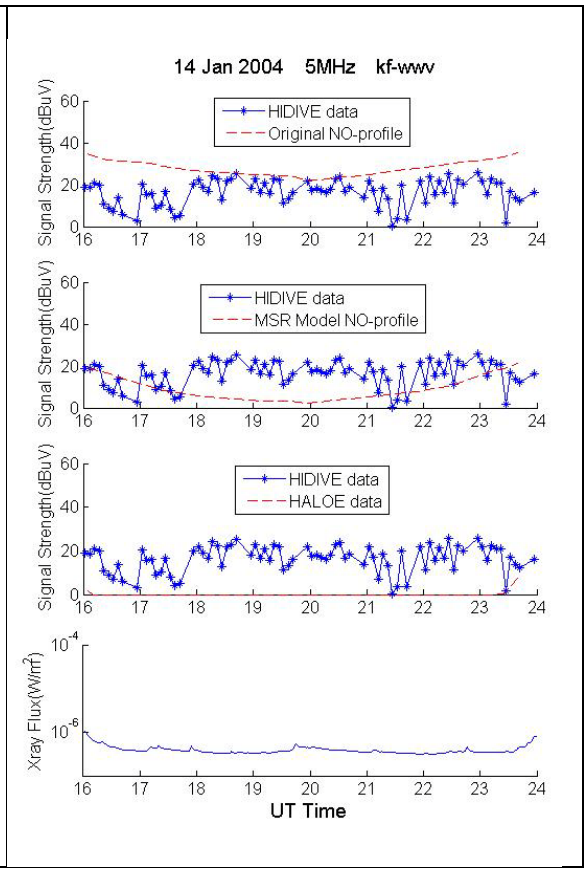

Figure D.4. HIDIVE data, GOES data, and AbbyNormal version predictions for the 5 MHz kf-wwv transmission on 14 January 2004.

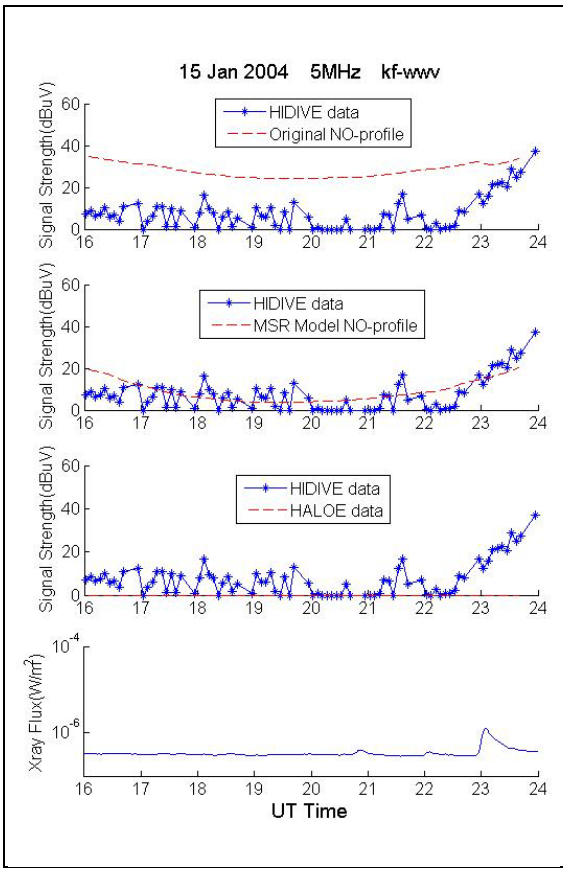

Figure D.5. HIDIVE data, GOES data, and AbbyNormal version predictions for the 5 MHz kf-wwv transmission on 15 January 2004.

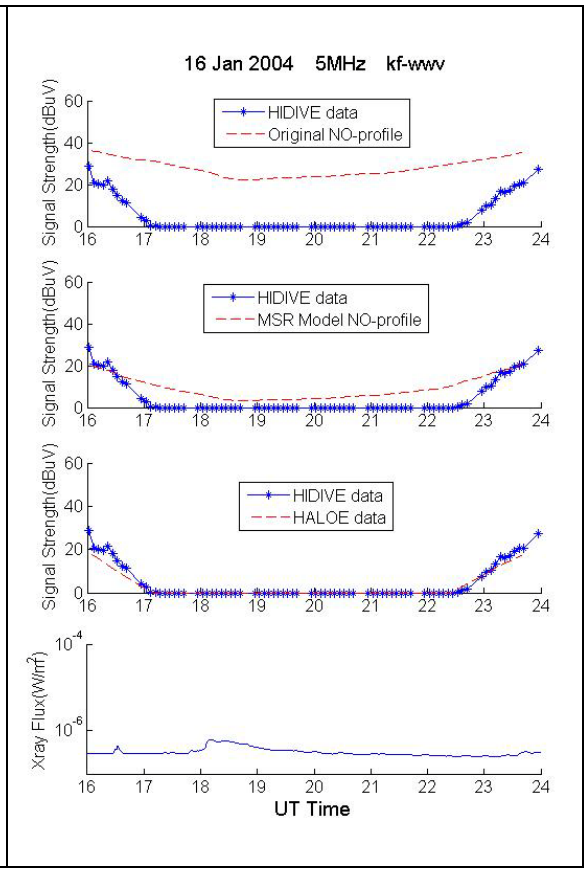

Figure D.6. HIDIVE data, GOES data, and AbbyNormal version predictions for the 5 MHz kf-wwv transmission on 16 January 2004.

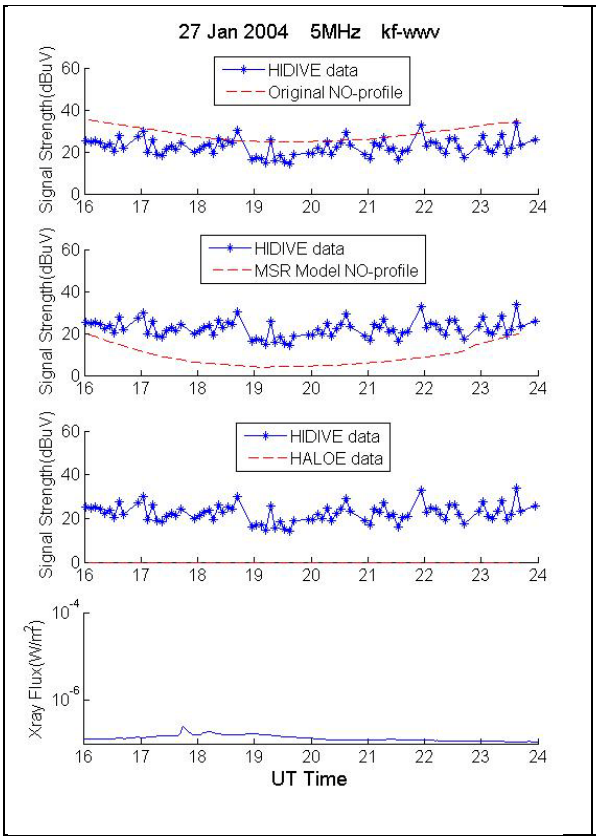

Figure D7. HIDIVE data, GOES data, and AbbyNormal version predictions for the 5 MHz kf-wwv transmission on 27 January 2004.

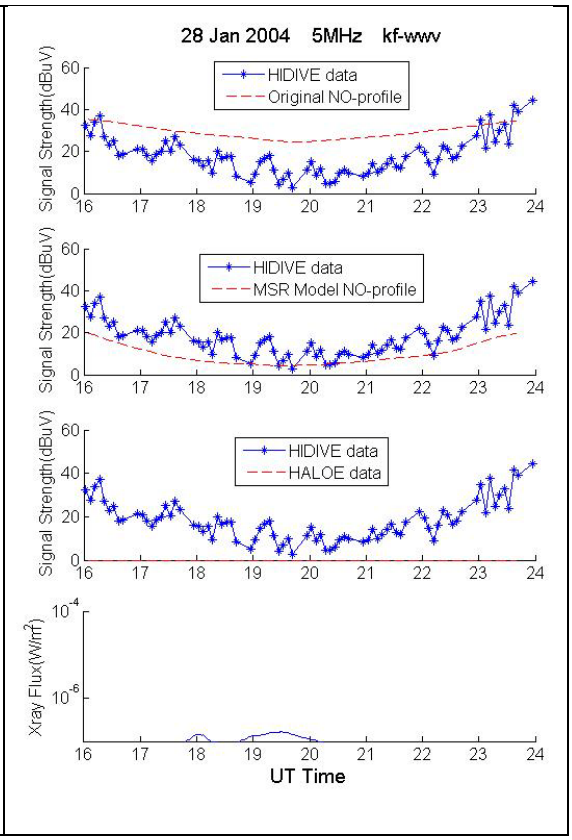

Figure D.8. HIDIVE data, GOES data, and AbbyNormal version predictions for the 5 MHz kf-wwv transmission on 28 January 2004.

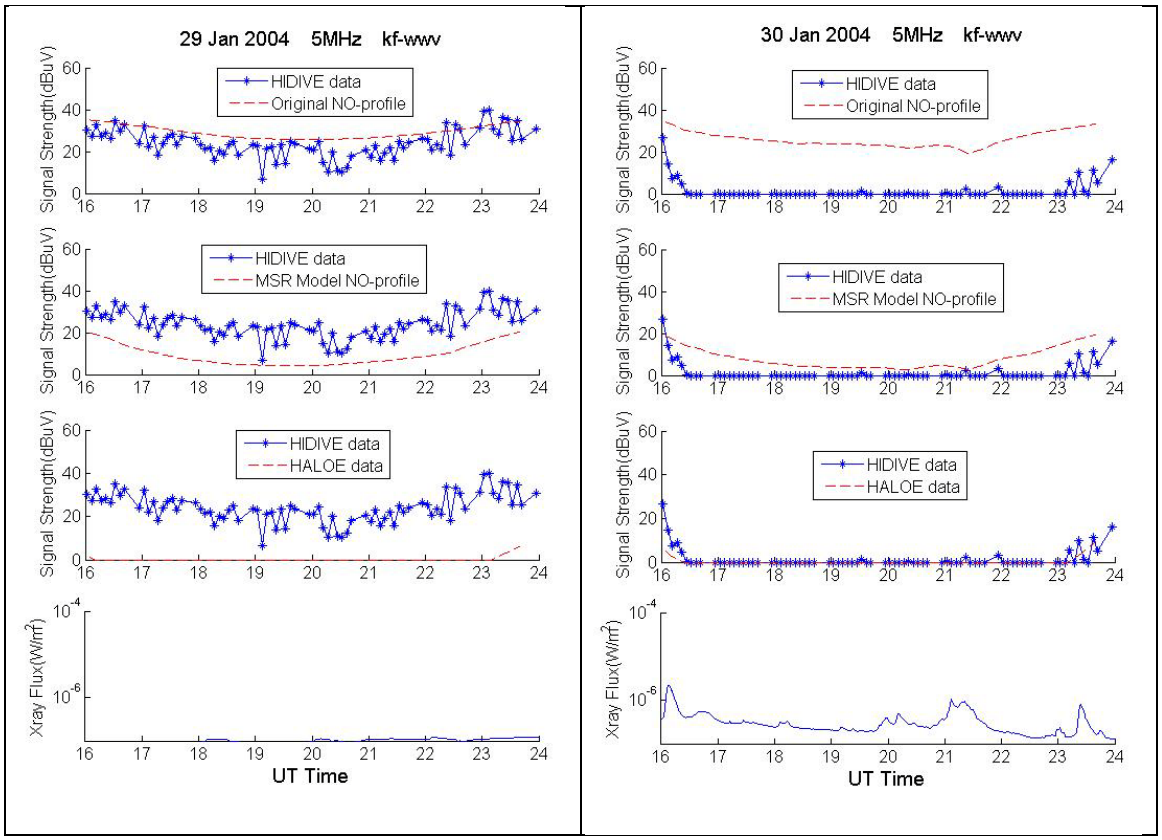

Figure D.9. HIDIVE data, GOES data, and AbbyNormal version predictions for the 5 MHz kf-wwv transmission on 29 January 2004.

Figure D.10. HIDIVE data, GOES data, and AbbyNormal version predictions for the 5 MHz kf-wwv transmission on 30 January 2004.

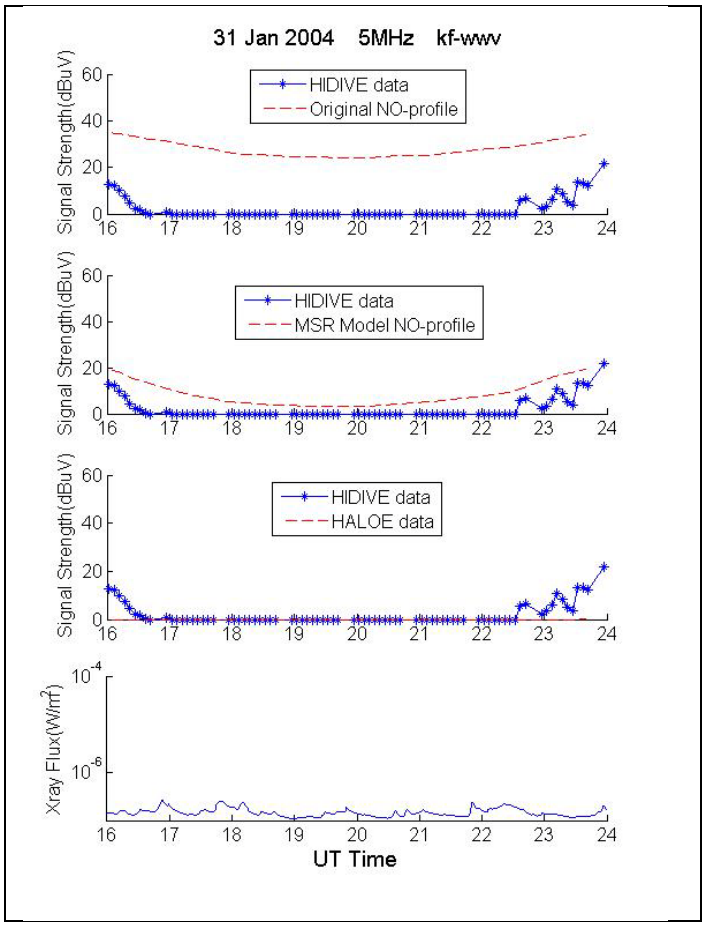

Figure D.11. HIDIVE data, GOES data, and AbbyNormal version predictions for the 5 MHz kf-wwv transmission on 31 January 2004.

Appendix E. AbbyNormal model versions predictions of 10 MHz kf-wwv transmission

The figures in this section show the predictions obtained from three versions of the AbbyNormal model (§9.4) for the 10 MHz kf-wwv HIDIVE transmission on eleven nearly consecutive dates in January 2004, and each figure shows the signal strength predictions of the three AbbyNormal versions, HIDIVE data, and GOES data for a given date. The three AbbyNormal versions all differ in how the NO profile is defined within the model. The top panel in each figure shows the prediction produced by the original AbbyNormal version in which the NO density profile is defined by equation 9.3.1. The second panel in each figure shows the prediction from the AbbyNormal version in which the NO profile is defined by the Empirical NO Model [*Marsh et al.*, 2004], and the third panel shows the prediction from the version in which HALOE data are used to define atmospheric NO densities. Also, GOES 0.1-0.8 nm flux data for the given date are shown in the bottom panel of each figure.

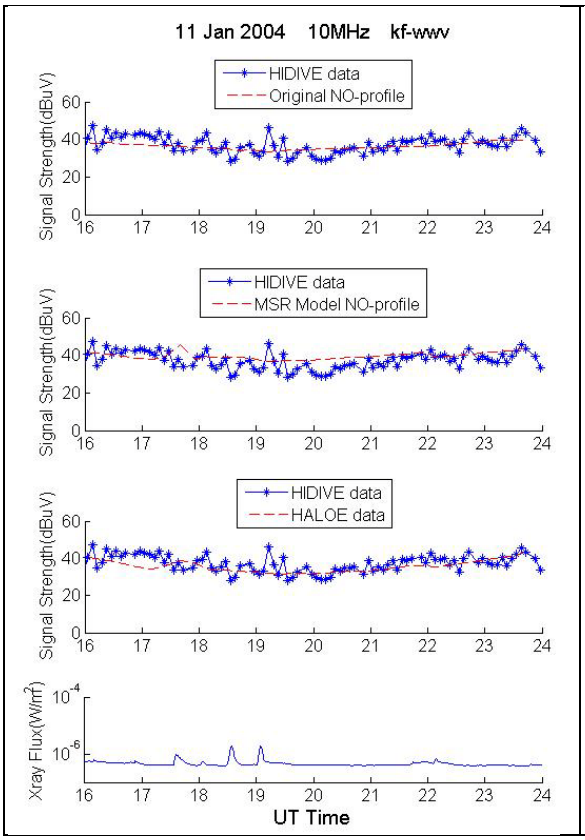

Figure E.1. HIDIVE data, GOES data, and AbbyNormal version predictions for the 10 MHz kf-wwv transmission on 11 January 2004.

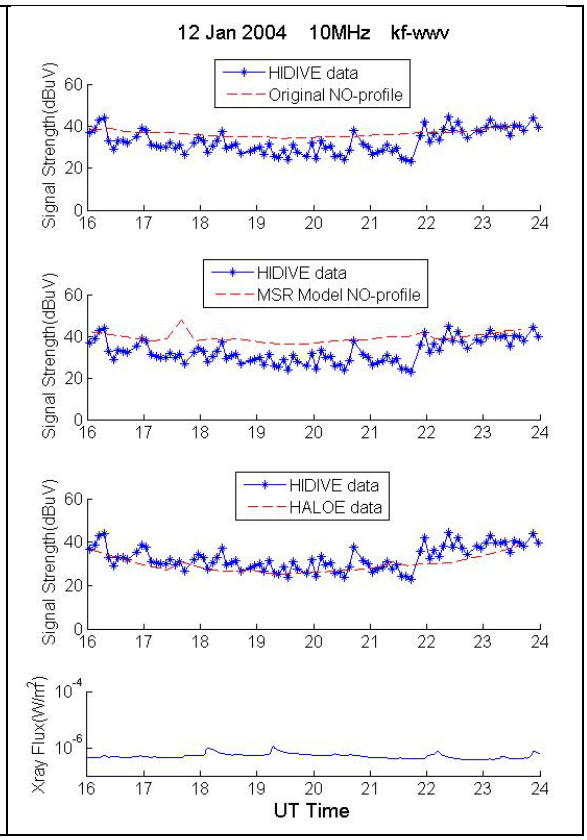

Figure E.2. HIDIVE data, GOES data, and AbbyNormal version predictions for the 10 MHz kf-wwv transmission on 12 January 2004.

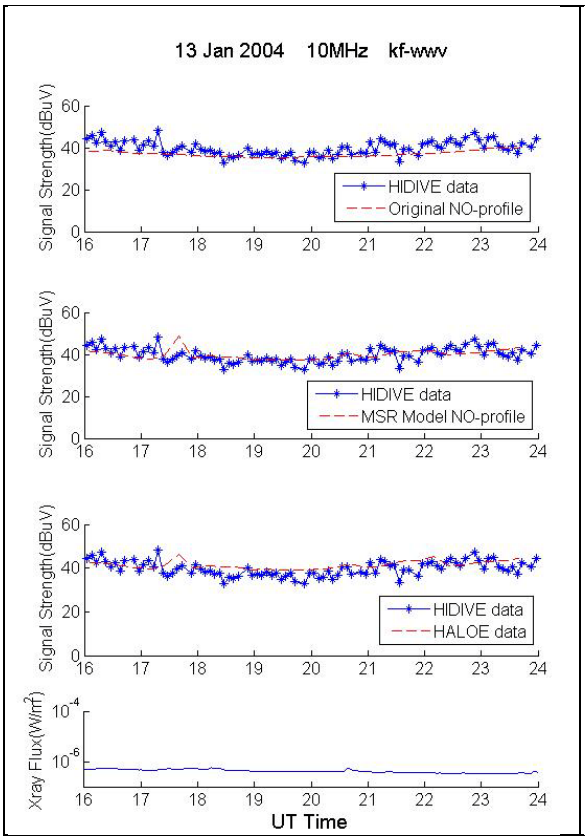

Figure E.3. HIDIVE data, GOES data, and AbbyNormal version predictions for the 10 MHz kf-wwv transmission on 13 January 2004.

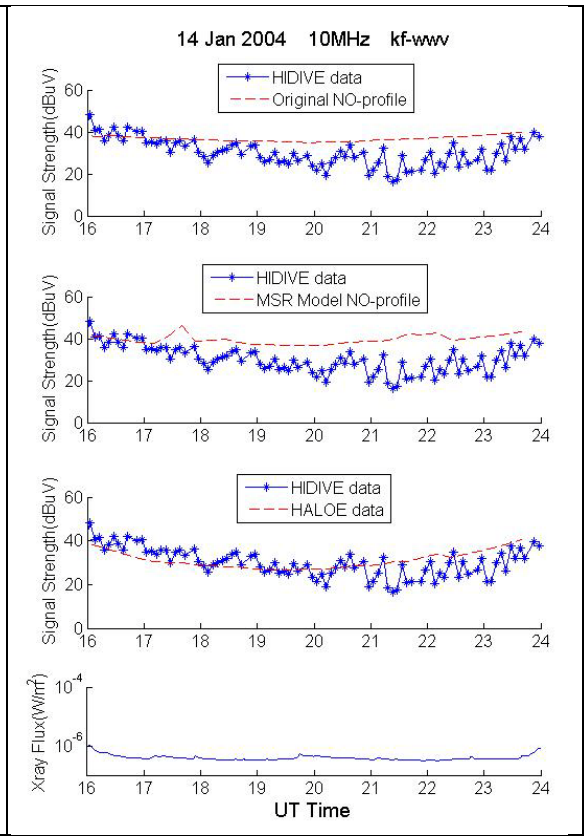

Figure E.4. HIDIVE data, GOES data, and AbbyNormal version predictions for the 10 MHz kf-wwv transmission on 14 January 2004.

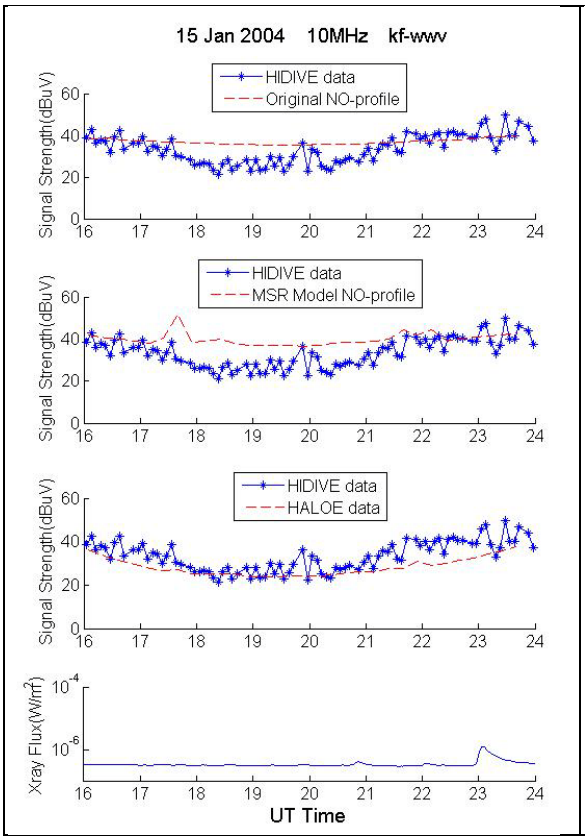

Figure E.5. HIDIVE data, GOES data, and AbbyNormal version predictions for the 10 MHz kf-wwv transmission on 15 January 2004.

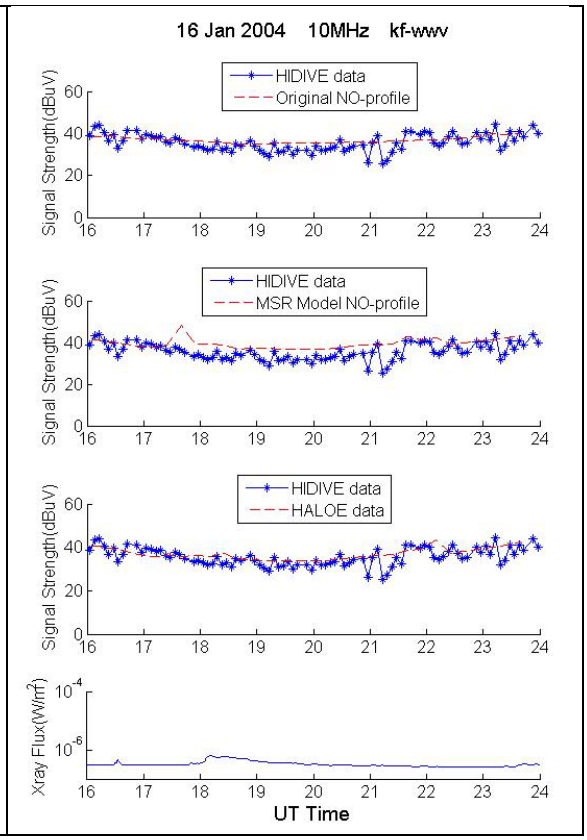

Figure E.6. HIDIVE data, GOES data, and AbbyNormal version predictions for the 10 MHz kf-wwv transmission on 16 January 2004.

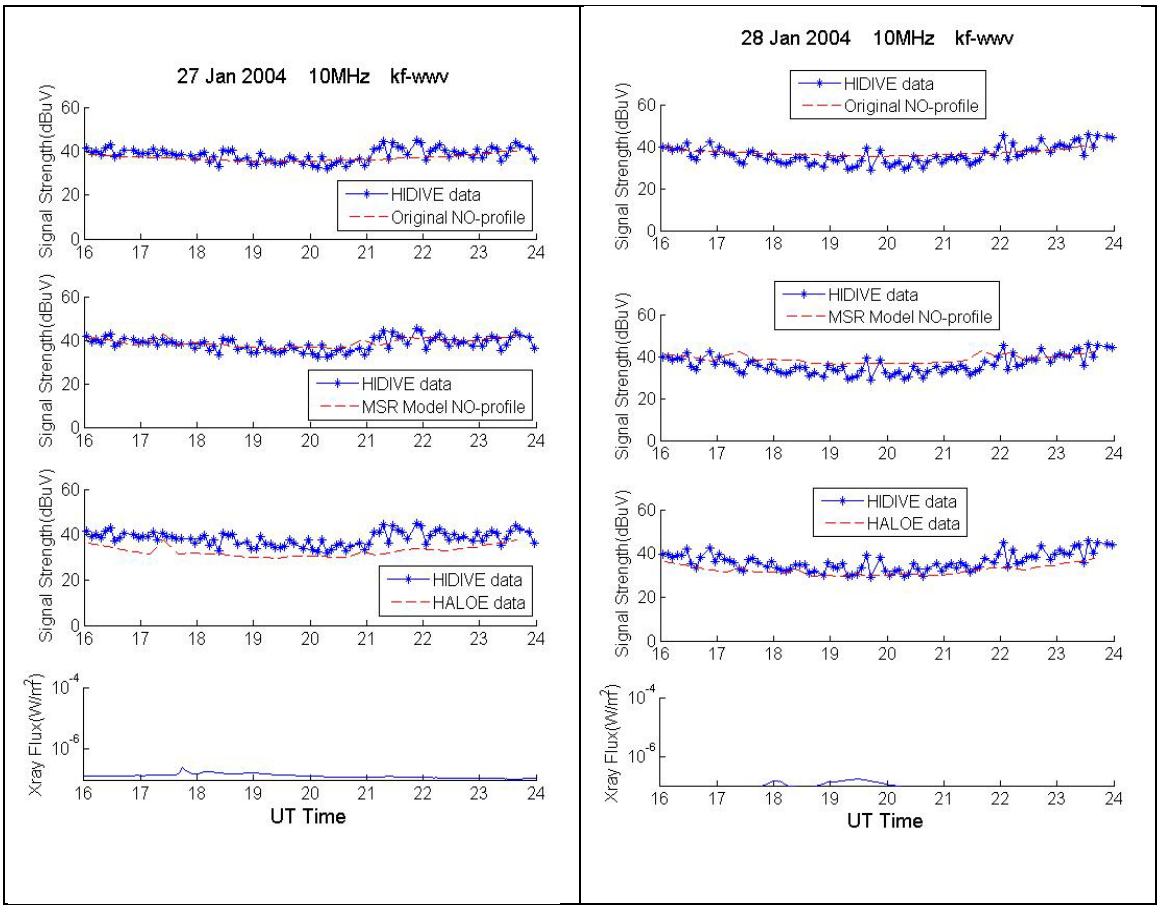

Figure E.7. HIDIVE data, GOES data, and AbbyNormal version predictions for the 10 MHz kf-wwv transmission on 27 January 2004.

Figure E.8. HIDIVE data, GOES data, and AbbyNormal version predictions for the 10 MHz kf-wwv transmission on 28 January 2004.

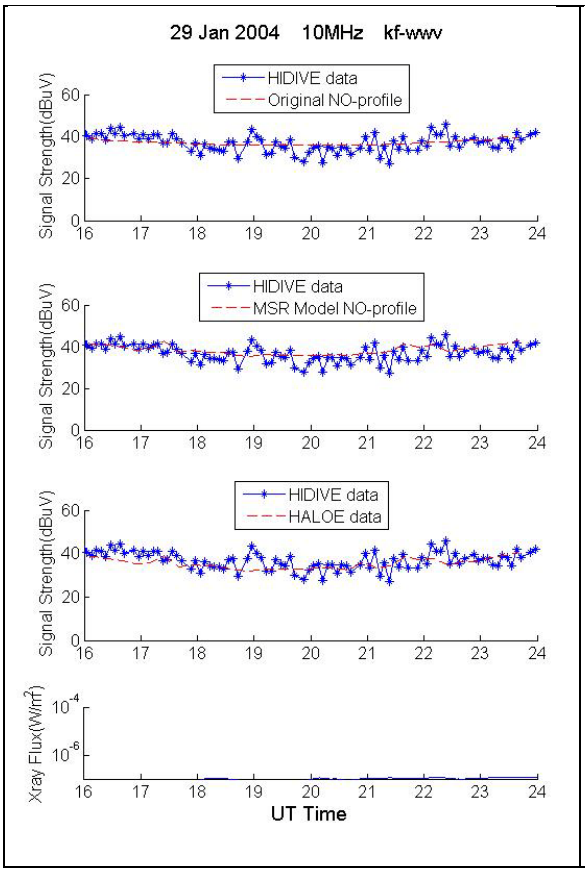

Figure E.9. HIDIVE data, GOES data, and AbbyNormal version predictions for the 10 MHz kf-wwv transmission on 29 January 2004.

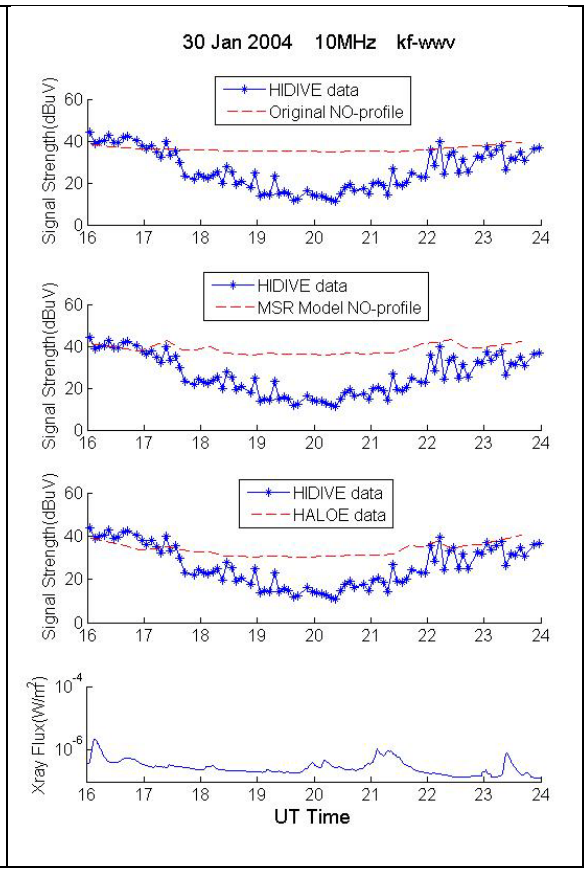

Figure E.10. HIDIVE data, GOES data, and AbbyNormal version predictions for the 10 MHz kf-wwv transmission on 30 January 2004.

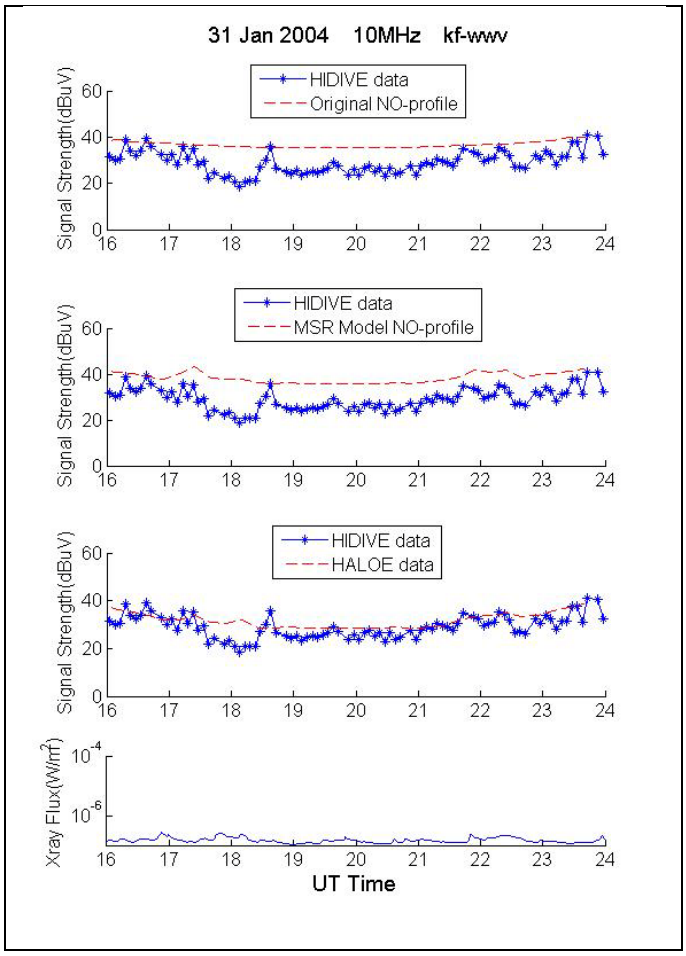

Figure E.11. HIDIVE data, GOES data, and AbbyNormal version predictions for the 10 MHz kf-wwv transmission on 31 January 2004.

Appendix F. AbbyNormal model versions predictions of 15 MHz kf-wwv transmission

The figures in this section show the predictions obtained from three versions of the AbbyNormal model (§9.4) for the 15 MHz kf-wwv HIDIVE transmission on eleven nearly consecutive dates in January 2004, and each figure shows the signal strength predictions of the three AbbyNormal versions, HIDIVE data, and GOES data for a given date. The three AbbyNormal versions all differ in how the NO profile is defined within the model. The top panel in each figure shows the prediction produced by the original AbbyNormal version in which the NO density profile is defined by equation 9.3.1. The second panel in each figure shows the prediction from the AbbyNormal version in which the NO profile is defined by the Empirical NO Model [*Marsh et al.*, 2004], and the third panel shows the prediction from the version in which HALOE data are used to define atmospheric NO densities. Also, GOES 0.1-0.8 nm flux data for the given date are shown in the bottom panel of each figure.

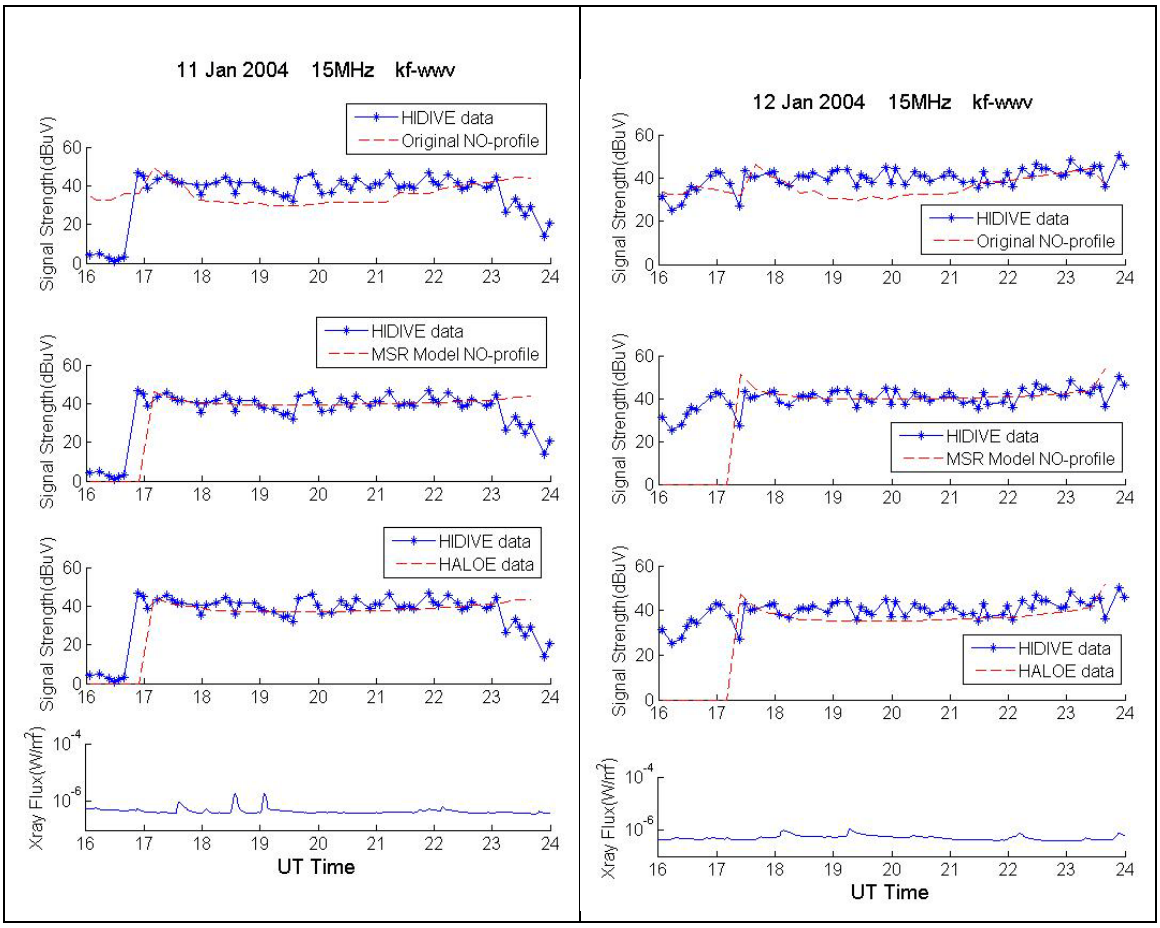

Figure F.1. HIDIVE data, GOES data, and AbbyNormal version predictions for the 15 MHz kf-wwv transmission on 11 January 2004.

Figure F.2. HIDIVE data, GOES data, and AbbyNormal version predictions for the 15 MHz kf-wwv transmission on 12 January 2004.

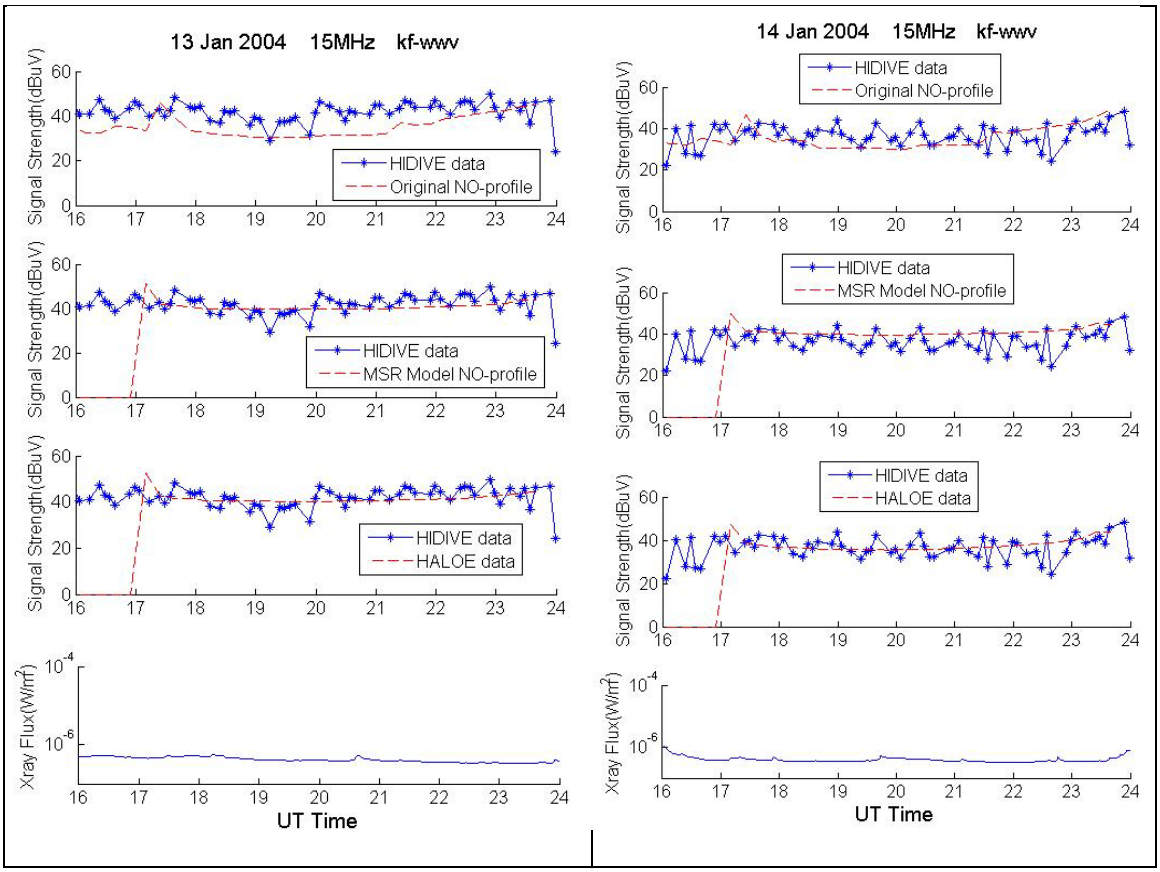

Figure F.3. HIDIVE data, GOES data, and AbbyNormal version predictions for the 15 MHz kf-wwv transmission on 13 January 2004.

Figure F.4. HIDIVE data, GOES data, and AbbyNormal version predictions for the 15 MHz kf-wwv transmission on 14 January 2004.

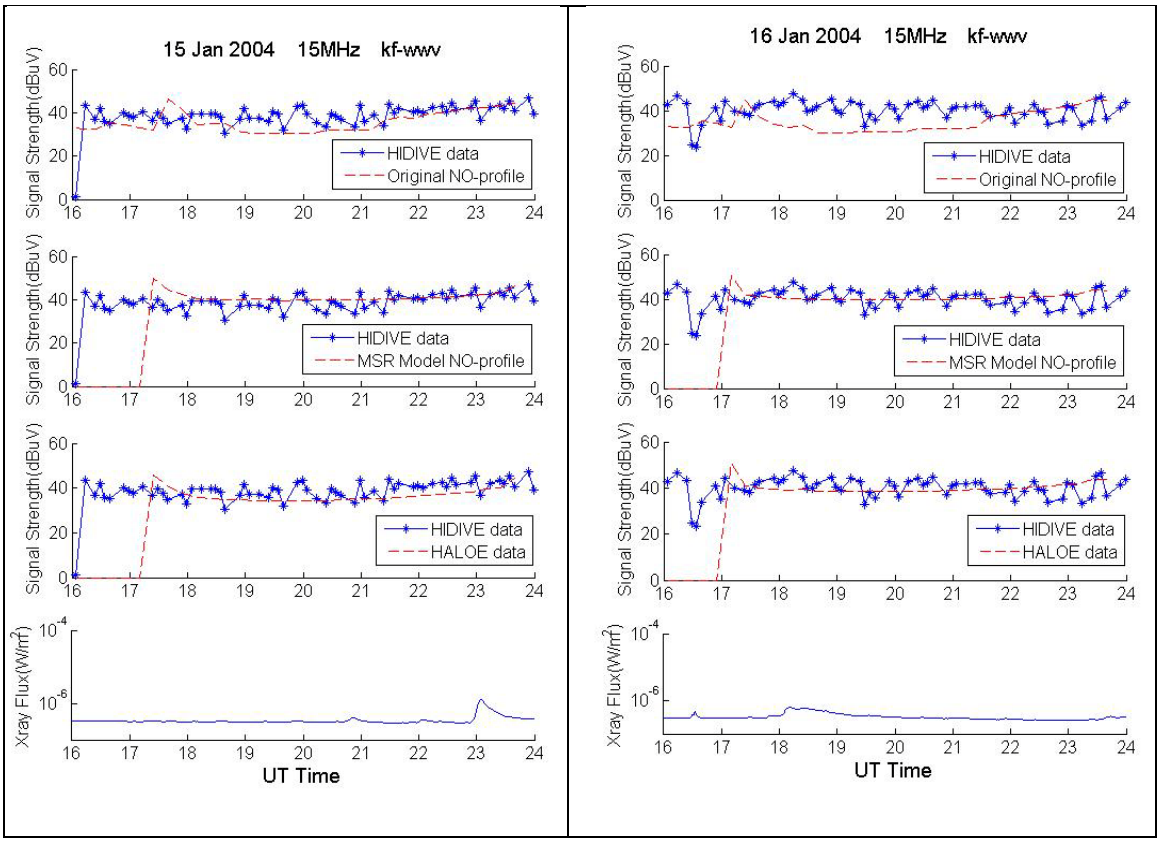

Figure F.5. HIDIVE data, GOES data, and AbbyNormal version predictions for the 15 MHz kf-wwv transmission on 15 January 2004.

Figure F.6. HIDIVE data, GOES data, and AbbyNormal version predictions for the 15 MHz kf-wwv transmission on 16 January 2004.

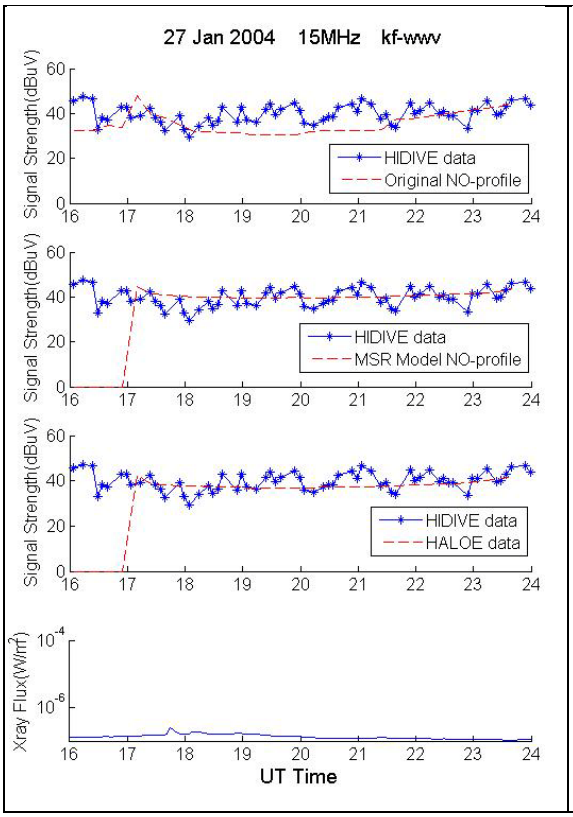

Figure F.7. HIDIVE data, GOES data, and AbbyNormal version predictions for the 15 MHz kf-wwv transmission on 27 January 2004.

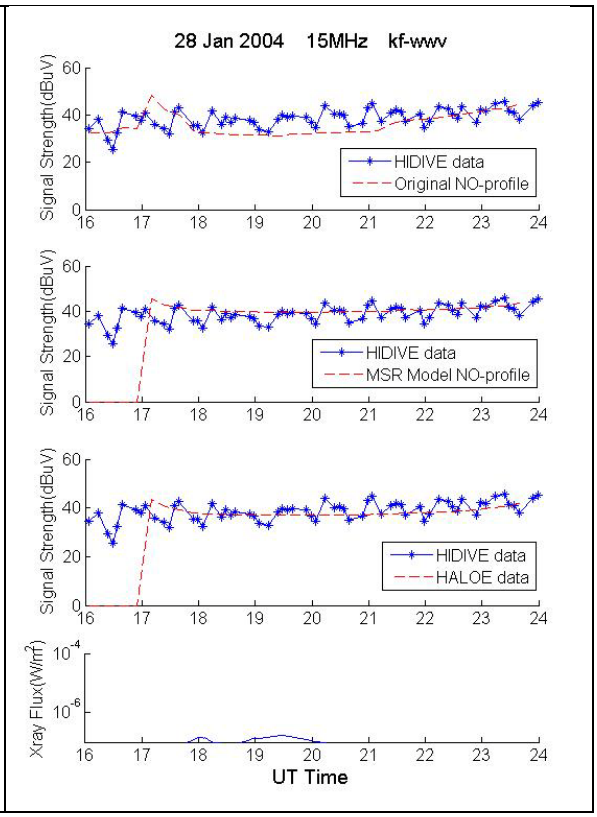

Figure F.8. HIDIVE data, GOES data, and AbbyNormal version predictions for the 15 MHz kf-wwv transmission on 28 January 2004.

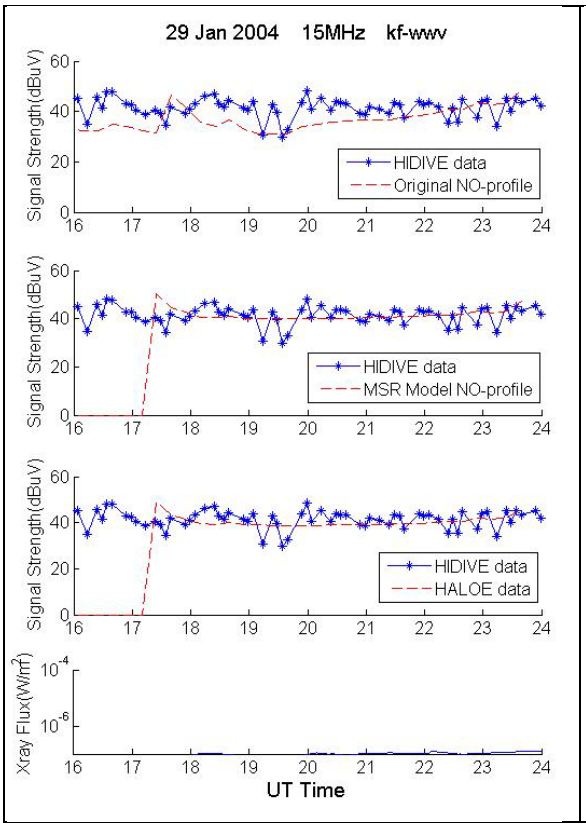

Figure F.9. HIDIVE data, GOES data, and AbbyNormal version predictions for the 15 MHz kf-wwv transmission on 29 January 2004.

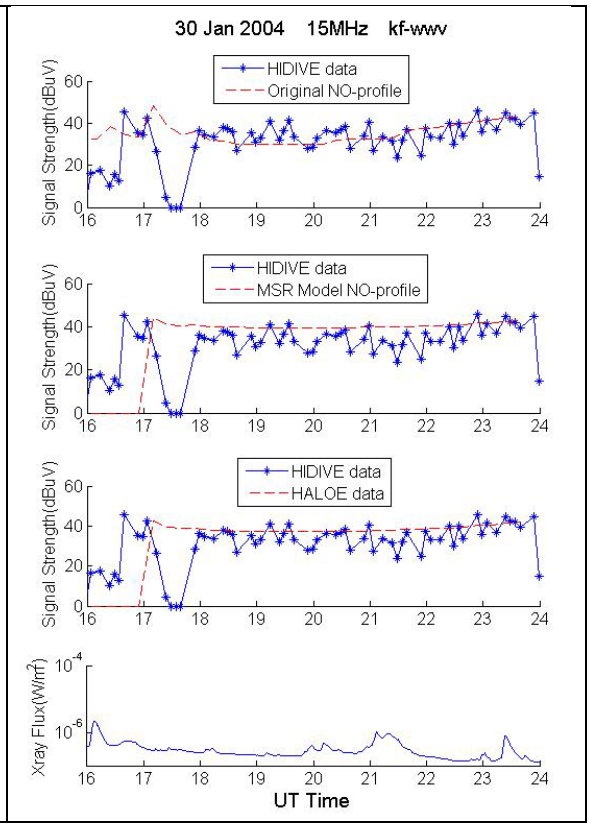

Figure F.10. HIDIVE data, GOES data, and AbbyNormal version predictions for the 15 MHz kf-wwv transmission on 30 January 2004.

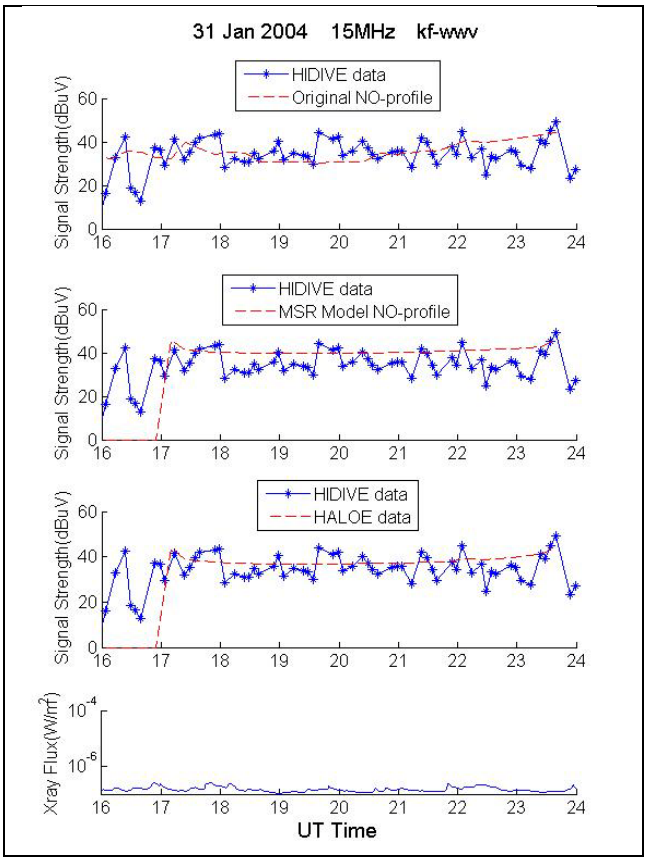

Figure F.11. HIDIVE data, GOES data, and AbbyNormal version predictions for the 15 MHz kf-wwv transmission on 31 January 2004.

Appendix G. Flare Availability

Table G.1. The table lists the availability of flare-induced absorption data for the various HIDIVE transmissions for absorption events fitting the initial selection criteria, which were (1) the flare had to occur between 1 November 2003 and 31 December 2006, (2) flare duration must be longer than 20 minutes, and (3) flare onset must be after 1800 UT.

		KF-WWV Signals			BLO-WWV Signals		
		5 MHz	10 MHz	15 MHz	5 MHz	10 MHz	15 MHz
1.	20031101		X	X			
2.	20031104		X	X			
3.	20031202		X				
4.	20031226		X	X	X	X	X
5.	20040117	X	X	X	X	X	
6.	20040226	X					X
7.	20040226	X	X	X	X	X	X
8.	20040318	X	X	X	X		X
9.	20040324						
10.	20040324		X	X	X	X	X
11.	20040521		X	X			
12.	20040713		X	X	X		
13.	20040715		X	X	X	X	
14.	20040715						
15.	20040717		X	X	X		
16.	20040717						
17.	20040722		X	X	X		
18.	20040723		X	X	X	X	
19.	20040724		X	X	X		
20.	20040727		X	X	X		
21.	20040813		X	X	X		
22.	20040813		X	X	X		
23.	20040817						
24.	20040817		X	X	X		
25.	20040817		X	X	X	X	
26.	20041024	X	X	X	X	X	X
27.	20041104		X	X	X		
28.	20041104		X	X	X		
29.	20050114		X	X			
30.	20050114	X	X	X			
31.	20050115		X	X	X	X	
32.	20050116		X	X	X		
33.	20050515		X	X	X		
34.	20050616		X	X	X	X	
35.	20050709		X	X	X		
36.	20050728		X	X	X	X	
37.	20050802						
38.	20050802		X	X	X		

Table G.1. Continued

	KF-WWV Signals			BLO-WWV Signals		
	5 MHz	10 MHz	5 MHz	10 MHz	5 MHz	10 MHz
39. 20050908		X	X	X		
40. 20050909		X		X		
41. 20050909		X		X		
42. 20050910		X	X	X	X	
43. 20050910		X		X		
44. 20050912		X		X		
45. 20050913		X		X		
46. 20050913		X		X		
47. 20050916		X	X	X	X	
48. 20051202	X	X		X		
Number of cases available	7	42	34	36	13	6

Table G.2. The table lists the availability of flare-induced absorption data for the various HIDIVE transmissions for absorption events fitting the final "Premeir" selection criteria, which included the following in addition to the initial criteria: (1) No local interference is suspected during the day of the flare, (2) HIDIVE data show no apparent delay between flare onset and the start of flare-induced absorption, (3) HIDIVE data show no delay between flare peak and maximum flare-induced absorption, and (4) No suspected propagation mode changes are occurring on the day of the flare

	Flare Classification	Date	5 MHz BLO-WWV	10 MHz KF-WWV	15 MHz KF-WWV
1	M 1.1	20031101		X	
2	M 3.2	20031101		X	
3	M 1.5	20031226	X	X	
4	M 5.0	20040117	X	X	
5	C 7.5	20040226	X	X	
6	M 5.6	20040226	X	X	X
7	M 1.5	20040318		X	
8	M 2.6	20040521		X	
9	M 1.2	20040713		X	
10	X 1.6	20040715		X	
11	C 7.9	20040715		X	X
12	M 2.5	20040717		X	X
13	M 2.0	20040717		X	X
14	M 1.2	20040717		X	X
15	M 1.6	20040722			
16	M 2.3	20040723		X	X
17	M 1.2	20040723		X	X

Table G.2. Continued

	Flare Classification	Date	5 MHz BLO-WWV	10 MHz KF-WWV	15 MHz KF-WWV
18	M 2.5	20040724		X	X
19	M 1.5	20040727			
20	M 3.1	20040813		X	
21	C 7.2	20040817		X	X
22	M 2.4	20040817		X	
23	M 1.9	20040817			X
24	M 2.3	20041024		X	
25	M 2.5	20041104	X		
26	M 1.5	20050114		X	
27	C 8.8	20050115			
28	X 2.6	20050115		X	
29	M 2.4	20050116	X	X	
30	M 3.5	20050515		X	
31	M 4.0	20050616			
32	M 2.8	20050709		X	X
33	M 4.8	20050728			X
34	M 4.2	20050802		X	X
35	C 6.7	20050802		X	
36	M 2.1	20050908		X	
37	M 2.1	20050908		X	
38	X 5.4	20050908		X	
39	M 1.9	20050909	X	X	
40	X 6.2	20050909	X		
41	X 1.2	20050910		X	
42	M 4.1	20050910		X	X
43	X 2.1	20050910			
44	M 1.5	20050912			
45	X 1.7	20050913			
46	X 1.5	20050913			
47	M 1.4	20050916	X	X	X
48	M 3.5	20050916	X	X	X
49	M 2.0	20051202	X	X	
	Number of Flares Available		9	36	16

Bibliography

Anderson, G. P., A. Berk, P. K. Acharya, M. W. Matthew, L. S. Bernstein, J. H. Chetwynd, H. Dothe, S. M. Adler-Golden, A. J. Ratkowski, G. W. Felde, J. A. Gardner, M. L. Hoke, S. C. Richtsmeier, B. Pukall, J. Mello and L. S. Jeong, MODTRAN4: Radiative Transfer Modeling for Remote Sensing, In Algorithms for Multispectral, Hyperspectral, and Ultraspectral Imagery VI , *Proceedings of SPIE* Vol. 4049, pg. 176-183, 2000.

Aune, S.C. Comparison of Ray Tracing through Ionospheric Models. Thesis. Air Force Institute of Technology, Wright-Patterson AFB, Ohio, School of Engineering and Management, ADA451343, 2006.

Bailey, S.M., C.A. Barth and S.C. Solomon, A model of nitric oxide in the lower thermosphere, *J. Geophys. Res.*, 107, 10.1029/2001JA000258, 2002.

Beaver, G.M., L.L. Gordley, J.M. Russell, Halogen Occultation Experiment (HALOE) altitude registration of atmospheric profile measurements: lessons learned and improvements made during the data validation phase, SPIE Vol. 2266, p. 266-280, 1994.

Bilitza, D., International Reference Ionosphere 2000, *Radio Sci*., 36, 261–275, 2001.

Bishop, C.M., Neural Networks for Pattern Recognition. Oxford University Press: New York, 1995.

Bonadonna, Michael F. "Living with a star DoD prespective." *Living with a Star Workshop*, NASA Goddard Space Flight Center, Greenbelt, Maryland. 11 May 2000.

Budden, K.G., Radio Waves in the Ionosphere. Cambridge University Press: New York, 1961.

Burns, C.J., *et al.*, Chemical modeling of the quiet cummer D and E regions usgin EISCAT electron density profiles, *J. Atmos. Terr. Phys.*, 53, 115, 1991.

Butcher, N., "Daily ionospheric forecasting service (DIFS) III." *Annales Geophysicae*, 23, 3591-3598, 2005.

"CANOPUS Quiet Day Curve Generation," http://aurora.phys.ucalgary.ca/norstar/rio/doc/CANOPUS_Riometer_Baselining.pfd , 13 September 2008.

Chaimberlin, P.C., The flare irradiance spectral model (FISM). *Diss*. U of Colorado, 2005.

Chandrasekhar, S., Radiative Transfer. Dover Publications, Inc.: New York, 1960.

Chapman, S., and J. Bartels, Geomagnetism. Oxford University Press: New York, 1940.

Chen, F., Introduction to Plasma Physics and Controlled Fusion, Volume 1: Plasma Physics. Plenum Press: New York, 1984.

Coleman, C.J., A general purpose ionospheric ray tracing procedure, *Rep. SRL0130TR*, Def. Sci. and Technol. Org., Adelaide, S.A., Australia, 1993.

Cook, S.C. "HF communication in the information age." *7th International Comference on HF Radio Systems and Technigques*, Inst. Of Electr. Eng., Stevenage, U.K., 1997.

Cravens, T.E., Physics of Solar System Plasmas. Cambridge University Press: New York, 1997.

Davies, K., Ionospheric Radio. Peter Peregrinus Ltd: London, 1990.

Dellinger, J.H., Direct Effects of Particular Solar Eruptions on Terrestrial Phenomena. *Phys. Rev.* 50, 12, 1189-1189, 1936.

Deshpande, S.D., C.V. Subrahmanyam, and A.P. Mitra, Ionospheric effects of solar flares: The statistical relationship between X-ray flares and SID's, *J. Atm. Terr. Phys*., 34, 211-227, 1972.

Eccles, J.V., R.D. Hunsucker, D. Rice, J.J. Sojka, Space weather effects on midlatitude HF propagation paths: Observations and a data-driven D region model, *Space Weather*, 3, S01002, doi:10.1029/2004SW000094, 2005.

Gombosi, T.I., Physics of the Space Environment. Cambridge University Press: New York, 1998.

Goodman, J.M., D.R. Uffelman, HF SPECTRUM: New concepts and technologies. George Washington University Press: Washington D.C., 1984.

Grubor, D., D. Sulic, and V. Zigman, Influence of solar X-ray flares on the earth-ionosphere waveguide, *Serb. Astron. J*., doi:10.2298/SAJ0571029G, 171, 29-35, 2005.

Hargreaves, J. K.: Auroral Absorption of HF Radio Waves in the Ionosphere: A Review of Results from the First Decade of Riometry, Proceedings of the IEEE, 57(8), 1348–1373, 1969.

Hargreaves, J.K., The Solar-Terrestrial Environment. Cambridge University Press: UK, 1992.

Hargreaves, J.K., and M. Friedrich, The estimation of D-region electron densities from riometer data, *Annales Geophysicae*, 21, 603-613, 2003.

Harvey, G., Some relationships between 10.7 cm solar noise bursts, flares, and SWF, *ApJ* 139 p.16 1964.

Hedin, A. E., Extension of the MSIS Thermosphere Model into the Middle and Lower Atmosphere, *J. Geophys. Res.*, VOL. 96, NO. A2, PAGES 1159–1172, 1991.

Hervig, M.E.J.M. Russell, L.L. Gordley, J. Daniels, S.R. Drayson, J.H. Park, Aerosol effects and corrections in the Halogan Occultation Experiment, *J. Geophys. Res.*, 100, 1067-1080, 10.1029/94JD02143, 1995.

Huang, X., and B. W. Reinisch (2006), Real-time HF ray tracing through a tilted ionosphere, *Radio Science*, *41*(8).

Hunsucker, R.D., and J.K. Hargreaves, The High-Latitude Ionosphere and Its Effects on Radio Propagation. Cambridge University Press: New York, 2003.Jackson, J.D., Classical Electrodynamics. John Wiley and Sons, Inc.: New York, 1999.

Jackson, J.D., Classical Electrodynamics. John Wiley & Sons, Inc., 1999.

Jones, R.M., and J.J. Stephenson, A versatile three-dimensional ray tracing computer program for radio waves in the ionosphere, Institute for Telecommunication Sciences, U.S. Dept. of Commerce, Office of Telecommunications, Washington, Report 75-76. PB2488567, 1975.

Jursa, A.S., Handbook of Geophysics and the Space Environment. Air Force Geophysics Laboratory, Air Force Systems Command, US Air Force, 1985.

Keller, John. "The coming HF radio renaissance." Military and Aerospace Electronics, (http://mae.pennnet.com/display_article/153704/32/ARTCL/none/none/1/The-coming-HF-radio-renaissance/). September, 2002.

Lean, J.L., The sun's variable radiation and its relevance for Earth, *Annu. Rev. Astron. Astrophys.*, 35, 33, 1997.

Liu, J.Y., *et al.*, Ionospheric solar flare effects monitored by the gound-based GPS receivers: Theory and observation, *J. Goephys. Res.*, 109, doi:1029/ 2003JA009931, 2004.

Marsh, D.R., and J.M. Russell III, A tidal explanation for the sunrise/sunset anomaly in HALOE low-latitude nitric oxide observations, *Goephys. Res. Letters*. 27, 19, 3197-3200, 1 Oct 2000.

Marsh, D.R., S.C. Solomon, and A.E. Reynolds, Empirical model of nitric oxide in the lower thermosphere, *J. Goephys. Res.*, 109, A07301, doi:10.1029/2003JA010199, 2004.

McNamara, L., The Ionosphere: Communications, Surveillance, and Direction Finding. Krieger Publishing Company: Malabar, 1991.

Minschwaner, K., G.P. Anderson, L.A. Hall, R.J. Thomas, D. Rusch, A. Berk, J. Conant, Scattered Ultraviolet Radiation in the Upper Stratosphere, II: Modeling and Analysis, *J. Geophys. Res*., 100, 11165-11172, 1995.

Nickisch, L. J. (1988), Focusing in the stationary phase approximation, *Radio Sci.*, 23(2), 171-182.

Oyinloye, J.O., A new form of representation for temporal and spatial variations in radiowave absorption in the ionosphere. *J. Atmos. Terr. Phys*. 42, 437-441, 1980.

Oyinloye, J.O., On the seasonal variation of absorption of radio waves in the equatorial ionosphere. *J. Atmos. Terr. Phys*. 40, 793-798, 1978.

Phillips, K.J.H., Guide to the sun. New York, Cambridge University Press, 1995.

Poppoff, I.G., R.C. Whitten, and R.S. Edmonds, The Role of Nonflare X Radiation in the D Region. *J. Geophys. Res.* 69, 4081-4085, 1964.

Raizer, Y.P., J.E. Allen, and V.I. Kisin, Gas Discharge Physics. New York, Springer-Verlag, 1991.

Rees, W.G., Physics and Chemistry of the Upper Atmosphere. Cambridge University Press: Cambridge, 1989.

Renfree, P. "The US Navy returns to HF with STANAG5066 as the path." *Milcom 2001 Proceedings: Communications for Network-Centric Operations: Creating the Information Force*, Tysons Corner, McLean, Virginia USA, Vol 1., p 471-476, IEEE Press, Piscataway, N.J., 28-31 October 2001.

Rishbeth, H., and O.K. Garriott, Introduction to Ionospheric Physics. Academic Press, Inc.: New York, 1969.

Schunk, R.W., and A.F. Nagy, Ionospheres: Physics, Plasma Physics, and Chemistry. Cambridge University Press: New York, 2000.

SEC, *D-Region Absorption Documentation*, http://www.sec.noaa.gov/rt_plots/dregionDoc.html, 1 Jan 2007.

Spanswick, E.; Donovan, E.; Baker, G. Pc5 modulation of high energy electron precipitation: particle interaction regions and scattering efficiency . Annales Geophysicae, Volume 23, Issue 5, 2005, pp.1533-1542.

Stonehocker, G. H.: Advanced telecommunication forecasting technique in AGY, 5th., Ionospheric forecasting, AGARD Conf. Proc., 29, 27–31, 1970.

Strobel, D.F., C.B. Opal, and R.R. Meier, Photoionization rates in the night-time E- and F-region ionosphere. *Planetary and Space Science*, 28, 11, 1027-1033, 1980.

Tascione, T.F., Introduction to the Space Environment. Krieger Publishing Company: Malabar, 1994.

The Universe: Secrets of the Sun. The History Channel, 3 June 2007.

Titheridge, J.E., Model results for the ionospheric E region: solar and seasonal changes, *Annales Goephysicae*, 15, 63-78, 1997.

U.S. Government, U.S. Standard Atmosphere 1976, U.S. Government Printing Office: Washington, D.C., 1976.

Woods, T.N., G. Kopp, and P.C. Chamberlin, Contributions of the solar ultraviolet irradiance to the total solar irradiance during large flares, *J. Geophys. Res.*, 111, A10, 2006.

REPORT DOCUMENTATION PAGE

Form Approved
OMB No. 074-0188

1. REPORT DATE *(DD-MM-YYYY)*	**2. REPORT TYPE**	**3. DATES COVERED** *(From – To)*
25-03-2010	Doctoral Dissertation	Mar 2007 - March 2010

4. TITLE AND SUBTITLE

Improved Modeling of Midlatitude D-region Ionospheric Absorption of High Frequency Radio Signals during Solar X-ray Flares

5a. CONTRACT NUMBER

5b. GRANT NUMBER

5c. PROGRAM ELEMENT NUMBER

6. AUTHOR(S)

Schumer, Evelyn, A., Major, USAF

5d. PROJECT NUMBER

5e. TASK NUMBER

5f. WORK UNIT NUMBER

7. PERFORMING ORGANIZATION NAMES(S) AND ADDRESS(S)

Air Force Institute of Technology
Graduate School of Engineering and Management (AFIT/EN)
2950 Hobson Way
WPAFB OH 45433-7765

8. PERFORMING ORGANIZATION REPORT NUMBER

AFIT/DS/ENP/09-J01

9. SPONSORING/MONITORING AGENCY NAME(S) AND ADDRESS(ES)

Dr. Kent Miller
Air Force Office of Scientific Research (AFOSR/NE)
875 N. Randolph Street, Room 3112
Arlington, VA 22203

10. SPONSOR/MONITOR'S ACRONYM(S)

AFOSR

11. SPONSOR/MONITOR'S REPORT NUMBER(S)

12. DISTRIBUTION/AVAILABILITY STATEMENT

APPROVED FOR PUBLIC RELEASE; DISTRIBUTION UNLIMITED

13. SUPPLEMENTARY NOTES

14. ABSTRACT

The purpose of this research was to improve modeling of midlatitude D-region ionospheric absorption of high frequency radio signals during solar X-ray flares through analysis of HF propagation data obtained during the HF Investigation of D-region Ionospheric Variation Experiment (HIDIVE) and obtained at the Canadian Space Agency NORSTAR riometer in Pinawa, Manitoba, Canada and X-ray flux data, as reported by GOES satellites. The findings of the data analysis were then used to validate and suggest improvements for two existing HF absorption models, the operational Space Weather Prediction Center (SWPC) D-region Absorption model and the physical AbbyNormal model. Analysis of the HIDIVE data revealed an absorption dependence on signal frequency and a dependence on solar zenith angle which differ from those used in the SWPC model. Analysis of nitric oxide (NO) density data obtained with the Student Nitric Oxide Explorer and during the Halogen Occultation Experiment provided improved methods of defining NO profiles within AbbyNormal.

15. SUBJECT TERMS

Midlatitude D-region Ionospheric Absorption, High Frequency Radio Signals, Solar X-ray Flares, Ionospheric Modeling, HF propagation Prediction, HF Absorption

16. SECURITY CLASSIFICATION OF:			**17. LIMITATION OF ABSTRACT**	**18. NUMBER OF PAGES**	**19a. NAME OF RESPONSIBLE PERSON**
a. REPORT	**b. ABSTRACT**	**c. THIS PAGE**			William F. Bailey (AFIT/ENP)
U	U	**U**	**UU**	253	**19b. TELEPHONE NUMBER** *(Include area code)* (937)255-3636,ext 4501; william bailey@afit.edu